International Committee for Future Accelerators

Sponsored by the Particles and Fields Commission of IUPAP

Beam Dynamics Newsletter

No. 68

Issue Editor:
J. Wang

Editor in Chief:
W. Chou

December 2015

Contents

1 Foreword

1.1 From the Chair

Weiren Chou, Fermilab
Mail to: chou@fnal.gov

The year of 2015 ended on a high note – before its winter shutdown, the LHC Run2 announced in mid-December that both ATLAS and CMS observed a new resonance in the di-photon distribution at an invariant mass of 750 GeV. Although the collected data was too small to either confirm or discard it, there was an instant enormous interest in the world HEP community. In less than two weeks, more than 150 papers were written and distributed trying to develop theories explaining the nature of this new resonance. This was a genuine display of the great expectation people have on the LHC Run2. No matter what happens to this bump – real or just a coincidence – we need to fasten our seat belts because 2016 will no doubt be an exciting year in high gear.

2016 will also be important for the ILC. The Japanese MEXT ILC Advisory Panel is expected to release a final report in summer, which will give recommendation to the Japanese government about whether or not Japan should host the construction of the ILC. In preparation for the case of a "Green Light" from MEXT, KEK compiled and published an ILC Action Plan. The plan defines three phases: pre-preparation (present), main preparation (4 years) and construction (9 years). The earliest possible experiment start would be 2029.

On the future circular collider side, both CERN and IHEP are working hard and making significant progresses. There will be a number of meetings and workshops for the FCC as well as for the CEPC-SPPC in 2016.

As the traditional acceleration technology by using radiofrequency systems is reaching its limit, it is of utmost importance to develop advanced technologies such as dielectric wakefield, laser-plasma and beam-plasma acceleration. The US DOE is organizing a workshop in February to chart a roadmap for these researches. Europe and Asia are taking similar action.

The 9th International Accelerator School for Linear Colliders co-organized by the Linear Collider Collaboration (LCC), ICFA Beam Dynamics Panel and TRIUMF took place Oct 26 – Nov 6, 2015 in Whistler, British Columbia, Canada. A school report can be found in Section 3.3. (http://www.linearcollider.org/school/2015/)

The editor of this issue is Dr. Jiuqing Wang, a panel member and a senior scientist at IHEP, China. The theme is "*ERL and the Beam Dynamics Challenges.*" He collected 9 well-written articles. The first ERL paper was published in 1965. 2015 marks the 50th anniversary. The author of the original paper, Maury Tigner wrote an overview of past, present and future of the ERL principle as a leading article. It was followed by eight articles discussing in detail the beam physics issues and applications in several laboratories around the world.

In this issue there are also two ICFA workshop reports (*ERL2015, Beam Commissioning for High Intensity Accelerators*), four recent doctoral thesis abstracts

(Michaela Schaumann of Aachen University, Germany; Zhe Duan, Yuanyuan Guo and Saike Tian, all three from IHEP, China) and three workshop announcements (*Cyclotron 2016, HB 2016, IBIC 2016*). I want to thank Jiuqing for editing a valuable newsletter of high quality for the accelerator community.

1.2 From the Editor

Jiuqing Wang
IHEP, P.O. Box 918, Beijing 100049, China
Mail to: wangjq@ihep.ac.cn

Since this year 2015 is the 50th anniversary of the publication of the ERL principal, and also with the inspiration from the 56th ICFA Advanced Beam Dynamics Workshop on Energy Recovery Linacs (ERL2015), the topic for the theme section of this issue of Beam Dynamics Newsletter is chosen as "ERL and the beam dynamics challenges." In the 50 years, ERL was developed from the original idea to the test facilities of the principle, and then the beginning of applications in discovery researches. Thanks to the enthusiastic support of the corresponding authors, I collected 9 articles in the theme section. They are arranged as the follows:

The first article by Maury Tigner provides a very comprehensive overview on the development of ERL tracing the path from the invention to the first test of principal as well as some recent and currently operating machines, and then the concepts of future. Following are two papers on the aspect of application of ERL as high brightness synchrotron radiation light sources, Michael Abo-Bakr and Alexander Matveenko review the beam dynamics issues of ERL based light sources, Hiroshi Kawata reports the successful commissioning on compact ERL (cERL) in KEK. Then three papers are on the aspect of application of ERL on electron-ion and electron-proton colliders, O. Brüning and collaborators report the development of an ERL based TeV energy ep and eA collider at CERN, Yue Hao and Vadim Ptitsyn discuss the beam dynamics issues for ERL-based Electron-Ion Colliders. Dmitry Kayran for the ERL team reports the commissioning progress of the Energy Recovery Linac at Brookhaven National Laboratory. The last three papers are on the aspect of some common challenges of ERL on beam dynamics and technologies, Stephen Brooks, Dejan Trbojevic, and Scott J. Berg discuss FFAG's in ERLs, Simone Di Mitri reports the design of transverse emittance preserving arc compressor, Wencan Xu discusses the considerations of SRF linac for high current ERL.

In the section of workshop and conference report, the 56th ICFA Advanced Beam Dynamics Workshop on Energy Recovery Linacs (ERL2015) and the ICFA Mini-Workshop on Beam Commissioning for High Intensity Accelerators are reported.

In section 4, there are abstracts of four recently finished doctoral theses.

In section 5, three future beam dynamics events can be found: 1) the 21th International Conference on Cyclotrons and their Applications, 2) The 57th Advanced Beam Dynamics Workshop on High Intensity and High Brightness Hadron Beams (HB2016), 3) International Beam Instrumentation Conference (IBIC 2016).

I would like to thank all of the authors for their hard work and excellent contributions to this issue of newsletter. Finally, I would also thank Ms. Ning Zhao, secretary of the accelerator division of IHEP, for her professional editing of this issue.

2 Theme Section: ERL, and the Beam Dynamics Challenges

2.1 ERL: Past, Present and Future

Maury Tigner
Cornell University, Ithaca, NY 14853
Mail to: mt52@cornell.edu

2.1.1 Introduction

This year we celebrate the 50th anniversary of the publication of the ERL principle. The invention of this idea was driven by the concern that achieving multi-GeV energies with colliding electron (positron) beams would eventually be prohibited by the synchrotron radiation that would be produced by circular colliders in that energy range. History has shown that only just now have we reached energies where serious contemplation of linear colliders and linear on circular colliders is underway. Other uses for the technology have been contemplated in the meantime as well as we shall see. We trace the path of development from the original publication through a long fallow period and then the test of the principle and the beginnings of application for discovery science. In addition, it is only recently that the acceptable yield of high field, high Q structures has become reliable enough for basing facilities on the ERL principle.

2.1.2 The Invention

The result of pursuing the consequences of the concern mentioned above was an article in Nuovo Cimento for Feb. 1965, the cover page of which is shown in Figure 1.

LETTERE ALLA REDAZIONE

(La responsabilità scientifica degli scritti inseriti in questa rubrica è completamente lasciata dalla Direzione del periodico ai singoli autori)

A Possible Apparatus for Electron Clashing-Beam Experiments (*).

M. TIGNER

Laboratory of Nuclear Studies, Cornell University - Ithaca, N. Y.

(ricevuto il 2 Febbraio 1965)

Figure 1: Title page of 1965 article.

Two arrangements of the apparatus as presented in tha article are shown in Figures 2a and 2b. The spacings are arranged so that when a beam emerges from an acceleration section, it has slipped one odd multiple half wavelength of the exciting rf at the point of entry into the decelerating section where it gives up its kinetic energy to the field in the guide.

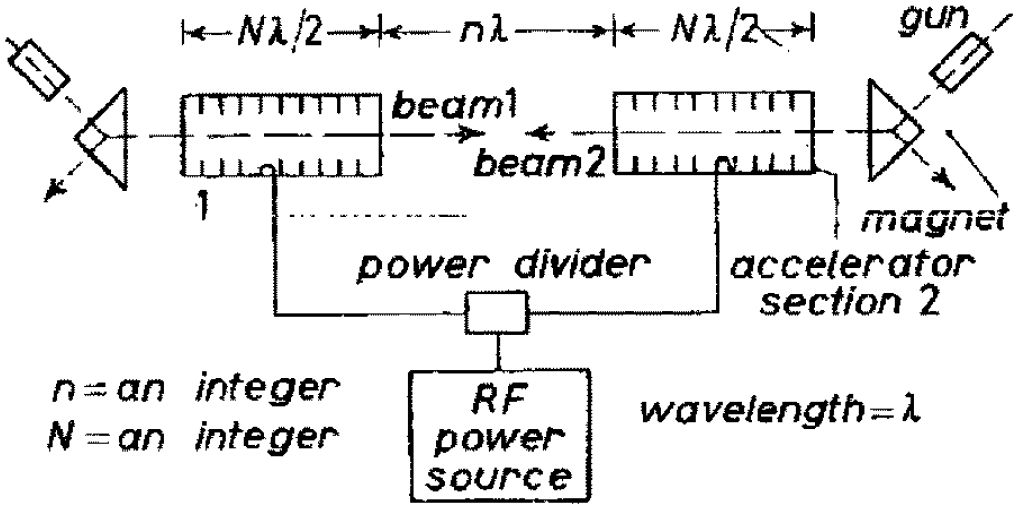

Figure 2a: Idealized arrangement for colliding particles of either equal or opposite charges.

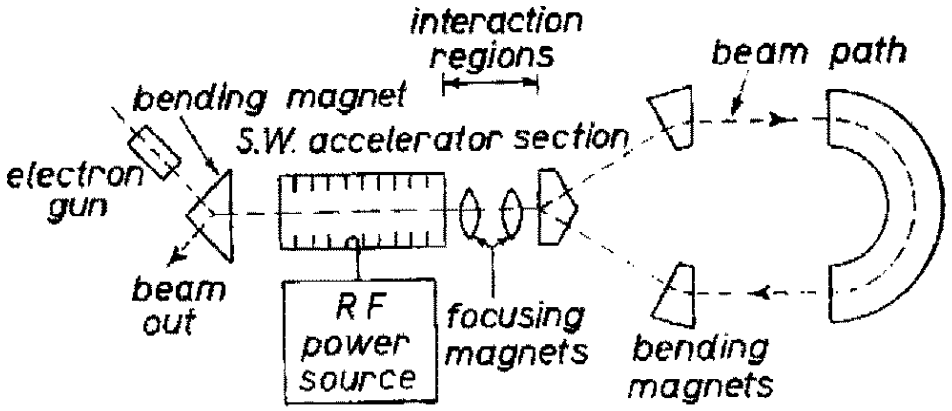

Figure 2b: Idealized arrangement for colliding particles of equal charge at energies below which synchrotron radiaiton becomes significant in the turnaround arc.

Of course neither of these configurations using rf superconductivity would have been possible back then owing to the rather primitive status of the technology. Further, for beams of significant current, the layouts are too simple as some means of avoiding beam-beam collisioins other than at the designated collision points is needed. At that time, understanding of beam-beam effects was just at the very beginning. It is only quite recently that the reliable yield of high field, high Q superconducting cavities has become sufficient for making the ERL ready for prime time.

2.1.3 **First Test**

Already in 1975 [1] a demonstration in which a beam is accelerated and decelerated in the same cavity was made in a normal conducting linac. The first superconducting ERL demonstration was done at the Stanford SCA in 1986 [2]. The layout and primary parameters are shown in Figure 3.

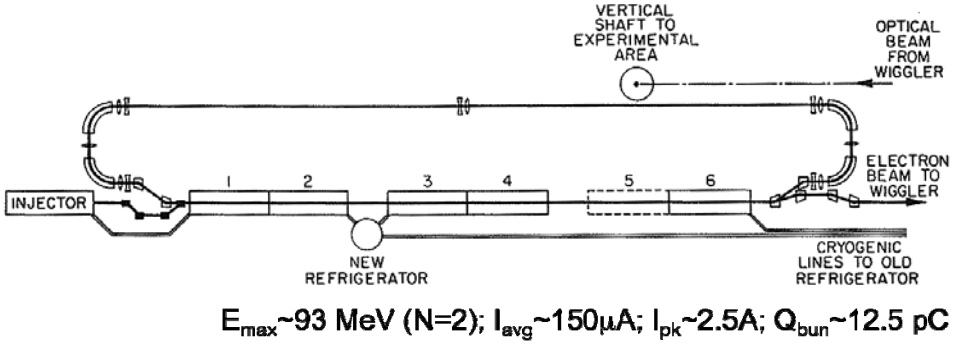

Figure 3: Layout of the SCA at Stanford in which the ERL principle was demonstrated.

2.1.4 Some Recent and Currently Operating Machines

2.1.4.1 *JAEA ERL FEL*

Figure 4 shows the JAEA 17 MeV ERL [3].

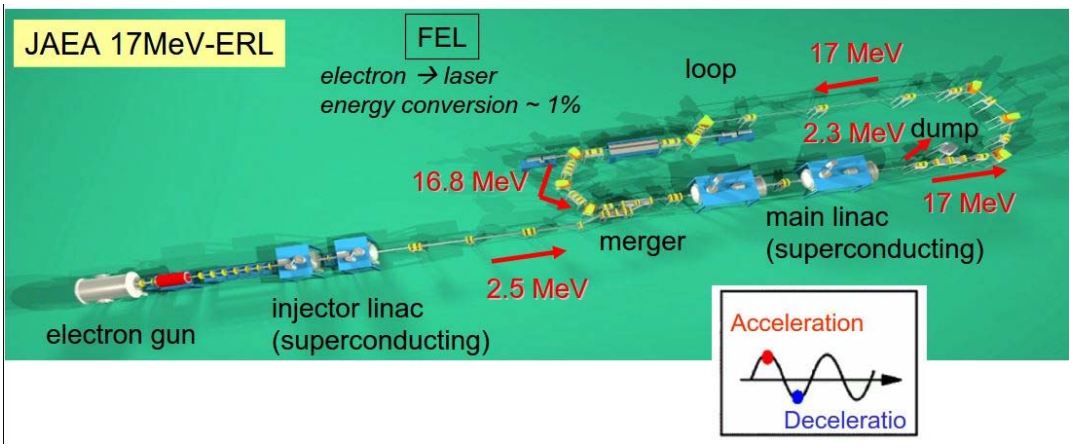

$$I_{inj} = 10ma;\ P_{FEL} = 0.7kW$$

Figure 4: The JAEA FEL showing the full machine from gun to dump at 2.3 MeV.

2.1.4.2 *The Jefferson Lab ERL FEL*

The Jefferson Lab IR FEL upgrade [4] layout is shown in Figure 5.

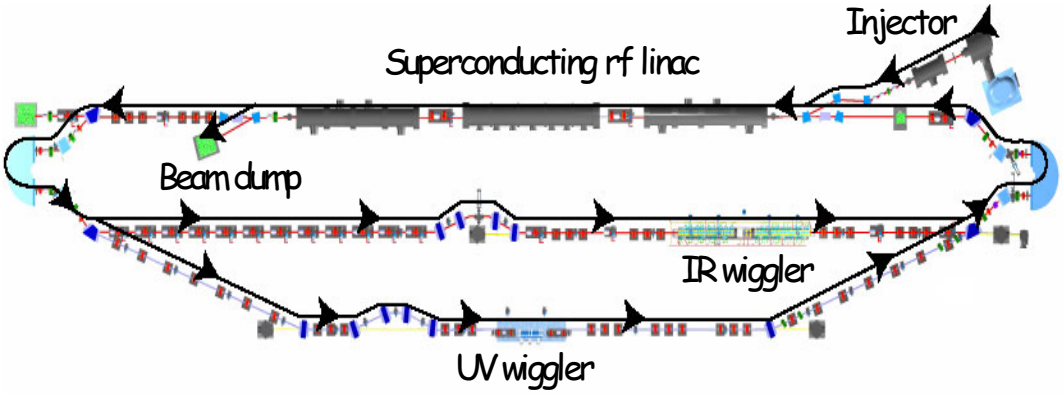

E_{max}=200 MeV; I_{pk}=270A; ε<11 μm; Q_{max}=135 pC; f_{bun}=4.7 – 75 MHz; $P_{beam,\ max}$=2 MW – largest anywhere to date

Figure 5: Jefferson Lab FEL , the most powerful to date.

2.1.4.3 *The Novosibirsk ERL with 3 FEL's*

A 4 turn, normal conducting ERL with 3 FEL's [5] is now operating at Budker Institute of Nuclear Physics, BINP. The layout and photo are shown in Figures 6 and 7

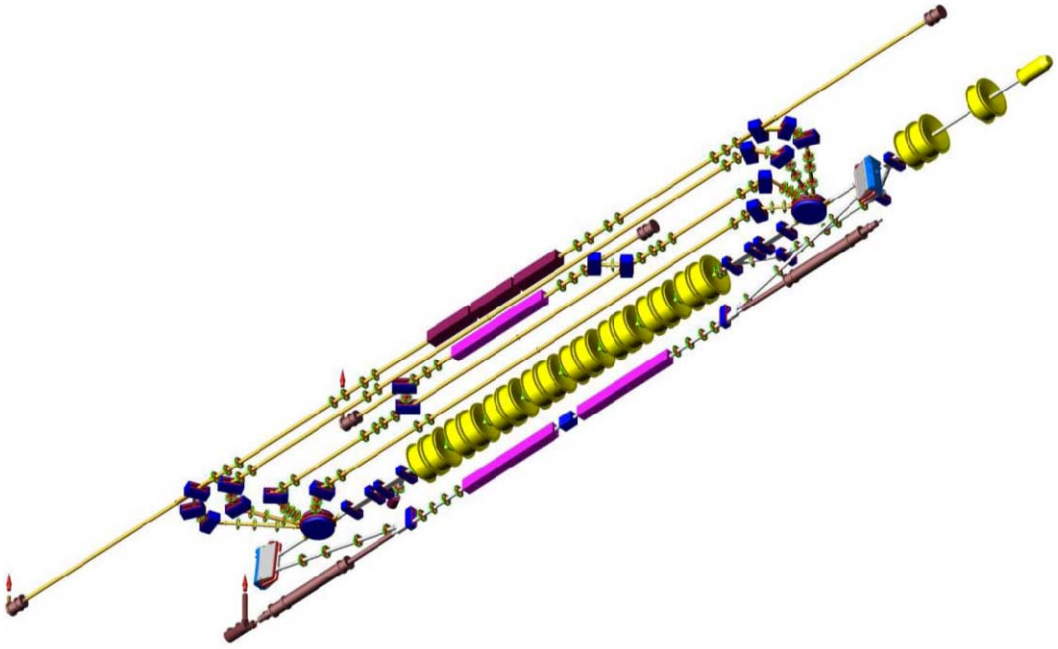

$E_{inj} = 2MeV;\ E_{mainlinacgain} = 10MeV;\ Q_{bun} = 1.5nC;\ I_{avg} = 5mA$

$\varepsilon = 20\mu m;\ f_{rf} = 180MHz;\ f_{bun} = 90MHz;\ N_{turns} = 3$ (4 in commissioning)

Figure 6: Normal conducting FEL at BINP.

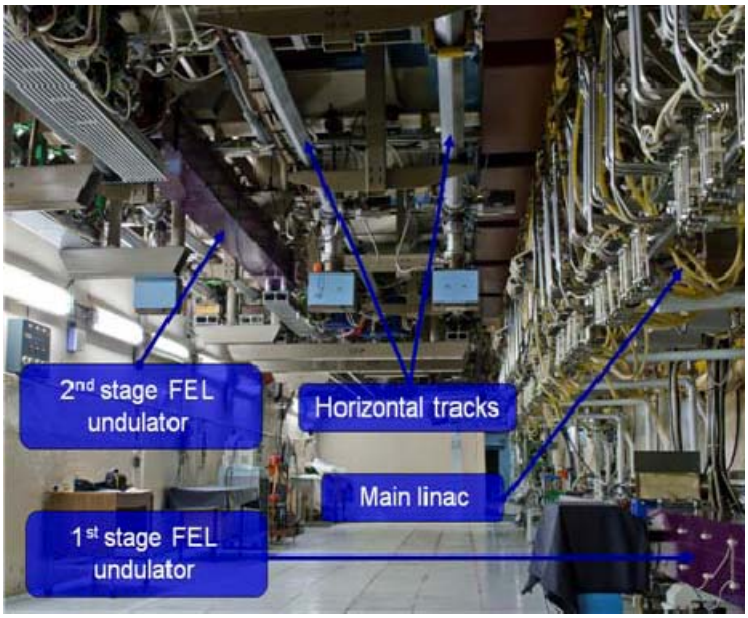

Figure 7: Photo of the BINP 3 pass ERL.

2.1.4.4 *cERL at KEK*

This compact ERL at KEK [6] serves as prototype for a future 3 GeV x-ray generating ERL.

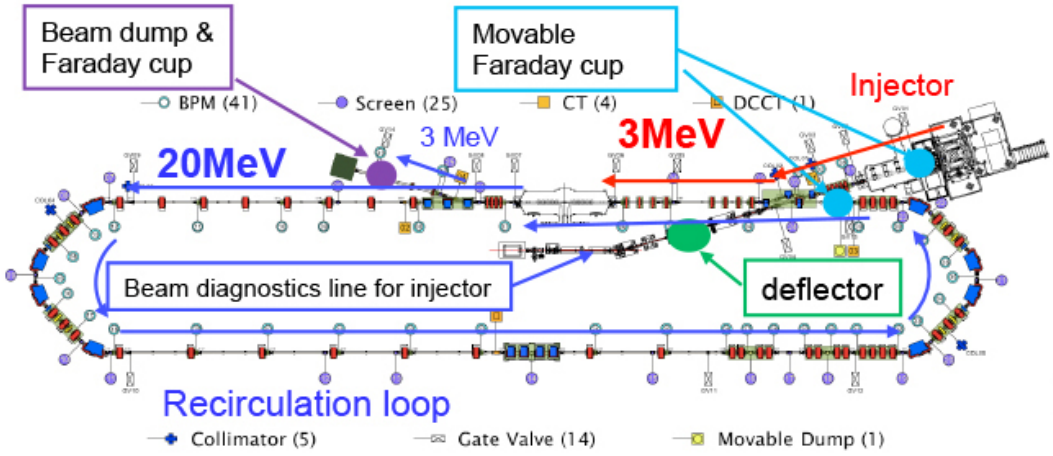

$E_{inj,goal} = 5MeV;\ (E_{in,,oper} = 2.9MeV);\ E_{\max,goal} = 35MeV;\ (E_{\max,oper} = 20MeV)$

$I_{b\max,goal} = 10mA;\ (I_{bcwrecirc,oper} = 80\mu A);\ \varepsilon_{goal} = 0.1\mu m;\ (\varepsilon_{oper} = 0.3\mu m)$

Figure 8: Layout of the Compact ERL at KEK with primary parameters, both goals and achieved. 7 keV x-rays have been produced via the inverse Compton scattering process.

2.1.5 **Concepts for the Future**

A number of possible applications of the ERL for the future have been studied and proposed. Among others there are: an R&D FFAG loop as model for the electron side of eRHC; the eRHIC application itself; a high brightness, hard x-ray source using CESR the Cornell Electron Storage Ring as the high energy turn around; and the Large Hadron electron Collider. These concepts are sketched below.

2.1.5.1 *4 Pass FFAG R&D Loop for eRHIC*

It has been proposed to economize on the electron arm of eRHIC by using a multi-pass ERL that employs the FFAG principle for the confinement system [7]. Given the novelty of this idea an R&D model for exploring potential pitfalls has been proposed as shown in the sketch Figure 9.

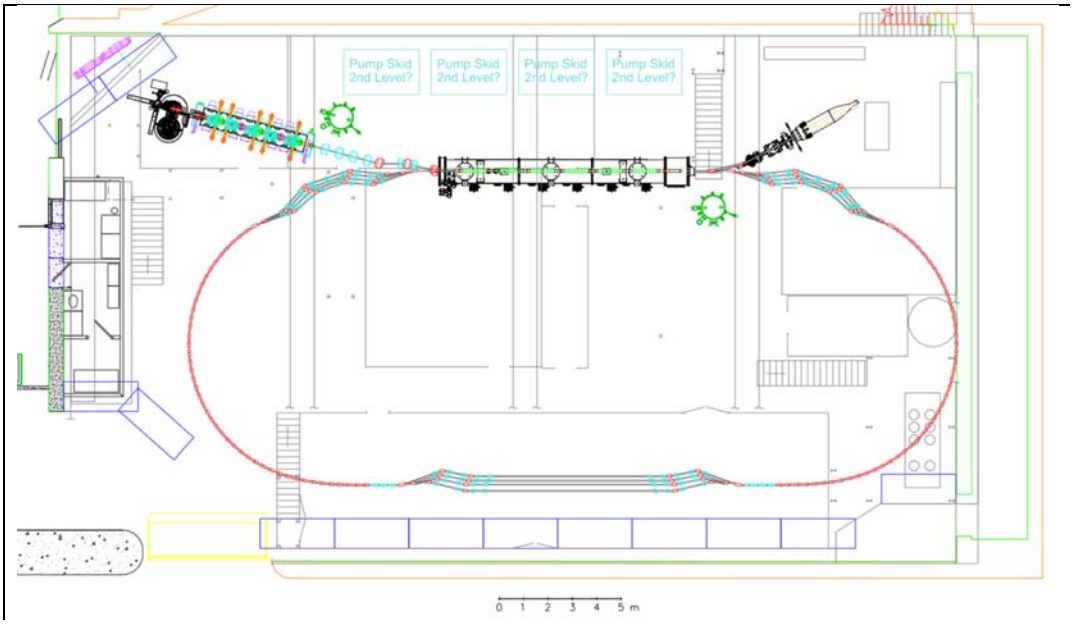

$E_{inj} = 6 MeV;\ E_{\max} = 250 MeV;\ Q_{\max} = 80 pC;\ I_{inj,\max} = 100 mA;\ \varepsilon$=0.3$\mu$m

a staged approach is being studied

Figure 9: R&D 4pass FFAG loop as model for eRHIC.

2.1.5.2 *eRHC FFAG Concept*

It is proposed [8] to minimize the number of rings and thus the cost by employing the FFAG principle in a multi-pass ERL system as shown in Figure 10. The combinations of beam energy and current are limited by a 2.4MW synchrotron radiation limit. The SRF system comprises 422 MHz, 5 cell 18.5 MV/m gradient cavities.

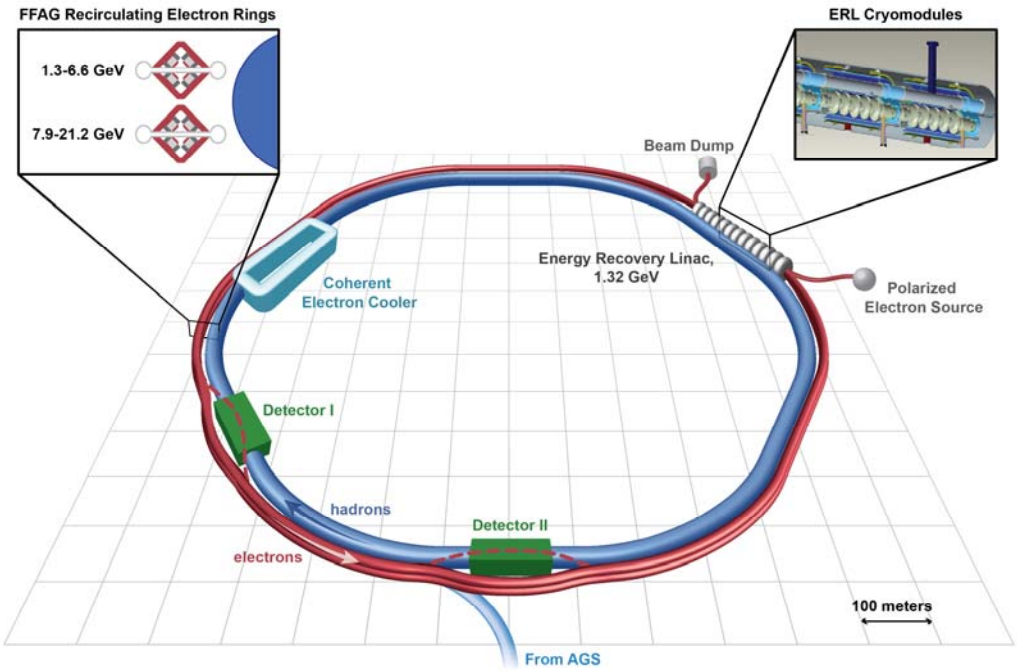

$$10 \le E_{\max} \le 21.2 GeV;\ 3.7 mA \le i_b \le 50 mA;\ 23 \le \varepsilon \le 58 \mu\text{m}$$

Figure 10: Proposed ERL FFAG loops for eRHIC.

SR power is compensated with 2nd harmonic system with energy spread compensation by a 5th harmonic system. There will be another ERL to provide the electron beam for the Coherent electron Cooling system for the ions.

2.1.5.3 *High Brightness X-ray Source as CESR Upgrade*

Using the emittance preserving feature of a linac [9] the beam is accelerated to 5 GeV, passes through an array of undulators of various kinds to produce hard x-rays, turned around using the ring of CESR, extracted and introduced into a second set of undulators, energy recovered and dumped. The scheme is depicted in Figure 11 below.

2.1.5.4 *ERL for the Large Hadron electron Collider, LHeC*

An ERL electron machine is proposed for the electron side of LHeC [10]. Figures 12 and 13 below show the overall scheme and the ERL scheme respectively. It is planned that this configuration will do electron scattering from both protons and ions. Given the announced plans for LHC running and high luminosity upgrade, addition of electron scattering capability will lie quite far in the future and one may expect, therefore, several changes in the design to accommodate advances in technology that will occur in the meantime.

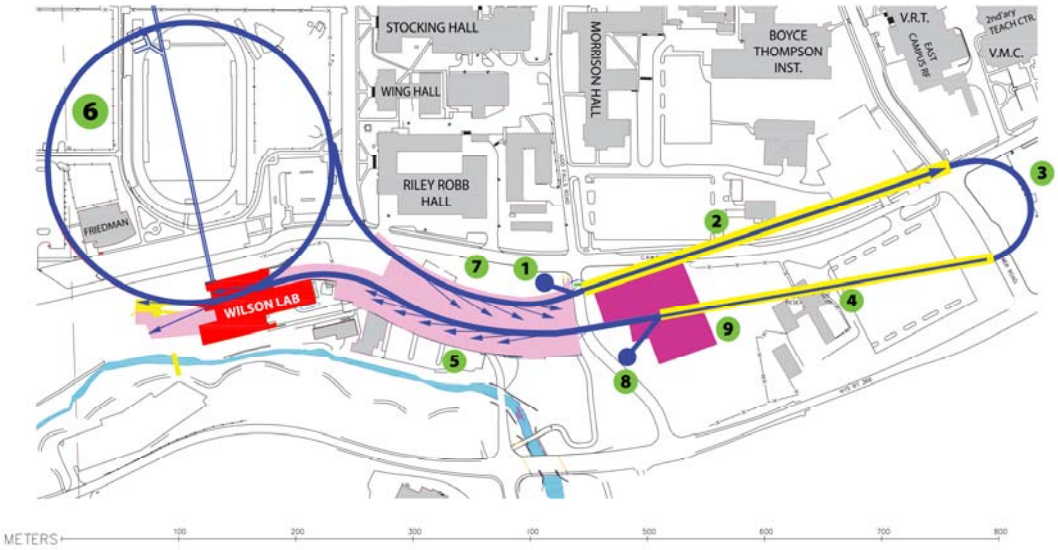

Figure 11: 1 injector 100mA; 2&4 SRF linac; 3 turnaround arc; 5&7 x-ray beamlines; 6 CESR arc return loop; 8 beam stop; 9 cryoplant.

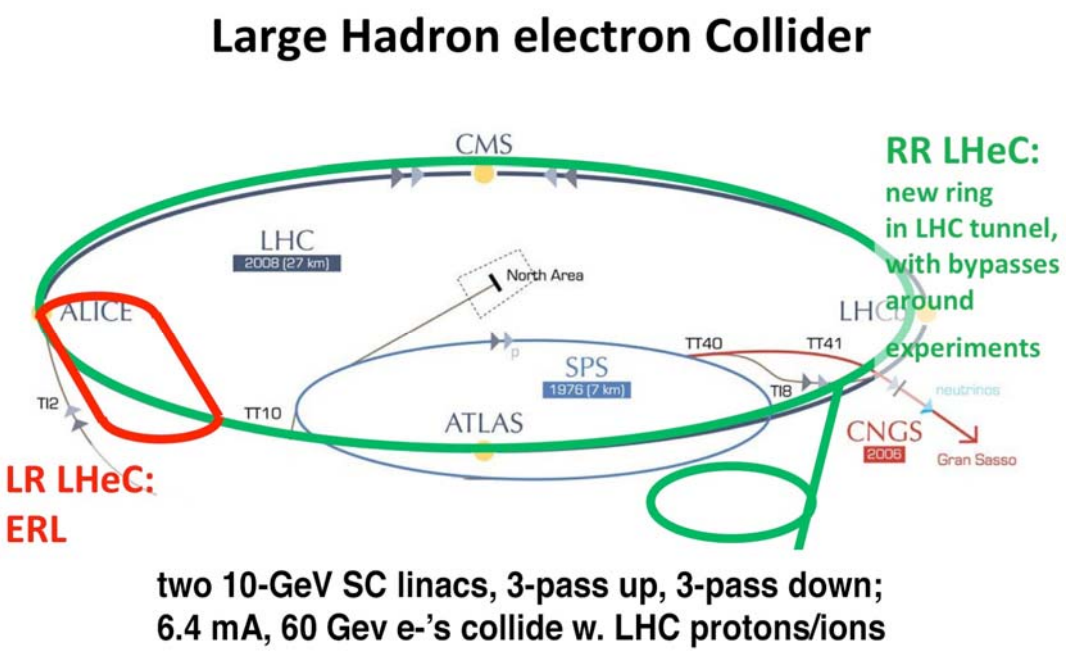

Figure 12: Overall layout of an LHeC scheme for adding electron scattering capability to the LHC.

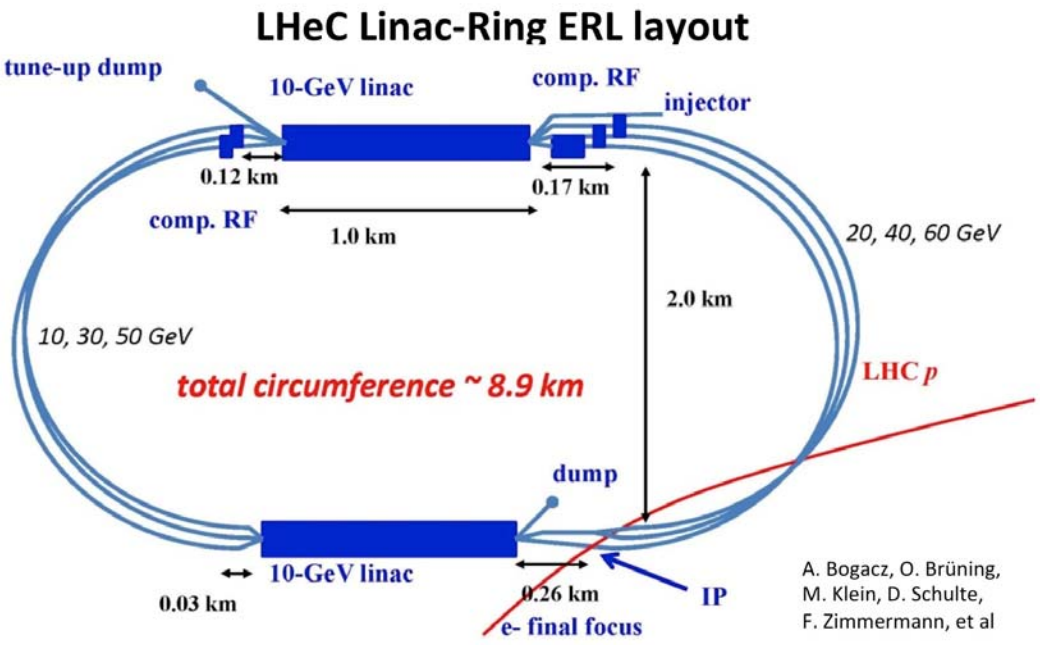

Figure 13: Closer look at the electron system of LHeC, note the rather large dimensions.

2.1.6 **Challenges to Realization of such Plans and Needed R&D**

Following is a list of various challenges that must be met for success in these endeavors:

- Many of the projects require large scale-up with respect to existing machines, e.g. ERL incorporating FFAG
- Very precise phase and amplitude control required over large spatial extent with varying ground vibration conditions
- Unprecedented beam currents in SRF linacs with potential for BBU and halo
- Beam dynamics of unprecedented numbers of spatially superposed bunches in SRF linacs
- High power of high energy x-rays to be protected against

Below we list some of the R&D that will be needed for mitigation of the implied risks

- Large scale-up risks need mitigation by excellent full scale machine modeling including realistic error distributions derived from real hardware prototypes together with the putative performance goals
- Phase and amplitude control challenges are multidimensional. Here we mention only one, i.e. vibration induced detuning of the very high Q cavities. Successful mitigation will require great attention to the vibration sources and design of the cryomodules for favorable source-cavity transfer functions. Enough prototypes are needed to assure robustness of design. RF and beam measurements in R&D loops can help.

- Advanced evaluation of ion effects and Touschek scattering and halos caused by intra-beam scattering and disruption of e-beams at the IP's with mitigating designs as needed
- Assurance of high enough BBU threshold requires advanced cavity design with realistic error distributions to determine the conservative number of cells per cavity allowed and a concomitant QC program for manufacturing.
- Radiation checks of prototype magnets using simulated distribution of radiation power and spectrum-look for asymmetric demagnetization

2.1.7 **Conclusion**

Early examples of ERL applications have shown the potential utility of the technique. These examples have led to bold designs for machines of much higher energy and power in several applications. While we can be optimistic about future uses of the concept that will help us to minimize power demand for next generation projects, we need to be cautious in insisting on sufficient pre construction R&D that failures do not give the method a bad name

2.1.8 **Acknowledgments**

Many thanks for furnishing of graphics and tender of advice are due to colleagues at BNL, CERN, Cornell, Jlab and KEK

2.1.9 **References**

1. S. O. Schriber and E. A. Heighway, Double Pass Linear Accelerator – Reflexotron, IEEE Trans. Nucl. Sci. 22(3), 1060, June 1975
2. T. I. Smith et al., Development of the SCA/FEL for use in Biomedical and Materials Science Experiments, NIM A259, 1-7 (1987)
3. R. Hajima, Overview of Energy Recovery Linacs, Proc APAC 2007, 11, RRCAT, Indore, India (2007)
4. G. R. Neil et al., The Jefferson Lab IR FEL Upgrade, NIM A557, 9 (2006)
5. A. Shevchenko, Commissioning Status and Further Development of the Novosibirsk Multi-turn ERL, Proc. ERL 2013, 6 Novosibirsk (2013)
6. S. Sakanaka et al., Recent Progress and Operational Status of the Compact ERL at KEK, Proc IPAC 2015, 1359, Jefferson Lab (2015)
7. http://arxiv.org/abs/1504.00588
8. http://arxiv.org/abs/1409.1633
9. http://www.classe.cornell.edu/Research/ERL/PDDR.html
10. https://indico.cern.ch/event/278903/timetable/#all.detailed

2.2 Beam Dynamics Challenges in ERL-based Light Sources

Michael Abo-Bakr, Alexander Matveenko
Helmholtz-Zentrum Berlin, Albert-Einstein Str. 15, 12489 Berlin
Mail to: Michael.Abo-Bakr@helmholtz-berlin.de
Aleksandr.Matveenko@helmholtz-berlin.de

2.2.1 Introduction

ERLs can generate high energy electron beams of huge virtual power and high density, thus capable to base a Synchrotron Radiation Light Source of ultimate brightness on. Short pulses and high peak currents will also allow the generation of coherent radiation. While THz radiation can be emitted from short bunches, low gain FEL operation (FEL amplifier) is possible. Even high gain FEL operation is feasible, as long as the beam degradation remains within the machine acceptance (transverse & momentum). Another application option is to use an ERL as Compton source, generating hard X-rays from low energy electrons.

In storage rings the beam dimensions result from an equilibrium state between radiation excitation and damping, and hence are totally independent of the beam quality from the source and all pre-accelerators. In ERLs as single or few turn machines the passage time is much too short to reach this equilibrium and the beam quality is defined by the electron source. While for a given storage ring the emittance scales with $\varepsilon \sim E^2$, in ERL's the adiabatic damping causes a $\varepsilon \sim E^{-1}$ scaling. Thus with increasing energy the ERL bunch quality improves more and more. Using present day high brightness electron sources, based on laser induced photo emission from the gun cathode, ERLs have the potential to significantly exceed the bunch quality of modern SR based, third Generation Light Sources. The physics of these sources is a large topic of its own and will not be covered here [1, 2].

The central goal parameter for almost any kind of present and future accelerators and especially for synchrotron radiation light sources is the brilliance $B \sim \dot{N}/\varepsilon_x \varepsilon_y$, scaling with the number of electrons per second $\dot{N}$ and the transverse emittances ε_x and ε_y. Small emittances of bunches with high charge and repetition rate maximize the average brilliance. Short pulses from ERLs enable insights in the dynamics of sub-ps processes and can produce extreme peak brilliance $\hat{B} \sim B/\sigma_s$. The spectral brilliance from long insertion devices scales inversely with the energy spread $D(\omega) \sim 1/\sigma_E$. Thus ultimate spectral brilliance – average as well as peak – requires beams of highest electron densities, not only in 3D but also in the 6-dimensional phase space.

As ERLs can reach and exceeded storage ring beam parameters in any phase space dimension many beam dynamics challenges, known from those, are relevant for ERLs as well and can affect their performance possibly even to a higher degree.
Beam dynamics challenges in an ERL arise from its general layout and target parameters and vary with beam energy and function of the various machine sections:

- Injector: high brightness beam generation and low energy beam transport under the influence of strong Space Charge (SC) forces.
- Merger: guiding both, the low energy fresh beam and the high energy used beam into the same linac section.

- Linac section(s): acceleration and deceleration of the beam. Depending on target energy, available linac length and average accelerating gradients a layout based on single linac, split linac or multi pass linac can be chosen.
- Spreader: using a multi-turn layout the various beams must be merged onto the linac section and after acceleration/deceleration be sent to beam lines according to their energy.
- Recirculation section: lossless beam transport at conserved beam quality with the option of beam manipulation, arc lattice variants (Bates, DBA, TBA, MBA, FFAG), generate conditions for most efficient energy recovery.
- Splitter & dump line: analogous to the merger downstream the linac section the fresh and the used bunched needs to be separated, for further acceleration or light generation with the first one and to guide the second one into the dump line.

For this overview report we separate beam dynamics issues of ERL based synchrotron radiation facilities into two main categories:

- **Beam optics**, dealing mostly with charge and current independent problems of linear and nonlinear beam transport, manipulation and acceleration and
- **Collective effects**, caused by the high electron density and average current, that can degrade the beam quality, drive instabilities and ultimately even lead to partial or total beam losses.

In the first, "beam optics" part we will introduce general magnet optics designs, applicable for ERLs and discuss design philosophies of its subcomponents. Requirements to the beam optics are collected and magnet lattice configurations best satisfying them are compared. Nonlinear effects and their compensation by adjusting linear optics as well as and higher order magnetic multipoles elements are considered.

In the second part the physics of potentially harmful collective effects is introduced. Options to counteract them by special optics settings are discussed.

Since derivations of the fundamental formula presented here are far beyond the scope of this report, a selection of references to specialized papers is given for any issue considered. In general the Phys. Rev. ST Accel. Beams online journal [3] and the JACoW [4] hosted proceedings of IPACs and ERL workshops provide an excellent source of information for all fields of ERL beam dynamics issues.

As the authors were involved in the design of two ERL projects, we would like to refer the reader also to the CDRs of these projects, giving a good insight in beam dynamics aspects for low and high energy ERLs: bERLinPro [5,6], currently under construction at the Helmholtz-Zentrum Berlin, and FSF [7], an HZB design study for a 6 GeV ERL based synchrotron light source.

2.2.2 **Beam Optics**

The magnetic lattice is defined by the type, number and arrangement of multipole magnets and radio frequency (RF) structures. These devices are tuned to form a beam optics, capable to transport (including acceleration and deceleration) the beam throughout the machine while

- maintaining the beam quality delivered from the source;
- ensuring lowest electron losses;
- merging/splitting beams of various energies, e.g. injected and recirculated beam(s);

- performing bunch manipulations, e.g. compression, emittance exchange & plane rotation;
- establishing conditions for efficient energy recovery.

As mentioned many challenges are related to specific parts of an ERL. In contrast particle losses and beam size is an issue in all machine sections and thus will be covered here first.

2.2.2.1 *Beam Size and Losses*

Within optics simulations the beam is described by its 6D phase space sizes $\sigma_x, \sigma_{x'}, \sigma_y, \sigma_{y'}, \sigma_z, \sigma_E$, its emittances $\varepsilon_x, \varepsilon_y, \varepsilon_z$ and its Twiss parameters β, α, γ, assuming Gaussian particle distributions. The behaviour of energy deviating electrons is described by the dispersion function η. Various, partially contradictory demands are made on the beam size:

- For a **high brilliance light source** according electron bunches at the point(s) of radiation generation are required. Small beam sizes in all dimensions enable generation of diffraction limited light pulses with high transverse and longitudinal coherence fractions. For the minimum radiation wavelength λ_γ to be generated, diffraction puts a lower limit on the transverse emittances $\varepsilon_{x,y} \approx \frac{\lambda_\gamma}{4\pi}$, where even smaller electron beam emittances do not further reduce the photon beam size [8].
- **Particle losses** are at least of equal importance as compared to storage rings. While beam decay (like in storage rings) is no issue, radiation and activation issues as well as RF power limits are of eminent importance. Especially losses on high energy turns need to be minimized as far as possible. The beam size is directly involved in two mechanisms:
  - Losses at the machine aperture: the transverse beam size must be small compared to vacuum chamber dimensions A: $A_{x,y}(s) \gg N\,\sigma_{x,y}(s)$. In large storage rings N is quite high: $N \sim 10^8 \ldots 10^9$, while in the lower energy parts of ERLs this number can be much smaller. In dispersive sections passed by a chirped beam N can be in the order of ten and even below. To reach SR like relative loss rates of 10^{-10} per turn, one needs $N \geq 7$ for a Gaussian distributed beam. Already from the electron source, any emission of electrons into these extreme distribution tails must be prevented. Nevertheless halo electrons independent of an assumed distribution function can contribute to particle losses.
  - Touschek losses [see Sec. 2.2.2.4]: electron collisions within one bunch (intra beam scattering) lead to a momentum transfer between transverse and longitudinal motion and can be one of the source of beam halo formation and losses in ERLs. The loss rate from these Touschek events scales with the electron density and thus with bunch charge and volume. A low density, i.e. a large bunch volume reduces Touschek losses.

- **Collective effects** like e.g. space charge, coherent synchrotron radiation and other kinds of wake fields [see Secs. 2.2.3.1, 2.2.3.2] interact with the beam by imprinting an energy modulation along the bunch, that finally deteriorate the beam quality. As the strength of all these effects scales with the peak current and thus inversely with the bunch length, if possible, bunches should be kept long during transport and only tuned short when generating radiation.
- **RF curvature**: while passing the RF structures for acceleration or deceleration the bunches scan the temporal and spatial field variation in the cavities, generating a correlation in the longitudinal phase space. Its nonlinear part can limit bunch manipulation techniques e.g. bunch compression and increases the energy spread. As short bunches scan a smaller RF phase ranges nonlinearities are reduced compared to longer bunches.

The optimal beam size is a compromise of these demands and has to be found for the various machine sections. Beside the beam size many more aspects needs to be considered – the most important ones will be covered in the following.

2.2.2.2 *Injector Line & Merger*

The first machine section guiding the beam from the source to the first multi beam linac is referred to as injection line here. On exit the low energy beam must be merged with the high energy beam to pass the linac on the same centered trajectory.

Beam transport in the injection line at energies of few MeV only is space charge dominated. Spatially varying forces due to self-generated fields in the bunch can cause a significant emittance growth. Following an emittance compensation scheme [9, 10], a sophisticated beam optics can reverse these SC effects and cancel the emittance degradation to a major degree. The basic concept is described in Sec. 2.2.3.1.

As SC scales strongly with the beam energy, a pre-acceleration in the injection line and before the first major acceleration will reduce initial emittance growth. On the other hand it is this energy that will not be recovered in an ERL and RF and dump power considerations will limit its value.

At the end of the injector line the new and the recirculated beam have to be merged into the linac section. This is achieved by a series of bending magnets, where the last one is passed by both beams, which are bent at different angles according to their respective energies. While in the beginning of the injector line the optics can be kept axial-symmetric and solenoids provide sufficient focusing, the symmetry is broken in the merger. Quadrupole magnets are applied to control dispersion (to form an achromatic bump) and to shape the beam size throughout the merger. Mergers with four different layouts, shown in Figure 1, are considered for ERL (test) facilities [11]: dogleg- (a,b), chicane- (c) and zig-zag-type (d) mergers.

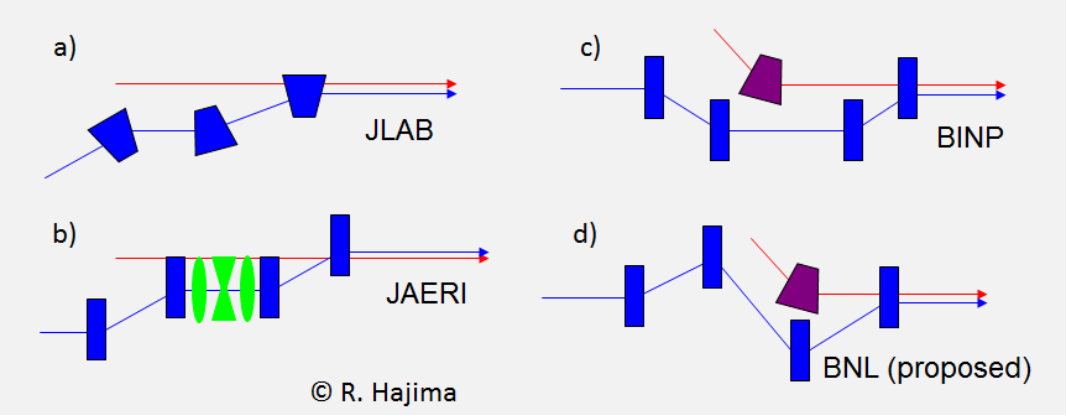

Figure 1: Mergers for existing and proposed ERLs: a) deflecting 3-bend dogleg, b) four bend dogleg, c) 4-bend chicane, d) "zig-zag" merger.

In contrast to the start of the injection line, in the merger the longitudinal SC induced energy modulation takes place in a dispersive section. Thus with any energy change an oscillation around the shifted, new reference path is excited. Since the energy modulation varies along the bunch from the tail to its head, the centroids of longitudinal bunch slices oscillate as well. Leaving the merger the projected emittance in the merger plane can be significantly increased. The emittance growth of bunch parts with linear energy modulation $\Delta E(s) \sim s$ (s: long. position in the bunch) can be removed by adjusting the dispersion at the merger exit. Doing so, the achromaticity of the merger is broken, so that initial energy variations now cause an emittance growth at the merger exit. Finally the merger is set up to minimize the overall emittance growth due to space charge dispersion and un-closed merger dispersion.

The same physics applies to the splitter, dividing the accelerated, high energy beam from the decelerated, low energy one, which is sent into the dump line.

Stray fields: although unwanted in general, interfering fields like the magnetic earth field, remnant fields from the optics magnets or magnet fields from vacuum pump and gauges are most distorting in the injection line due to the low beam energy and rigidity respectively. Shielding of fields, magnet cycling procedures and careful placing of vacuum devices reduce these stray fields. For the remaining fields, trajectory offsets have to be corrected with a sufficient number of steerer magnets.

2.2.2.3 *Linac Sections*

One or more ERL sections are equipped with linacs to accelerate the beam on one or multiple turns up to its final energy. Regarding the beam dynamics several aspects have to be considered:

RF focusing: the cavity fields focus the beam [12], both horizontally and vertically, when entering the cavity and defocus when leaving it. On acceleration, due to the energy increase in the cavity the focusing on the low energy side prevails the defocusing on the high energy side. The opposite effect happens on deceleration. Especially at low energies the focal strength is high and needs to be carefully considered when setting up the linac section beam optics.

RF Phase slip: at low injection energies the beam is not sufficiently relativistic and time of flight effects can cause a phase slip compared to the recirculated, high energy

beam. A power mismatch in the RF cavities is the consequence and beam loading problems arise. The effect can be reduced by increasing the injection energy, clearly on the cost of the RF and dump power respectively.

Multi-energy beam lines: linac sections are passed by beams with different energies, sharing the same focusing elements: magnets and RF structures. The difficulty to find a suited optics for all beams scales with the span of the energy in the beam line. Due to its lowest magnetic rigidity the optics is mainly tuned with respect to the lowest energy beam. Any other strategy would lead to strong over-focusing and an inapplicable beam size. The lack of focusing for the high energy beam has to be compensated for in separate beam transport section(s).

Spreader: the separation of the multiple beams into their energy adjusted beam lines is done by a spreader, using the energy dependence of the bending angle in the first, shared dipole magnet(s). The challenge here is to create a compact layout, using a small number of magnets even for several beams of different energies. The dispersion in the spreader plane should be closed at its exit and the beam size must be matched with the recirculation arcs to avoid emittance degradation.

BBU: the beam break up instability [see Sec. 2.2.3.5] is driven by a positive feedback of the beam into higher order mode fields of the superconducting RF cavities. While the most important countermeasure is the usage of cavities with minimized a HOM spectrum, also the beam optics influences BBU: a betatron phase advance of $\Delta\psi = n \cdot \pi$ between subsequent cavity passages sets the transport matrix element $R_{12} = 0$, so that the cavity is passed on axis after recirculation and no power is fed into the HOM (see eq. (2)). In addition optimized Twiss parameters within the linac can be calculated [13]. Both settings can significantly increase the instability's thresholds.

Effective measures against BBU become even more important for multi turn ERLs, where various beam (multiplying the total current) traverse simultaneously the linac sections.

2.2.2.4 *Recirculators*

The transfer lines connecting the ERL linac sections and the full energy section dedicated to radiation generation are referred to here as recirculators. Together with the linac sections they form the majority of machine sections in an ERL. A careful beam optics setup, fulfilling a variety of demands is mandatory.

Several basic lattice concepts are suited for ERL recirculator arcs, depending on their energy and the available space and number of magnets [14]. In low to medium energy ERLs of moderate size Double [15] and Triple Bend Achromats [16], Bates-Arcs [17], but also individual, non-standard schemes have been applied, as shown in Figure 2.

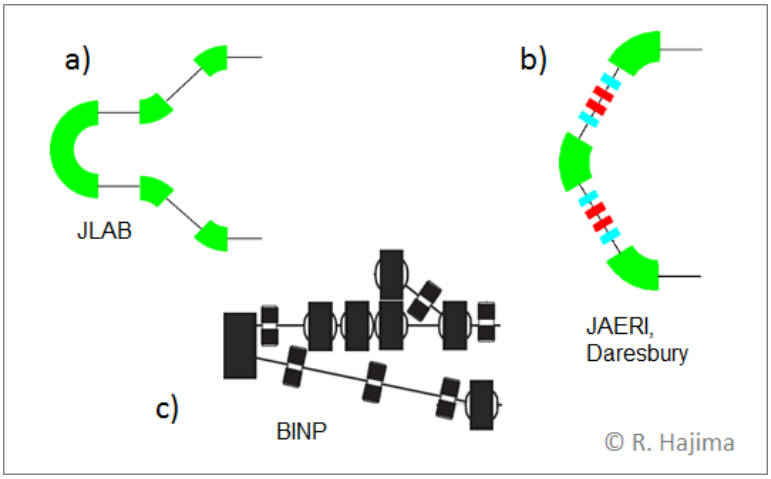

Figure 2: Recirculator arc lattice types: a) Bates arc, b) Triple Bend Achromat, c) BINP arc.

For large scale ERL based light sources with energies in the GeV range multi-bend achromat lattices as well as FFAG lattices have been considered. [18, 19, 20, 21, 22].

The various lattice types differ in tunability, space and magnet number requirements and finally in performance with respect to emittance conservation, lossless beam transport and beam manipulation capabilities.

A flexible control of the linear and nonlinear beam optics is the key to cover all of aspects mentioned above.

Lossless beam transport: as mentioned, Touschek scattering is one of the two dominant loss processes. Beside a large bunch volume, contrary to radiation generation requirements, the optics momentum acceptance A_p is of crucial significance.

While at intra beam scattering energy transfer into the transverse motion is of minor importance, the longitudinal momentum change is Lorentz transformed into the lab frame and thus strongly enhanced.

With the momentum change $\frac{\Delta p}{p}$ from the scattering event the downstream reference trajectory shifts on a dispersive path: $x_{ref}(s) = \eta(s) \cdot \frac{\Delta p}{p}$. Depending on the dispersion function at the scatter position in addition a betatron oscillation of initial amplitude $\begin{pmatrix} x \\ x' \end{pmatrix} = \frac{\Delta p}{p} \cdot \begin{pmatrix} \eta \\ \eta' \end{pmatrix}$ is excited. It is equivalent to a single particle emittance of

$$\varepsilon_0 = \gamma x^2 + 2\alpha x x' + \beta x'^2 = (\Delta p/p)^2(\gamma\eta^2 + 2\alpha\eta\eta' + \beta\eta'^2) = (\Delta p/p)^2 \mathcal{H}$$

$$\mathcal{H} = \gamma\eta^2 + 2\alpha\eta\eta' + \beta\eta'^2, \qquad (1)$$

(Twiss parameter, dispersion and $\mathcal{H}$-function at the scattering position $s = s_0$ each).

The general expression for the scattered electrons downstream trajectory is

$$x(s) = \sqrt{\varepsilon_0 \beta(s)}\cos(\psi(s) - \varphi_0) + \eta(s) \cdot \frac{\Delta p}{p}$$

$$= \frac{\Delta p}{p}\left[\sqrt{\mathcal{H}_0 \beta(s)}\cos(\psi(s) - \varphi_0) + \eta(s)\right]$$

being directly proportional to $\Delta p/p$. Scattering events, causing a downstream offset, larger than the available horizontal aperture $A_x(s)$, lead to particle losses. The

maximum $\Delta p/p$ deviation with $x(s) = f(\frac{\Delta p}{p}) \leq A_x(s)$ defines the optics momentum acceptance $A_x(s)$.

The Touschek loss rate [23] scales with: $\dot{N}/N \sim 1/A_p^3$, therefore a large momentum acceptance is essential for low losses. A small overall dispersion and lower maxima of β- and dispersion function, optimizing the $\mathcal{H}$-function (reducing its maximum value) and thus increasing the momentum acceptance (see also ISR subsection). Lattices with lower bending angles of the dipole magnets are advantageous, but require more magnets at increased costs.

The loss rate due to elastic scattering on the residual gas atomic nuclei is the second main loss mechanism. The loss rate scales $\dot{N}/N \sim 1/(\theta_x^2 + \theta_y^2)$, with the angular acceptance $\theta_{x,y}^2 \approx A_{x,y}^{\perp\,2}/(\beta_{x,y} \cdot \beta_{x,y}^{max})$. Smaller transverse beta functions with lower maximal values increase the angular acceptance, thus reducing the loss rate.

Beside the intendedly generated "wanted beam", there are a few sources of unwanted beam, e.g. gun laser stray light, extreme distribution tails or ghost pulses, dark current by field emission from the (superconducting) RF structures. This unwanted beam, often referred to as beam halo, can be simulated, if the generating process is known. Unfortunately the dominating contributor becomes apparent only in the real machine, and even may change its origin. The best measure to control beam halo is a large acceptance of the magnet optics to transport both the core beam and the halo.

Bunch manipulation: in order to generate most brilliant light pulses several manipulation techniques are applied, that exchange parts of phase space between two planes by means of quasi phase space rotations. Conservation of the uninvolved phase space dimensions and the overall beam quality is mandatory.

In many linear accelerators and ERLs the bunch compression is used, where in a first step a chirp (mostly linear $z - p_z$ correlation: $\Delta p/p = C \cdot \Delta z$) is imprinted by passing the RF structures off crest. In a second step a dispersive section $\eta \neq 0$ is passed, where the path length depends on the particle momentum: $\Delta L = R_{56} \cdot \Delta p/p + T_{566} \cdot \Delta p/p^2 + \cdots$ with $R_{56} = \int \eta/\rho \, ds$ and T_{566} as first and second order beam transport matrix elements. Nonlinearities (RF curvature, T_{566}, etc) can be corrected using higher order multipole magnets, starting with sextupole magnets in the lowest order. While in linacs often extra bunch compressor sections are foreseen, in ERLs the recirculation arcs can be alternatively used. The various lattice types offer different variability in optics tuning: considering an achromatic arc ($\eta_{in} = \eta_{out} = 0$) the DBA lattice offers no R_{56} tunability at all, while e.g. in a TBA lattice R_{56} can be tuned via the dispersion function in the middle bend. With more quadrupole magnets in the more complex lattice types one generates free knobs to adjust dispersion and beta functions for nonlinear corrections, minimizing the required multipole strengths. Also the phase advances over certain sections can be tuned with respect to emittance degrading effects like e.g. CSR.

Another manipulation in ERLs is the so called "beam rotation", where the two transverse phase spaces are completely switched. It can increase the BBU thresholds for polarized cavities, since no further excitation of the kicking HOM occurs on the return pass. A section with a set of skew quadrupole magnets is required to swap transversal planes, ideally transforming the beam $\vec{X_1} = M \cdot \vec{X_0}$, with $M = \begin{bmatrix} 0 & E \\ E & 0 \end{bmatrix}, E = \begin{bmatrix} 1 & 0 \\ 0 & 1 \end{bmatrix}$. There are more manipulation techniques like e.g. emittance exchange, but they are either not used or not required on ERLs so far.

Energy recovery: a further important task of recirculator arcs is to provide path length adjustment options, enabling one to set up accurately the required RF phase advances of 0 or 180 degree between the linac sections. Depending on the ERL layout these tuning options are not only needed on deceleration but also possibly on the accelerating pass. Common options are movable arcs for small ERLs with 180° DBA, TBA or Bates (only the big, centre magnet) arcs, two longitudinal moveable bends within an arc (e.g. bERLinPro) or high amplitude, steering bumps in large recirculators with sufficient mechanical aperture. Also chicanes outside the recirculators can be used, but they can significantly contribute to the R_{56} budget and only lengthen the pass (compared to the straight option with all bends off). Moreover, lengthening in the order of the RF wavelength with a chicane demands large offsets and can hardly be covered with a single wide vacuum chamber.

For the efficiency of the recovery process the beam matching especially for the last deceleration to the lowest energy is of vital importance. The minimization of the energy spread at the low energy side is a precondition for a high recovery rate and a safe transport of the high power beam into the dump. One option to cancel out rf curvature effects is to adjust a bunch length equal to that on acceleration. In this case any bunch compression needs to be reversed. Due to beam loading effects this can be done only by inverting the R_{56} sign in the corresponding recirculator sections, which again favours highly tuneable lattice types with a wide R_{56} value range. In the case where the bunch length differs between acceleration and deceleration sextupole magnets can be used to remove RF nonlinearities.

Any remaining nonlinearities from the magnet optics or from collective effects (CSR, wakes…) have to be minimized using higher order multipole magnets.

For efficient recovery the transverse beam size in the linac needs to be adjusted to take the rf focussing into account and also provide suitable BBU conditions.

Radiation excitation: despite the transfer line character of ERLs and the short passage times the emission of incoherent synchrotron radiation (ISR) can cause a considerable emittance growth. Since the energy loss due to emission of synchrotron radiation scales with $\Delta E \sim E^4/\rho \sim E^3 \cdot B$, high energy ERLs are most affected. Moreover the critical photon energy scales nonlinear with energy: $\varepsilon_c \sim E^3/\rho \sim E^2 \cdot B$, extending the photon spectrum equivalently to higher values and thus the resulting energy change and spread of the emitting electrons. Similar to a Touschek event the energy change in a dispersive section excites a betatron oscillation around the new reference orbit. The according emittance growth is described by the function $\mathcal{H}$ (see eq.(1)), relating a momentum change to the downstream transverse betatron oscillation amplitude. A low $\mathcal{H}$-function represents an optics, where momentum changes cause a smaller transversal phase space blow up and thus reduced emittance growth. Assuming an achromatic arc tuning, for the various lattice types minimal form factors F~ $\mathcal{H}$ can be calculated for comparison [24]. Compared to the DBA lattice the theoretical minimum for a MBA lattice is reduced by a factor of 3, when Twiss parameters and dispersion function are optimized to reduce $\mathcal{H}$ and extra bends at the beginning and end of the cell close the dispersion. Thus with a MBA lattice the emittance growth will be the smallest, but zero dispersion sections, e.g. for insertion devices, are not available without lattice modifications.

2.2.2.5 *Dumpline & Dump*

The ERL's last section is the dump line, guiding the low energy but high power beam into the beam dump, where sufficient cooling power is provided to safely absorb the beam in the dump walls. Losses in the dump line are no longer relevant for RF budget, but the high power beam has a substantial damage potential. When mis-steered the beam is easily able to weld holes into vacuum chamber components on a very short time scale. Thus lossless beam transport is the main task of beam optics. Large apertures are essential therefore, even allowing for a safe beam transport at increased emittance (compared to that from the injector) and a moderate, further emittance degradation, due to SC effects in the dump line.

In the dump the full beam power of hundreds of kW or even MW is mostly transferred into heat (and radiation). Clearly this must not happen in a point of few mm² or even cm². Instead the beam power needs to be carefully distributed along the inner dump surface. Two options exist:

- Beam widening by massively increasing (orders of magnitude) the beta functions in the last dump line part and into the dump
- Beam sweeping using two rapid cycling (tens of Hz), transversal steerers, equally distributing the beam impact point in the dump

Ideally the combination of both is used to relax hardware requirements and improve "Machine Protection System" reaction times in case of device failures.

2.2.3 **Collective Effects**

The intensity and quality of the beam in an accelerator is usually limited by collective effects. In the following, characteristic effects and their peculiarities in ERLs are discussed.

2.2.3.1 *Space Charge*

Space charge effects typically limit the performance of low energy beam transport in high brightness photo-injectors. A direct effect is the defocusing of the beam by the space charge forces inside the bunch. The linear part of the forces can be compensated by external focusing (solenoids or quadrupoles), though the non-linear part still affects the beam quality.

Emittance degradation due to the collective space charge forces is one of the important issues by the design of the injector optics. Flat-top cathode laser profiles, both transversally and longitudinally, linearizing SC forces in the central beam parts, are routinely used to achieve highest beam brightness [1, 25].

If an ERL aims for high brightness electron beam, its injector design should be made with the emittance compensation technique [9] in mind. The critical difference of ERL to conventional linac injector is the merger section, where axial symmetry of the beam can be no longer assumed. It means, emittance compensation with a solenoid is not enough anymore to achieve the minimal beam emittance in both planes. A theory of the so called "2D emittance compensation" was developed in [10]. Application of the method to the superconducting RF photo-injector for the project bERLinPro [5] is described in [26].

Space charge effects determine the choice of the merger geometry. An overview of practical merger designs can be found e.g. in [11]. One problem of a space charge

dominated merger is the longitudinal space charge force, affecting transversal motion of individual bunch slices in dispersive section. Transversal defocusing and energy change of a slice, caused by space charge forces, can modify the achromatic condition significantly. This effect favors merger designs that are short and have a low dispersion [26]. The linear part of the effect can be corrected if the bunch has a sufficiently large correlated energy spread.

Particle tracking codes (e.g. Parmela [27], ASTRA [28], GPT [29]) can be used for modelling of the space charge dominated beams. Usually, the programs require extensive resources for the tracking, which make optimization of beam lines time- and resource-consuming. There are space charge codes (e.g. Trace3D [30], SCO [31], HOMDYN [32]), which allow fast tracking of a model charge distribution (Kapchinsky-Vladimirsky, applied to the whole bunch or slice-wise). These codes allow an initial optimization to be achieved quickly; afterwards tracking with "full" space charge codes can be done.

2.2.3.2 *Coherent Synchrotron Radiation*

While usually emitted incoherently (ISR) very short electron bunches generate coherent synchrotron radiation (CSR) at wavelength comparable to the bunch length. The resulting energy loss can become very significant. For typical bunch lengths in storage rings (20 - 100 ps) CSR is shielded by the vacuum chamber and plays only a minor role in the beam dynamics. In linacs, where the bunch can easily be compressed, CSR can strongly influence beam parameters. Moreover, with ERL-typical, high average beam currents, CSR can cause damage to vacuum system components due to its high average power.

As an example [5], CSR losses in normal operation of bERLinPro with 2 ps bunches and 100 mA average current are estimated to be 2.5 kW. For short pulse operation mode at full current (100 mA) and down to 150 fs bunch length the losses would increase to ca. 25 kW.

Main problems and solutions in the treatment of CSR effects on the beam emittance are investigated e.g. for short wave length FEL's (FLASH, LCLS, XFEL). If the key effect of the CSR wake on the bunch is the longitudinal position dependent transverse kick of the bunch slices, the 1-D model can be a good approximation. Comprehensive derivation of the 1-D CSR wake functions for different cases is presented in [33]. This model is also implemented in a number of packages (Elegant, Opal) [34, 35].

For very short bunches (if the bunch is in its reference frame equally long or even shorter compared to its transverse sizes) full 3-D radiation fields should be taken into account. Appropriate simulation codes (e.g. CSRTrack [36]) should be used in this case. However, the 1-D model usually gives an overestimation of the effect and still can be used for quick checks.

CSR induced emittance growth can be reduced by several methods. The increase of the transverse emittance is proportional to the function $\mathcal{H}$ (eq.(1)), so keeping it low reduces emittance degradation. In an ERL these measures are essential in the magnets, where the bunch is the shortest.

If the effect on the bunch is small, magnetic optics with a repetitive symmetry and appropriate betatron phase advance between cells can cancel the CSR kicks (see e.g. [37] for the implementation on FERMI@Elettra and references therein). The idea is good to understand in case the bunch length does not change along the beam line (isochronous arc, or no correlated energy spread in the bunch). In this case the

imprinted energy change on every bunch slice is the same in each cell of the periodic focusing system. The final slice displacement and angle are the sum of displacements and angles from each cell (superposition). If the betatron phase advance from cell to cell is $2\pi k/N$, where k is any integer and N is the number of cells, then

$$\begin{pmatrix} x \\ x' \end{pmatrix} = \begin{pmatrix} x_1 \\ x_1' \end{pmatrix} \sum_{k=1}^{N} e^{2\pi i k/N} = 0$$

i.e. all slices are aligned again.

A similar approach is possible even for a periodic arc with bunch compression. In this case the assumption of a self-similar CSR wake is necessary, which is not always satisfied. E.g. CSR-wakes in the drifts are not self-similar. The implementation of such emittance correction is described e.g. in [7].

2.2.3.3 *Microbunching Instability*

The average power, coherently emitted from a short bunch, is $P_{coh} \sim Q_B^2 / R^{2/3} \sigma_z^{4/3}$, capable to cause a significant beam quality degradation. The effect can be greatly intensified, if the bunch is structured at much shorter scales than the bunch length.

The mechanisms of such "microbunching" can involve different wakes, most important being the longitudinal space charge (LSC) and coherent synchrotron radiation (CSR) itself [38, 39, 40]. The CSR wake shows a weak dependency of the beam energy only, whereas the LSC wake scales with $1/\gamma^2$ and therefore plays an important role in the low energy, injector part of an accelerator.

The wake imprints an energy modulation along the bunch, which can be transformed further into the longitudinal density modulation (microbunching). In a storage ring the momentum compaction factor α and in a linear accelerator the R_{56} element of the transport matrix is responsible for that. This is the same matrix element necessary for bunch compression, so both processes are intrinsically dependent.

The amplification factor for the density modulation (gain) in a beam line can be found e.g. in [40]. The initial density modulation can be imprinted in the RF photo gun already, e.g. from the longitudinal laser profile, generated with a pulse shaper. Some details of the analysis for LCLS can be found in [42]. Shot noise in the beam is another possibility, which usually gives much lower initial modulation amplitude.

The gain of the instability scales with the peak current of the bunch. Uncorrelated energy spread in the bunch smears out the bunching and can be used to suppress the instability [43]. A laser heater [44] is one option to increase the slice energy spread controllably. Using a strong wiggler to induce energy spread through emission of ISR is another one.

2.2.3.4 *Wakes & Impedances*

Resistive wall, surface roughness and geometric wakes are other sources of distortions in ERL beam dynamics. Usually they are smaller than CSR and LSC wakes. However, if the countermeasures are taken to reduce or (ideally) completely compensate the effects of CSR wake, they can become the main concern.

The resistive wall impedance is usually higher for ERLs compared to storage rings due to the short bunch length achievable. The scaling is $k_L \sim \sigma_z^{-3/2}$ (for $\sigma_z \gg a/\gamma$),

where k_L is the longitudinal loss factor, σ_z is the bunch length, a is the radius (half gap) of the vacuum chamber, γ is the relativistic factor [45].

Surface roughness can also be an issue. E.g. smooth NEG coating of the vacuum chambers can be necessary. Resonances in geometric wakes should be avoided at the design stage, as it has been done e.g. for bERLinPro [46].

2.2.3.5 *Linac Configuration & BBU*

Dipole mode driven transverse BBU can be a serious limitation for high current operation of an ERL. This is primarily an ERL specific problem, since accelerators with high quality factor cavities (superconducting) and operating with high average current are vulnerable to the instability.

Transversal BBU was observed and understood well at JLab ERL [47]. A simple analytical scaling can be derived for a "one cavity – one mode – one turn" case:

$$I_{th} = -\frac{2pc^2}{e\omega\left(\frac{R}{Q}\right)QR_{12}\sin(\omega T)}, \qquad (2)$$

where I_{th} is the threshold current of the instability, p is the beam momentum, ω is the dipole mode frequency, $\left(\frac{R}{Q}\right)Q$ is the mode impedance, R_{12} is the element of the transport matrix of the recirculation, and T is the recirculation time. In case of coupled optics and arbitrary polarisation angle α of the mode,

$$R_{12}^{*} = R_{12}\cos^2\alpha + (R_{14} + R_{32})\sin\alpha\cdot\cos\alpha + R_{34}\sin^2\alpha$$

should be used instead of R_{12} [48].

The threshold current is proportional to the beam energy, so the most problematic cavities are those where the beam has its lowest energy.

The threshold current for the transverse beam breakup for the case of a single cavity and single TM_{110} mode for a multi-pass ERL can be estimated as [49]:

$$I_b \approx I_0 \frac{\lambda\!\!\!^{-2}}{QL_{eff}\sqrt{\sum_{m=1}^{2N-1}\sum_{n=m+1}^{2N}\frac{\beta_m\beta_n}{\gamma_m\gamma_n}}},$$

where I_0- Alfven current, Q is the quality factor of HOM, $\lambda\!\!\!^{-} = \lambda/2\pi$, λ is the wavelength corresponding to the resonant frequency of the mode, γ_m is the relativistic factor at the m^{th} pass through the cavity, β_m – is the Twiss parameter, L_{eff} – is the effective length of the cavity, N is the number of acceleration passes. This expression indicates the limitation for the number of passes and proposes an optic design with β-functions as low as possible in cavities with low beam energy.

As it was shown in [50] the BBU threshold current for an N-turn ERL might be roughly estimated as $N(2N-1)$ times smaller than in a single turn machine. The worst case scenario of betatron phase advances between all pairs of passes through the cavity $\sin(\mu_{nm}) = 1$ is assumed there. The expression in [49] gives another estimation assuming random phases, which is closer to reality for a "large" number of cavities and passes.

Numerical modelling of the transverse BBU instability is necessary to take into account many linac cavities with all relevant modes. A number of codes for that exist [51, 52, 53].

Also a high arc chromaticity has been proposed as a measure to stabilise the beam against transversal BBU [54].

Longitudinal BBU driven by monopole modes is another issue for ERLs. In this case longitudinal dispersion R_{56} replaces R_{12} in the estimation for the threshold current (2) (see e.g. [55]). If single-turn ERLs operate with $R_{56} = 0$, they are not vulnerable to the instability (at least in theory). However, in a multi-turn ERL with bunch compression in arcs $R_{56} \neq 0$ and analysis of the instability is necessary.

2.2.3.6 *Ion Trapping*

ERLs are vulnerable to the effects of ions, accumulated in the potential well of the electron beam. The effects include

- Optical errors due to strong focusing of the electron beam with the space charge of the ion cloud,
- Higher electron beam scattering rates leading to the beam halo formation and increased beam losses,
- Ion-induced beam instabilities.

The ions are produced by electron ionisation of the residual gas (also possible is ionisation by synchrotron radiation). Confined inside the "time averaged electrostatic potential" of the electron beam, ions can stay in the beam for relatively long times, oscillating near the minima of the potential. Those coincide with the minima of the beam size for axially symmetrical beams.

Simulation of the ion cloud formation and dynamics is complicated by complex trajectories of ions in a potential of a non-axisymmetrical electron beam and the fact, that the dynamical equilibrium for the neutralisation factor of the electron beam is defined by a competing process of the ion heating (scattering on the electrons).

Modelling of the processes is a complex task, some results can be found e.g. here [56].

The methods for ion clearing in an ERL are basically the same as in storage ring. Clearing electrodes, gap in a bunch train, resonant excitation of the ion cloud are discussed e.g. in [57, 58].

For small scale machines a gap is not a good option due to short recirculation time. The variable beam loading due to the fluctuating beam current is a general concern.

2.2.4 References

1. S. J. Russell, "Overview of high-brightness, high-average-current photoinjectors for FELs", NIM-A, Volume 507, Issues 1–2, 2003.
2. A. Arnold, J. Teichert, "Overview on superconducting photoinjectors", Phys. Rev. ST Accel. Beams 14, 024801, 2011.
3. Phys. Rev. ST Accel. Beams: http://journals.aps.org/prstab/
4. JACoW: http://www.jacow.org/
5. "Conceptual Design Report BERLinPro", Ed. B. Kuske, N. Paulick, A. Jankowiak, J. Knobloch, 2012.
6. M. Abo-Bakr, et al., "Progress Report of the Berlin Energy Recovery Project BERLinPro", Proc. of IPAC15, Richmond, USA, 2015.
7. T. Atkinson, A. Bondarenko, A. Matveenko, Y. Petenev, "Conceptual Design Report for a multi-turn Energy Recovery Linac-based Synchrotron Light Facility (Femto-Science Factory)", Chap. 5.2.3, doi:10.5442/R0002.
8. H. Wiedemann, "Particle Accelerator Physics", Springer, 1993.
9. L. Serafini, J. Rosenzweig, "Envelope analysis of intense relativistic quasilaminar beams in rf photoinjectors: A theory of emittance compensation", Phys. Rev. E 55(6),

1997.
10. S.V. Miginsky, “Emittance compensation of elliptical beams”, NIM A 603 (2009), pp 32-34.
11. V.N. Litvinenko, R. Hajima, D. Kayran, “Merger designs for ERLs”, NIM A 557, V.1 (2006) pp. 165-175.
12. J. Rosenzweig, L. Serafini, “Transverse particle motion in radio-frequency linear accelerators”, Phys. Rev. E 49 (2), 1599.
13. Y. Petenev, “Analysis of injection and recovery schemes for ERL based light source”, Diss., HU Berlin, 2014.
14. R. Hajima: “Optics and beam transport in energy-recovery linacs”, NIM A 557 (2006) 45–50.
15. R. Chasman, et al., "Preliminary Design of a Dedicated Synchrotron Radiation Facility”, Proc. of PAC 1975, Washington, DC, USA, 1975.
16. H. Owen, B. Muratori, “Choice of Arc Design for the ERL Prototype at Daresbury Laboratory”, Proc. of EPAC 2004, Lucerne, Swiss, 2004.
17. J. B. Flanz, et al., “An Isochronous Beam Recirculation Magnet System”, Proc. of PAC 1981, Washington, DC, USA, 1981.
18. D. Trbojevic, et al., “ERL with Non-Scaling Fixed Field Alternating Gradient Lattice for eRHIC”, Proc. of IPAC’15, Richmond, USA, 2015.
19. D. Trbojevic, et al., “Lattice Design for the Future ERL-Based Electron Hadron Colliders eRHIC and LHeC“, Proc. of PAC11, New York, USA, 2011.
20. E. Jensen , et al., “Design Study of an ERL Test Facility at CERN”, Proc. of IPAC’14, Dresden, Germany, 2014.
21. E. Cruz-Alaniz, et al., “Tracking Studies in the LHeC Lattice”, Proc. of IPAC15, Richmond, USA, 2015.
22. E.C. Aschenauer et al., “eRHIC Design Study: An Electron-Ion Collider at BNL”, arXiv:1409.1633
23. A. Piwinski, “The Touschek Effect in Strong Focusing Storage Rings”, DESY 98-179, arXiv:physics/9903034.
24. S. Y. Lee: “Emittance optimization in three- and multiple-bend achromats”, Phys. Rev. E 54(2), 1996.
25. F. Stephan, et al., “Detailed characterization of electron sources yielding first demonstration of European X-ray Free-Electron Laser beam quality“,Phys. Rev. ST Accel. Beams 13, 020704 (2010).
26. A.V. Bondarenko, A.N. Matveenko, “Emittance compensation scheme for the bERLinPro injector”, Proc. of IPAC’11, San Sebastian, Spain, 2011.
27. L. M. Young, J. H. Billen, PARMELA documentation, LA-UR-96-1835.
28. K. Floettmann, “ASTRA: A Space Charge Tracking Algorithm”, http://www.desy.de/~mpyflo/
29. S.B. van der Geer, et al., “GPT: the General Particle Tracer“, http://www.pulsar.nl/gpt.
30. D. Rusthoi, W. Lysenko, K. Crandall, "Further Improvements on Trace 3-D," Proc. of the PAC (1997).
31. A.V. Bondarenko, A.N. Matveenko, “Implementation of 2D-Emittance Compensation Scheme in the BERLinPro Injector”, Proc. FEL 2011, pp 564-567.
32. M. Ferrario: “HOMDYN User Guide”, SLAC 3/1/02, 1999.
33. E.L. Saldin, E.A. Schneidmiller, M.V. Yurkov, “On the coherent radiation of an electron bunch moving in an arc of a circle”, NIM A 398 (1997) pp. 373-394.
34. M. Borland, “Simple method for particle tracking with coherent synchrotron radiation”, Phys. Rev. ST Accel. Beams 4, 070701 (2001).
35. Opal website, https://amas.psi.ch/OPAL
36. M. Dohlus, T. Limberg, CSRTrack User’s Manual: http://www.desy.de/xfel-beam/csrtrack/
37. S. Di Mitri, M. Cornacchia, S. Spampinati, ‘‘Cancellation of Coherent Synchro-tron

Radiation Kicks with Optics Balance'', Physical Review Letters 110, 014801, 2013.
38. G. Stupakov, "Theory and Observations of Microbunching Instability in Electron Machines", SLAC–PUB–9880, (2003).
39. S. Heifets and G. Stupakov, "Beam instability and microbunching due to coherent synchrotron radiation", Phys. Rev. ST Accel. Beams 5, 054402 (2002).
40. Ya. S. Derbenev, J. Rossbach, E. L. Saldin, and V. D.Shiltsev, „Microbunch Radiative Tail-Head Interaction", Deutsches Elektronen-Synchrotron Report No. TESLA-FEL 95-05, 1995.
41. E. Saldin, E. Schneidmiller, and M. Yurkov, "Klystron instability of a relativistic electron beam in a bunch compressor", Nucl. Instrum. Methods A 490, 1 (2002).
42. J. Wu et al., "Temporal Profile of the LCLS Photocathode Ultraviolet Drive Laser Tolerated by the Microbunching Instability", SLAC-PUB-10430, 2004.
43. S. Heifets, et al., "Coherent synchrotron radiation instability in a bunch compressor", Phys. Rev. ST-AB 5, 064401 (2002).
44. Z. Huang et al., "Suppression of microbunching instability in the linac coherent light source", Phys. Rev. ST-AB 7, 074401 (2004).
45. A. Chao, M. Tigner, (Ed.) "Handbook of Accelerator Physics and Engineering", World Scientific, 1999.
46. H.-W. Glock, et al., "Loss Factor and Impedance Analysis of Warm Components of BERLinPro", Proc. of IPAC15, Richmond, USA, 2015.
47. C. Tennant, E. Pozdeyev, "First observations and suppression of multipass, multibunch beam breakup in the Jefferson Laboratory free electron laser upgrade", Phys. Rev. ST Accel. Beams 8, 074403 (2005)
48. E. Pozdeyev, "Regenerative multipass beam breakup in two dimensions", Phys. Rev. ST Accel. Beams 8, 054401 (2005).
49. N.A. Vinokurov et al., "Critical Issues for High-Power FEL Based on Microtron Recuperator/Electron Out-Coupling Scheme" Proc. of SPIE Vol. 2988, (1997).
50. G.H. Hoffstaetter, I.V. Bazarov, „Beam-breakup instability theory for the energy recovery linacs", Phys. Rev. ST AB 7, 054401 (2004).
51. E. Pozdeyev et al., "Multipass beam breakup in energy recovery linacs", NIM-A 557 (2006) 176–188.
52. I. Bazarov, bi - Beam Instability BBU Code: http://www.lepp.cornell.edu/~ib38/bbu/
53. L. Merminga, I.E. Campisi, "Higher-Order-Models and Beam Breakup Simula-tions in the Jefferson Lab FEL Recirculating Linac", XIX International Linear Accelerator Conference, 1998.
54. V.N. Litvinenko, "Chromaticity of the lattice and beam stability in energy-recovery linacs", Phys. Rev. ST Accel. Beams 15, 074401 (2012).
55. J. Bisognano and M. Fripp, "Requirements for Longitudinal HOM Damping in Superconducting Linacs", CEBAF-PR-89-018.
56. G. Pöplau, U. van Rienen, A. Meseck, „Numerical studies of the behavior of ionized residual gas in an energy recovering linac",Phys. Rev. ST Accel. Beams 18, 044401 (2015).
57. G. H. Hoffstaetter, M. Liepe, "Ion clearing in an ERL", NIM A 557 (2006) 205–212.
58. S. Full, et al., "Detection and clearing of trapped ions in the high current Cornell photoinjector", http://arxiv.org/pdf/1508.00923.pdf

2.3 Successful Commissioning on Compact ERL in KEK

Hiroshi Kawata
ERL Project Office, KEK, Oho 1-1, Tsukuba, Ibaraki 305-0801, Japan
Mail to: kawata@post.kek.jp

2.3.1 Introduction

KEK established an Energy Recovery Linac (ERL) Project Office in April 2006. Because a GeV-class ERL machine had not been constructed anywhere in the world, it was necessary to first construct a compact ERL (cERL) with an energy of 35 MeV that could be used for the development of several critical accelerator components such as a high-brilliance DC photocathode electron gun and superconducting cavities for the injector and main accelerator. In FY2013, the components of cERL were successfully installed in an ERL test facility and the energy recovery beam operation was successfully demonstrated. Figure 1 shows the bird's-eye view of the cERL and figure 2 shows a photograph of the cERL accelerator in radiation shielding.

The following three targets were set for FY2014. First, with regard to beam development, a small emittance should be maintained during operation; two, achieving beam current operation at 100 μA, and three, production of the laser Compton scattering (LCS) X-ray system with the collaboration between KEK and JAEA.

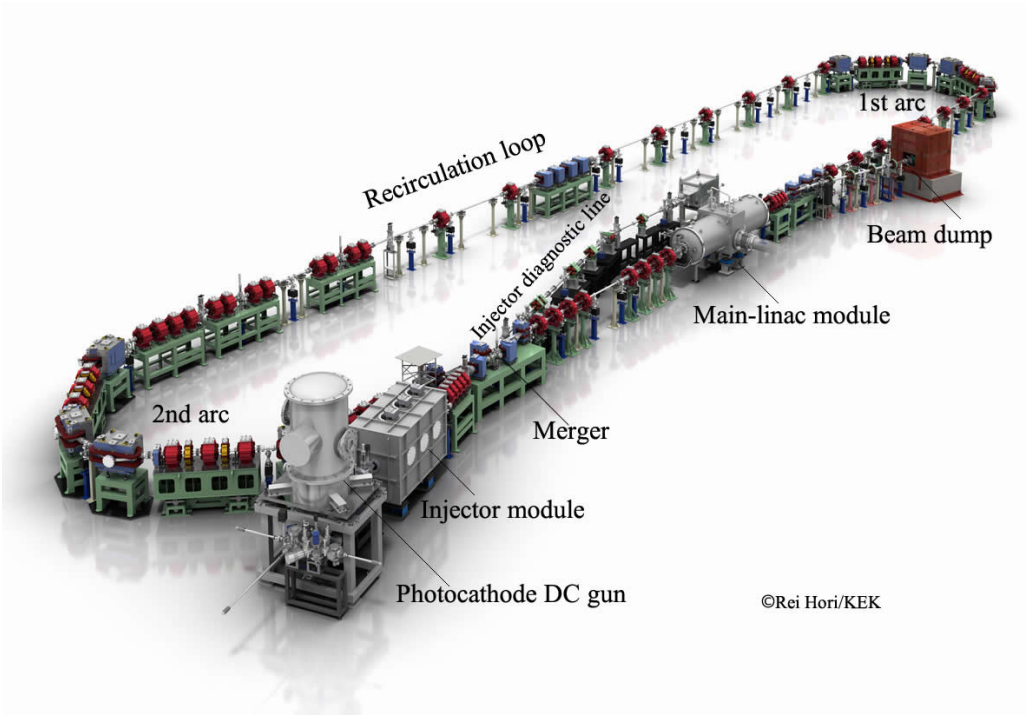

Figure 1: Bird's-eye view (CG) of the cERL.

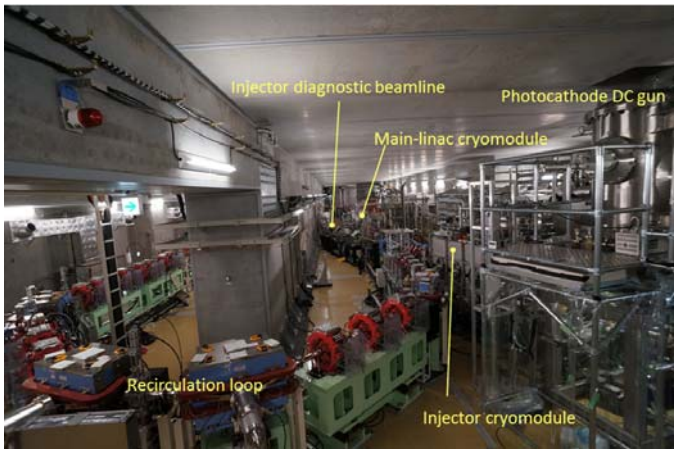

Figure 2: cERL accelerator in the radiation shielding.

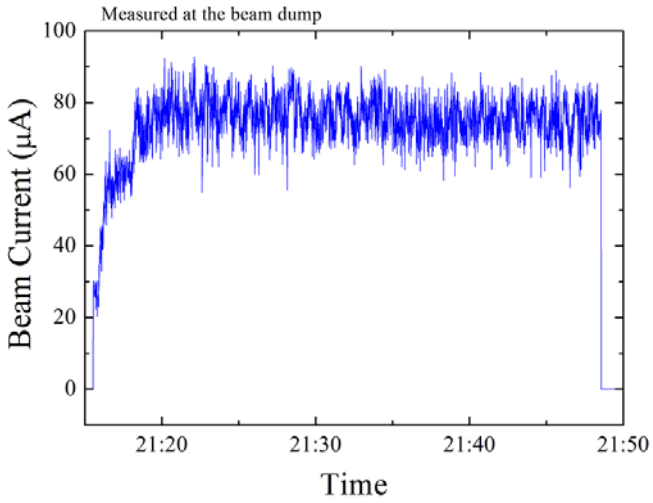

Figure 3: Successful demonstration of a beam current of ~80 μA.

Beam development was carried out from May until the end of June 2014. It was possible to maintain normalized beam emittance below 0.17 μm· rad at 0.02 pC/bunch, and 0.8 μm· rad at 7.7 pC/bunch at the injector part. At the recirculation loop of the ERL operation, normalized beam emittance was obtained as 0.14 μm· rad at 14 fC/bunch. Therefore, beam development at the small bunch charge was successfully demonstrated during FY2014. Beam development at a high bunch charge is set as a target for FY2015. During the beam operation from January to March of 2015, higher beam current operation of ~80 μA was carried out without any issues regarding radiation safety until March 2015 (the end of FY2014) as shown in Fig. 3. For FY2015, the beam current will be increased gradually up to 1 mA. Beamline and laser systems for LCS production were installed between July and December 2014. The LCS signal was successfully obtained by mid-February and the application of the LCS on X-ray imaging was demonstrated. In the following sections, the above-mentioned topics will be discussed in detail.

2.3.2 Recirculation and Beam Tuning in the cERL

2.3.2.1 *Overview of the Operation of the cERL*

The principal parameters of the cERL are given in Table 1. Figure 4 shows the statistics of beam operation time, (the time for which the beam was on) during FY2013–2014 [1]. The first continuous-wave (CW) beams of 20 MeV were successfully transported through the recirculation loop in February 2014 [2, 3]. After the commissioning of operation, various accelerator studies have been carried out. They include the establishment of start-up tuning, correction of beam optical functions, study on beam losses [4], and measurements of beam emittances in a recirculating loop. In the summer of 2014, the authorities requested a change in the maximum beam current (from 10 μA to 100 μA), and the approval was received in September.

From September to December 2014, an LCS system was installed. The LCS system aims to demonstrate technology for future high-flux g-ray sources [5, 6] and to develop advanced X-ray imaging technology using compact accelerators [7, 8]. The LCS system consists of an optical cavity resonator, a 1064 nm drive laser, an X-ray beamline, and an experimental hut. The LCS system was operated from February to April 2015. Accelerator issues related to the LCS system are reported in Sec. 2-4. The commissioning results of the LCS system are primarily reported in [6, 8].

Table 1: The principal parameters of the cERL.

	Design	**In operation**
Beam energy	35 MeV	20 MeV
Injector energy	5 MeV	2.9-6 MeV
Normalized emittance	0.1 μm· rad @7.7 pC 1 μm· rad @77 pC	under study
Beam current	10 mA	80 μA

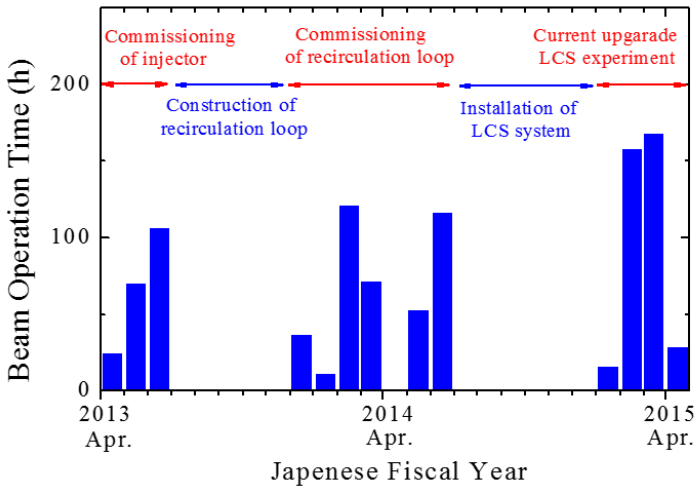

Figure 4: Statistics of beam operation time per month.

2.3.2.2 *Beam Development*

A layout of the cERL is shown in Fig. 5. Thirty fluorescent screens are used to measure both the positions and profiles of beams at low average currents. Forty-five stripline beam position monitors (BPMs) are used to measure beam positions non-invasively. Beam currents are measured at the beam dump point and at the gun power supply by subtracting offset currents. They can also be measured using three movable Faraday cups along the beamline.

During machine tuning, low-intensity macro-pulse beams were produced by the photocathode DC gun with a cathode voltage of 390 kV. The typical parameters of the beam pulses were as follows: macro-pulse width of 1.2 μs, macro-pulse repetition rate of 5 Hz, and bunch frequency of 1.3 GHz.

First, we set up the injector beams. The RF phases in three injector cavities were adjusted to on-crest acceleration while a buncher cavity was turned off. The beams were steered at the centers of two solenoids and of the first injector cavity. The total energy of the injector beams was adjusted to 2.9 MeV. Next, we steered beams through a three-dipole merger and main linac (ML) cavities. The RF phases in ML cavities were then adjusted to on-crest acceleration, which yielded total beam energy of 19.9 MeV.

We transported beams through the first arc, the south straight section, and the second arc. The beams were steered at approximately the centers of major quadrupoles while changing the strength of each quadrupole and monitoring the beam positions downstream. The recirculated beams passed further through an injection chicane where a dipole kick due to a merger dipole is canceled by the other two dipoles. We set the momentum ratio of the recirculated beam to the injected beam to be 7:1. The momentum ratio should be larger than 6:1 because of the finite aperture in the injection chicane.

Both injected and recirculated bunches pass through the ML section between the injection chicane and the dump chicane while they are separated longitudinally by approximately half a RF wavelength. We measured the beam positions using four BPMs to ensure non-invasive measurements. The signals were detected at 1.3 GHz, and the signals from the two beams were separated using their timing difference by a beam-recirculation time of 300 ns. We steered beams in this section using corrector magnets located upstream the injection chicane because the use of correctors in the main linac section affected both beams. This procedure required delicate tuning of beam recirculation.

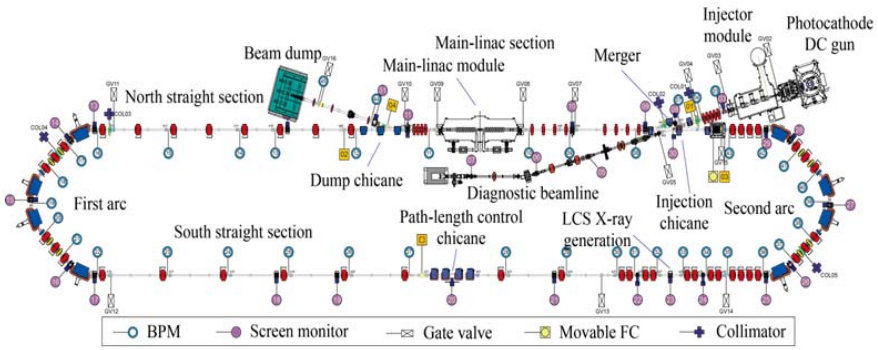

Figure 5**:** Layout of the cERL lattice configuration. The blue and red symbols denote dipole and quadrupole magnets, respectively.

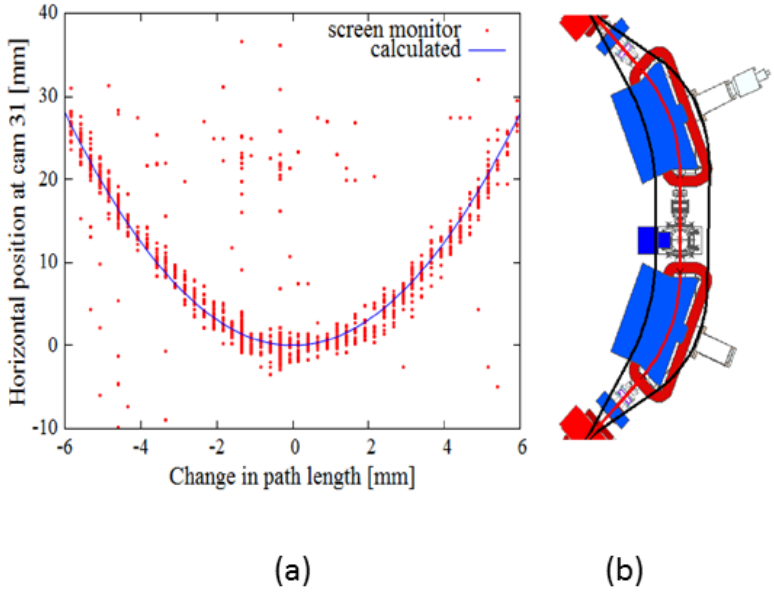

Figure 6: Tuning of decelerating phase. (a) Horizontal beam positions at the dump line as a function of the path length and (b) path length control in the second arc section are shown.

The recirculated beams decelerated when they passed through the ML cavities. We adjusted an RF phase of deceleration by changing the path length of the recirculation loop, as shown in an example in Fig. 6. The path length was changed by an orbit bump in the second arc section, shown in Fig. 6(b). The corresponding momenta of decelerated beams were measured at a screen in the dump line. The path length was adjusted so that the momenta require a minimum value. The path length can be changed by ±10 mm in each arc, and by ±5 mm in a path-length control chicane. The former method was mainly used because the latter chicane produced some hysteresis in the beam orbit. We found that an initial path length was very close (within a few mm) to the optimum one.

Figure 7 shows a demonstration of energy recovery in the ML cavities under CW operation. First, we conducted a non-ERL operation by reversing an RF phase in the downstream (ML2) cavity. A 2.9-MeV beam was accelerated and decelerated in ML1 and ML2 cavities, respectively, and was transported directly to the dump. Under this operation, both positive and negative beam loadings were observed in the ML1 and ML2 cavities, respectively. However, under the usual ERL operation, we observed little beam loading in these cavities.

Beam emittances were measured using the quadrupole-scan method. We varied the field strength of a single quadrupole located upstream a screen and measured beam sizes. Measurements at four locations showed that the normalized emittances could be preserved through the ML and the first arc at low bunch charges. For example, horizontal and vertical normalized emittances were both 0.14 μm· rad just after the first arc at a bunch charge of 14 fC/bunch (macro-pulse beam). At a medium bunch charge of 0.5 pC, the normalized emittances of 0.41 μm· rad in the horizontal direction (ε_{nx}) and 0.3 μm· rad in the vertical direction (ε_{ny}) were obtained after several tunings [9].

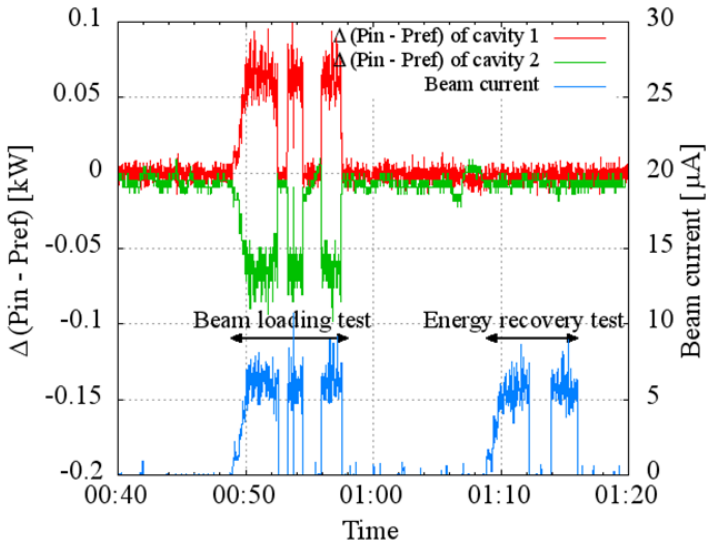

Figure 7: Demonstration of energy recovery in the ML cavities. Differences in the input and reflected RF powers are shown for the ML cavity 1 (red) and 2(green).

2.3.2.3 *100 μA Beam Current Operation*

Small beam losses are essential to realize the high-current operation. To this end, careful beam tuning and optics matching were carried out. To control beam losses, beam collimators were used. There are five collimators, and each of them has four movable copper rods cooled by water. A collimator at a merger section (E = 2.9 MeV, η_x = 0.23 m) was found to be very effective to eliminate beam tails or halos with a modest increase in radiation. To avoid problems caused by large beam losses, we used a fast interlock system for stopping the gun laser when large signals were detected at the beam loss monitors [10].

At the end of FY2014, we succeeded in transporting the maximum beam current of 80 μA to the beam dump. Operational parameters included beam energies of 19.9 MeV at the loop and 2.9 MeV at the merger, a bunch repetition rate of 162.5 MHz, a bunch charge of 0.5 pC, and beam optics for the LCS experiment.

2.3.2.4 *Tuning for Laser Compton Scattering (LCS)*

In an operation for the LCS experiment, electron beams are focused to a very small size (typically, 30 μm rms) at an interaction point (IP) where the electron bunches collide with laser pulses. Beam losses in the LCS section should be minimized to avoid undesirable background radiation to detectors. Therefore, there is a tradeoff between small beam size and small beam losses close to the IP. Figure 8 shows an example of low-β optics in the LCS section. In this design, beam sizes at the IP are expected to be 21 μm the horizontal direction (σ_x^*) and 33 μm in the vertical direction (σ_y^*) using measured ε_{nx} of 0.47 μm· rad and ε_{ny} of 0.39 μm· rad at a bunch charge of 0.5 pC.

The tuning procedure established for the beam optics in the LCS section is as follows. First, we designed K-values of quadrupoles containing some errors. After the optics matching before the LCS section, we scanned the K-value of quadrupole QMLC04, shown in Fig. 8, and measured beam sizes using a screen monitor at the IP.

While observing the response curves, we adjusted the K-values of QMLC03 so that both horizontal and vertical beam sizes (σ_x, σ_y) had waists at the same K-value as QMLC04. The latter was determined so that both σ_x and σ_y took minima. After the tuning, we obtained σ_x* of 13 μm and σ_y* of 25 μm at the IP, which were estimated from the Q-scan measurement.

Using the "LCS optics" mentioned above, we succeeded in transporting the beam to the dump with small beam losses. We used a bunch repetition frequency of 162.5 MHz that was matched to the frequency of the LCS laser. After we adjusted both the positions and the phases of laser pulses, we succeeded in colliding the electron bunches with laser pulses at a bunch charge of 0.5 pC in CW operation and found that an average current value was approximately 80 μA. As a result, we observed a 6.9 keV X-ray signal at the end of the X-ray beamline using a detector [7, 9]. The typical count rate was 1200 counts/s in a detector with a diameter of 4.66 mm at a beam current of 58 μA at the experimental hut, located far from the IP of 16.6 m as shown in Fig.9. The success of sustained collision between beam and laser demonstrated both high quality and high stability of cERL beams.

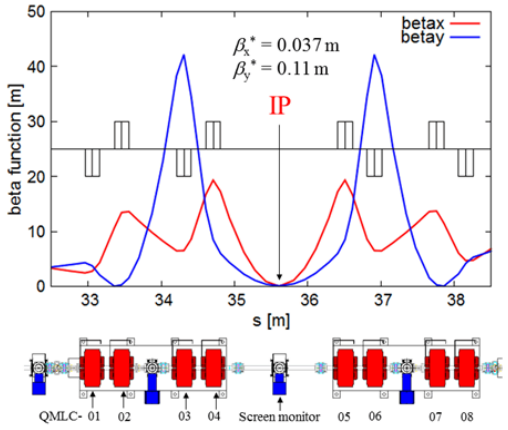

Figure 8: Design of low-optics in the LCS section.

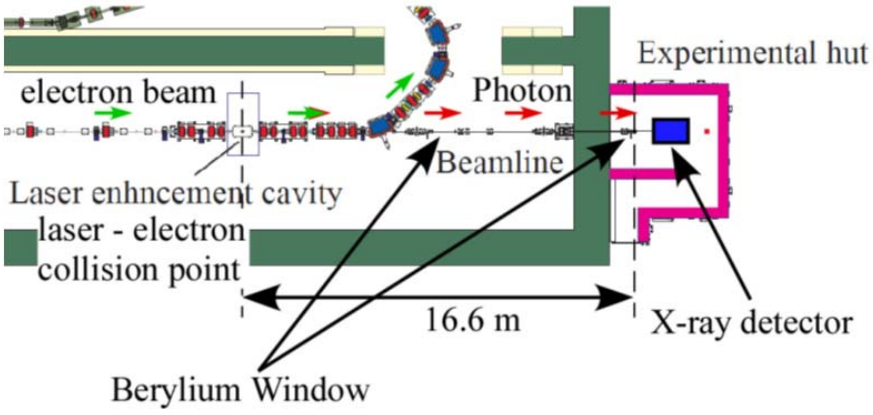

Figure 9: Schematic view of the layout of the LCS beamline.

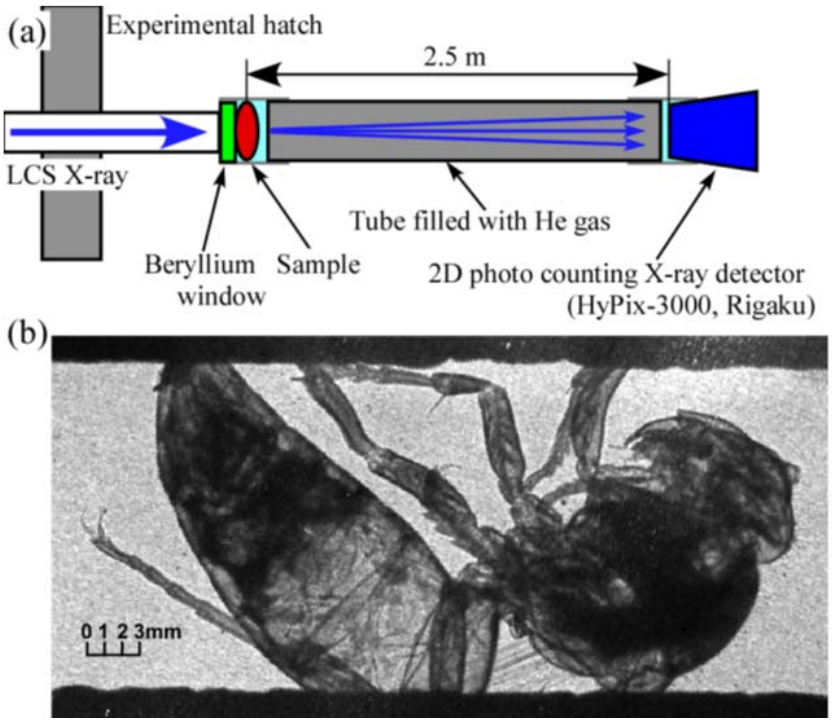

Figure 10: (a) Schematic layout of the LCS X-ray imaging experimental setup and (b) the LCS X-ray hornet imaging.

The LCS X-ray imaging was carried out by the setup shown in Fig. 10(a). The resulting X-ray image is shown in Fig. 10(b). This image was obtained by 10 min accumulation to achieve sufficient statistics. Due to the small source size of LCS X-rays, it is possible to perform refraction contrast imaging [11] that allows enhancing the edges of X-ray imaging. The detector was positioned 2.5 m from the specimen. Since the transmittance of a 7 keV X-ray in the air is low, the tube filled with He gas was placed between the beryllium window and the detector. The transmittance of the 7 keV X-rays in He is almost 100 %. Therefore, it was possible to obtain the high contrast X-ray image shown in Fig. 10(b).

2.3.3 **Conclusion**

Various accelerator studies are in progress in the cERL. We have achieved the maximum beam current of 80 μA in CW operation. The successful beam-laser collisions demonstrated both high quality and high stability of cERL beams. In FY2015, we will continuously study lower-emittance operation at high bunch charges, higher beam currents up to 1 mA, bunch compression, and higher X-ray flux in the LCS experiment.

2.3.4 References

1. S. Sakanaka, *et al*., "Recent Progress and Operational Status of the Compact ERL at KEK", proceedings of 6th International Particle Accelerator Conference, Richmond, VA, USA (2015).
2. N. Nakamura, *et al*., "Present Status of the Compact ERL at KEK", proceedings of 5th International Particle Accelerator Conference, Dresden, Germany (2014).
3. S. Sakanaka, *et al*., "The First Beam Recirculation and Beam Tuning in the Compact ERL at KEK", proceedings of 27th Linac Accelerator Conference, Geneva, Switzerland (2014)
4. O. Tanaka, *et al*., "Simulation Study of Beam Halo and Loss for KEK Compact ERL", proceedings of 6th International Particle Accelerator Conference, Richmond, VA, USA (2015).
5. R. Nagai, *et al*., "Construction of a Laser Compton Scattered Photon Source at cERL", proceedings of 5th International Particle Accelerator Conference, Dresden, Germany (2014).
6. R. Nagai, *et al*., "Demonstration of High-flux Photon Generation from an ERL-based Laser Compton Photon Source", proceedings of 6th International Particle Accelerator Conference, Richmond, VA, USA (2015).
7. T. Akagi, *et al*., "Development of an Optical Resonant Cavity for the LCS Experiment at cERL", proceedings of 5th International Particle Accelerator Conference, Dresden, Germany (2014).
8. A. Kosuge, *et al*., "Development of a High Average Power Laser for High Brightness X-ray Source and Imaging at cERL", proceedings of 6th International Particle Accelerator Conference, Richmond, VA, USA (2015).
9. T. Miyajima, *et al*., "Status of Higher Bunch Charge Operation in Compact ERL", proceedings of 6th International Particle Accelerator Conference, Richmond, VA, USA (2015).
10. R. Takai, *et al*., "Design and Initial Commissioning of Beam Diagnostics for the KEK Compact ERL", proceedings of International Beam Instrumentation Conference, Monterey, USA (2014).
11. S. W. Wilkins, T. E. Gureyev, D. Gao, A. Pogany, and A. W. Stevenson, "Phase-contrast imaging using polychromatic hard X-rays", *Nature* **384**, 335-338 (1996).

2.4 Development of an ERL Based TeV Energy ep and eA Collider at CERN

O. Brüning, E. Jensen, A. Milanese, E. Nissen, D. Pellegrini, R. Tomas, A. Valloni, F. Zimmermann
CERN, CH – 1211 Geneva 23
E. Cruz, M. Klein, P. Kostka, Liverpool University
Mail to: oliver.Bruning@cern.ch

2.4.1 Introduction

Several electron-ion and electron-proton collider projects have been or are being studied around the world (e.g. MEIC, eRHIC, LHeC, FCC-eh, etc.) since the end of the HERA project at DESY [1]. First ideas for an electron-hadron collider at CERN were already studied during the LHC design phase in 1997 [2] and later reiterated at the end of the LHC construction work in 2006 [3]. A dedicated LHeC study at CERN was put

into action in 2007 just before the start of the LHC commissioning in 2008. The goal of the LHeC study group was to evaluate different options for the LHeC (Ring-Ring based and Linac-Ring based options) and to prepare a conceptual design report (CDR) within a period of 4 years. The LHeC efforts were sponsored and supported by CERN, ECFA and NuPECC and the CDR was published in summer 2012 [4]. It described the physics, a detector and in considerable detail the design of a new electron-proton (ep) and electron-ion (eA) collider for high luminosity, 10^33 cm-2 s-1 and a cms energy beyond 1 TeV The main conclusions from the LHeC CDR were already reported in the ICFA Newsletter 58.

The LHeC CDR identified the Linac-Ring implementation with Energy Recovery operation as the most feasible option for the LHeC and the publication of the CDR was followed by a second series of workshops that addressed the needs for technology developments and test facilities for demonstrating the viability of an ERL based LHeC project. This article reports on the main tentative conclusions from this second series of workshops. At the time of the publication of the CDR, the Higgs boson was discovered. This moved the striking ep Higgs physics potential sketched already in the CDR [4] into a second focus: The LHeC may not only become the most powerful microscope for the substructure of matter the world can build, it may also be the next collider with which the Higgs phenomenon can be studied. That combination put a more ambitious luminosity goal of near to 10^34 cm-2 s-1 on the agenda of the further LHeC development.

2.4.2 **ERL Design Considerations**

An electron beam energy of 60 GeV, together with a luminosity of $1x10^{34}$ $cm^{-2}s^{-1}$ allows the ultimate application of the LHeC as a Higgs factory. These are to be delivered with a realistic power budget within 100 MW. It should be noted that such beam energy had already been exceeded during the LEP era, when, in the same tunnel now being used by the LHC, electron and positron beams of 104.5 GeV were achieved. Therefore, a natural option consists in fitting a new lepton ring into the existing LHC tunnel. Such machine would meet the key beam parameters with no major challenges except the ones arising from the integration into the LHC site. Indeed such an implementation would require km long bypasses that had to be dug around the existing experimental caverns, and sections of the LHC, such as the RF and the dump kickers, needed strong interventions to accommodate the additional ring. Although part of the construction could be scheduled while operating the LHC, the installation would require several years of shutdown of the LHC.

An alternative design approach to the electron facility aims at an installation in a dedicated tunnel, completely decoupled from the LHC with the only exception of the Interaction Region. Linac designs can be adapted from linear collider studies and fitted in few kilometers of straight tunnel, easily exceeding the target energy of 60 GeV. However, a linac would not be capable of delivering a significant number of Higgs events within the given power consumption budget of 100 MW. While linear colliders achieve high luminosity by taking advantages of small emittance and strong focussing of the flat leptonic beams, this path is excluded at the LHeC by the round hadronic beam. The only alternative for boosting the luminosity at the LHeC is therefore to increase the average electron current.

High currents and, consequently, the luminosity goal, can be achieved with a linac adopting the energy recovery scheme, in which the spent electron beam is decelerated in

order to extract its energy and reuse it to accelerate a fresh beam. At the LHeC this is realized by bending the beam to re-inject it into the linac at the decelerating phase. From the beam dynamics point of view the main advantage of the ERL over a ring is that it allows to deliver a smaller emittance beam and to exploit it with a stronger beam-beam effect that would not be tolerable in a ring. Table 1 summarizes a possible set of parameters for collisions with the ultimate HL-LHC beam. The computation of the luminosity does not take into account the hourglass effect and the pinch enhancement factor. It can be noted that with the linac, with no restriction on the electron tune shift, one can reach very a similar luminosity even with smaller beam current.

Table 1: comparison between the parameters of the ERL and the 27 km Ring electron facilities coupled to the HL-LHC beam based on the 'ultimate' LHC beam parameter sets of the CDR.

	ERL		**27 km Ring**	
	p	**e^-**	**p**	**e^-**
Beam Energy [GeV]	7000	60	7000	60
Bunch Spacing [ns]	25	25	25	25
Bunch Intensity [10^{10}]	17	0.2	17	2
Beam Current [mA]	1110	6.4	860	100
RMS Bunch Length [mm]	75.5	0.6	75.5	6
Normalized RMS emittance [mm mrad]	3.75	50	3.75	$590_x/290_y$
IP Beta Function [m]	0.1/0.1	0.12/0.12	1.8/0.5	$0.18_x/0.1_y$
IP Spot Size [µm]	7	7	30/15	30/15
Beam-Beam Tune Shift	0.0001	0.76	0.0009/0.0005	$0.085_x/0.089_y$
Luminosity [10^{33} $cm^{-2}s^{-1}$]	1.1		1.34	

Comparing the ERL with a similarly sized 9 km ring, we get more striking results. The increased radiation imposes a lower current to fit within the power constraints, but also lead to bigger emittances which require a relaxation of the spot size to keep the tune shift at acceptable values. The luminosity reduction is approximately a factor 10.

In conclusion, although technologically challenging, an ERL allows delivering competitive luminosities compared to a ring. This is especially true if the two of them are similarly sized. Considering also the technical difficulties of the integration of an electron ring into the LHC tunnel, the ERL has therefore been chosen as the baseline design for the LHeC.

The ERL design for the LHeC electron facility is sketched in Figure 1. The racetrack layout hosts two superconducting linacs on the straight sections and three recirculating arcs on each side. Its total length is 9 km: 1/3 of the LHC circumference. An integer fraction is required to guarantee that, in the presence of an ion-cleaning gap in the electron beam, the proton bunches collide with electrons either always or never. While this might turn out not be a strong requirement in the end, but intuitively felt as an appropriate boundary condition for these studies.

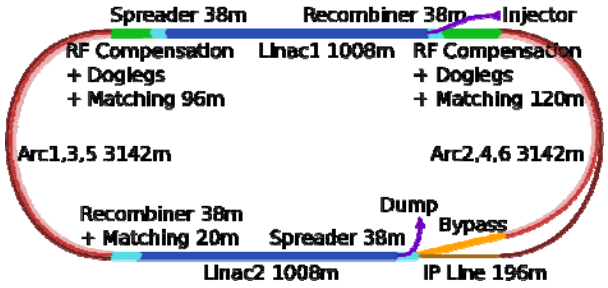

Figure 1: Scheme of the LHeC ERL-based electron facility.

Each of the two linacs is about 1 km long and provides a total acceleration of 10 GeV. The injection energy has been chosen to be 500 MeV. In order to reach the collision energy of 60 GeV, the electrons are re-circulated three times. Beams of different energies are directed into the corresponding recirculation arcs via beam spreaders/re-combiners which introduce/remove vertical separation at each end of the linacs. Arc2 and Arc4 are equipped with bypasses that provide separation from the detector.

After the collision with the LHC proton or ion beam, the electron beam is delayed by half of the RF period and re-injected into the same linacs to be decelerated in three subsequent turns. Its energy is released into the RF and used to accelerate the next fresh beam. This allows one to increase the beam current and luminosity while limiting the RF power consumption.

The number of recirculating turns follows from a cost estimation (see Section 1.2.1). The key effect is synchrotron radiation which leads to a scaling of the arc length with E_e^4 while the linac length scales with E_e. On the other hand the linac cost per meter is much higher than the one of the arc. For these reasons, aiming at a lower energy, one obtains smaller arcs and can save on the linac cost adding more recirculating turns, while at higher energies is better to reduce the turn number increasing the length of the linac. This will be further discussed in the following section.

The operation of the ERL foresees continuous injection of bunches every 25 ns (as in the LHC). During the stable operation of the machine, bunches at all the possible turn numbers coexist in the racetrack leading to a six times higher beam current in the SRF cavities as the beam current at the Interaction Point (IP) and given in Table 1. In the linacs they appear in particular patterns depending on the lengths of the arcs, giving specific times of flight. Gaps in the electron train may be inserted to match the LHC filling pattern and to allow for ion cleaning.

2.4.2.1 *Size and Energy Considerations*

The choice of the LHeC electron beam energy E_e is dictated both by physics and by practical considerations. Physics wants it to be maximum, cost and effort minimum.

The physics program has three cornerstones:

i) Higgs physics - the cross section for Higgs production is approximately proportional to the electron beam energy and the acceptance for forward going particles shrinks when the energy gets reduced, the potential for precision Higgs physics therefore rises more than linearly with E_e;

ii) Beyond Standard Model (BSM) and electroweak physics – a key example is top physics for which the LHeC has a unique potential both to find anomalous or flavour changing couplings and to perform salient high precision measurements.

The top production cross section is close to threshold and rises by a factor of ten when E_e increases from 30 to 60 GeV;

iii) Novel QCD physics – for which the discovery of gluon saturation would be key. That requires to cover the smallest possible Bjorken x values. Since x decreases proportional to $1/E_e$ one wants large E_e.

The racetrack LHeC footprint scales in its accelerator parts roughly in proportion to E_e, notably the length of the linacs, whereas the return arc radius scales like E_e^4, because of synchrotron radiation losses. The synchronisation with the proton beams, along with the possible need for ion gaps and the goal of keeping the LHC ptoton bunches at constant collision patterns, requires that the circumference U_e of the LHeC electron beam is a fraction, 1/n, of the LHC circumference. All these considerations have led to choose n=3, U_e=8.9km and E_e=60 GeV obtained in three passes as the default LHeC ERL configuration. Note that the SPS length is 1/4 of the LHC circumference and 1/5 would scale to about 52 GeV electron beam energy. Going much beyond 60 GeV becomes readily very expensive.

In 2012 it was decided to keep 60 GeV as the default energy of the electron beam so as to also approximately match the initial LHC discovery potential for lepto-quarks, extending to about and somewhat beyond 1 TeV. In the current LHeC design the CMS energy $\sqrt{s}=2\sqrt{E_eE_p}$ is equal to 1.3 TeV. A choice of E_e around 60 GeV appears also attractive in view of HERA, compared with which this doubles the electron beam energy and permits more precise measurements in areas, such as the longitudinal structure function, where controlling data at the smallest fraction of scattered electron energy versus beam energy is important. A final decision on the electron energy E_e will be made when the project goes ahead towards its realisation.

Table 2: High Luminosity LHC parameters (LHC nominal ones for comparison).

Parameter	**Nominal LHC (design report)**	**HL-LHC 25ns (standard)**	**HL-LHC 25ns (BCMS) [9]**
Beam energy in collision [TeV]	7	7	7
N_b	1.15E+11	2.2E+11	2.2E+11
n_b	2808	2748	2604
Number of collisions in IP1 and IP5 [1]	2808	2736	2592
N_{tot}	3.2E+14	6.0E+14	5.7E+14
beam current [A]	0.58	1.09	1.03
x-ing angle [μrad]	285	590	590
beam separation [σ]	9.4	12.5	12.5
β^* [m]	0.55	0.15	0.15
ε_n [μm]	3.75	2.50	2.50
ε_L [eVs]	2.50	2.50	2.50
r.m.s. energy spread	1.13E-04	1.13E-04	1.13E-04
r.m.s. bunch length [m]	7.55E-02	7.55E-02	7.55E-02
IBS horizontal [h]	80 -> 106	18.5	18.5
IBS longitudinal [h]	61 -> 60	20.4	20.4
Piwinski parameter	0.65	3.14	3.14

Total loss factor R0 without crab-cavity	0.836	0.305	0.305
Total loss factor R1 with crab-cavity	(0.981)	0.829	0.829
beam-beam / IP without Crab Cavity	3.1E-03	3.3E-03	3.3E-03
beam-beam / IP with Crab cavity	3.8E-03	1.1E-02	1.1E-02
Peak Luminosity without crab-cavity [cm^{-2} s^{-1}]	1.00E+34	7.18E+34	6.80E+34
Virtual Luminosity with crab-cavity: L_{peak}*R1/R0 [cm^{-2} s^{-1}]	(1.18E+34)	19.54E+34	18.52E+34
Events / crossing without leveling and crab-cavity	27	198	198
Levelled Luminosity [cm^{-2} s^{-1}]	-	5.00E+34 [5]	5.00E+34
Events / crossing (with leveling and crab-cavities for HL-LHC) [8]	27	138	146
Peak line density of pile up event [event/mm] (max over stable beams)	0.21	1.25	1.31
Leveling time [h] (assuming no emittance growth) [8]	-	8.3	7.6
Number of collisions in IP2/IP8	2808	2452/2524 [7]	2288/2396
N_b at LHC injection [2]	1.20E+11	2.30E+11	2.30E+11
n_b / injection	288	288	288
N_{tot} / injection	3.46E+13	6.62E+13	6.62E+13
ε_n at SPS extraction [μm] [3]	3.40	2.00	< 2.00 [6]

[1] Assuming one less batch from the PS for machine protection (pilot injection, TL steering with 12 nominal bunches) and non-colliding bunches for experiments (background studies…). Note that due to RF beam loading the abort gap length must not exceed the 3μs design value.

[2] An intensity loss of 5% distributed along the cycle is assumed from SPS extraction to collisions in the LHC.

[3] A transvere emittance blow-up of 10 to 15% on the average H/V emittance in addition to the 15% to 20% expected from intra-beam scattering (IBS) is assumed (to reach the 2.5 μm/3.0 μm of emitance in collision for 25ns/50ns operation)

[4] As of 2012 ALICE collided main bunches against low intensity. satellite bunches (few per-mill of main bunch) produced during the generation of the 50ns beam in the injectors rather than two main bunches, hence the number of collisions is given as zero.

[5] For the design of the HL-LHC systems (collimators, triplet magnets,..), a design margin of 50% on the stated peak luminosity was agreed upon.

[6] For the BCMS scheme emittances down to 1.7 μm have already been achieved at LHC injection which might be used to mitigate excessive emittance blowup in the LHC during injection and ramp.

[7] The lower number of collisions in IR2/8 wrt to the general purpose detectors is a result of the agreed filling scheme, aiming as much as possible at a democratic sharing of collisions between the experiments.

[8] The total number of events/crossing is calculated with an inelastic cross-section of 85 mb (also for nominal), while 100 mb is still assumed for calculating the proton burn off and the resulting levelling time

2.4.2.2 *Performance Projections for High Luminosity*

The discovery of the Higgs Boson at the LHC in the summer of 2012 triggered studies on how future colliders could best be used for high precision studies of the new particle. The relatively light mass of the Higgs Boson of 125 GeV suggested also the possibility of studying the new particle at the LHeC. Realizing that the production cross section for the Higgs Boson in e-p collisions (from W*W*□ Z) is comparable to that at a future e^+-e^- collider (via Z*□ZH) initiated studies to increase the performance reach of

the LHeC beyond those quoted in the LHeC CDR and to a level that could produce sufficient statistics for such studies.

The performance projections of the LHeC CDR were based on the 'ultimate' proton beam parameters of the LHC TDR [5, 6] that were used for specifying the LHC vacuum and cryogenic systems (luminosity of 2.5 $10^{34}cm^{-2}s^{-1}$ and 1.7 10^{11} ppb with ε_n = 3.75 μm normalized emittance as compared to the nominal values of 1 $10^{34}cm^{-2}s^{-1}$ and 1.15 10^{11} ppb with ε_n = 3.75 μm). However, the HL-LHC Design study started exploring more ambitious beam parameters in 2011 in the framework of the EU funded FP7 EuCARD AccNet and HiLumi Design studies (see for example [7]). Realizing that sufficient luminosity lifetimes for the HL-LHC require most of all an increase in the proton beam currents started a series of discussions between the LHC Injector Upgrade (LIU) and HL-LHC projects that resulted in the definition of the HL-LHC beam parameters that are specified in the HL-LHC Preliminary Design Report (PDR) [8] and quoted in [9]. Table 2 summarizes the main HL-LHC beam parameters from these documents.

Using the HL-LHC rather than the more conservative 'ultimate' LHC beam parameters, pushing the electron beam current for the ERL by a factor 2 (from ca. 7mA to 15mA) and the optical functions for the proton beam at the Interaction Point (IP) by a factor 2 wrt the CDR values (β^* reduction below 10cm - the β^* value for the electron beam stays with 10cm close to the LHeC CDR value) boosts the LHeC performance reach from the CDR value to $10^{34}cm^{-2}s^{-1}$. The factor 2 increase in the ERL beam current seems reasonable when comparing the parameters with those of other future ERL based collider projects (e.g. eRHIC [10]). In fact, when comparing the LHeC parameters with those of the eRHIC project, there even seems to be some margin for even higher electron beam currents. Reducing the optical functions at the IP by a factor 2 wrt the CDR value is certainly ambitious. However, first studies in this direction are encouraging and have not yet ruled out β^* values of 5cm for the LHC. The final β^* reach depends to a large extent on the magnet apertures and the ability to correct chromatic aberrations in the HL-LHC (see Section 1.1.5). There is clearly room for further iterations on these parameters. But first studies seem to indicate that a high performance level of $L = 10^{34}cm^{-2}s^{-1}$ is within reach for the LHeC.

2.4.3 **Interaction Region Optics & Lattice Design and Integration into the HL-LHC ATS Optics**

2.4.3.1 ***Nominal Design***

The design of the LHeC interaction region (IR) aims at focusing the counter-clockwise rotating proton Beam2 and colliding it with the electron beam of the ERL while the clockwise proton Beam1 bypasses the interaction.

A first conceptual design of the LHeC Linac-Ring IR was presented in [11]. The aim of this design was to achieve head-on electron-proton collisions in the interaction region at a luminosity $L=10^{33}$ $cm^{-2}s^{-1}$, requiring a low β^* (β function at the interaction point) of 10 cm. This low β^* was achieved by implementing a new inner triplet (IT) of quadrupoles, positioned as close as possible to the interaction point (IP) to reduce chromaticity.

An illustration of the three beams passing through the inner triplet is shown in Fig. 2. The closest quadrupole to the IP (Q1) is based on a half aperture design to minimize the synchrotron radiation produced by the electron beam. A new type of magnet has been proposed for the Q1 to overcome some of the present challenges of the design [12].

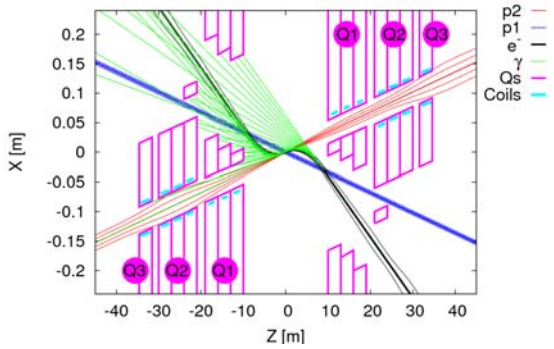

Figure 2: Focussed proton Beam2 (red) colliding with electron beam (black) while the unfocussed proton Beam1 bypasses the interaction. Each proton and electron beam passes through its corresponding aperture in the inner triplet.

It was initially hoped that a compact Nb_3Sn triplet at a distance (L^*) of 10 m from the interaction point would allow the use of a conventional scheme for chromaticity correction using the arc sextupoles. However, after matching the new triplet to the LHC and correcting the chromaticity the chromatic beta beating at dp/p=±0.001 is about 100%, which is not tolerable regarding collimation and machine protection issues [13].

The challenge consists in developing an optics that not only achieves the β^* of 10 cm while leaving the HL-LHC insertions undisturbed but that also provides a dedicated chromaticity correction scheme.

2.4.3.2 *Extension of the ATS to the LHeC*

The Achromatic Telescopic Squeezing scheme is a novel technique proposed for the HL-LHC project in IR1 and IR5 (ATLAS and CMS respectively) to reduce the β^*, overcoming the limitations of the optics given by the quadrupole strengths in the IR's and the chromatic correction efficiency limits [14].

The ATS consists of creating and absorbing a β-beating wave in the arcs adjacent to the low β insertions. By adjusting the phase advance in the arc cell to π/2, this β-beating wave is carefully constructed in a way that will increase the β function at the location of every alternate sextupole in the arcs, and consequently increase its efficiency for chromatic correction, at the same rate than the β* gets reduced.

Although reducing β^* increases the IR chromaticity, the improvement in sextupole efficiency in the arcs leads to a net benefit.

Following a proposal to integrate the LHeC IR into the HL-LHC lattice using the ATS scheme [15], a first study of the required proton optics for the nominal case was presented in [16]. This procedure involved extending the β-beating wave in the arc between IR2 and IR3 by adjusting the arc cells in sector 23 to the phase advance of π/2 and imposing the ATS matching conditions for proton beam 2 for the left and right phase advance of IR2 (with respect to IP2) resulting in a β* of 10 cm in IR2 for the LHeC and a β*of 15 cm in IR1 and IR5 for the HL-LHC. The β functions along the LHC with this optics are shown in Fig. 3.

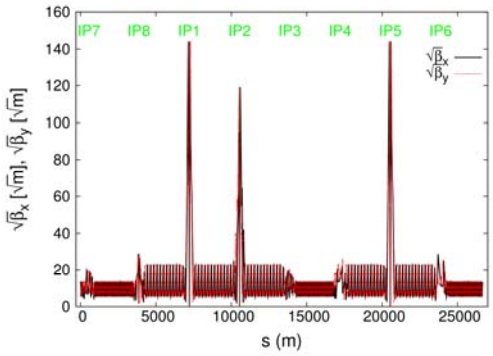

Figure 3: LHeC ATS collision optics for beam 2 with β^*=10 cm and L^*=10 m in IP2 and β^*=15 cm in IP1 and IP5.

2.4.3.3 *Flexibility of the Design*

The flexibility of the design described above (based on the ATS scheme) is of great interest because of the benefits that could be obtained in terms of synchrotron radiation power and luminosity.

Two methods were used to assess the flexibility. First, β^* is reduced as far as possible, to determine the maximum luminosity that can be achieved. Second, L^* is increased as far as possible, to minimize the synchrotron radiation power from the electron beam: with larger L^*, less bending is required to guide the electron beam into the field-free aperture of the proton inner triplet.

Keeping the optics parameters at either end of IR2 fixed, the strengths of the quadrupoles in the IR2 can be used as variables to find solutions for different values of β^* and L^*.

Stable solutions for optical designs with L^* between 10 m and 20 m and β^* fixed at 10 cm have been found, as well as the cases with β^* = {5,6,7,8,9,10,20} cm and L^* fixed at 10 m [17].

2.4.3.4 *Chromaticity Correction*

The chromaticity correction for the HL-LHC case was achieved using only one family of sextupoles at each side of the IPs. However, in the LHeC, an imbalance exists due to the β wave produced to perform the telescopic squeeze in both IP1 and IP2. The path to follow is then trying to achieve a global correction that might break the locality of the chromatic correction but that will certainly bring benefits in terms of controlling the chromatic aberrations.

The strengths of all sextupole families are varied to fix the horizontal and vertical chromaticities to values $Q'_x=Q'_y=2$, and to reduce the chromatic betatron amplitude functions in the collimation insertions IR3 and IR7 to W_x, $W_y<200$.

Chromatic correction including control of the tune spread to avoid resonances up to order 9 was achieved for a minimum β^* of 8 cm with L^*=10 m, and a maximum L^* of 18 m with β^*=10 cm.

The natural chromaticity for the different optical designs in terms of L^* and β^* along with the limit of the chromatic correction is shown in Fig. 4.

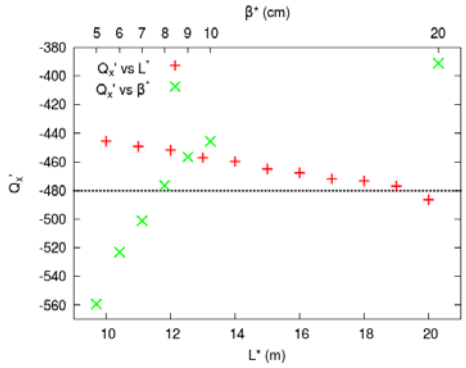

Figure 4: Limit of the chromatic correction (black dashed line) overlaid in the plot Q_x' vs L* (red) and Q_x' vs β^*(green).

2.4.3.5 *Tracking Studies*

Dynamic Aperture (DA) studies were performed to study the impact of the different lattices on long term stability of the beam. The DA calculations were carried out in SixTrack[1] over 10^5 turns and considering 60 different realisations (seeds) of the LHC magnet errors. So far, the errors of the new IT and recombination dipoles D1 and D2 for IR1, IR2 and IR5 have not been included, as well as the errors for the additional quadrupoles Q4, Q5 for the HL insertions IR1 and IR5.

Figure 5 shows a comparison between the cases L^*=10, 15, 16 and 17 m with β^* fixed at 10 cm. A small reduction of DA is observed for the case L^*=15 m but it is still very close to the DA found for L^*=10 m. However, for L^*>15 m the higher β functions reached in the location of the inner triplet causes aperture losses and therefore a significant reduction of DA.

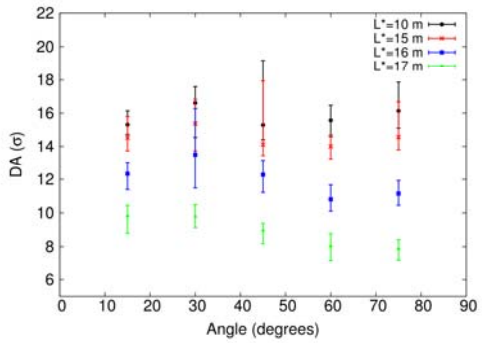

Figure 5: Comparison of DA for lattices with L^*=10, 15, 16 and 17 m with a fixed β^* at 10 cm.

In summary we have demonstrated the feasibility of integrating the LHeC into the HL-LHC by extending the ATS scheme. For the baseline L^*=10 m the minimum achievable β^* is between 8cm and 10cm. For the baseline β^*=10 cm the longest possible L^* is 15 m.

[1] http://sixtrack.web.cern.ch/SixTrack

2.4.3.6 *Arc Magnet Design Options*

This chapter briefly presents conceptual designs for the main bending magnets of the arcs. The main quadrupoles are not treated here, as they can be considered of a more traditional design; furthermore, their requirements for integrated gradients and number of magnets can change significantly, for example if a quadrupolar component were introduced in the dipoles, in a "combined function" layout.

The requirements of the main bending magnets – as spelled out in the CDR [4] – are recalled in Table 3. Considering the moderate fields though the long integrated dipole length of 14.0 km, the challenge is clearly of economic nature. Cost minimization needs to be tackled at a project level, with the design of the arc magnets coupled in particular to studies of the power converters, the vacuum system and cooling / ventilation. LEP and the HERA electron ring are valuable references of machines with many low field dipoles; the cross-section of those magnets can be found for example in [18] and [19].

Figure 6 shows the cross-section of a classical C type dipole, with 4 bus-bars providing the required Ampere-turns. This is the option described in more detail in [5]. In the highest energy arc, the required field of 0.264 T is achieved with 2.7 kA per bar. Taking a current density of 1 A/mm^2 – hence, a generous amount of conductor – the dipoles in arc #6 would dissipate 186 (293) W/m, for a total of 434 (684) kW, using copper (aluminum). If the number or size of the conductor is adjusted throughout the arcs, for example to keep a similar current density, the overall resistive power for the main bending magnets in the six arcs would be of a few MW. This type of design would involve physically separate units, similar for example to CEBAF [20].

Table 3: Basic requirements for the LHeC main bending magnets of the arcs.

arc	*energy [GeV]*	*number of dipoles*	*field [T]*	*length [m]*	*vertical gap [mm]*
#1	10.5	584	0.046	4.0	25
#2	20.5	584	0.089	4.0	25
#3	30.5	584	0.133	4.0	25
#4	40.5	584	0.177	4.0	25
#5	50.5	584	0.221	4.0	25
#6	60.5	584	0.264	4.0	25

The conceptual designs of Figures 6 to 8 combine separate aperture in a single yoke, to divide by 3 the count of dipoles, from 3504 to 1168 units. Magnetic cross-talk between gaps is not an issue, considering in particular that the magnets will be operated in dc mode.

In Figure 7, the gaps are stacked vertically on top of each other. This can be thought of as separate C dipoles merged together. The bus-bars can be connected in series – possibly with trims – but still they would drive the flux in the various apertures one at the time.

On the other hand, Figure 8 shows an alternative vertical stacking, with the gaps offset both vertically and horizontally. This arrangement allows to "recycle" Ampere-turn, with either a saving in amount of conductor, or dissipated power.

Finally, Figure 9 shows the layout of a rather wide C dipole, with gaps put side-by-side transversally. This is the most efficient arrangement from a magnetic viewpoint, as the same Ampere-turns drive at once the field in the various gaps. This design is a sort of "combined function", where the hyperbolic (or other) pole geometry is substituted

with piecewise flat and parallel poles. The vertical distances of such poles as shown here allows for a 1:2:3 ratio of the field, which can be trimmed by additional windings hosted in two of the poles. The transversal spacing is tentative, such to provide a field uniformity of $\pm 1 \cdot 10^{-3}$ in ±30 mm (for each pole). The inherent quadrupole component of this design could be either exploited, or easily compensated by the arc quadrupoles.

A further design, not shown here, is an evolution of the same concept of Figure 9: the piecewise flat poles are substituted with a proper continuous geometry, which provides an approximation to an exponential distribution of the field in the midplane. This more exotic field profile involves quadrupole and sextupole components (as well as higher order terms), though their ratio to the main dipole would remain the same when moving in the transverse direction. Were this option interesting from the beam dynamics side, it would result in a more compact yoke design for the dipoles. Also the option of a common vacuum chamber for the various beams, circulating side-by-side, could be possibly envisaged.

Table 4 lists the total Ampere-turns and iron per meter for the concepts shown in Figures 6 to 9, fixing 0.264 T in the gap with the highest field and a 1:2:3 ratio in case of multiple apertures, corresponding to arcs 2, 4 and 6. These values shall be taken for first order comparison purposes only, as no optimization for example of the iron – cutting out low field regions, or optimizing the width of the pole and of the magnetic circuit considering actual field quality requirements – has been performed. Also in all cases no heavy dilution of the iron is considered. This could be introduced in all designs, with the possible exception of case c) that is depicted in Figure 8. Mixing the iron with concrete, plastic or even air would be driven by economic considerations and not magnetic reasons, exactly as it was for LEP, with its iron-concrete yokes. From Table 4, a combination of the separate apertures of a) into b) yields no savings in terms of Ampere-turns, as expected. Case c) is in between b) and d) for the needed excitation current. The side-by-side configuration of d) is the most parsimonious for Ampere-turns, with a factor of about 2 less with respect to three separate dipoles.

Table 4: Ampere-turns (total) and iron mass per meter for various dipole concepts.

case	*description*	*NI [kA]*	*iron [kg/m]*
a)	separate C dipole, Figure 6	10.6	351
b)	vertical apertures, Figure 7	19.8	565
c)	vertical offset apertures, Figure 8	14.0	814
d)	apertures side-by-side, Figure 9	11.4	906

To reduce the costs of making a coil, bus-bars are considered in all cases. No matter the option chosen, with or without "recycled" Ampere-turns, the dissipated power remains in the order of only a few MW for 14.0 km of dipole length – thanks to the 25 mm vertical gap and rather low fields. The choices of the conductor material (copper or aluminum) and whether this is water cooled or not enter in the wider realm of overall cost optimization and they are not discussed at this stage.

Finally, from the magnet side adding a "combined function" quadrupolar component would have negligible (if any) impact on the cost of the bending magnets, though it could result in significant savings in terms of number of main arc quadrupoles. This possibility could hence be considered in an iterated version of the optics.

2.4.4 Recent Improvements in the ERL Lattice Design

2.4.4.1 *Linacs*

The CDR linac optics consists of 18 FODO cells with a linearly increasing strength, keeping constant beta functions for the low energy passage. A lattice composed by 36 FODO cells has been investigated after the CDR studies. The stronger focusing reduces the instability induced by wakefields and contains better the beam envelope, allowing injecting/decelerating the beam at/to a lower energy. As a result the efficiency of the deceleration increase and the requirements on the injector are relaxed. If the original number of quadrupoles has to be preserved, similar improvements could be obtained by moving a few of them towards the low energy end of the linacs and allowing the beta function to grow with the energy.

2.4.4.2 *Arcs*

The arc design based on flexible momentum compaction cells has been proven very effective. While all the arcs share the same footprint, each of them can be tuned according to the beam energy. This allows minimizing the emittance dilution from synchrotron radiation, while keeping a small beam envelope at low energy and an overall quasi-isochronous optics.

Designs based on combined function magnets are also being investigated. These allow improving the bending filling factor while keeping at the same time smaller beta functions, and thus reducing the impact of synchrotron radiation. Preliminary studies show promising results. The possibility to transport multiple energies in the same beam pipe will also be investigated.

2.4.4.3 *Spreader and Recombiner*

The spreaders/recombiners are sections placed at each end of the linacs in order to provide/suppress the vertical separation between the beams at different energies. In their original design, adapted from the CEBAF accelerator, the final separation is accomplished in two steps, which simplify the suppression of the vertical dispersion and reduces the strengths of the matching quadrupoles. On the other hand the beta functions are raised to very high values and the extra bending causes significant energy losses, which reach 50 MeV in Arc4. A smoother, single step translation has therefore been designed. Employing seven quadrupoles (with a max gradient of 80 T/m) in between the two dipoles to match the optics, reduces the energy loss in Arc4 by a factor 5.

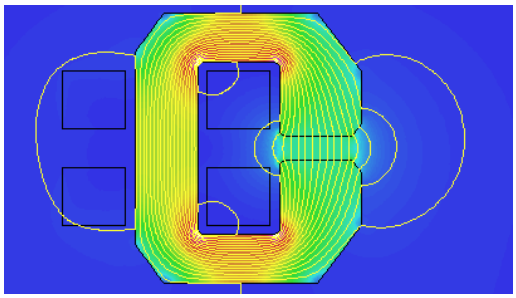

(All cross sections shown here are in the same scale, with the vertical gap fixed at 25mm)

Figure 6: Classical C dipole, as proposed in CDR.

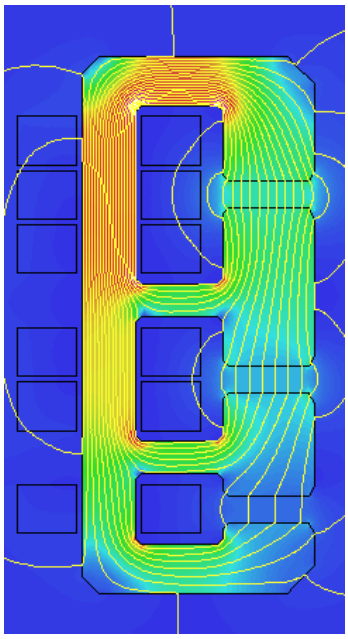

Figure 7: Dipoles with apertures stacked vertically: gaps aligned, **no** recycling of Ampere-turns (field ratios 1:2:3).

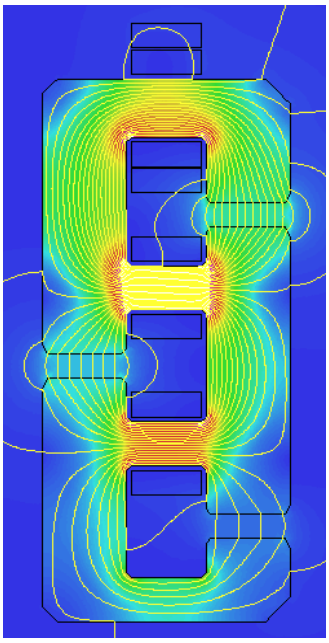

Figure 8: Dipoles with apertures stacked **vertically**, gaps offset horizontally, Ampere-turns shared (field ratios 1:2:3).

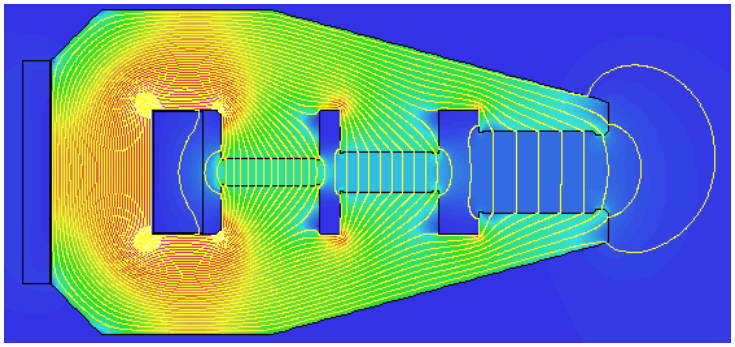

Figure 9: Dipoles with apertures side-by-side horizontally (field ratios 1:2:3).

2.4.4.4 *Bypasses*

At the end of Linac1, while the 60 GeV beam goes straight to the IP, the vertical separation provided by the spreader is not sufficient for the 20 GeV and 40 GeV beams to avoid the detector and bypass lines have been designed. They start right after the spreader, providing and initial bending towards the inside of the racetrack. The bending is such that a horizontal separation of 10 m is introduced with respect to the IP. The connection with Arc6 is then accomplished with an increased strength in a few bending cells of Arc2 and Arc4.

2.4.4.5 *Compensating RF*

As the beam loses energy while travelling the arcs, if no countermeasures are adopted, the energy of the beam in the decelerating phase is lower than one in the corresponding accelerating phase, precluding the transport in the same arcs. To prevent the issue, second harmonic RF cavities installed in the arcs replenish the energy lost by both the accelerating and the decelerating beams, so that they both reach the entrance of each arc with the design energy.

An estimation of the parameter of these cavities and cryomodules is collected in Table 5. They have been extrapolated from the ILC cavity design, expecting that the higher frequency and lower gradient allow for continuous operation. Table 6 shows the energy loss for each arc, together with the required number of cryomodules.

Table 5: Tentative parameters for the compensating RF extrapolated from the ILC cavity.

Frequency	**1604 MHz**
Gradient	30 MV/m
Design	9 Cells
Structure Length	< 1 m
Cavities per Cryomodule	6
Cryomodule Length	6 m
Cryomodule Voltage	150 MV

Table 6: Energy loss and required number of cryomodules for each arc.

Turn Number	**E [GeV]**	**ΔE [GeV]**	**Cryomodules #**
1	10.4	0.7	0
2	20.3	9.9	0
3	30.3	48.5	1
4	40.2	151	1
5	50.1	365	3
6	60.0	751	6

2.4.4.6 *Doglegs for Path Length Adjustments*

In order to obtain and keep on-crest acceleration the beam time-of-flight will have to be tuned in the commissioning and continuously adjusted in the operation to compensate for ground motion.

In the CDR design this is accomplished by means of four-bend chicanes which employ 1 m long dipoles and are placed next to the RF compensating sections. Synchrotron radiation poses upper limits to the bending angle in those chicanes, in particular for the highest energy beams. These are collected in Table 7.

Table 7: Maximum bending angle, length variation and field for a 6 m long, four-points chicane assuming a maximum energy loss of 4 MeV (1 MeV in each dipole).

Energy [GeV]	Theta [Rad]	Delta L [m]	B [T]
10	0.256	0.2023	2.14
20	0.064	0.0123	1.07
30	0.028	0.0024	0.71
40	0.016	0.0008	0.53
50	0.010	0.0003	0.43
60	0.007	0.0002	0.36

While at low energy the few chicanes allow for tuning the path length over a range exceeding the linac wavelength (0.374 m), at higher energy they are not very effective even in big numbers. A possibly better solution for path length adjustments in Arc5 and Arc6 may consist in introducing a betatron oscillation in the beam orbit. The whole arc can then be exploited, and the perturbation can be much smaller. The feasibility and the effectiveness of this scheme have not yet been investigated. For Arc4 and Arc2 one can also take advantage of the bypass section to install a long chicane.

2.4.5 **Electron Beam Dynamics and Simulations for the ERL**

The effects that are mostly expected to have an impact on the quality and the stability of the electron beam at the LHeC are:

- optics (bunch compression and elongation in the arcs, induced energy spread from the RF curvature),
- synchrotron radiation,
- beam-beam disruption,
- short and long-range wakefields,
- ion cloud,
- machine imperfections, field quality, phase and timing errors.

To describe the machine layout and operation in an appropriate way the PLACET2 code [21] was developed and applied. The aforementioned effects have been studied in detail with the only exception of the ion cloud and the imperfections: the first is a planned addition to PLACET2 while the second requires the development of effective correction schemes which goes beyond this study.

The simulation includes the two linacs and the six arcs, properly connected together, with the spreaders and matching sections. The synchrotron radiation is computed in the whole arcs excluding the spreaders-recombiners, as their current two-step design causes unacceptable energy losses. The computation of the beam-beam effect relies on GUINEA-PIG [22].

2.4.5.1 ***Single-bunch Tracking***

The transport of a single bunch from the injector to the dump is the first step to validate the machine design. Figure 10 shows the Twiss parameters obtained following a bunch along its path from the injector to the dump. The linacs are easily identifiable by looking at the energy profile. In the arcs the energy stays almost constant, the only variation being caused by the synchrotron radiation. It is possible to note the different

average values of the β functions in different arcs, deriving from their different tunings of the momentum compaction.

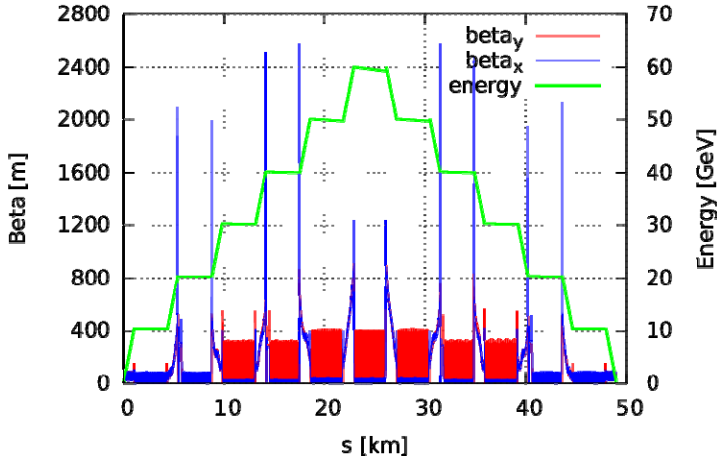

Figure 10: β functions and energy profile obtained following a bunch for six turns in the ERL.

Incoherent synchrotron radiation has the main impact on the beam quality, as it introduces uncorrelated energy spread and emittance growth. Short range wakefields were also investigated in the CDR. More recent studies, simultaneously calculating the two of them, showed that the wakefields are almost completely masked by the radiation as shown in Figure 11. A small beneficial effect of wakefields has been found during the deceleration as they may help to remove correlated energy spread. This hints that further marginal improvements may be obtained with a fine tuning of the arc lengths, adjusting the phases at the linac injections.

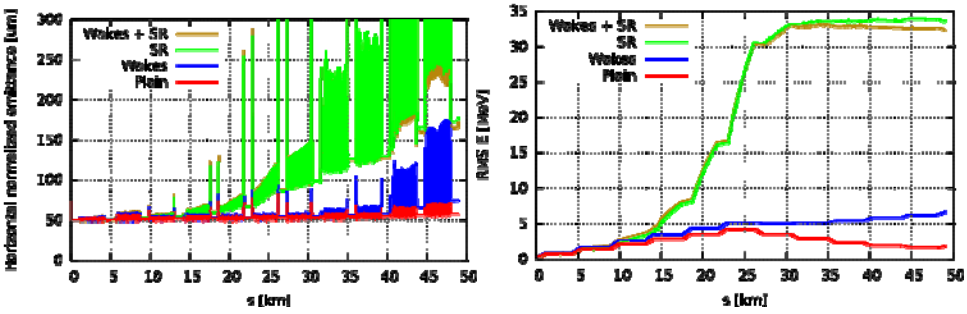

Figure 11: Horizontal emittance and Energy RMS of a bunch tracked from the injector to the dump with an initial offset of 1 mm (required to excite transverse wakefields). The blow up caused by synchrotron radiation and wakefields are compared. The IP is approximately at s=23 km, the beam-beam is not included. The emittance includes the contribution from the dispersion, thus its value in the arc is not significant.

The limited beam degradation during the transport to the IP is acceptable, however the beam-beam disruption and the strong radiation in Arc6 make the deceleration more critical and pose a lower limit the dump energy. As shown in Figure 12, for an injection/dump energy of 500 MeV, the beam keeps a good clearance even at the last irises, with irrelevant tail losses. Tables 8 and 9 collects the beam sizes at the IP and at the dump respectively.

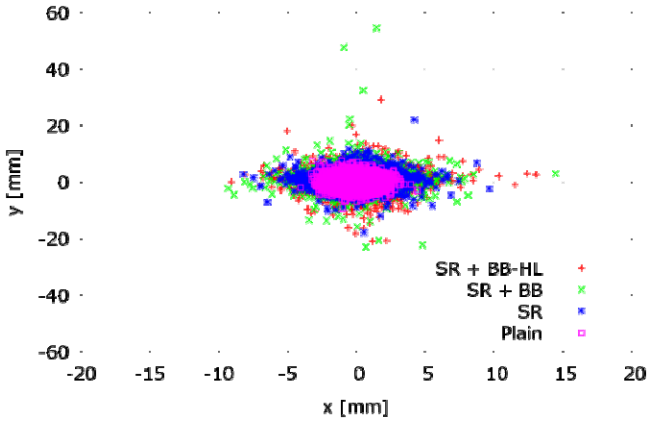

Figure 12: Beam transverse section at the end of the last linac, after the deceleration down to 500 MeV, including Synchrotron Radiation and Beam-Beam with standard and Higgs Factory (High Lumi) parameters. The beam contains 5000 macroparticles and the initial distribution is gaussian with no cuts.

Table 8: Initial beam parameters compared to the ones at the IP in presence of synchrotron radiation.

	Initial/CDR	**IP**
Normalized Emittance X [mm mrad]	50	57.4
Normalized Emittance Y [mm mrad]	50	50.8
ΔE/E [%]	0.2	0.026
RMS X [μm]	7.20	7.66
RMS Y [μm]	7.20	7.21
RMS Z [mm]	0.600	0.601
RMS E [MeV]	1.00	15.4

Table 9: Beam parameters at the dump. The columns show the values for SR only, SR and Beam-Beam, SR and Beam-Beam with Higgs Factory (High-Lumi) parameters.

	SR	**SR + BB**	**SR + BB-HL**
Normalized Emittance X [mm mrad]	107	133	165
Normalized Emittance X [mm mrad]	87	125	158
ΔE/E [%]	5.9	5.9	5.9
RMS X [mm]	1.52	1.67	1.86
RMS Y [mm]	2.42	3.03	3.15
RMS Z [mm]	0.66	0.66	0.66
RMS E [MeV]	29.7	29.5	29.6

2.4.5.2 *Beam-beam Dynamics and Luminosity Optimization*

Due to the asymmetric rigidities between a 7 TeV proton beam and a 60 GeV electron beam, the proton beam acts as a strong nonlinear lens on the electron beam. Assuming there is no offset this lensing effect can be used to increase the luminosity by changing where the foci of the interacting beams are with respect to each other. The focusing action keeps the electron beam within the proton beam for a greater percentage of its length. An optimum is found by scanning possible waist shifts resulting in a 1.1% increase in luminosity for the baseline LHeC design. If the β* is likewise scanned, the luminosity can be increased further. In Figure 13 we see this example where shifting the waist and relaxing the β* can bring a luminosity increase of 7.4%.

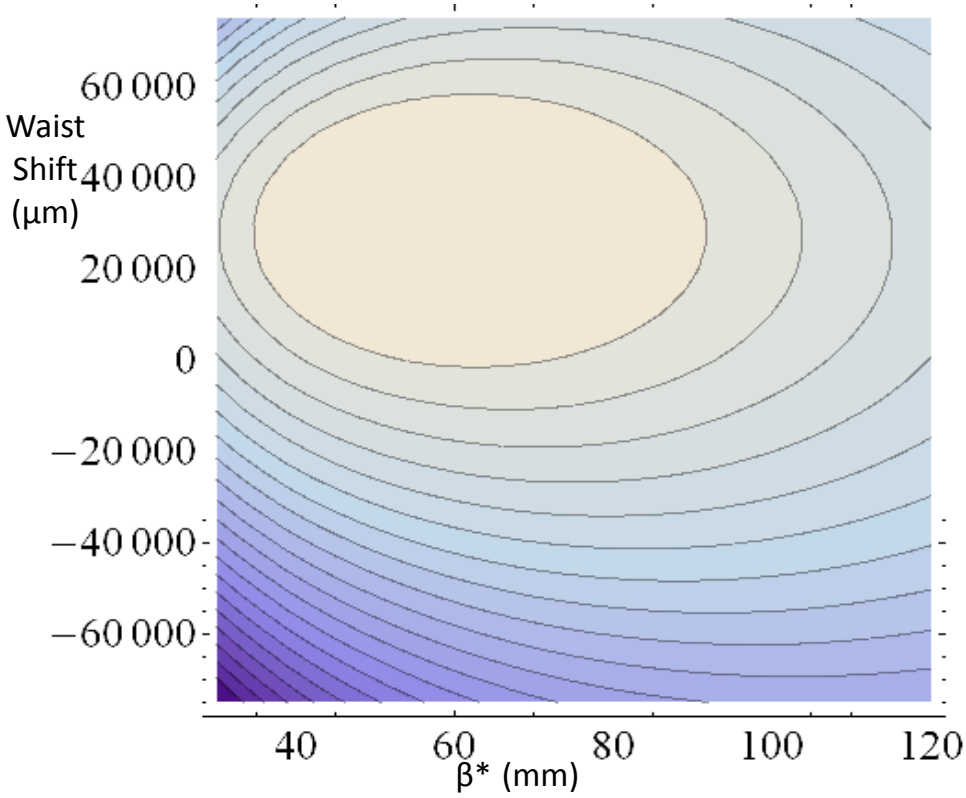

Figure 13: This contour plot shows the shift in the waist of the beam with a scan of the β*. While a waist shift alone would only give a 1.1% luminosity increase, in combination with relaxing the β* this leads to a 7.4% increase.
The contours range from 7.45×10^{33}-$1.10 \times 10^{34} cm^{-2}s^{-1}$.

The beam-beam disruption parameter, the ratio of the beam-beam focal length to the bunch length, is 5.99 and the beam-beam tune shift is 0.76. These relatively strong interactions lead to an emittance growth. While the actual phase space has a small change, any offset between the two beams is amplified, resulting in a larger beam envelope. A fast feed-forward system installed across Arc6 aims at damping the transverse motion and recovering the beam emittance as shown in Figure 14. Using two sets of kickers placed at the center and at the end of the arc, an offset of 0.16σ can be

damped. A single set cutting across the whole arc can correct a 1σ offset with ~4.4 kV. Unless nonlinearities are added to the arc, the conventional single set of correctors will be sufficient.

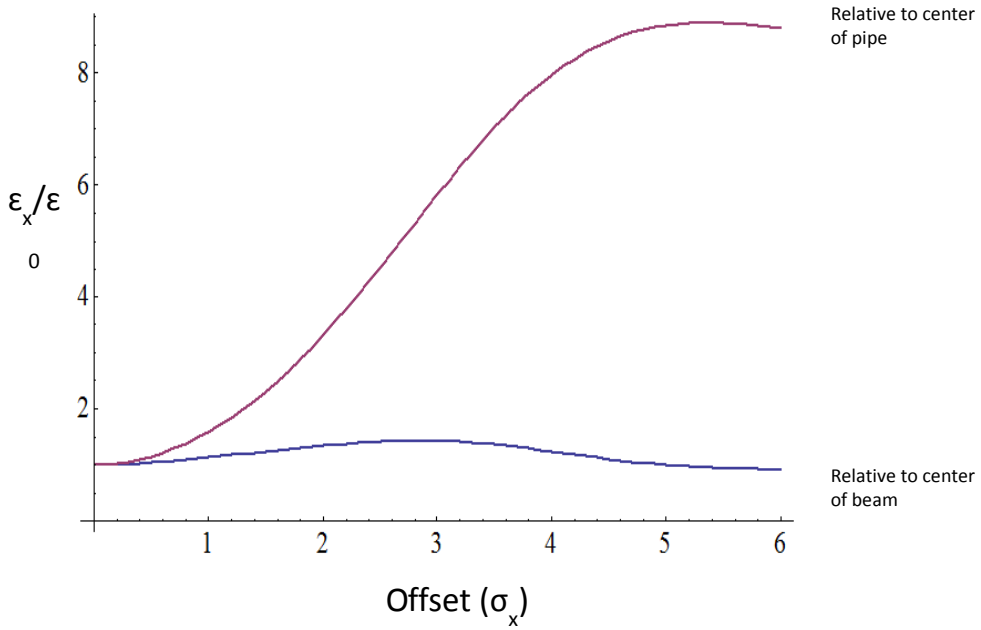

Figure 14: Relative change in the emittance of the electron beam with respect to its own centroid, and with respect to the center of the beamline.

2.4.5.3 *Multibunch Tracking*

A major concern for the operation of ERL facilities at high currents are long-range wakefields, in particular the ones related to transverse dipole modes that are easily excited by orbit errors.

The modes of the SPL cavity design, scaled to 802 MHz are considered. The Q values of all the modes are conservatively set to 10^5: the worst value for the TESLA cavities. The computation times have been reduced using single particle bunches, which is a conservative approach, as the tune spread is known to improve the threshold current [23]. The full computation of the beam-beam effect has been substituted with an amplitude dependent kick. This is also a conservative approach as the electrons oscillate around the proton beam and the total kick that they receive is thus smaller that that. A cavity detuning of 10^{-3} has been set together with a recombination pattern that maximize the separation between the bunches at the lowest energies.

The beam stability studies are performed filling completely the machine with bunches carrying null action. One misaligned bunch is then injected followed by many bunches again with null action. One can then look at the action of the outgoing bunches checking its trend, which determines if and how fast the perturbation is damped. The total amplification is summarized by the F parameter, defined as the squared sum of all the amplitudes [24]. The result of this procedure is shown in Figure 15, where the amplitudes, normalized to the one of the exciting bunch, are computed at the IP for two

cases: with and without the beam-beam kick. The coupling of the beam-beam with wakefields increases the persistence of the excitation.

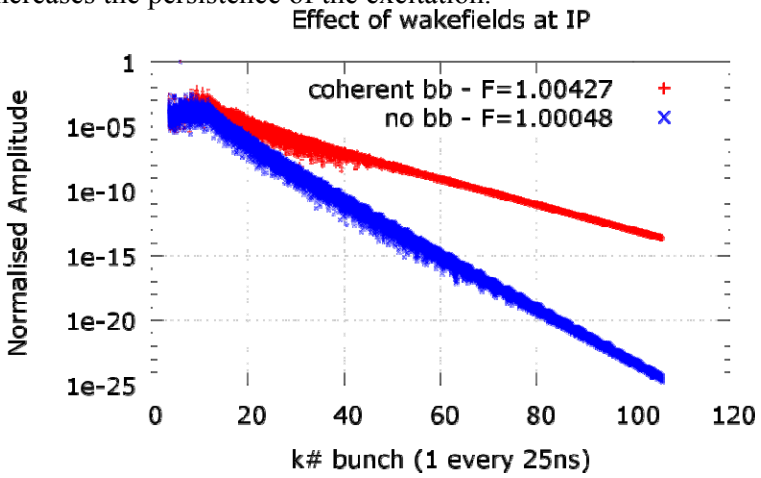

Figure 15: Propagation the excitation from a single bunch caused by long range wakefields for the Higgs Factory parameters.

Nevertheless the beam stability is preserved in both cases and the F parameter maintains acceptable values. A feed forward system installed in Arc6, aims at reducing the jittering. A study of the ion cloud, including their coupling with wakefields, will follow.

2.4.6 **Proton Beam Dynamics and Simulations for the ERL**

The interaction of a 60 GeV electron beam with one of the proton beams in the LHC can cause an increase in the emittance of one of these beams due to the beam-beam effect. The asymmetric energies and rigidities of the beams means that while the electron beam perceives a very high disruption parameter (5.99), the proton beam perceives a very small one (3.62×10^{-6}). However, this seemingly small effect can build up over time into an unacceptably large emittance growth.

Due to the asymmetric rigidities, if there is an offset between the electron and proton beam, the electron beam will be pulled through the center of the proton beam [25]. This causes part of the proton beam to be kicked in the direction of the offset and part of the beam to be kicked in the direction opposite the offset. This results in an increase to the mean squared value of the momentum spread which leads to an increase in the emittance. If we assume that this increase in mean squared momentum spread is the only change from the beam-beam interaction, then we can calculate the emittance growth per turn as [26]:

$$\Delta\varepsilon_n = \frac{1}{2}\gamma\beta^* < \Delta p_x^2 > \frac{2\pi N_p r_p}{\sigma_x^2} \quad (1)$$

In order to calculate this we need to determine $<\Delta p_x^2>$ for which we have used 2 methods. We can begin by using a strong-strong code such as Guinea-Pig [27] to directly calculate the momentum change to the macroparticles. But we can also use the calculated path of the electron beam through the proton beam to calculate the momentum change analytically using the Basetti-Erskine formula [28,29]. The path of

the electron beam through the proton beam is shown in Fig 16, while the longitudinal dependence of the momentum is shown in Fig 17.

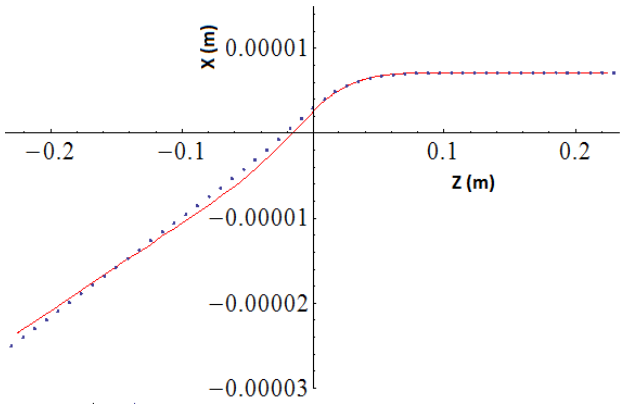

Figure 16: The path of the electron beam through the proton beam with a $1\sigma_x$ offset. The dotted line is calculated using Guinea Pig, while the red line is numerically solved using the Bassetti-Erskine formula.

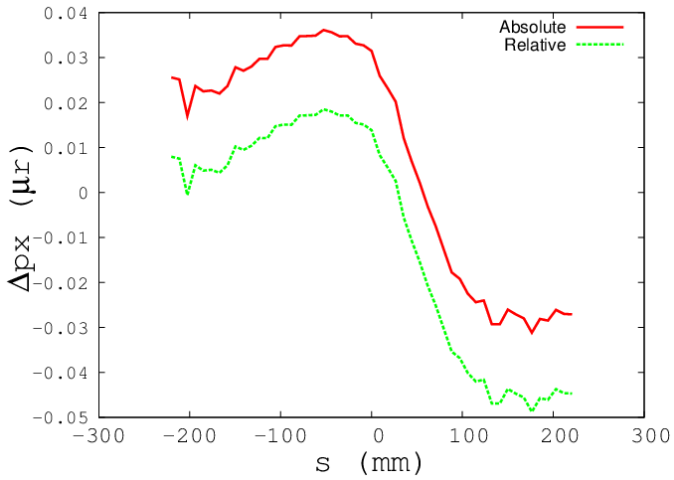

Figure 17: In this figure we see the different average momentum changes along the length of the beam using due to a $1\sigma_x$ offset, calculated with Guinea Pig. The red line shows the absolute change while the green line shows the relative change with respect to the centre of the beam.

To test these predictions a simple model of the proton beam in the LHC was developed. This model uses Guinea-Pig to calculate the beam-beam interaction between the proton beam and the electron beam. The perturbed protons are then advanced through a 6D 1st order map of the LHC with synchrotron motion. This process allows us to measure the change in emittance of the beam due to the beam-beam effect over 5000 turns. The results of these simulations and the predictions given are shown in Fig 18.

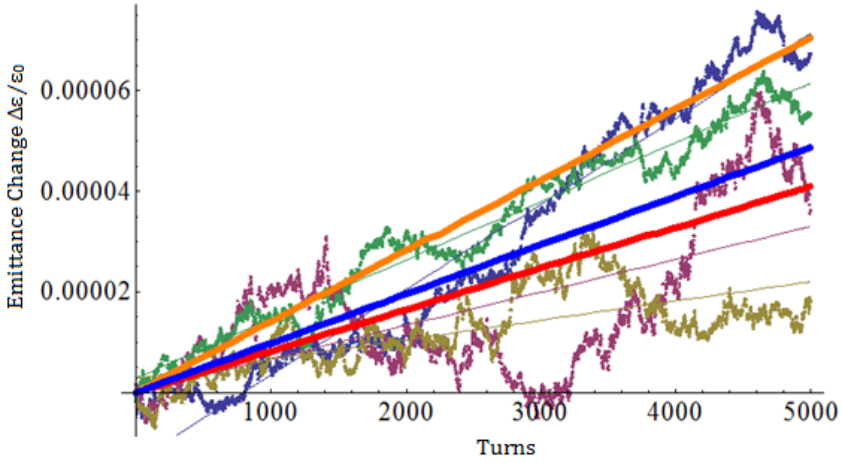

Figure 18: This shows the evolution of the proton beam emittance over 5000 turns with an offset jitter of $0.2\sigma_x$. The orange line represents the fit of Eq. 1 using Guinea Pig numbers for $<\Delta p_x^2>$, the red line represents the fit for the numerically calculated beam path, and the blue line is the average of the four test beams' growth rates.

Table 10: This table shows the growth rates for the three examples shown in Fig 18. The growth rates shown use a jitter of 20% of σ_x.

	Growth Rate (m/turn)	**Growth Rate (%/turn)**	**Growth Rate %/s**	**Jitter for doubling time of 1 day (σ_x)**
Average Fitted	$3.66\text{x}10^{-14}$	9.76x10-7	.011	6.53%
Guinea-Pig	$5.2838\text{x}10^{-14}$	1.41x10-6	.016	5.43%
Numerically Solved	$3.08\text{x}10^{-14}$	8.21x10-7	.009	7.12%

The results of the simulation are in good agreement with predictions for an offset jitter of 20% σ_x. This offset was determined both as an upper limit to inter bunch spacing in the LHC, and because the emittance changes are being tracked within a range that is so small double floating point errors can wash out the effect we wish to measure with smaller offsets. The methods calculated in Eq. 1 can be used to determine the effective doubling time of the beam emittance, and the offset jitter constraints for the beams, is shown in Table 10. So long as adequate control of the bunches is maintained this should lie within the shadow of other effect leading to emittance blow-up in the LHC (e.g. IBS).

2.4.7 **Studies Related to the Design of an ERL Test Facility**

2.4.7.1 ***Introduction***

The Energy Recovery Linac design of the LHeC pushes the ERL beam parameters beyond those currently achieved in ERL test facilities around the world. Existing facilities mainly explore the operation mode with a single re-circulation as a driver for a Free Electron Laser (FEL) (see for example JLab with ca. 8mA [30], ALICE with 6.5mA beam current [31] and the compact ERL at KEK with 10mA beam current [31] (leading to less than 20mA average beam current in the cavities). The only operational multi-turn ERL at Novosibirsk features 4 re-circulations with up to 5mA (with up to 20mA average beam current in the cavities) but operates with normal conducting RF systems [32]. Several proposals for superconducting multi-turn ERLs exist worldwide (e.g. at Cornell University and BNL [31]) and a test facility for a high current, single-turn ERL is under construction at BNL [33]. Bridging the experience from the existing ERL machines to the operational challenges of a large scale (two 1 km long superconducting linacs with a total ERL circumference of 9km, a beam energy of up-to 60 GeV and operation with average beam currents above 20mA) implies a significant leap from the existing ERL operational experience. Planning for and approving a large-scale facility such as the LHeC requires a solid understanding of the operational challenges and identification of the practical limitations of such a machine. We therefore consider a high beam current multi-turn ERL test set-up with a superconducting RF system as a prerequisite for the further development of the LHeC machine. Moreover, the successful development of a superconducting RF system for the LHeC (for example the HOM damper, coupler and LLRF etc.) will require extensive tests with beam operation. As there is at this stage no operational facility in sight that can address all these aspects, we consider the construction of such a test facility as the natural next step for the LHeC machine development. Evidently, such a test facility, besides its help in developing the operational experience for ERLs and being an SRF test bed at CERN, would provide valuable insight and information too for other future ERL projects around the world, such as eRHIC at BNL or the MEIC at JLAB.

2.4.7.2 ***Summary of the SCRF Development for a Future ERL***

Along with high-field magnets, superconducting radio-frequency (SRF) has been clearly identified as a key technology for future large accelerators, both for high energy physics and for linac-based light-source applications. At present, a vibrant global SRF R&D effort is underway in the framework of ILC, LCLS-II and PIP-II, aiming at high gradient and reduced cryogenic loss. Recent breakthroughs include the successful increase of the unloaded Q_0 by more than a factor 2 by means of nitrogen doping [34] as well as successful demonstration of Nb_3Sn coated Nb cavities, which could be operated at more economical 4.2 K [35]. These encouraging results have highly motivated scientists and engineers world-wide and given additional momentum to the research. A significant improvement in the quality of SC cavities certainly is of beneficial value for the performance and effort of the LHeC.

LEP2 at CERN was a major SRF installation with 288 superconducting 4-cell cavities, providing a total RF voltage of 3.5 GV and continuous RF power of 35 MW, which led to LEP's top energy of 104 GeV. After the decommissioning of LEP in the year 2000 and with the construction of LHC, CERN had to reduce its SRF R&D

program. The update of the European Strategy for Particle Physics in 2013 [36], however, mandated CERN to prepare the technologies required for a possible ambitious post-LHC accelerator with a vigorous R&D programme – this led to a newly strengthened SRF R&D programme at CERN.

CERN has since set up an SRF R&D programme to complement the global SRF R&D: while the global SRF R&D programme concentrates on bulk Nb, CERN will focus its R&D again on thin-film Nb on copper, a technology developed at CERN successfully in the 80-ies for LEP, but limited today to gradients well below bulk-Nb records. At the same time, CERN needs to keep competencies in the SRF technology, since it is used also for the operating machines LHC and HIE-ISOLDE. In collaboration with ESS and Myrrha, CERN equally invests some effort in bulk-Nb high-gradient cavities, but here the complementarity is aiming at new, potentially cheaper concepts for cryomodules. Also the HL-LHC crab cavities use bulk-Nb technology. In view of the newly established SRF R&D programme at CERN, an ERL facility could serve two purposes at the same time:

1) It would be the test bed and demonstrator for a larger ERL as needed for LHeC and possibly the FCC-he.
2) It would be a beam test facility for SRF cavities and cryomodules for the aforementioned general SRF R&D programme, as will be outlined in the next paragraph. Such a facility would also serve as ideal training ground for the next generation of scientists, engineers and technicians to become experts in SRF.

In parallel to design and construction, the typical SRF R&D process is accompanied by a large number of tests, starting with the test of samples, cryogenic tests in vertical cryostats of initially single-cell and later multi-cell cavities, initially bare cavities and later fully dressed cavities, followed by the integration in a cryomodule and horizontal tests with full power. The ultimate test of a new cavity/cryomodule, however, is the operation with beam to allow for correct evaluation of beam loading and higher-order mode excitation. An ERL facility would be the facility of choice for such tests. We have shown in [37] that the facility can be configured to allow for tests at practically all commonly used frequencies (401 MHz, 704 MHz, 802 MHz and 1.3 GHz).

The design of an initial 802 MHz RF system has started in collaboration with JLAB: it consists of large aperture ($\varnothing\,160$ mm) 5-cell cavities with a "low-loss" shape. The targeted Q_0 in excess of $2 \cdot 10^{10}$ and the accelerating gradient of 16 MV/m seem well within reach, in particular if nitrogen doping is considered. The same geometry will also be used for R&D on alternative forming techniques in collaboration with INFN/LNL. A cryomodule would consist of four such cavities – the initial cryomodule design is based on the SNS cryomodule elaborated by JLAB, alternatively the "SPL" cryomodule design is considered [38]. There is strong (and of course intended) synergy of this design work with the needs of FCC-ee and a possible harmonic system for the LHC, but also with ESS, PIP-II and LCLS-II.

2.4.8 **Summary of the ERL Test Facility Design Studies at CERN**

2.4.8.1 ***Design and Parameters***

In the past 2 years, a study was made of an ERL test facility at CERN with a variety of physics applications for which led to a design electron beam energy of about 1 GeV at high intensity. It needs to be noted, though, that the genuine ERL, SRF and LHeC

pre-studies can also be performed at a smaller set-up, keeping the high current and 3-turn ERL requirements. Such an ERL test set-up would follow from a rather straightforward downscaling of the larger facility described subsequently. The PERLE – Powerful Energy Recovery Linac Experiment – design study aims at a 1 GeV beam energy obtained in a recirculating SC linear accelerator layout operated in multi-turn and high intensity energy recovery mode.

PERLE is designed for construction in stages. The final baseline design (Figure 1) would consist of the following basic elements:

1. A 5 MeV injector;
2. Two 150 MeV linacs consisting of eight 5-cell SC structures;
3. Optics transport lines including spreader regions at the exit of each linac to separate and direct the beams via vertical bending, and recombiner sections to merge the beams and to match them for acceleration through the next linac;
4. Beam dump at 5 MeV.

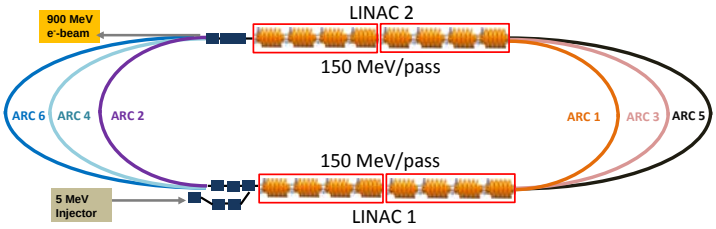

Figure 19: ERL accelerator complex of two parallel linacs comprising two 4-cavity cryomodules each to achieve 150 MeV acceleration per linac and 300MeV per pass.

Each beam recirculates up to three times through both linacs to boost the energy to about 900 MeV. To enable operation in the energy recovery mode after acceleration the beam is phase shifted by 180° and then sent back through the recirculating linac at a decelerating RF phase. The set of main parameters incorporated into the ERL prototype is shown in Table 11.

A first phase of the staged construction would only use two 4-cavity cryomodules and a single pass – it could reach 150 MeV and be used for injector studies and SC RF tests. A subsequent upgrade could be the installation of two additional arcs on each side to raise the beam energy up to 450 MeV. This configuration accommodates for available space for implementation of feedback, phase-space manipulations, and beam diagnostic instrumentation, giving the possibility of a full validation testing with energy recovery. In phase 3, four additional cavities in each linac are added to permit energy recovery recirculation tests at full energy.

Table 11: Basic Parameters of PERLE.

TARGET PARAMETER	VALUE
Injection Energy	5 MeV
Maximum Energy	900 MeV
Normalized Emittance $\gamma\varepsilon_{xy}$	< 25 mm mrad
Average Beam Current	> 12.8 mA
Beam charge	320 pC
Bunch Spacing	25 ns
RF frequency	801.58 MHz
Duty Factor	CW

2.4.8.2 *Injector*

The injector of the ERL test facility needs to deliver beams with an average current of 12.8 mA (with possibility of future upgrades to deliver polarised electrons or larger currents) and an energy of ~ 5 MeV. Bunches with a charge of 320 pC or higher follow with a repetition rate of 40.1 MHz (20^{th} sub-harmonic of 801.58 MHz). There are several possibilities to meet these specifications. One option is to use a grid modulated thermionic gun followed by a multi stage bunching-accelerating structure. This choice however will rule out any future upgrade to deliver polarised electrons. Photocathode guns where electrons are emitted from the photocathode illuminated with laser light are more flexible in terms of the beam charge and temporal structure and allow operation with both polarised and unpolarised photocathodes. Presently, only DC technology may be considered as mature and applicable to an ERL test facility.

To deliver beams with the parameters required for PERLE, preliminary simulations indicate the possibility of using a 350 kV DC gun operating with a Cs_3Sb photocathode. An optimal beam emittance of 2 π·mm·mrad can be obtained with a laser pulse with hat top spatial distribution with a diameter of 3 mm and a flat top 80ps laser pulse. The RMS bunch length at 1 m from the photocathode is 8.5 mm (36 ps) and depends only slightly on the laser pulse length.

Once emerged from the gun, an energy chirp should be introduced to longitudinally compress the bunch and compensate the bunch elongation due to the space charge repulsion (typically done with an RF buncher). In order to provide linear energy modulation the frequency of the buncher should be selected to have a bunch flight time at the buncher shorter than 10° of its RF phase. At 320 pC and rms buncher flight time of 36 ps the required frequency should be less than 775 MHz. Practically attractive is 400.8 MHz - the first sub-harmonic of the ERL frequency. Gradual beam compression and acceleration can be provided with a booster consisting of a series of single cell 801.58 MHz cavities with individual coupling and control of amplitude and RF phase.

2.4.8.3 *Transport Optics*

Appropriate recirculation optics are of fundamental concern in a multi-pass machine to preserve beam quality. The design comprises three different regions, the linac optics, the recirculation optics and the merger optics. A concise representation of multi-pass ERL linac optics for all six passes, with constraints imposed on Twiss functions by sharing the same return arcs by the accelerating and decelerating passes is presented in Figure 20.

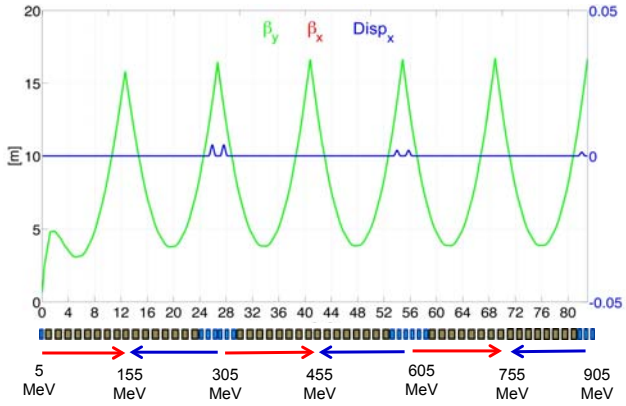

Figure 20: ERL multi-pass linac optics. The requirement of energy recovery puts a constraint on the exit/entrance Twiss functions for the two linacs. Green and blue curves show, respectively, the evolution of the beta functions amplitude and the horizontal dispersion for Linac 1. Red and blue arrows indicate the passages of acceleration and deceleration.

Due to the demand of providing a reasonable validation of the LHeC final design a Flexible Momentum Compaction (FMC) cell based lattice has been adopted. Specifications require isochronicity, path length controllability, large energy acceptance, small higher-order aberrations and tunability. An example layout, which fulfils these conditions, is shown in Figure 21 and represents the lowest energy arc optics as example. It includes a two-step achromatic spreader and a mirror symmetric combiner to direct the beam into the arc. The vertical dispersion introduced by the first step bend is suppressed by the quadrupoles located appropriately between the two stages. The switchyards separate all 3 arcs into a 90 cm high vertical stack; the highest energy arc is not elevated and remains at the linac-level. A horizontal dogleg, used for path length adjustment and made of 3 - 13 cm long dipoles, is placed downstream of each spreader providing a tunability of ±1 cm (10° of RF).

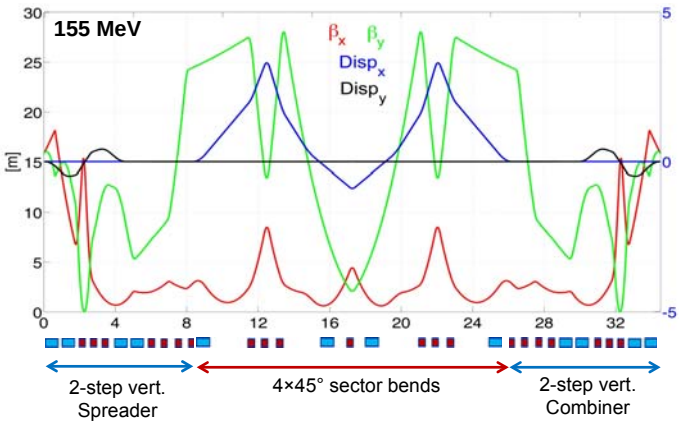

Figure 21: Optics based on an FMC cell of the lowest energy return arc. Horizontal (red curve) and vertical (green curve) beta-function amplitudes are illustrated. Blue and black curves show, respectively, the evolution of the horizontal and vertical dispersion.

The recirculating arc at 155 MeV is composed of 4 - 70 cm long dipoles to bend the beam by 180° and of a series of quadrupoles (two triplets and one singlet). A complete first-order layout for switchyards, arcs and linac-to-arc matching sections has been

accomplished for all the arcs. Injection into the racetrack at 5MeV is accomplished through a rectangular chicane, configured with four identical rectangular bends and 11 quadrupoles distributed in a mirror symmetric fashion, leaving six independent quadrupole gradients to control: betas and alphas at the beginning of the linac (4 parameters), momentum compaction (1 parameter) and the horizontal dispersion (1 parameter). The chicane optics features a horizontal achromat, by design, with tunable momentum compaction to facilitate bunch-length control and finally with Twiss functions matched to the specific values required by the linac.

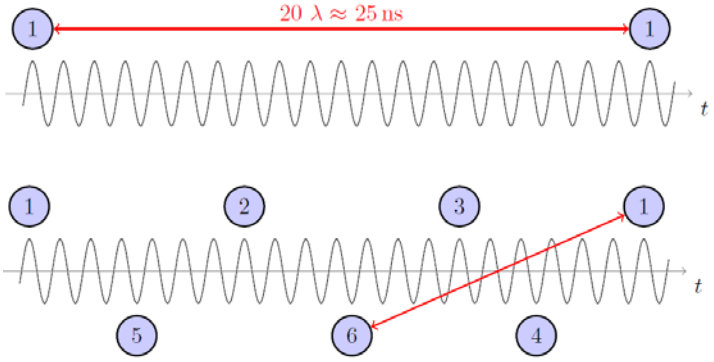

Figure 22: (Top) Basic RF structure, without recirculation with bunches injected every 25 ns. (Bottom) When the recirculation is in place, both linacs are populated with bunches at different turns. The shown recombination pattern maximizes the separation between the two low energy bunches (at the first and sixth turn).

The path of each pass is chosen to be precisely an integer number of RF wavelengths except for the highest energy pass whose length is shifted by half an RF wavelength to recover the energy through deceleration. In order to minimize collective effects, the number of RF wavelengths that determines the arc's lengths has been tuned to avoid different bunches in the same bucket, like it would happen with a full turn length equal to an integer number of 20 λ. The lattice is therefore adjusted to achieve nearly constant bunch spacing. Special care has been taken to select a pattern that maximizes the distance between the lowest energy bunches circulating into the machine at the first and last turn (bunches 1 and 6 in Figure 22). This comes from the fact that, with a nearly constant β function, the kicks from HOMs are more disruptive at lower rigidities, thus if two low energy bunches follow each other, the Beam Break Up (BBU) threshold current can be reduced. Figure 22 is obtained following a test bunch in its path from the injector to the dump. The energy profile shows that the arcs' lengths are properly tuned to obtain the maximum acceleration and deceleration.

The total beam path for a full 3 pass accelerating cycle is around 300 m leading to an approximate footprint of 43m x 16m of the ERL itself.

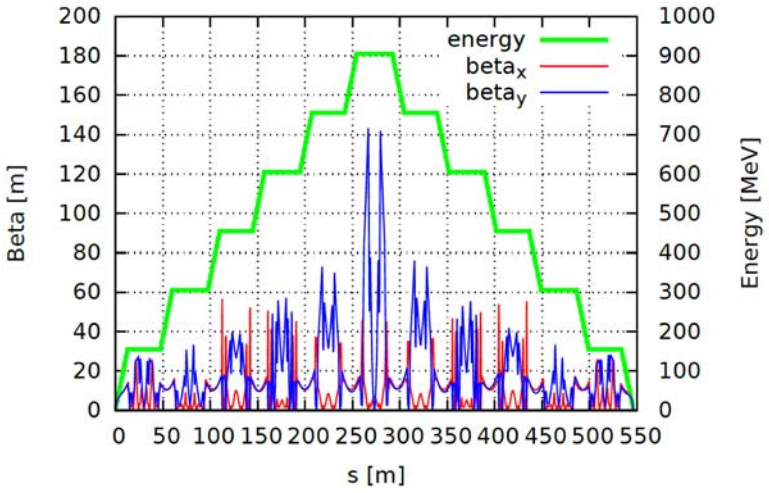

Figure 23: Energy and Twiss parameter tracked for the whole lattice.

2.4.8.4 *Arc Magnets*

A preliminary inventory of the magnets includes:

- 40 bending magnets (vertical field);
- 36 bending magnets (horizontal field) in the spreaders / combiners;
- 114 quadrupole magnets;
- 6 magnets in the injection / extraction parts;
- A few magnets for path length adjustment.

In the two lower energy arcs there are 4 dipoles, with a 45° bending angle. The higher energy arcs have on the other hand 8 dipoles of 22.5° each. Two families of bending magnets are then proposed: one to cover arcs 1 and 2, and another for arcs 3 to 6. The same cross-section could be used for both, though they would differ in terms of length and curvature radius. In both cases a curved construction is assumed, with possibly machined yokes. A tentative cross-section is shown in Figure . An H type yoke is proposed, rather narrow in the vertical direction, to minimize the vertical distance between the arcs. The dimensions could be further reduced – in particular horizontally – after a further iteration on the required field quality. The coils will need to be designed as part of an overall optimization, including the power converters. The shaded area in Figure 24 refers to 6-7 A/mm^2 of current density at the maximum field of 1.31 T of arc 6.

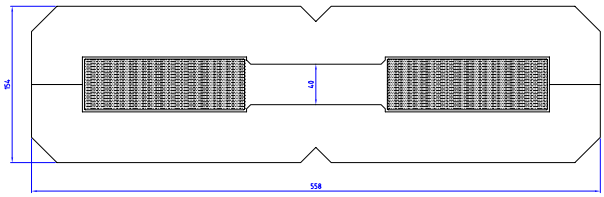

Figure 24: Preliminary cross-section of bending magnets for the PERLE facility.

2.4.8.5 *Dump and Beam Transfers*

The nominal operation of PERLE foresees to continuously dump the decelerated 5 MeV electron beam; this corresponds, for a nominal current of 12.8 mA, to a constant power deposition of 64 kW on the beam dump. The possibility of dumping the beams at all the different energies during the setup period is considered. In this case a system of Transfer Lines (TL) and a beam dump has to be installed at the end of each linac.

Two options are investigated for the operational beam dump. In the first case no additional magnet has to be installed in the main lattice. A 0.66 m long dipole (SBEND) with a 0.906 T magnetic field acts as a spectrometer and separates vertically the different energy beams to direct them towards the respective superimposed arc.

This magnet can be used to deflect the 5 MeV beam towards a vertical beam dump as shown in Figure 25. A *C*-shaped dipole has to be used to host a *T*-shaped vacuum chamber.

The second option foresees the installation of three additional small dipoles in the 1.42 m drift between the end of the linac and the start of the vertical spreader (k1, k2 and k3 in Figure 26). The first dipole has a magnetic length of 0.2 m, a magnetic field of 0.044 T and kicks the 5 MeV beam by 30° to extract it horizontally towards the beam dump. After a 5 m drift line the beam is dumped against a cylinder of graphite. Since k1 is operated in DC mode, all the beams are slightly affected by its magnetic field. The two remaining magnets are thus used to bring the other energy beams back on to the reference trajectory before the vertical spreader.

During the commissioning period of PERLE and in general during the beam setup, it is desirable to dump the beam at the different energies. The easiest solution is to keep switched off the first horizontal dipole of the arc corresponding to the energy of interest and let the beam go straight towards the dump (Figure 26). This dipole has to have a *C*-shape to allow the installation of a *Y* chamber for the recirculating and the extracted beam. The minimum bending angle of 22.5° guarantees enough clearance between the next dipole and the vacuum chamber of the extracted beam. If the dipoles of the arc are powered in series they can all be switched off during the setup period. Also in this case the line to the dump, one for each energy, corresponds to a 5 m drift.

Up to now only DC magnets have been considered. In the eventuality that the setup dumps have to be also used as emergency dumps, fast kickers have to be included in the lattice. The CW operation mode and the 25 ns bunch spacing requires a rise time of 23 ns to allow for some jitter. A system impedance of 25 Ω is assumed, and a rather conservative system voltage U of 60 kV. Assuming a full horizontal and vertical opening of 40 mm, the magnetic length of the fast kickers has to be 0.46 m and the gap field 0.038 T. One extraction system for each energy has to be installed after the vertical spreader when the beams are fully separated.

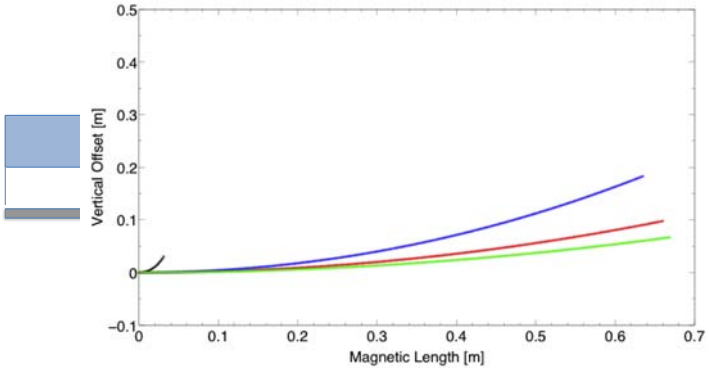

Figure 25: The first dipole of the vertical spreader is a C-Shaped SBEND which allows the extract the 5 MeV beam from the magnetic field region (between the dashed blue lines) towards the vertical dump.

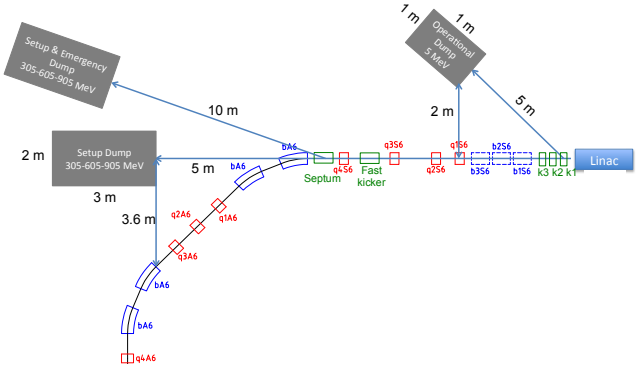

Figure 26: The transfer lines to the operational, setup and setup&emergency beam dumps are shown with respect to the 905 MeV beam arc**.**

2.4.9 **Physics Goals, Motivations and Requirements**

2.4.9.1 ***Physics Motivation and Performance Reach for the LHeC***

The Large Hadron electron Collider surpasses the characteristics of HERA, the first ep collider for deep inelastic scattering (DIS), by impressive amounts. The luminosity is designed to reach a 1000 fold increase of the integrated value, up to 1 ab^{-1}, while the centre of mass energy squared, s=4EeEp, is enlarged by a factor of 15. The corresponding increase in 4-momentum transfer squared, Q^2, has the consequence that the charged current (CC) reaction, ep νX, becomes a prime area for precision physics. The associated luminosity increase is so large that the LHeC appears as an attractive facility for the study of the Higgs boson, at a small fraction of the price of a future large-scale e^+e^- collider. The large targeted luminosity has the further very important consequence that the region of large Bjorken x, above x of 0.5, can be studied for the first time unambiguously: HERA's CC measurements, for limitations of the Q^2 range and luminosity, did not extend beyond this value while fixed target data are subject to very large uncertainties from so-called higher twist, target mass and nuclear corrections. The increase of luminosity at the LHC, in the HL LHC phase, however, is primarily

undertaken to explore the high mass region which yet is the region of large Bjorken x, because the mass of a new particle produced by two partons at the LHC is given as $M^2=sx_1x_2$. The LHeC provides the necessary independent information on the high x behaviour of the parton densities. When operated concurrently with the LHC, it appears as its ideal complement, especially in the area of Higgs and beyond the Standard Model physics, while having a unique, fundamental programme of research in ep and eA by itself too.

The physics programme of the LHeC [4, 39] may be characterised as follows:

i) **The LHeC is a Higgs facility**. The cross section in polarised CC e^-p scattering is about 200 fb, for E_e=60GeV, comparable to that at the ILC. The final state can be reconstructed in a state of the art detector, see below, uniquely and with high precision because the scattered electron or neutrino distinguish neutral and charged current reactions, with no pile-up even at 10^{34} $cm^{-2}s^{-1}$ luminosity. It has been demonstrated that the dominating decay channel H□ bb may be reconstructed to 1-2% precision, roughly ten times better than at the LHC. First results show that the charm decay H□ cc can be reconstructed to 5-10% precision, a decay mode that at the LHC may at best be sensed in J/ψ reactions. BSM Higgs physics, the potential for di-τ and the NC reaction ep□ eHX are equally promising and under study.

ii) **The LHeC is the ideal complement to the LHC**. That holds in two principal regards. The potential of Higgs physics at the LHC, especially in the di-photon and 4-lepton channels, is about to be compromised by QCD and parton distribution (PDF) uncertainties. The LHeC provides a single, complete and high precision set of PDFs in N^3LO^2 (theory permitting in a decade hence) which essentially removes the PDF, α_s and scale uncertainties for pp. Then the LHC facility, as a joint pp/ep complex, will appear as a competitive, realistic *precision* Higgs physics facility. Furthermore, as indicated above, proton structure at high x will eventually and uniquely be determined up to the edge of phase space, for masses M near to √s. This external certainty implies a gain of up to 0.5-1 TeV search range (for pair produced SUSY states) as demands the envisaged HL increase of the LHC performance. Should subtle new phenomena, such as contact interactions, appear at the LHC these could no further be confused with PDF behaviour nor QCD theory deficits, such as resummation at high x.

iii) **The LHeC is an ultimate facility for novel QCD physics**. QCD is the richest part of the SM and yet not tested in many areas. PDFs are only approximately known, some unknown such as the strange and top distribution. Parton interactions at low x must become non-linear for which HERA yet provided no evidence. The strong coupling is the worst measured constant, its quoted value fixed to lattice gauge theory while measurements are less precise and not unique, a problem which prevents clear statements about the unification of the electromagnetic, weak and strong couplings at the Planck scale. Instantons, a topological state long predicted in QCD, have not yet been found. The extension of the parton model to transverse degrees of freedom and towards amplitude definitions of (generalised) PDFs, the understanding of confinement possibly through diffraction - these and many more aspects of QCD require the LHeC to be built.

iv) **The LHeC has a strong Beyond Standard Model (BSM) search potential**. This concerns basically all areas of LHeC physics, anomalous top quark couplings, flavour changing NC, non-standard Higgs physics, excited leptons, contact interactions and substructure. The LHeC represents a huge increase in Deep Inelastic Scattering (DIS) sensitivity with its high luminosity, large Q^2 range and small x such that optimum conditions appear for new physics to be discovered. It shall also be seen in conjunction with the higher energy LHC the potential of which for discovery it substantially enhances.

v) **The LHeC will revolutionise the physics of nuclear structure.** HERA was given no time to study neither electron-deuteron nor electron-nucleus scattering. The understanding of neutron and nuclear substructure is therefore scarse. With the LHeC the Q^2 and 1/x range in DIS eA will be extended by 3-4 orders of magnitude and for the first time a reliable determination of nuclear parton distributions will become possible, accompanied by a QCD based study of novel phenomena predicted to characterise the physics of heavy ions, such as the quark-gluon plasma, gluon saturation, black body limit and others.

The physics of the LHeC reaches much further than is sketched here, for example in the area of electroweak interactions with ultra-precise high scale $\sin^2\Theta$ measurements. New SM and BSM physics might appear in which case the LHeC can be seen as an enrichment of the LHC of central importance for its appropriate exploitation. This holds *mutatis mutandis* as well for the further extended range of the hadron-electron configuration of the Future Circular Collider (FCC). One has long predicted a deeper substructure of matter, a substructure of the heaviest particles and a fusion of leptons with partons to resonant states. DIS is a crucial and far reaching part of high energy physics, and the LHeC its logical next step.

2.4.9.2 *Detector Design for the LHeC*

The extension of the LHC facility at CERN by an electron-proton/electron-ion interaction region (IR) is a technical challenge in many respects. Without disturbing the on-going pp experimental program of the HL-LHC phase, the IR of the LHeC has to be setup such that one of the LHC-proton beams passes undisturbed and the other collides with the electron beam where the optics ensures head-on collisions and high luminosity**.** The LHeC baseline configuration requires an extended dipole magnet structure, currently of ~9m length in both directions from the interaction point (IP), to achieve head-on ep/eA collisions. The dipoles have been integrated in the detector concept. The detailed layout of the IR is still under development, and any changes have consequences for magnets, beam-pipe layout, masks, absorbers and the vacuum and cooling systems.

The detector design guidelines in the context of IR requirements are mainly:

i) Synchrotron radiation effects require a very asymmetric detector beam pipe (x,y) accommodating the synchrotron radiation (SR) fan;

ii) Avoiding and blocking the primary/albedo impact of SR onto sensitive detectors;

iii) The near beam detector elements (Fig. 28) follow the beam pipe extension (Fig.27) as close as possible ensuring an optimum acceptance for trackers and forward/backward calorimeters;

The LHeC detector needs to be designed, constructed, installed and ready for use without disturbing significantly the HL-LHC program. This may be ensured because the ep detector requirements are less severe than those for the HL-LHC detectors: The

radiation level at the LHeC is much lower than in pp, and the total ep scattering cross section does not cause pile-up, which is above 100 in pp. The choice of components for the LHeC detector can rely on the experience obtained at HERA, at the LHC, including its detector upgrades currently being developed, and also on detector development studies for the ILC. The detector development, while requiring prototyping, may therefore proceed without an extended R&D program. Finally, a modular design with pre-installation at the surface enables a rather rapid installation and test sequence.

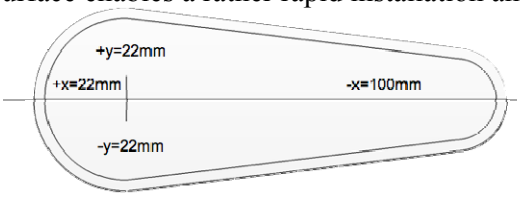

Figure 27: Beam pipe shape design, Beryllium 2.5-3 mm thickness, central beam pipe ~6m length and TiZrV NEG coated for distributed vacuum pumping.

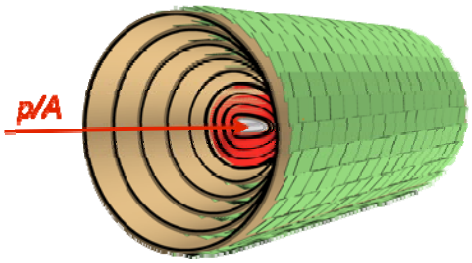

Figure 28: Central tracker 3d view in direction of incoming proton. Vertex Pixel Detector placement around the circular-elliptical pipe.

The tracking and calorimetry in the forward and backward direction have to be set up such that the extreme asymmetry of the interaction kinematics are taken into account by layout and choice of technology for the detector design and a high measurement efficiency is ensured in the largest possible angular range. The LHeC detector is asymmetric in design, Fig. 29, reflecting the beam energy asymmetry and for reducing cost. It is a general purpose 4π detector, which consists of an inner silicon tracker, with extended forward and backward parts, surrounded by an electromagnetic calorimeter, which is separated from the hadronic calorimeter by a solenoid with 3.5 T field. This incorporates the beam steering dipoles mentioned above as those cannot be of a too large radius to act on the beam and be affordable. The hadron calorimeter is enclosed in a muon tracker system currently outside the solenoid.

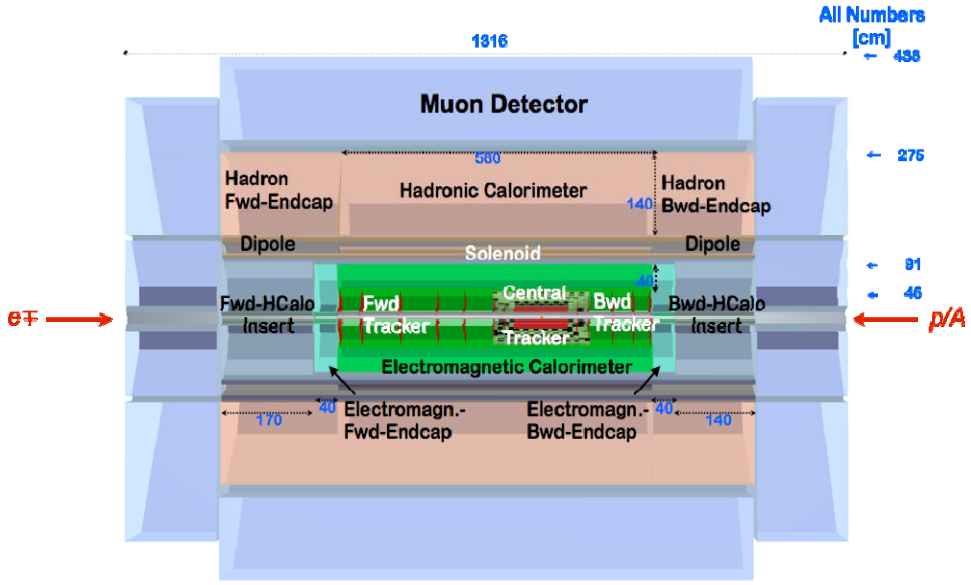

Figure 29: The detector in the r-z plane with all components and the characteristic dipole and solenoid placement between the electromagnetic and the hadronic calorimeters. The proton beam, from the right, collides with the electron beam, from the left, at the IP which is surrounded by a central tracker system complemented by large forward and backward tracker telescopes followed by sets of calorimeters. The hadron calorimeter is enclosed in a muon tracker system. The detector dimensions are ~14m in z with a diameter of ~9m. All numbers in the Figure are given in cm.

The physics programme relies on a high level of precision, required for example for the measurement of α_s, and on the reconstruction of complex final states, as appear in charged current single top events or in Higgs production and decay into b final states. The detector acceptance has to extend as close as possible to the beam axis because of the interest in the physics at small and at large Bjorken x. The longitudinal dimensions of the detector are constrained by the radial extension of the beam pipe, in combination with maximum polar angle coverage, down to about 1° and 179° for forward going final state particles and backward scattered electrons at low Q^2, respectively. Its radial size is mainly determined by the requirement of full energy containment of hadronic showers in the calorimeter.

For the physics performance, it is evidently advantageous placing the solenoid outside the hadronic calorimeter. In case of inner solenoid the hadronic tile calorimeter of ATLAS type serving also for the solenoid flux return. In case of outer solenoid a very bulky and expensive iron structure would have to be added or a second solenoid of inverted magnetic orientation, which is not cheap either but had been considered.

The main detector is complemented by tagging of forward scattered protons, neutrons and deuterons to fully investigate diffractive and deuteron physics and tagging of backward scattered photons and electrons for a precise measurement of luminosity and photoproduction physics described in detail in the CDR [4].

The developing physics programme poses additional requests on the detector performance compared to the CDR [4] published. A demanding extension of the physics programme is the study of Higgs production, which puts a focus on the detector performance for: i) Optimisation of b and c tagging in the forward direction with

maximum angle hadronic calorimetry too; ii) Good vertex resolution for decay particle secondary vertex tagging, which implies a small radius and thin beam pipe.

2.4.9.3 *Tracking*

The constraints given by the magnet system (dipole/solenoid) force the tracking detectors to be kept small in radius. Nevertheless, a high resolution tracking system is needed to provide excellent primary vertex resolution and resolution of secondary vertices down to small angles in forward direction for high x heavy flavor physics and searches. A precise p_T measurement, matched to calorimeter signals calibrated and aligned to an accuracy of 1 mrad is desirable. The compact tracking detector (Fig. 29) inside the electromagnetic calorimeter is chosen to be an all-Silicon detector, with very high resolution. It is, briefly, characterised by:

i) Very lightweight support structures and Si-detector modules avoiding heat dissipation by optimised R/O system are foreseen, most probably using separated trigger and measuring functionality for Si-pixel as well as or Si-strixel detectors; A design starting point could be the ALICE upgraded pixel-detector under development for the HL-LHC running [40];
ii) The forward and backward tracking wheels are equipped with Si-pixel detectors on the 2-3 innermost rings. The outer rings can be instrumented with Si-strixel detectors.

Table 12 illustrates the amount of Si-wafers of different types needed and the tracker coverage.

2.4.9.4 *Calorimetry*

The full coverage calorimetry is sketeched in Fig.29. The electron energy is measured to $10\%/\sqrt{E}$ and calibrated using the classic DIS kinematic peak and double angle methods to the per-mille level. The hadronic energy is designed to be measured to $40\%=\sqrt{E}$, with a calibrated P_T balance to an accuracy of about 1%. The LHeC detector installation constraints demand a modular structure and independent electromagnetic (EMC) and hadronic calorimeter (HAC) components. The design of the electromagnetic modules requires special care for the very forward region, where energies of up to a few TeV and dense jet-structures would occur. In the barrel and the backward region a precise measurement of the scattered electron kinematics with energy O(60 GeV) is paramount. Based on experience with H1 and ATLAS, the EMC default choice is a Liquid Argon (LAr) Calorimeter. The superconducting dipoles (dark grey in Fig. 28) are placed in a common cryostat with the detector solenoid (dark orange) and the LAr EMC (green) (see details in [4]). The HAC currently is an iron-scintillator tile calorimeter [4] providing the required mechanical stability for the inner LAr and Magnet cryostat and guiding the return flux of the magnetic field, as in ATLAS [41]. The restrictive geometry of the forward/backward insert calorimeters (Fig. 29) requires a non-conventional and challenging design based on previous developments e.g. [42] and is using tungsten as the absorber material, in particular for the forward inserts. For the hadronic absorber, also copper might be considered as an alternative. The choice of the sampling calorimetry, for all calorimeter parts, is motivated by the good experience from past experiments along with considerations on the available technologies, and cost, although other approaches (Dual Readout Calorimetry [43], etc.) are being considered.

Table 12: Some Tracker characteristics. The number of wheels, number of rings per wheel and number of layers, respectively for the **FST/BST** (**F**orward/**B**ackward **S**ilicon **T**racker), the **CFT/CBT** (**C**entral **F**orward/**B**ackward **T**racker), the **CPT** (**C**entral **P**ixel **T**racker) and the **CST** (**C**entral **S**ilicon **T**racker) are shown. The minimal/maximal azimuthal angles θ coverage reached by the tracker parts and their corresponding pseudo rapidity values η are quoted. The instrumented area (in m^2) for each part and a sum is given as well.

Tracker	FST_{pix}	FST_{strix}	CFT_{pix}	CPT_{pix}	CST_{strix}	CBT_{pix}	BST_{strix}	BST_{pix}
#Wheels	5		2	–	–	2	3	
#Rings/Wheel	2_{inner}	3_{outer}	3/4	–	–	3/4	3_{outer}	2_{inner}
#Layers	–	–	–	4	5	–	–	–
$\theta_{min/max}$ [^{0}]	0.7	3.8	3.0	5.1	24/155	177.8	173.1	178.7
$\eta_{max/min}$	5.1	3.4	3.6	±3.1	±1.4	-3.6	-2.8	-4.5
$Si_{pix/strix}$ [m^2]	6.9	9.5	2.8	5.4	33.7	2.8	5.7	4.1
Sum-Si [m^2]	70.9 double layers taken into account							

Table 13: Some Calorimeter characteristics. The minimal/maximal azimuthal angles θ coverage reached by the calorimeter parts and their corresponding pseudo rapidity values η for the **FHC/BHC** (**F**orward/**B**ackward **H**adronic **C**alorimeter), the **FEC**/**BEC** (**F**orward/**B**ackward **E**lectromagnetic **C**alorimeter), the **EMC** (central **E**lectro**m**agnetic **C**alorimeter) and the **HAC** (central **Ha**dronic **C**alorimeter) are quoted. The instrumented volume (either *Si*-wafer or *Sci*ntillator/*LAr* based in m^3) for each part and a sum is given as well.

Calo	FHC_{SiW}	FEC_{SiW}	$EMC_{SciPb/LAr}$	HAC_{SciFe}	BEC_{SiPb}	BHC_{SiFe}
$\theta_{min/max}$ [^{0}]	0.61	0.68	8/166	14.2/160	178.7	178.9
$\eta_{max/min}$	5.2	5.1	2.7/-2.1	2.1/-1.7	-4.5	-4.7
Volume [m^3]	6.7	1.6	15.1	165	1.6	5.5
Sum-Si/Sci [m^2]	195.5					

2.4.9.5 ***Muon Detector***

The baseline muon system consists of 2-3 layers, each with a double trigger layer and a layer for measurements, employing now commonly used technologies such as thin gap chambers, resistive plate chambers and drift tubes. In the default design, the muon system provides no independent measurement of the muon momentum which is measured by the inner tracker, in combination with tag signals from the muon system. A more refined physics programme may require a muon detector going beyond the tagging capability, as described in the CDR [4]. Outside muon momentum measurement may become important for the FCC-he detector which has the chance for a precision H□ μμ measurement. The current upgrades for the ATLAS muon detector [44] may serve as instrumentation options for the LHeC muon detector, and they are taken into account in detailed simulations. Several muon system extensions are possible, providing an independent momentum measurement, a larger solenoid or dual coil system (with all of calorimeter within inner coil) but require a strong physics and performance motivation for the complexity these would entail.

2.4.9.6 ***Simulation Framework***

Taking into account the status of LHeC accelerator, detector and IR design, a flexible and future proof simulation framework is very important for investigating questions which imply detector design changes. The DD4hep/DDG4 software

toolbox/framework used is being developed in the context of the ILC/CLIC and FCC detector R&D effort [45]. DD4hep/DDG4 interfacing GEANT4 and latest ROOT releases (5/6) are designed for detailed support of all phases of an experiment life cycle: detector concept development, detector optimization, construction, operation. The software will interface fast and detailed simulation and thus fulfill an essential requirement for fast response evaluation. It provides a full detector description of geometry, materials, visualization, readout, alignment as well as calibration and is a single source of detector information for simulation, reconstruction and analysis.

For reuse of current analysis packages in the ILC / LHC environment, DD4hep/DDG4 is providing interfaces for GAUDI and GEAR. As an illustration of the status of the LHeC software development, Figure 30 shows a simulated H bb̄ event.

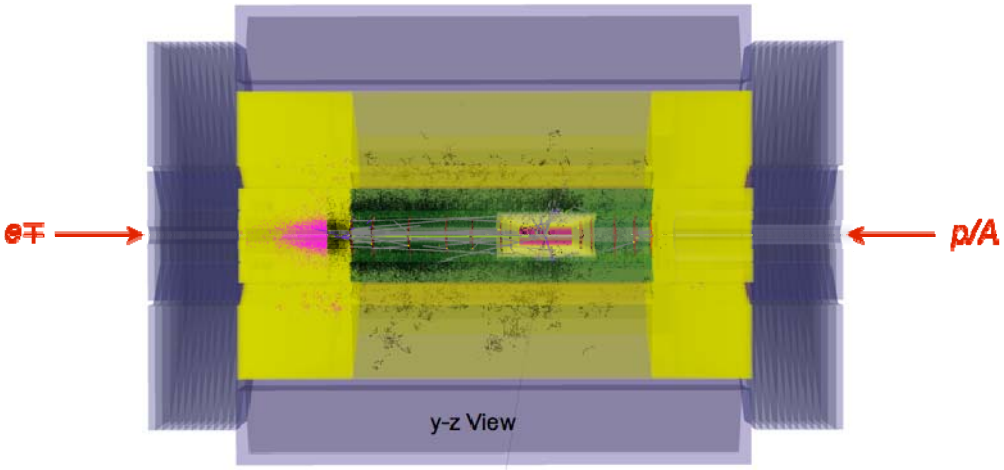

Figure 30: The LHeC detector showing a characteristic 2-jet H bb̄ event in y-z plane cut, simulated with all components active.

2.4.10 **Summary**

Following the detailed Conceptual Design Report of the LHeC, published in 2012, the project has been developed further, much influenced by the discovery of the Higgs boson and the conclusion that the energy recovery, racetrack configuration was the preferred choice for a possible maximum luminosity realization. The physics of the LHeC, as briefly presented, has been studied deeper with new insight in the unique potential of this machine as the world's best possible microscope for proton and nuclear substructure and precision Higgs and electroweak physics. The detector concept is being adapted to a high precision, large acceptance device for TeV scale deep inelastic scattering, with an interaction region under detailed design allowing for concurrent ep and pp operation. The base of the LHeC is considered to be a 60 GeV electron beam provided by two oppositely placed 10 GeV linacs, operated with superconducting 802 MHZ cavities in CW mode. A luminosity goal of 10^{34} cm^{-2} s^{-1} is reachable at a power limit of 100 MW with electron beam currents of about 20mA when this beam collides with one of the 7TeV HL-LHC proton beams and its energy recovered in the SC RF structures. The present letter informs about on-going studies on various important elements of the design, such as the choice of beam energy, luminosity performance, arc

magnet configuration, beam-beam effects. A key task for the LHeC will be the demonstration of its principle, a triple turn, efficient ERL, based on high quality SC cavities and using large electron beam currents. The article sketches a principal design of such a test facility allowing it to be adapted to a practical configuration in the time hence. The LHeC appears to be a realistic, unique and high performance next ep and eA collider extending the energy and luminosity frontier in deep inelastic scattering and thereby representing the next collider configuration to study the Higgs mechanism. This considerably strengthens the physics potential of the LHC for establishing new physics beyond the standard model. The ERL configuration as sketched here, is also considered to be the default configuration for a future electron-hadron collider based on the FCC. Overall the results of the LHeC study have been very encouraging. The studies have been conducted under the guidance and evaluation of an International Advisory Committee for the LHeC that has been mandated and been put in place by the CERN directorate following the publication of the LHeC CDR in 2012.

2.4.11 **Acknowledgments**

The authors are very grateful for a large, fruitful collaboration of physicists and engineers engaged in the development of the LHeC, many results of which are here summarised. They acknowledge the support of the CERN directorate and of the International Advisory Committee and its chair Herwig Schopper. They also are grateful for the inclusion of the principle ERL design here presented as a baseline for a future electron-hadron collider at the FCC. A. Milanese gratefully acknowledges fruitful discussions about multiple aperture dipoles with N. Marks and Y. Pupkov.

2.4.12 **References**

1. HERA, Technical Proposal, DESY-HERA-81-10 (1981), unpublished.
2. E. Keil, “LHC e-p Option”, CERN, LHC Project Report 93 (1997).
3. J. Dainton, M. Klein, P. Newman, E. Perez and F. Willeke, "Deep Inelastic Electron-Nucleon Scattering at the LHC", arXiv:hep-ex/0603016 (2006).
4. J.L. Abelleira Fernandez et al. “A Large Hadron Electron Collider at CERN: Report on the Physics and Design Concepts for Machine and Detector”, arXiv:1206.2913 [physics.acc-ph] (2012)
5. CERN/AC/95-05 (LHC), LHC CDR, October 1995.
6. CERN-2004-003, The LHC Design Report, Volume I, June 2004.
7. F. Zimmermann, ‘HL-LHC: Parameter Space, Constraints & Possible Options’, EuCARD-CON-2011-002. – 2011, published in the proceedings of the 2011 Chamonix workshop.
8. HL-LHC Preliminary Design Report, Deliverable: D1.5, CERN-ACC-2014-0300.
9. G. Apollinari [FERMILAB], O. Brüning and L. Rossi [CERN], ‘High Luminosity Project Description’, CERN-ACC-2014-0321, 2014.
10. eRHIC ‘Zeroth-Order Design Report’: https://www.bnl.gov/cad/eRhic/eRHIC_ZDR.asp
11. F. Zimmerman *et al,* “Interaction region design options for a Linac-Ring LHeC”, in Proceedings of the 1st International Particle Accelerator Conference, Kyoto, Japan, 2010, TUPEB037
12. B. Parker, presentation in the LHeC Workshop, Chavannes-de-Bogis, 2015, https://indico.cern.ch/event/356714/
13. J. L. Abelleira Fernandez *et al.* (LHeC Study Group), “A Large Hadron Collider at CERN”, J. Phys. G. 39 (2012) 075001.
14. S. Fartoukh, “Achromatic telescopic squeezing scheme and application to the LHC and

its luminosity upgrade", Phys. Rev. ST Accel. Beams 16, 111002 (2013).
15. R.Tomás, in the Meeting on LHeC with Daresbury group, Daresbury, UK, 2012, https://indico.cern.ch/event/207665/
16. M. Korostelev, E. Cruz-Alaniz, D. Newton, A. Wolski, O. Brüning, and R. Tomás, "LHeC IR optics design integrated into the HL_LHC lattice", in Proceedings of the 4th International Particle Accelerator Conference, Shanghai, China, 2013, MOPWO063.
17. E. Cruz-Alaniz, D. Newton, R. Tomás, and M. Korostelev, "Design of the large hadron electron collider interaction region", Phys. Rev. ST Accel. Beams **18**, 111001
18. The bending magnet system of LEP, M. Giesch and J.P. Gourber, MT11 1989, CERN LEP-MA/89-68
19. General layout of HERA, R. Brinkmann, CAS - CERN Accelerator School, Berlin, 1987, pp.131-140
20. L. Harwood, G. Biallas, A. Guerra, W. Heilbrunn, J. Karn, Magnet design and performance for the CEBAF beam transport system, EPAC 1992.
21. D. Pellegrini, A. Latina, and D. Schulte, "PLACET2: a Novel Code for Beam Dynamics in Recirculating Machines" in Proceedings of the IPAC15, (Richmond VA, USA), 2015. MOPJE068.
22. D. Schulte, Ph. D. Thesis, University of Hamburg 1996, Tesla-97-08.
23. V. N. Litvinenko, "Chromaticity of the lattice and beam stability in energy recovery linacs" Phys. Rev. ST Accel. Beams, vol. 15, p. 074401, Jul 2012.
24. D. Schulte, "Multi-bunch calculations in the CLIC main linac" in Proceedings of the PAC09, (Vancouver, BC, Canada), 2009, FR5RFP055.
25. S. A. Heifets, G.A. Krafft and M. Fripp, "On asymmetric Collisions with large disruption Parameters", in "Nuclear Instruments and Methods in Physics Research A295", 286-290 (1990).
26. E. Nissen, "A Method for Predicting Emittance Growth from Beam-Beam Interactions in the LHeC" LHeC Tech note LHeC-2015-001 ACC (submitted).
27. D. Schulte, Ph. D. Thesis, University of Hamburg 1996, Tesla-97-08.
28. M. Bassetti and G. A. Erskine, "closed expression for the electrical field of a two dimensional gaussian charge", CERN-ISRTH/80-06, 1980.
29. V. Ziemann, "Beyond Bassetti and Erskine: Beam-beam deflections for non-gaussian beams." Proceedings of 1991 ICFA workshop, Los Angeles, CA (USA) 1991.
30. S. Benson et al., 'High Power Lasing in the IR Upgrade FEL at Hefferon Lab', proceedings of the 2004 FEL conference, page 229-232, Trieste, Italy, 2014.
31. N. Nakamura, KEK, 'Review of the ERL Projects at KEK and Around the World', proceedings of the IPAC12 conference, New Orleans, U.S.A., 2012.
32. O. Shevchenko et al., "Commissioning Status and Further Development of the Novosibirsk Multiturn ERL", Proceedings of the ERL2013 workshop, Novosibirsk, Russia, 2013.
33. D. Gassner et al., 'Status of the BNL ERL Instrumentation proceedings of the ERL2013 workshop, Novosibirsk, Russia, 2013.
34. A. Grassellino et al. "Nitrogen and argon doping of niobium for superconducting radio frequency cavities: a pathway to highly efficient accelerating structures", Supercond. Sci. Technol., vol. **26** No. 102001.
35. S. Posen and A. Liepe, "RF Test results of the first NB2SN Cavities coated at Cornell", Proceedings of SRF2013, Paris France.
36. council/en/EuropeanStrategy/ESParticlePhysics.html
37. E. Jensen et al., "Plans for an ERL Test Facility at CERN", Linac14, Geneva, Switzerland.
38. V. Parma et al., "Status of the Superconducting Proton Linac (SPL) Cryomodule", Proceedings of SRF2013, Paris, France.
39. M. Klein ``Deep Inelastic Scattering at the Energy Frontier", Annals of Physics, in print (2015).

40. ALICE Collaboration "Conceptual Design Report for the Upgrade of the ALICE ITS" CERN-LHCC-2012-005 / LHCC-G-159 and http://aliceinfo.cern.ch/ITSUpgrade/
41. A. Airapetian and others, ATLAS calorimeter performance Technical Design Report, ATLAS, 1996.
42. ILC Collaboration "Technical Design Report" , 2013, http://www.linearcollider.org/ILC/Publications/Technical-Design-Report and "The International Linear Collider Progress Report 2015", http://ilcdoc.linearcollider.org/record/62872
43. R. Wigmans, Recent results from the DREAM project J. Phys. Conf. Ser., 160, 012018, 10.1088/1742-6596/160/1/012018, 2009.
44. ATLAS Collaboration "New Small Wheel Technical Design Report", ATLAS-TDR-20-2013, see references: http://inspirehep.net//record/1315605/references
45. DD4Hep web page, http://aidasoft.web.cern.ch/DD4hep

2.5 Beam Dynamics Issues for ERL-based Electron-ion Colliders

Yue Hao and Vadim Ptitsyn
Brookhaven National Laboratory, Upton, New York, 11973
Mail to: yhao@bnl.gov, vadimp@bnl.gov

2.5.1 Introduction

Currently few accelerator proposals for future electron-ion colliders are under consideration in several laboratories from all over the world. The future accelerators intend to exceed the luminosity of the first lepton-proton collider HERA (that completed its operation in 2007) by two orders of magnitude, as well as to cover the different ranges of center-of-mass collision energies. The research capabilities will be extended by including the collisions of electrons with heavy ions, as well as, in some designs, with polarized protons and polarized ions. The future electron-ion colliders would serve as high-resolution femtoscopes able to reveal unprecedented details of the structure of nucleons and ions, including their spin content and the state of high gluon density matter. The colliders will provide us with ultimate capabilities to test both the ways Quantum Chromodynamics works as well as to look for new physics beyond the Standard Model.

Presently the preferred choice for EIC designs being developed at Brookhaven National Laboratory (eRHIC [1]) and CERN (LHeC [2]) is based on the linac-ring collision scheme, when the proton (or ion) beam is accelerated and stored in a circular accelerator while the electron beam is accelerated by multiple re-circulations through an energy recovery linac. Main parameters, including luminosities, of these ERL-based EICs are listed in Table 1.

Table 1: Main beam parameters of ERL-based Electron-Ion Colliders.

	eRHIC		LHeC	
	e	p	e	p
Energy (GeV)	15.9	250	60	7000
Bunch spacing (ns)	106		25	
Current (mA)	10	415	6.6	860
rms norm. emit. (mm-mrad)	23	0.2	50	3.75
$\beta_{x/y}$ at IP (cm)	5	5	12	10
rms bunch length (cm)	0.4	5	0.06	7.6
IP rms spot size (μ m)	6		7	
Polarization, %	80	70	90	None
Luminosity, 10^{33} cm^{-2} s^{-1}	3.3		1.3	

Relativistic Heavy Ion Collider (RHIC) has been operating at BNL (USA) for more than decade, producing either polarized p-p collisions (with the proton energy up to 250 GeV) or unpolarized heavy ions collisions (with ions up to U and the ion energy up to 100 GeV/u). eRHIC will add an electron accelerator inside the present RHIC tunnel. One of the straight tunnel section will accommodate the 1.67 GeV ERL. Using multiple re-circulations through the ERL eRHIC will be able to use the electrons in large energy range (5-20 GeV). The re-circulations will be realized with two FFAG beam lines, each capable of electron beam transport with the energy ratio of 3. Both electron and proton beams of eRHIC will be highly polarized.

In the baseline design of the LHeC linac-ring approach a 60 GeV ERL-based accelerator will be placed in the vicinity of e-p collision point, with most electron accelerator components outside of the LHC tunnel. The ERL accelerator will utilize two 10 GeV ERLs with three e-beam recirculation scheme. The LHeC design includes polarized electrons but does not aim to have the polarization of the proton beam.

The high luminosity in the linac-ring scheme is related with the fact that the electron beam-beam limitation, typical for storage rings, can be overcome, since electrons pass through the collision point just once. In addition the linac-ring designs also provide simpler treatment of the polarized electron beam, eliminating depolarizing problem related with spin resonances.

The energy recovery is required to operate with sufficiently high electron currents (from few mA to 50 mA) in CW mode. Thus, one important area of design studies is concerned with high power ERL issues, such as development of high current SRF cavities with efficient HOM damping, machine protection and beam loss control, multi-pass BBU.

Other technological challenges include a high intensity polarized electron source, a low beta* interaction region design. In the case of eRHIC an efficient cooling of high energy ion beam is required. Together with the conventional electron cooling, a new cooling technique, Coherent electron Cooling [3], has been under rapid development and the Proof-of-Principle experiment is being prepared at RHIC [4]. For LHeC novel techniques to produce intense positron beam are being explored.

Both eRHIC and LHeC are considering low energy test facilities, at Cornell University Cbeta [5]) and at CERN [6], based on energy recovery linacs with multiple re-circulations. The facilities will test involved technologies, including FFAG-based

transport (Cbeta) and SRF cavities, and verify beam dynamics related with multiple re-circulations of high beam currents.

There are several beam dynamics effects, which are specific for ERL-based electron-ion colliders with multiple re-circulations and we will concentrate on them in the rest of this article. One of them is related with constructing the ERL optics with specific restrictions coming for multi-pass transport. Understanding the limit of multi-pass beam-breakup instability is crucial to achieving the high beam current with multiple re-circulations. Ion accumulation and possible effect of it on the electron beam has to be understood. Full understanding of beam-beam interactions in the linac-ring scheme is very important. On one side the electron beam disrupted by the collision with ions has to be decelerated without losses, thus the electron beam disruption has to be well understood. On the other side specific effect from the collision on the ion beam, the kink instability, may limit the collider performance unless one stays below its limit or employs remedies against it.

2.5.2 **Linac Optics for Multi-Pass ERL**

eRHIC electron accelerator adopts a N-pass energy recovery linac design. After entering the ERL, the electron will pass through the linac N times with accelerating phases and N times with decelerating phases. Between the passages through linac, the particle travels through the first N-1 recirculating passes twice, one in accelerating stage and one in decelerating stage, and only once through the highest energy passes which includes the interaction region of electron ion collider.

The optics function in the linac has to be carefully designed for each pass in the accelerating and decelerating stages, since it plays an important role in various beam dynamics topics such as the beam break-up instability due to un-damped HOM in the SRF cavity. We adopted a quadrupole-free design due to the limited length of the straight section in the tunnel. The lattice of the recirculating passes is abstracted as linear transfer map without transverse coupling.

To control the linac optics at both the accelerating stage and decelerating stage, we adopt symmetric constrains, which requires the optics of decelerating stage to be the mirror reflection of that of the accelerating stage. If we denote optics function ($\beta_{i,1}$, $\alpha_{i,1}$) at the entrance and ($\beta_{i,2}$, $\alpha_{i,2}$) at the exit of the i^{th} passage of the linac in accelerating stage, in the decelerating stage, the optics functions at entrance and exit becomes ($\beta_{i,2}$, $-\alpha_{i,2}$) and ($\beta_{i,1}$, $-\alpha_{i,1}$) respectively. In addition, the j^{th} recirculating passes, which connects the exit of j^{th} linac passage and the entrance of the $(j+1)^{th}$ passage, shall transform the optics ($\beta_{j,2}$, $\alpha_{j,2}$) □($\beta_{j+1,1}$, $\alpha_{j+1,1}$) in accelerating stage and ($\beta_{j+1,1}$, $-\alpha_{j+1,1}$) □($\beta_{j,2}$, $-\alpha_{j,2}$). To satisfy this symmetric condition, we have to design the linac to be mirror symmetric with respect to its middle point and each recirculating pass (except the highest energy pass) to have transfer matrix as:

$$M = \begin{pmatrix} d & (d^2-1)/b \\ b & d \end{pmatrix}$$

This form of the matrix can be achieved by two approaches.

1. The optics in each linac passage is individually designed, so that ($\beta_{j,2}$, $\alpha_{j,2}$) and ($\beta_{j+1,1}$, $\alpha_{j+1,1}$) are given conditions for the recirculating passes. The phase advance is then calculated from the optics functions to fulfill the constrain.

2. The optics of (j+1)th passage's entrance is determined by those of jth passage's exit, i.e. ($\beta_{j+1,1} = \beta_{j,2}$, $\alpha_{j+1,1} = -\alpha_{j,2}$). Then the phase advances of each pass are free parameters.

We choose the approach 2 because the freedom of choice of the phase advances will not only simplify the spreader/combiner design which connects the linac and the FFAG recirculating pass, but also is important for elevating the threshold of the beam break-up instability. And the only free parameter in this approach is the initial optics function at the entrance of the ERL.

The highest energy pass needs to transform ($\beta_{N,2}$, $\alpha_{N,2}$) to ($\beta_{N,2}$, $-\alpha_{N,2}$). The phase advance of this pass is also a free parameter. Figure 1 shows linac optics design of the 16-pass ERL. Only the accelerating stage is plotted. The focusing effect of in the RF cavity follows the treatment in [7].

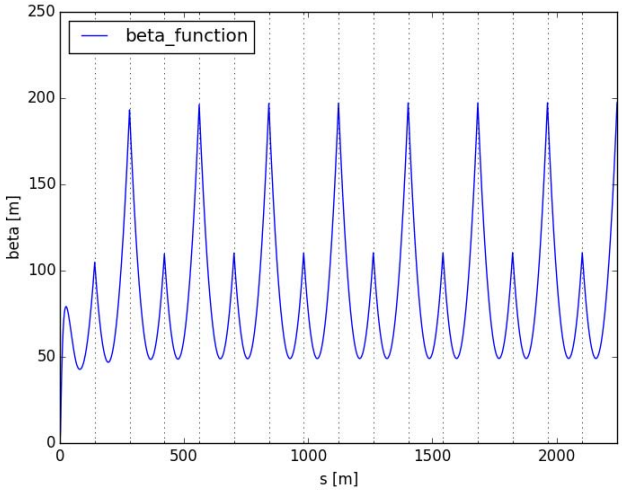

Figure 1: The optics of the 16-pass eRHIC lattice. The horizontal and vertical beta functions overlap with each other. The figure only shows the optics in linac, whereas the grid lines represent the missing recirculating passes.

2.5.3 **Beam Break-up Instability**

The beam break-up (BBU) instability is the major limiting factor of the maximum average current in the ERL [8]. The BBU threshold current is determined by the un-damped higher order modes in the RF cavity, the optics of the ERL, as well as the bunch pattern in ERL. In a multi-pass ERL with long RF cavities, simulation is required to determine the threshold. We use the code GBBU to evaluate the threshold current of eRHIC ERL [9]. As 422 MHz 5-cell elliptical cavity is used in the beam break-up simulation.

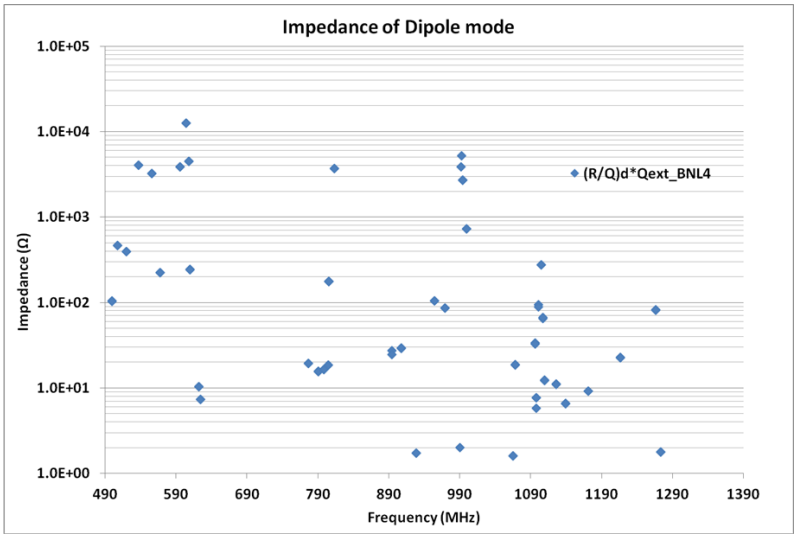

Figure 2: The R/Q and quality factor of the 422MHz SRF cavity.

In this example, there are 16 phase advances in each transverse direction can be adjusted to maximize the threshold current. A preliminary optimization scan shows that the following choices (in Table 2 yield satisfactory threshold BBU current for eRHIC, as shown in Table 3.

Table 2: Phase advance choices for 16 pass eRHIC.

1-15 recirculating passes:	π
16th recirculating passes:	$\pi/2$

Table 3: The threshold current of eRHIC.

	Design current (mA)	Threshold current (mA), zero HOM freq. spread)	Threshold current (mA), 10^{-3} rms HOM freq. spread)
12 passes,16 GeV	3	84	138+/-9 (rms)
16 passes, 21 GeV	10	127	193+/-13 (rms)

The natural HOM frequency spread of the cavities in linac will help to increase the BBU threshold currents, since it reduces the coherent interaction between the cavities, which is illustrated in the table with the average threshold current and its rms spread over 50 sets of random HOM frequency error. Even with zero frequency spread, the HOM threshold currents of eRHIC ERL are much larger than the design currents.

2.5.4 **Ion Effects in ERL**

The residue gas molecule in the vacuum pipe can be ionized by the high energy electron beam. The line density of the ion can be calculated as $\frac{d\lambda}{dz} = \sigma_i n_g I_e$, where σ_i is the cross section of the ionization, n_g is the particle density of residue gas and I_e is the incident electron beam. The ionization cross section can be either achieved from the Binary-Encounter-Bethe (BEB) model [10] or the experimental data. For high electron

energies, the cross sections for common gas are in order of $10^{-18}cm^2$. Within the super conducting linac, the major residue gas is helium, while in the warm section, there are various gas species such as H_2O, H_2, CO etc.

A potential beam dynamics issue is that the residue ion can resonantly interact with the electron bunches, which causes the coherent osculation of the centroid of the electron beam, named 'fast ion instability (FII)'. It was first predicted in [11] and experimentally observed in [12]. This effect is evaluated with simulation in the FFAG transport line of eRHIC ERL [13].

The simulation reveals that FII will cause the beam centroid oscillation up to few percent of the electron beam size (in the left figure of Figure 3). By introducing the ion clearing gap in the electron bunch train, illustrated in the right figure of Figure 3, the fast ion instability of the beam centroid is suppressed. The length of the ion clearing gap has the same length of the abort gap of the opposing ion beam. Therefore, the ion clearing gap will not affect the luminosity of eRHIC.

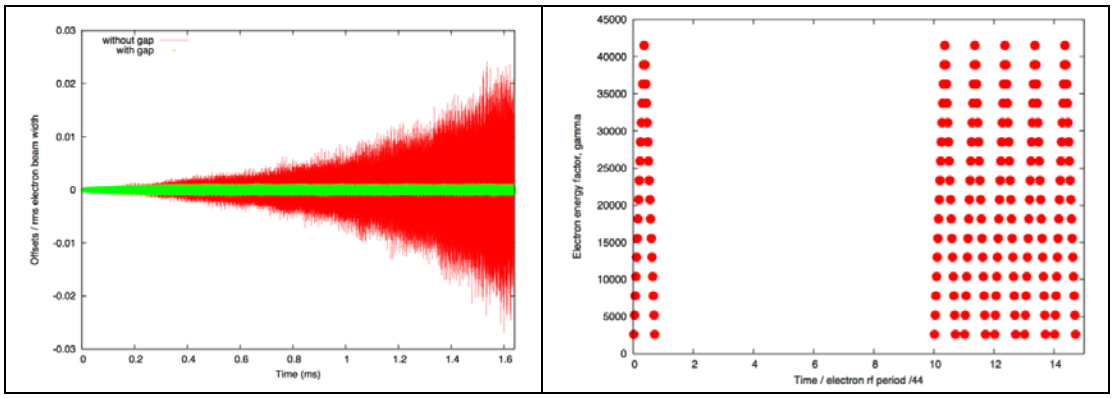

Figure 3: The electron beam centroid evolution (left) as function of time as result of the fast ion instability and its stabilization with the ion clearing gap in the bunch train (right).

2.5.5 **Beam-beam Effects in ERL-based eRHIC**

Beam-beam effects present one of the major restrictions in achieving the higher luminosities in the traditional ring-ring colliders. The electron-ion collider based on ERL electron accelerator removes the beam-beam limitation of the electron beam, therefore, higher luminosity is expected [1]. However the new ERL-ring collision scheme also introduces unique beam dynamics challenges, including the electron disruption effects [14], pinch effect [14], the kink instability [15][16] of the ion beam and noise heating of the ion beam.

The electron disruption effect and the pinch effect rise due to the large beam-beam parameter of the electron beam. The strong nonlinear beam interaction field will distort the electron beam distribution and the large linear beam-beam tune shift leads to significant mismatch between the design optics and the electron beam distribution. The disruption effect is illustrated in the left of Figure 4. The mismatch effect can be demonstrated by the difference of the geometric emittance (blue curve in right of Figure 4) and the effective emittance (red curve in right of Figure 4). The geometric emittance is determined only by the electron beam distribution and the effective emittance is calculated from the action of the electrons using the design optics of the IP. This is the

leading factor of the emittance growth in the electron accelerator and determines the minimum aperture of the ERL magnets.

The pinch effect reflects the over-focusing effect of the electron beam inside the ion bunch due to the strong focusing beam-beam force, which is demonstrated by the difference between the green curve (electron rms beam-size with the beam-beam effect) and the black curve (the rms beam-size without beam-beam effect) in right of Figure 4. The pinch effect in one hand will enhance the luminosity, e.g., eRHIC 's luminosity is boosted from 3.3×10^{33} $cm^{-2}s^{-1}$ to 4.9×10^{33} $cm^{-2}s^{-1}$, a factor of 1.48. However, this effect also boosts the local beam-beam force to the opposing ions beam, which must be included in the dynamics aperture study.

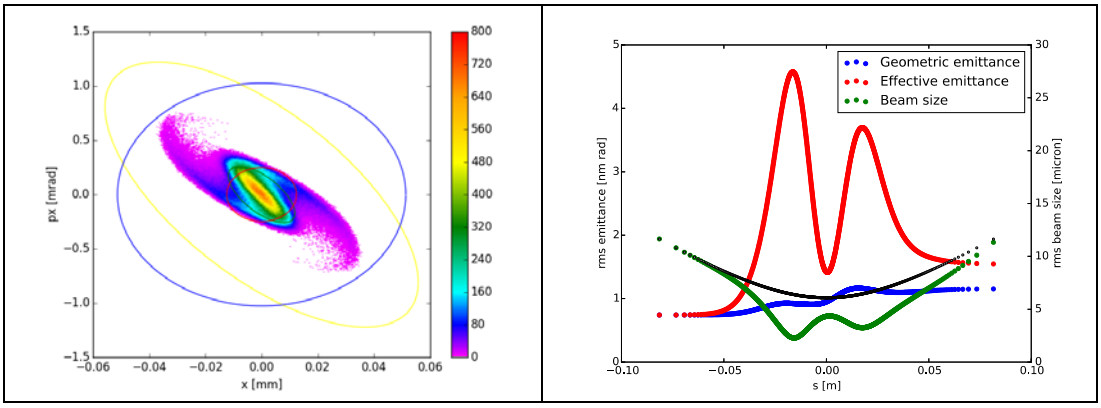

Figure 3: Left figure: The electron beam distribution after one collision with the opposing ion beam; right figure: the electron beam evolution (right) inside the ion beam. The geometric emittance is determined only by the electron beam distribution and the effective emittance is calculated from the action of the electrons using the design optics of the IP.

For the ion beam, the largest challenge is the kink instability [16], which arise due to the effective wake field of the beam-beam interaction with the electron beam. The electron beam is affected by the head of the ion beam and passes the imperfection of the head portion to its tail. The threshold of the instability can be estimated by the strong head-tail model, which gives:

$$d_e \xi_y \lesssim 4\nu_s/\pi$$

where d_e is the disruption parameter of the electron beam and ξ_y is the beam-beam parameter of the ion beam. A more precise multi-particle model confirms this relation when disruption parameter is not too large [16]. eRHIC beam-beam related parameters exceed this limit. Simulation studies also predict that the instability cannot be suppressed by the current chromaticity in RHIC. The feedback system is required to suppress the instability. Two types of feedback system were proposed. The first one is the feedback system acting on the electron beam [16] and the second one is the pickup-kicker type in the ion ring [17]. In the nominal parameter of eRHIC, the pickup-kicker system is suitable. The inner-bunch modes of the instability can be picked up, amplified through a broad-band amplifier and corrected by the high band-width kicker. For the 5 cm eRHIC ion bunch length, the bandwidth of the feed-back system should be no narrower than 50-300 MHz.

The noise carried by the fresh electron bunches may heat up the ion beam in the ring due to the beam-beam interaction. The random electron beam offset at the IP causes a dipole-like error for the ion beam, while the electron beamsize and density variation at

the IP act as quadrupole-like errors. Simulations shows that the emittance growth rate for a 1 micron electron beam position offset at the IP cause an ion beam emittance growth of 20% per hour, which should be suppressed by the advanced cooling technique (~7 min cooling time). The same cooling time also allows the quad error (the electron distribution density) of 0.1% [1].

2.5.6 References

1. "eRHIC Design Study" report, arXiv:1409.1633. (2014).
2. "A Large Hadron Electron Collider at CERN", Journal oh Physics G, v.39-7, 075001 (2012).
3. V. N. Litvinenko, Y.S. Derbenev, Physical Review Letters 102, 114801 (2009).
4. V. N. Litvinenko, et al., IPAC2014, Dreseden, Germany, MOPRO013 (2014).
5. "The Cornell-BNL FFAG-ERL Test Accelerator: White Paper", arXiv:1504.00588 (2015).
6. E. Jensen, et al., LINAC2014, Geneva, Switzerland, IL, THPP031 (2014).
7. J. Rosenzweig, L. Serafini, Phys. Rev. E 49, p. 1599-1602 (1994).
8. G.H. Hoffstaetter and I.V. Bazarov, Phys. Rev. ST Accel. Beam. 7, 054401 (2004).
9. E.Pozdeyev, Phys. Rev. ST Accel. Beams 8, 054401 (2005).
10. Kim Y-K, Rudd ME. Phys. Rev. A 1994; 50: 3954.
11. T. O. Raubenheimer, and F. Zimmermann, Phys Rev. E 52 (1995),5487.
12. J. Byrd et al., Physical Review Letters 79 (1997),79.
13. G. Wang et al., IPAC2014, Dresden, Germany, MOPRO012 (2014).
14. Y.Hao and V.Ptitsyn, Phys. Rev. ST Accel. Beams 13, 071003 (2010).
15. R.Li, B.C.Yunn, V.Lebedev, J.J.Bisognano, PAC'01, Chicago, IL, (2001).
16. Y. Hao, V.N. Litvinenko and V. Ptitsyn, Phys. Rev. ST Accel. Beams 16, 101001(2013).
17. Y. Hao, M. Blaskiewicz, V.N. Litvinenko and V. Ptitsyn, IPAC 2012, New Orleans, TUPPR083 (2012).

2.6 Commissioning progress of the Energy Recovery Linac at Brookhaven National Laboratory

Dmitry Kayran, BNL, Upton, New York, 11973
Mail to: dkayran@bnl.gov

2.6.1 Introduction

An ampere class 20 MeV superconducting Energy Recovery Linac (ERL) is presently under commissioning at Brookhaven National Laboratory (BNL) for testing of concepts relevant to high-energy coherent electron cooling and electron-ion colliders [1]. The injector subsystems tests and installation were finished in fall 2013. The injector includes: SRF photoelectron gun with 1 MW amplifier, 10W green drive-laser system, multi-alkaline cathode deposition system, cathode transport system, beam instrumentation and control. First beam test was conducted in June 2014. During the test only dark current has been measured [2]. The first photocurrent from ERL SRF gun has been observed in fall 2014 after second attempt [3]. The ERL returning loop components were installed and new cathode with Ta tip was conditioned in Spring 2015. With new cathode stalk QE of 4% has been observed. Bunch charge 0.55 nC was

achieved with new cathode. After ERL commissioning in BLDG912 the ERL will be relocated to RHIC IP2 to be used for LEReC project.

2.6.2 **BNL R&D ERL Design**

The R&D ERL facility at BNL aims to demonstrate CW operation of ERL with average beam current up to 0.3 ampere, combined with very high efficiency of energy recovery. The ERL is being installed in one of the spacious bays in Bldg. 912 of the RHIC/AGS complex. The intensive R&D program geared towards the construction of the prototype ERL is under way [4]: from development of high efficiency photo-cathodes [5], design, construction and commissioning SRF gun [6], to the development of new merging system compatible with emittance compensation technic [7]. The R&D ERL will test many generic issues relevant with ultra-high current continuously operation ERLs: 1) SRF photo-injector (704 MHz SRF Gun, photocathode, laser) capable of 300 mA; 2) preservation of low emittance for high-charge, bunches in ERL merger; 3) high current 5-cell SRF linac with efficient HOM absorbers [8]; 4) BBU studies using flexible optics; 5) stability criteria of amp class CW beams.

BNL ERL design has one re-circulating loop with achromatic flexible optics [9]. Schematic layout is shown in Fig. 1. Electrons are generated and accelerated in superconducting half-cell gun to 1-2 MeV. Electrons then are injected into the ERL loop through the merging system, which incorporate emittance compensation scheme. The SRF linac accelerates electrons up to 20 MeV. Accelerated electron beam passes through two achromatic arcs and a straight section between them, and returns to the same linac. The path-length of the loop provides for 180 degrees change of the RF phase, causing electron deceleration in the linac (hence the energy recovery) down to injection energy. Decelerated beam is separated from the higher energy beam and is directed to the beam-dump.

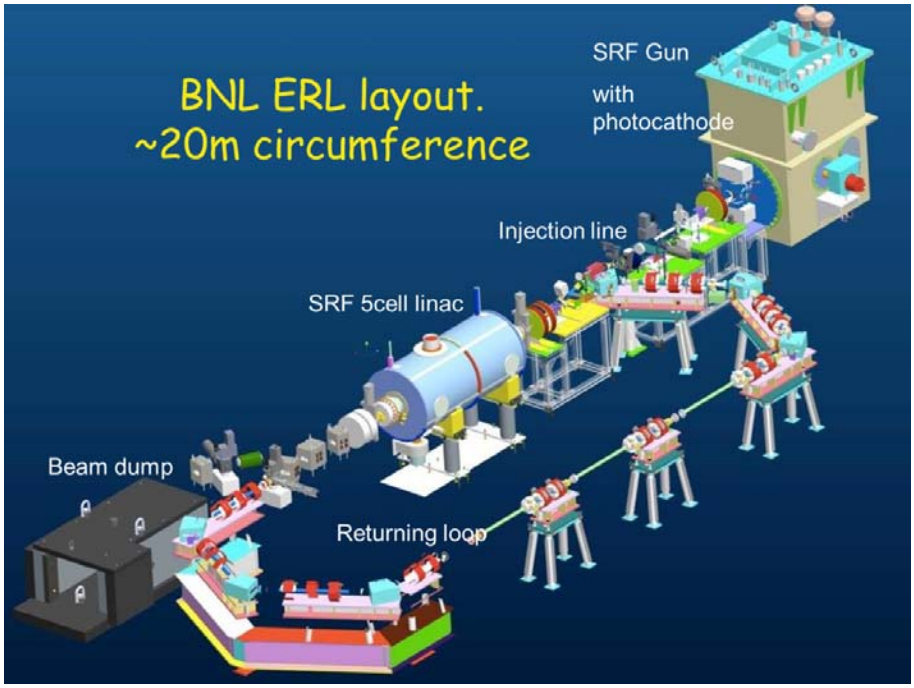

Figure 1: Schematic layout of the R&D ERL at BNL.

Two operating modes will be investigated, namely the high current mode and the high charge mode. Beam parameters for each mode and recent tests results summarized at Table 1. In the high current (0.3 A) mode ERL will operate electron bunches with lower emittance 0.5 nC bunches with 703 MHz rep-rate. In this case the kinetic energy of electrons at gun exit is limited to 2.0 MeV by the available RF of 1 MW. In a high charge mode, ERL will have electron beam with 5 nC per bunch and 10 MHz repetition rate, i.e. it will produce 50 mA average current. In this mode, the electrons energy at the gun exit can be pushed higher. The maximum voltage at the gun is 2.5 MV limited by power coupler design and available RF power.

Table 1: Designed and measured beam parameters.

Parameter	**High Charge**	**High Current**	**Measured***
Gun energy	3 MeV	2.5 MeV	1.4 MeV
Max. Energy	20 MeV	20 MeV	N/A
Charge per bunch	5 nC	0.5 nC	0.55 nC
Current	50 mA	350 mA	20 uA
Laser Rep. Rate	9.38 MHz	350 MHz	9.38 MHz
Laser Bunch Length	30 ps	8-20 ps	8.5, 22 ps
Norm. emittance	5 um	1.4 um	2.2/1.6 um **
Energy spread	1%	0.35%	
Beam dump Power	150 kW	875 kW	8 W (FC)

*) Listed parameters have been achieved in different modes of operation. **) Preliminary results.

2.6.3 **SRF Components**

2.6.3.1 ***SRF 704 MHz Gun***

The most important element of BNL ERL is SRF photo-injector. BNL 704 MHz SRF gun has been designed with a short 8.5 cm cell. The short length was chosen to provide high electric field at the cathode at low accelerating voltage. In order to provide effective damping of high order mode (HOM) this gun has rather large iris radius of 5 cm. Ferrate dumpers are installed around ceramic break at the exit of the gun. Gun has been installed at ERL in 2012. SRF gun now routinely operates CW without the cathode at 2 MV accelerating voltage.

With new cathode stalk installed the gun operated at 1.25 MV [10] with good vacuum and no radiation. (Fig. 2).

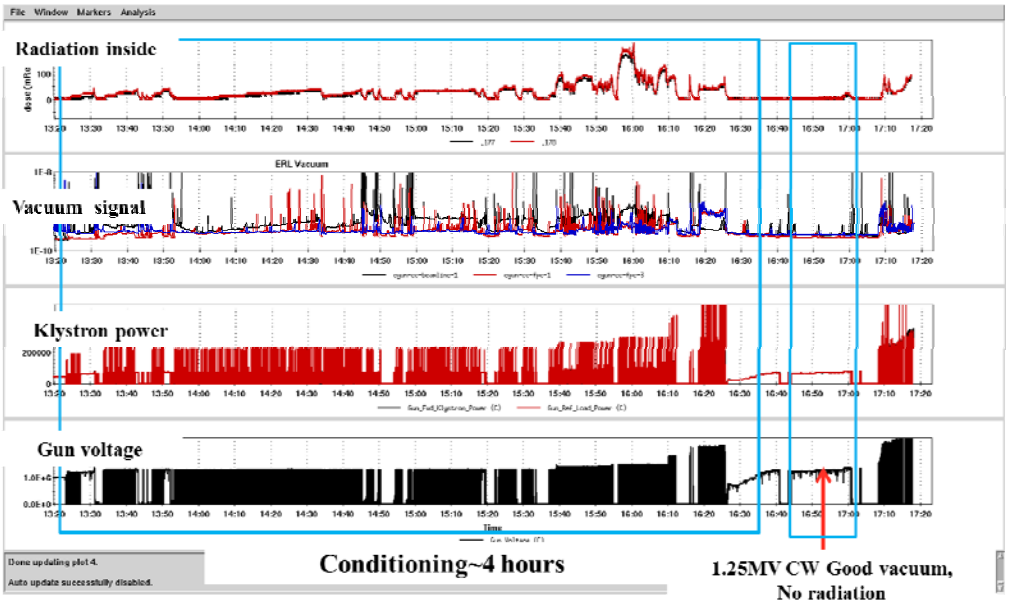

Figure 2: Radiation, beam-line vacuum, klystron power and gun voltage signal during conditioning ERL 704MHz SRF gun and CW operation with new cathode stalk. CW operation at 1.25MV has been achieved.

2.6.3.2 *ERL Linac: 5-cell 704 MHz SRF Cavity*

The heart of the ERL facility is 5-cell 704MHz SRF linac, which is designed for operating with ampere-class CW beam current. The cavity was designed as a "single-mode" cavity, in which all Higher Order Modes (HOMs) propagate to HOM ferrite absorbers through the large beam pipe. This design provides for very low Q's for HOMs and hence very high ERL stability. Measurements of the damped Q and R/Q of the HOMs and simulations show that in nominal operation regime the cavity is stable to over 20 amperes in one pass ERL and over 2 amperes for two passes ERL. The 5cell cavity has been commissioned in 2010. In cold emission tests high gradients have been achieved for short period of time [8].

A thermal problem has been discovered during commissioning SRF 5-cell cavity, which prevents CW operation at gradients above ~12 MV/m. However, the prototype program can still be pursued if the cavity can be operated in a pulsed "quasi-cw' mode up to 20 MV/m.

We found out that by adopting a duty cycle of ~1:15 (on:off), we can safely turn the cavity up to an accelerating gradient of 18 MV/m. We demonstrated continuous running for 30 minutes with a pulse length of 2 seconds, and an off time of 30 seconds. During the "off" phase, the gradient is held at 3 MV/m. The longest pulse achieved before quenching was 5 seconds. (as shown in Fig. 3).

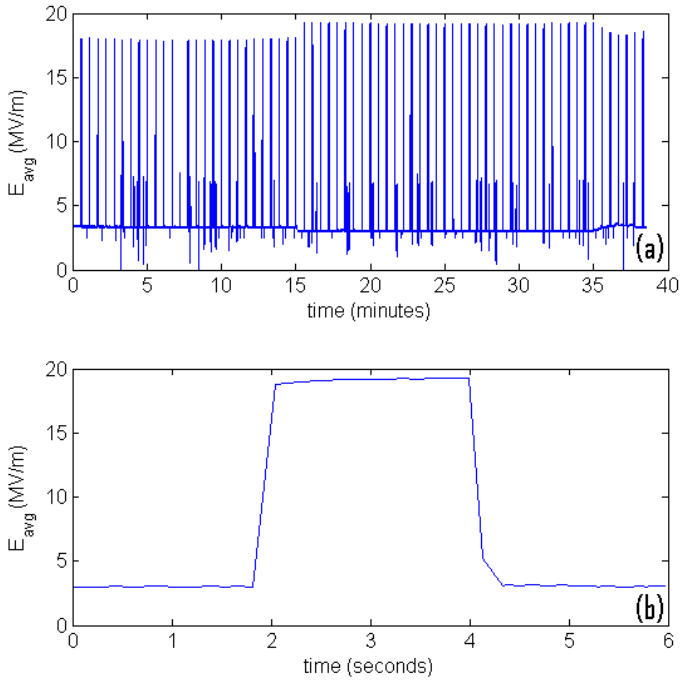

Figure 3: 5 cell cavity performance during horizontal test. Quasi CW operation: field gradient 19MV/m, pulses are 2 seconds long with a 30 second interval.

2.6.4 **Beam Commissioning Results**

2.6.4.1 ***SRF Photoinjector Beam Test Setup***

The beam commissioning of ERL SRF gun started in June 2014. The first beam test schematic setup is shown in Fig. 4. The ERL injection dipole is off during the first beam test. The current coming from the SRF gun goes straight to the faraday cup where current can be measured. Steering magnet is installed next to the laser cross. The retractable beam profile monitor (YAG crystal) is installed just before the faraday cup to measure beam size.

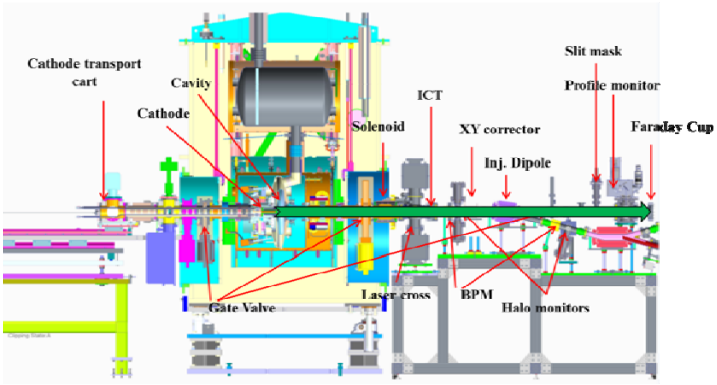

Figure 4: Schematic layout of the SRF injector at BNL R&D ERL. Instead of using HTS solenoid, normal-conductive solenoid has been installed at the exit of the gun to provide sufficient focusing.

High temperature superconductive solenoid (HTSS) is installed in 35 cm distance from the cathode has not been used due to copper leads heating up at 10A and some initial assembly problems. Normal-conductive temporary solenoid is installed between exit from the gun and laser cross. Solenoid provides sufficient focusing to let beam propagate to faraday cup.

For the first beam test, a Cs3Sb cathode was fabricated using copper substrate and QE has been measured 2E-3 in deposition chamber. During cathode stalk transfer to the gun the cathode QE significantly degraded. Additional QE reduction observed was due to usage of cathode at liquid nitrogen temperature. Final QE measured was very low value at 2.7e-5. With maximum available laser power we were able to extract only 7.7 pC per bunch and reach maximum 1uA average current (see Fig. 5).

Figure 5: Faraday cup (1MOhm termination) signal during the first beam test SRF 704 MHz SRF Gun. Gun: voltage 1.2MV, 500 msec pulses, every 1 sec. 9.38MHz Laser: 7 □sec macro pulses, every 500□sec. (Top: laser shutter closed dark current 38nA. Bottom: laser shutter open photocurent during RF pulse 1.09 uA.)

2.6.4.2 *Test Results with New Cathode Stalk*

New cathode stalk with Ta tip has been fabricated [10] (see Fig. 6). We tested 3.8% QE K2CsSb cathode in the 704MHz SRF gun. The cathode survived the gun and stalk RF conditioning well. The cathode QE inside the gun (cold) is 1%. We didn't see any QE degradation after two days of high bunch charge operation. The vacuum at the gun exit was at 10^{-9} scale during gun operation. After extracting the cathode out of the gun, the QE was still at 3.8% (measured at room temperature) [11].

1) 

2) 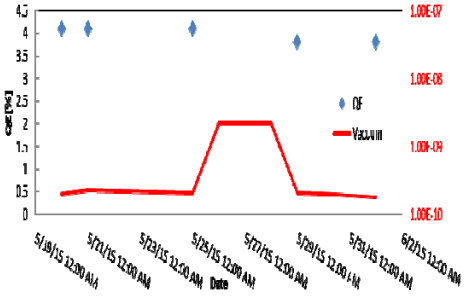

Figure 6: New cathode stalk with Ta tip. 1) Stalk has been cleaned and ready to be installed in cathode transport system. 2) QE of K2CsSb cathode deposited to new cathode stalk and vacuum measured at room temperature before beam test (4%) and after beam test (3.8%).

During the beam test bunch charge was measured by FC and ICT [12] (Fig. 7). Both measurements agreed. With new photocathode 550pC charge per single bunch has been achieved (see Fig. 8).

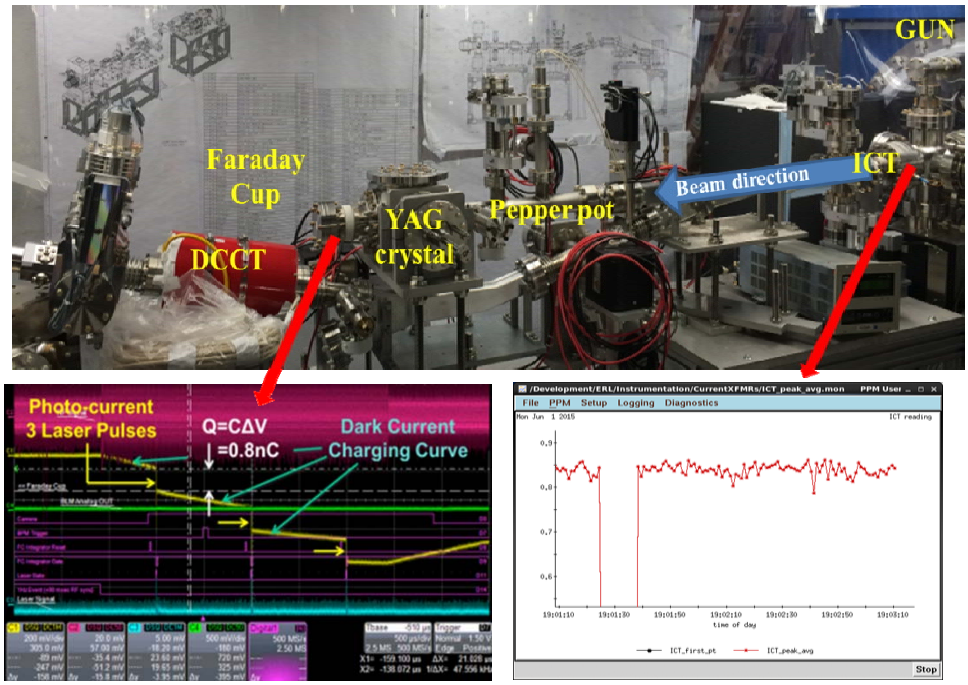

Figure 7: Straight line with beam diagnostics components (top). Dark current (slope) and photocurrent (spikes) measured one faraday cup (left bottom). Cross calibration charge measurements at ICT (right bottom).

a) 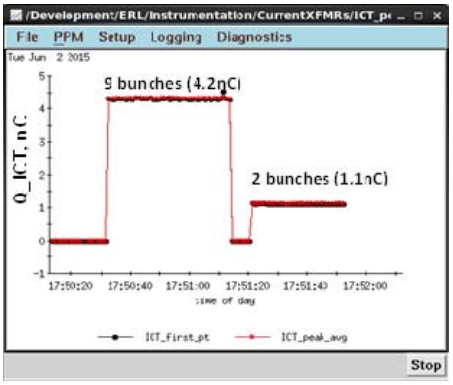

b) 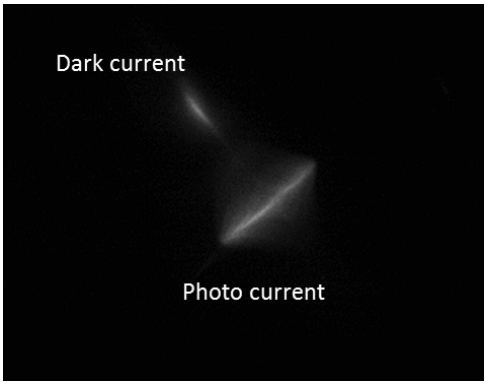

Figure 8: a) ICT signal during high charge operation of 704MHz SRF gun. Maximum charge per single bunch 550 pC. b) Dark current and photocurrent clearly observed at beam profile monitor.

With initial laser spot size at the photocathode of 2 mm FWHM, we observed saturation of the extracted charge per bunch at 200 pC. Increasing spot size to 4 mm allowed us to extract more charge with the same gun voltage and laser power (see Fig 9).

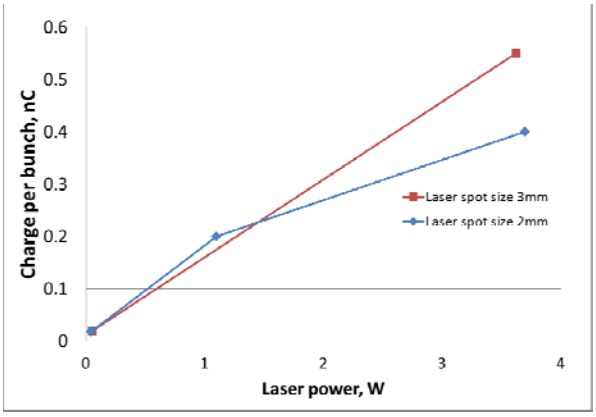

Figure 9: Charge per pulse vs laser average power. Due to space charge limitation some saturation has been observed at high average laser power (blue diamonds). In order to achieve higher charge laser spot size has been increased (red diamonds).

In order to continue the commissioning of the rest of the ERL systems we had to carry out set of fault studies to confirm that ERL block house shielding satisfies radiation safety committee requirements. Laser power has been reduced while macropulse length has been increased to 4 msec to match with maximum available RF pulse length 5 msec (see Fig. 10). The highest average current 20uA from SRF gun has been achieved (see Fig. 11).

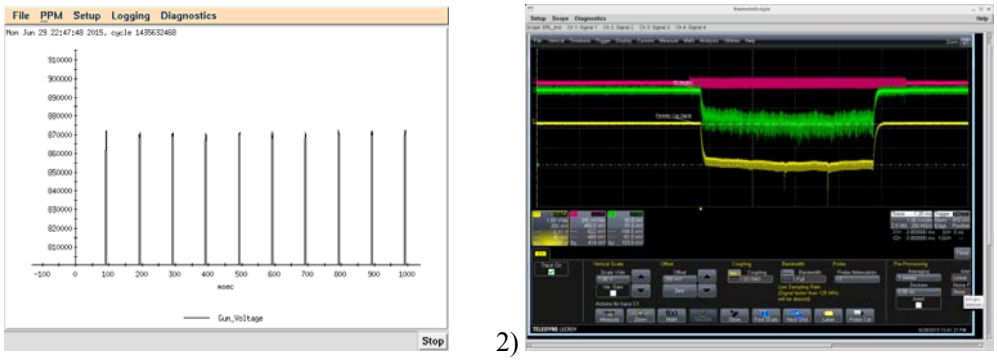

1) 2)

Figure 10: Beam time structure during fault studies.1) RF pulses structure 5 msec, 10Hz (at the top). 2) One single RF pulse 5msec (magenta), laser pulses 4msec (green) and faraday cup signal 4 msec (yellow).

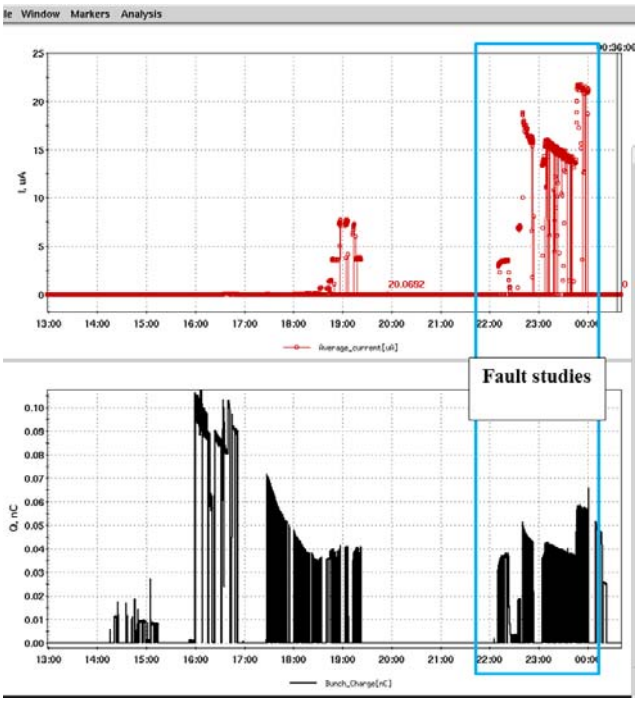

Figure 11: Average current (top) and charge per bunch (bottom) ICT measured after the gun during fault studies.

2.6.4.3 *Astigmatism and Emittance Measurements*

Instrumentation beam line is equipped with beam profile monitors YAG crystal. Several attempts have been made in order to measure emittance. The straight gun-to-FC line is axial symmetric system except RF fundamental power couplers (FPC). During solenoid scan very strong astigmatism has been observed (see Fig 12.).

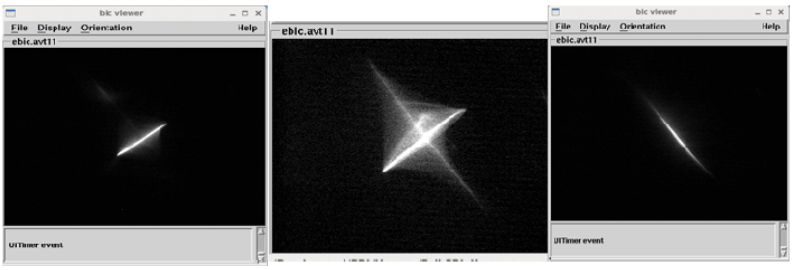

Figure 12: Beam image at beam profile monitor for three different solenoid current settings. The star-like shape can be clearly observed (middle plot).

Based on these measurements, we suspected that there is strong quadrupole focusing in the system. One of the suspects is FPC quadrupole kick. We estimated that the quadrupole with focus length of 55 cm placed in location of FPC results the same effect. This requires further investigation.

Solenoid focuses and rotates the beam. Using solenoid scan we measured normalized emittance of 2.2 μm in one plane and 1.6 μm in orthogonal plane (see Fig 13).

1) 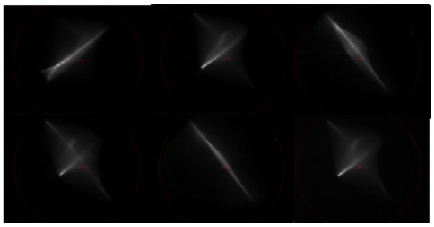

2) 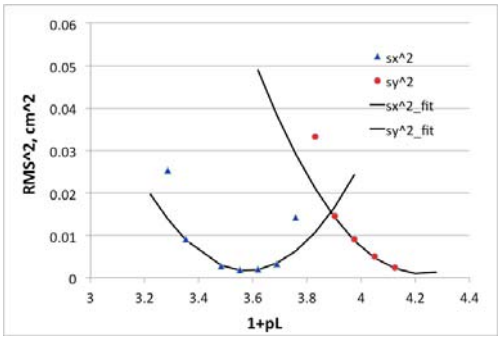

Figure 13: Solenoid scan for 130pC charge per bunch. 1) Beam images during solenoid scan.2) Beam profiles parabola fits.

2.6.4.4 *Cathode Life Time*

Due to limited supply of liquid He the cathode stalk has to be retracted from the gun at the end of each beam test day and inserted before next beam test. After the first week of testing QE droped from 1% to 0.4% (June 1-5). Applying heat to the cathode tip outside the gun recovered cathode quality (July 5). However, this procedure led to additional time spent for conditioning stalk inside the gun at liquid He temperature. With limited liquid He available for tests, any time spend for preconditioning leaves less time for beam commissioning itself. We decided to stop heating up cathode tip and used cathode as is. After that, cathode QE stayed relatively stable at level of 4e-4 (at liquid N temperature) after each cathode insertion to the gun.

By moving laser spot slightly around the cathode area with higher QE could be found (QE=3-6 e-4). History of 3 months of single cathode QE measurements in the SRF gun is presented in Fig. 14.

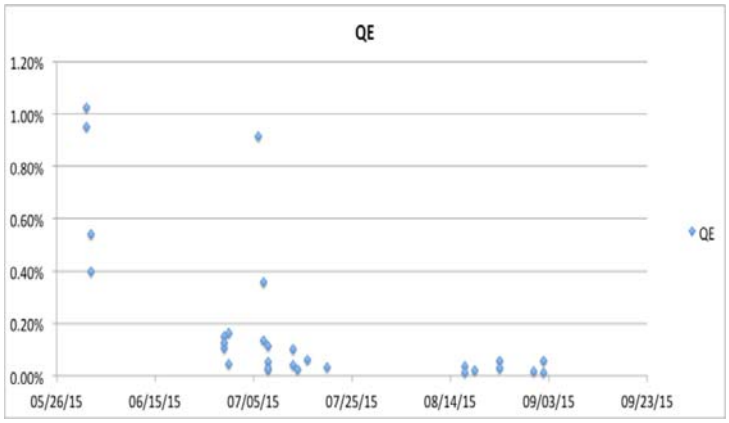

Figure 14: Photocathode cold tip QE measured inside the SRF gun at the beginning and at the end of each beam test day.

2.6.5 Gun to Dump Beam Commissioning Progress

Next stage of ERL commissioning is to transport beam through ERL injection system, 5 cell cavity linac, the extraction system, and then to the beam dump. Schematic of gun to dump commissioning stage is shown in Fig 15.

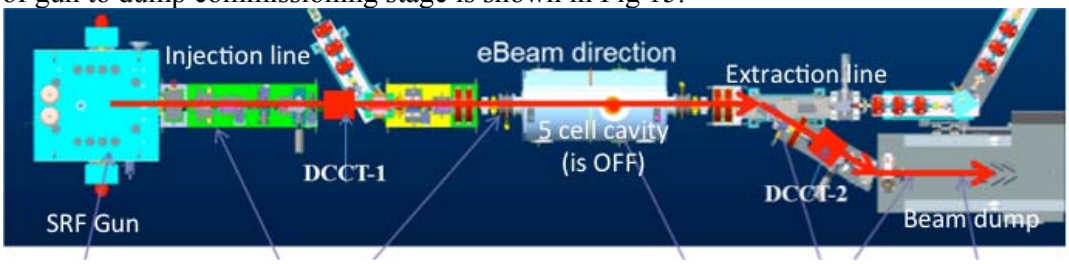

Figure 15: Gun to dump commissioning set up**.**

During the gun to dump stage of ERL commissioning 5cell cavity stays off. Two DCCTs (Fig 16) and beam dump measure beam transport efficiency at three locations: injection line, extraction line, and the beam dump.

During gun to dump beam tests we will continue commissioning and calibration of beam instrumentation: beam position monitors (BPM), DCCTs, and beam loss monitor (BLM) system.

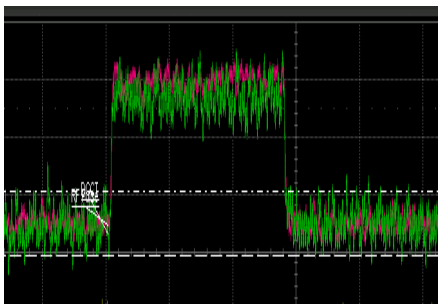

Figure 16: Beam current measured by injection line DCCT (magenta) and by extraction line DCCT (green). 90% transport efficiency has been achieved.

2.6.6 **Summary and Plans**

An ampere class 20 MeV superconducting Energy Recovery Linac (ERL) is presently under commissioning at Brookhaven National Laboratory (BNL) for testing of concepts relevant to high-energy electron cooling and electron-ion colliders. Beam commissioning started in July, 2014.

The first photo current from ERL SRF gun has been observed in November 2014 (1 uA per 500msec RF pulse).

New "multipactor free" Ta tip cathode stalks conditioned for CW in March, 2015. ERL returning loop components installation was completed in May, 2015. QE with Ta cathode tip: at room temperature measured 4% , in gun 1%.

The first test with new cathode took place in June, 2015. The highest charge from SRF gun .55 nC has been achieved. Max average current from this gun 20 uA has been was demonstrated.

The Gun to dump beam commissioning is under way. The 85% gun to dump transport efficiency has been achieved in July 2015. The ceramic shielding for beam instrumentation has been designed and will be installed in December 2015.

The ERL loop commissioning is scheduled for beginning of 2016.

After ERL commissioning in BLDG912 the ERL components will be relocated to RHIC IP2 to be used for low energy RHIC electron cooler (LEReC) [13].

2.6.7 **Acknowledgments**

We would like thank you BNL R&D ERL team: Z. Altinbas, D. Beavis, S. Belomestnykh, I. Ben-Zvi, S. Deonarine, D.M. Gassner, R. C. Gupta, H. Hahn, L.R. Hammons, Chung Ho, J. Jamilkowski, P. Kankiya, N. Laloudakis, R. Lambiase, V.N. Litvinenko, G. Mahler, L. Masi, G. McIntyre, T.A. Miller, J. Morris, D. Phillips, V. Ptitsyn, T. Seda, B. Sheehy, L. Smart, K. Smith, T. Srinivasan-Rao, A.N. Steszyn, T. R. Than, E. Wang, D. Weiss, Huamu Xie, Wencan Xu, A. Zaltsman and all people at the Collider-Accelerator Department of BNL who are actively working on the R&D ERL project.

This work is supported by Brookhaven Science Associates, LLC under Contract No. DE-AC02-98CH10886 with the U.S. DOE.

2.6.8 **References**

1. I. Ben-Zvi et al., Extremely High Current, High Brightness Energy Recovery Linac, PAC2005.
2. D. Kayran et al., First Test Results from SRF Photoinjector for the R&D ERL at BNL. IPAC'14, pp. 748-750.
3. Wencan Xu, et al., First beam Commissioning at BNL ERL SRF gun, IPAC'2015, pp 1941-1943.
4. D. Kayran et al., Status of High Current R&D Energy Recovery Linac at BNL, PAC'11, pp. 2148-2150.
5. E.Wang et al., Fabrication of alkali antimonite photocathode for SRF gun, IPAC2014, pp. 742-744
6. Wencan Xu et al., Commissioning SRF gun for the R&D ERL at BNL, IPAC2013, pp. 2492-2494.
7. V.N. Litvinenko, R. Hajima, D. Kayran, NIMA557, (2006) pp 165-175.
8. B. Sheehy et al., BNL 703 MHz Superconducting RF cavity testing, PAC'11, pp. 913-

915.
9. D. Kayran et al., Optics for High Brightness and High Current ERL Project at BNL, PAC 2005, pp. 1775- 1777.
10. Wencan Xu, et al., Multipacting-free quarter-wavelength choke joint design for BNL SRF gun, IPAC'2015, pp 1935-1937.
11. E. Wang, et al., Characterization of Multi-alkali Antimonide Cathode at Cryogenic Temperatures and its Performance in SRF Gun. TUICLH1027, ERL2015 in preparation.
12. T. Miller, et al., Current Measurement and Associated Machine Protection in the ERL at BNL. WEIALH248, ERL2015 in preparation.
13. J. Kewisch, et al., ERL for Low Energy Electron Cooling at RHIC (LEReC). WEICLH1058, ERL2015 in preparation.

2.7 FFAG's in ERLs

Stephen Brooks, Dejan Trbojevic, and Scott J. Berg
Brookhaven National Laboratory, Upton, New York, 11973
Mail to: dejan@bnl.gov brooks@bnl.gov jsberg@bnl.gov

2.7.1 Introduction

The revival of scaling Fixed Field Alternating Gradient (S-FFAG) accelerators in the recent two decades is very evident. They were previously developed in the 1950s, independently by Keith R. Symon, Tihiro Okhawa, and Andrei Kolomenski [1,2,3]. They have a very large momentum acceptance with beams accelerated within a constant magnetic field that varies across the aperture according to the scaling law $B_R \sim B_o(r/r_o)^k$, where k should be as large as possible (k~150). S-FFAGs have mostly been built in Japan: initially with the proof of principle (POP) proton accelerator at KEK, followed by the 150 MeV proton accelerator (presently at the Kyushu University), the 150 MeV accelerator at Osaka University, and many smaller size electron S-FFAGs built for different applications such as food processing. Although S-FFAGs have the advantages of fixed magnetic fields, zero chromaticity and fixed tunes, synchrotrons are still the dominant accelerators in spite of their requirement of pulsed magnets. This is mostly due to significantly smaller aperture requirements: a few cm in synchrotrons compared to ~1 m for S-FFAGs, where large aperture magnets have to accommodate the orbit offsets. The author (Trbojevic) came to the concept of non-scaling FFAGs (NS-FFAGs) [4] by trying to reduce the required aperture of the S-FFAG by following the synchrotron light source lattice designed for minimum beam emittance. There was a publication by C. Johnstone a few months earlier about a FODO cell NS-FFAG [5]. Light sources require the smallest possible beam emittance, obtained by the minimizing the dispersion action $<H>$ integral [6, 7, 8]. This corresponds to searching for the smallest value of the dispersion function at the largest bending element. The connection to aperture size becomes evident from the definition of dispersion: the orbit offset $\Delta x = D_x \, \delta p/p$, where D_x is the dispersion function, while $\delta p/p$ is the momentum offset. If the dispersion is of the order of a few centimeters (~3-4 cm) the orbit offsets will be ± 15-20 mm for $\delta p/p$ =±50 % or a total energy range of 3 times for relativistic particles. An additional important novelty in the NS-FFAG is that the magnetic field is a linear function across the aperture in contrast to the non-linear radial field variation required in S-FFAGs. All magnets are linear combined function magnets. Abandoning the scaling

law makes the tunes vary with energy, as well as the chromaticity. The time of flight is a parabolic-shaped function of energy. The minimum horizontal beta function is found at the middle of the bending element, as it is in the light source lattices, and this is the place where the orbit offsets are smallest, being the minimum of the dispersion function. The largest orbit offsets are in the focusing element together with the maximum of both the horizontal betatron function and dispersion function. The first NS-FFAG proof of principle machine was built and tested at Daresbury Laboratory [9].

2.7.1.1 *First Non-scaling FFAG Combined with an Energy Recovery Linac*

The present relativistic heavy ion collider (RHIC), made of two superconducting rings, has been very successfully colliding a large variety of ion combinations like fully stripped gold ions (Au^{79+}-Au^{79+}), polarized protons on polarized protons, protons with gold, deuterons with gold, fully stripped Uranium with Uranium and so on. During the last fifteen years of running it has produced tremendous results: discovering the perfect liquid state of quark-gluon plasma in heavy ion collisions, and the contributions from quarks and gluons to the proton spin. RHIC produces ultra-relativistic heavy ion collisions and obtains results that shed light on the fundamental theory of the strong interaction of Quantum Chromodynamics. These theories provide qualitative and even quantitative insight into a wealth of remarkable phenomena observed in nucleus-nucleus or deuteron-nucleus collisions at RHIC, like the suppression of particle production and azimuthal correlations at forward rapidities, the energy and centrality dependence of the multiplicities, the ridge effect, the limiting fragmentation, jet quenching, or the di-jet asymmetry.

The design of the future electron ion-collider eRHIC is based on an energy recovery linac (ERL) using the existing RHIC tunnel together with one of the two superconducting hadron rings for accelerating polarized protons, ^{3}He, deuterons and heavy ions. The polarized electron beam, created by the polarized electron source and 20 MeV injector, will accelerate through the superconducting linac twelve times (or 13 times if an additional separate beam line for collisions is used). The electron beam will gain the maximum energy of 20 GeV before it collides with either polarized protons, with an energy of up to 250 GeV, or ^{3}He or heavy ions at 100 GeV/u. After collisions, the electron energy is recovered as the electron passes through the linac twelve more times 180 degrees out of phase, being decelerated down to the initial energy and brought the dump. To reduce the maximum linac energy and the number of beam lines for bringing electrons of different energy back to the linac, we accepted the NS-FFAG concept using only two beam lines. This is possible as each NS-FFAG can transfer beams with an energy ratio of up to four times within a small aperture not much different from that of a synchrotron. This solution allows beam transport from the linac around the present RHIC tunnel and back to the linac during the acceleration process.

2.7.1.2 *Layout of the eRHIC: ERL, Spreaders/Combiners, Arcs and Straight*

The eRHIC layout is shown in Fig. 1: the 1.665 GeV linac (upper right with a magnified picture of the cryo-module) is in the 2 o'clock straight section of RHIC, together with an injector and polarized electron source (the Gatling gun is shown on the right of Fig. 1). From the linac, spreaders (layout upper middle in Fig. 1) bring the electron beam to the low and high-energy NS-FFAG beam lines (red arcs in Fig. 1). Multiple electron energies from the arcs are merged into the straight section (process

shown in Fig. 6). The coherent electron cooling is placed in the 10 o'clock straight section (upper left in Fig. 1). The schematic picture of the two NS-FFAG beam lines is shown in upper left corner, while the orbits in the basic arc cells of the low and high energy are shown in the middle left side of the Fig. 1. The magnets of the Interaction Point are shown on the lower middle of Fig.1. The magnified picture of the detector is shown at the center of Fig. 1. Only one "blue" ion beam line is injected clockwise in the lower middle part of Fig. 1. Electrons are traveling counter clockwise in the "red" beam line and are extracted into a separate line before the two detectors, shown schematically as a dotted red line. They are brought back to the NS-FFAG arc as they continue with a phase difference of 180 degrees through the NS-FFAG beam line going back to the linac to be decelerated.

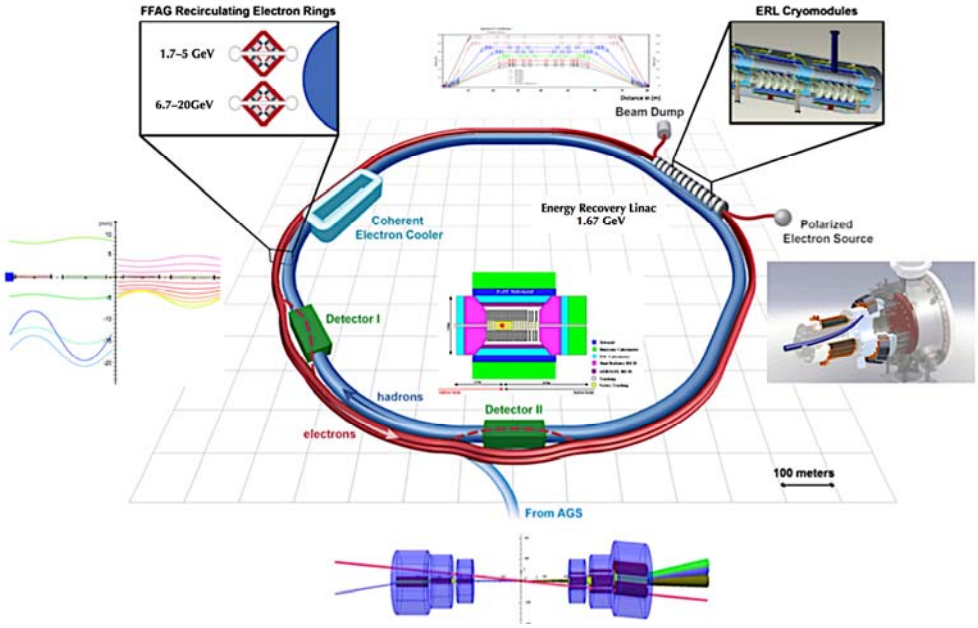

Figure 1: Layout of eRHIC: Linac (upper right corner), Injector, spreaders or combiners (upper middle), Coherent Electron cooling (upper left corner), Detectors (green), IP interaction point (lower middle), arcs and straight section.

2.7.1.3 *Basic NS-FFAG Arc Cell*

There are two NS-FFAG beam lines: one for the low-energy range 1.685 – 5.015 GeV with three passes, and a second one for the high-energy range from 6.685 – 20.0 GeV,

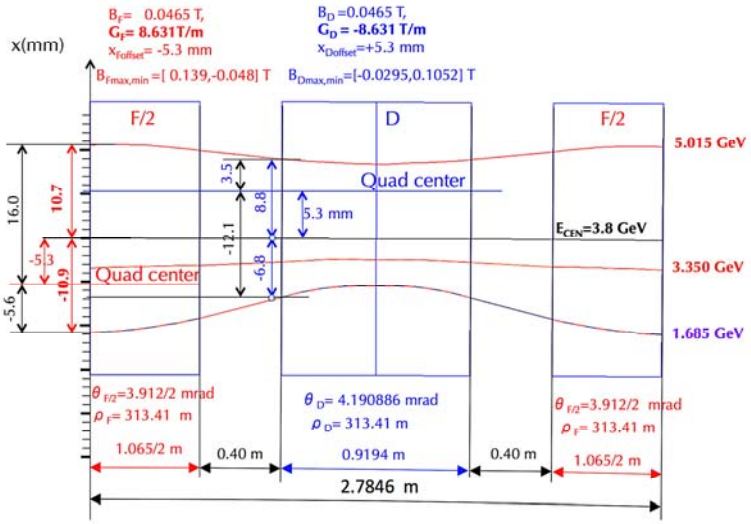

Figure 2: Magnets and magnified orbits in the basic cell of the low-energy beam line.

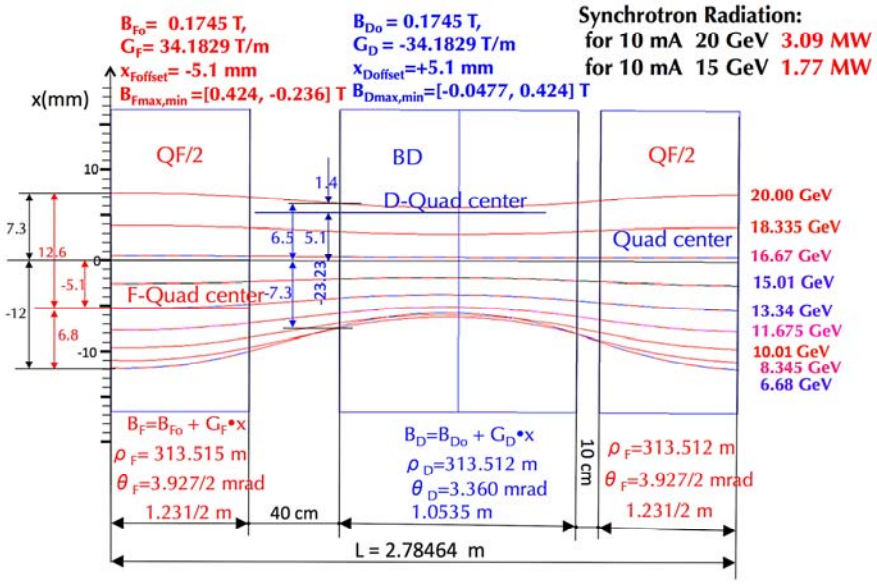

Figure 3: Magnets and magnified orbits in the basic cell of the high-energy beam line.

with nine passes, making a total of twelve passes through the linac during acceleration. The basic cell is a doublet with combined function magnets made of displaced focusing and defocusing quadrupoles. The combined function magnets can be made of displaced quadrupoles as their displacement relative to the beam is very small due to the large bending radius ~320 m.

2.7.1.4 *Tune vs. Momentum Dependence in the Basic Cells*

The tune variation as a function energy for the eRHIC low and high-energy NS-FFAG cell is shown in Fig. 4.

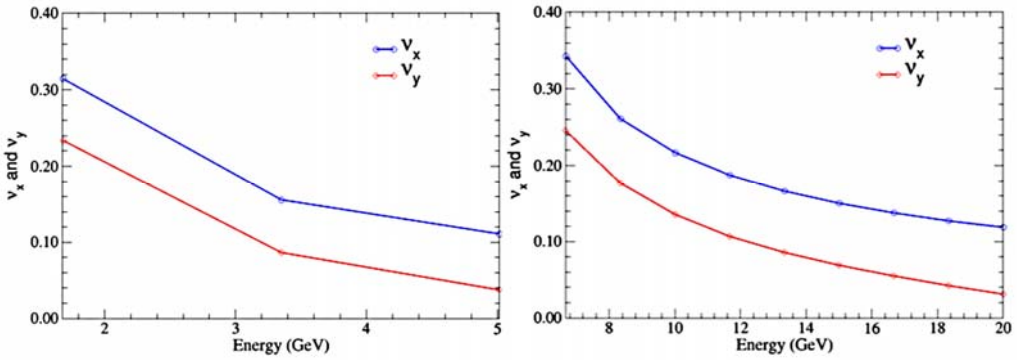

Figure 4: Tune dependence on energy for the low and high-energy cells.

2.7.1.5 *Time of Flight Dependence on Energy*

The time of flight for the two NS-FFAG beam lines is shown in Fig. 5.

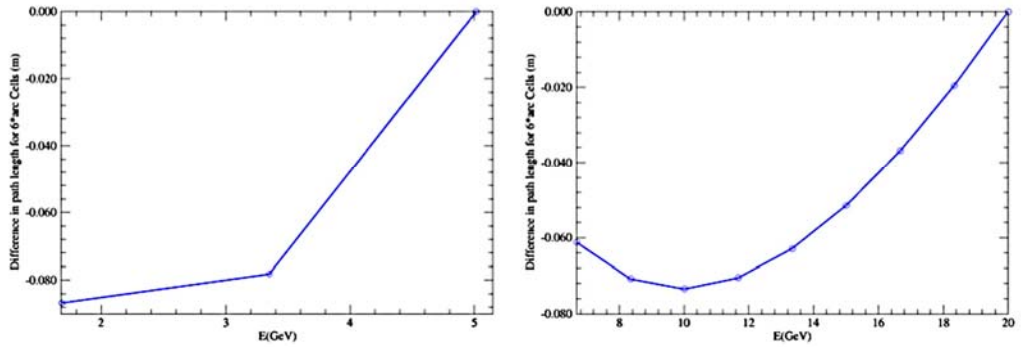

Figure 5: A difference in orbit time of flight or path length in the six FFAG arcs, for the low energy 1.685-5.015 GeV (left figure) and the high energy 6.8-20 GeV (right figure).

2.7.1.6 *Cell Optimization to Minimize the Synchrotron Radiation*

The electron beam emits synchrotron radiation whenever it is bent in the magnets. The synchrotron radiation loss power is proportional to $\sim B^2E^2$. A first reaction during the basic cell design is to make the orbit circular for the highest electron energy. But as the highest energy beam passes the NS-FFAG only once, while all other energies pass the same magnets twice: first during acceleration and the second time during deceleration, it is clear that optimization needs to be done quite differently. As it could be noticed in Fig. 3 the orbits in the basic cell are further apart in the focusing element. It is desirable to have the smallest magnetic field for the highest energies in the focusing element as the magnetic field could be presented as $B_F = B_{Fo} + G_F * x_{max}$.

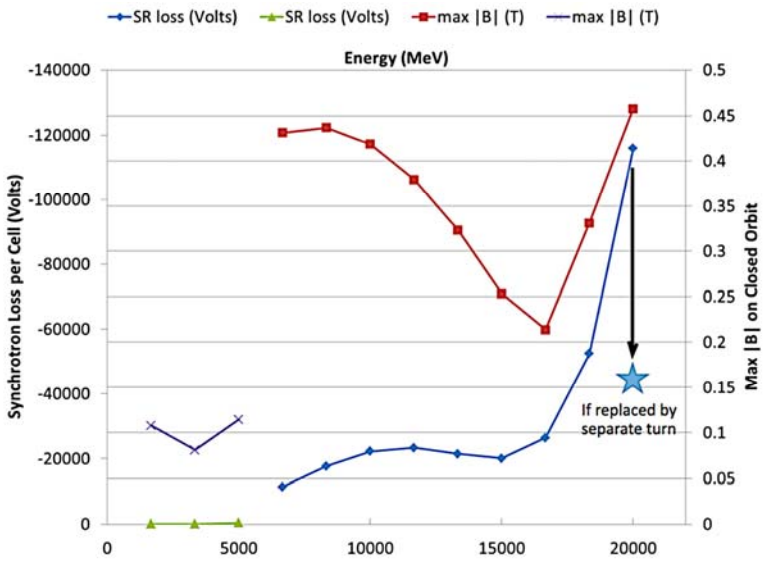

Figure 6: Synchrotron radiation loss for all energies.

The smaller the gradient GF the smaller the effect of the largest orbit offsets on synchrotron radiation loss is. This indicates that it is preferable to have longer focusing than the defocusing magnet as the maximum if the magnetic field of the defocusing magnet is at the radially inward part of the orbits as: $B_D = B_{Do} + G_D * \square x_{max}$ as the G_D has a negative sign. The optimized synchrotron radiation for all energies is shown in Fig. 7.

2.7.1.7 *Matching the NS-FFAG Arcs with Straight Sections and Bypasses*

There was a previous conceptual proposal for a racetrack Recirculating Linac Accelerator (RLA) using the NS-FFAG [10] for muon acceleration with Halbach permanent magnets. In that proposal the two straight sections were partially matched to the NS-FFAG arcs. A very successful matching of the NS-FFAG arcs to the straight sections, for all electron beam energies, has been developed for eRHIC by Stephen Brooks as shown in Figs. 7 and 8. The two NS-FFAG beam lines, placed in the existing RHIC tunnel, follow the curvature of the existing superconducting hadron beam line. The RHIC tunnel has six ~200-meter long straight sections the lines have to match. The straight section design provided the basis of the bypass design of the NS-FFAG beam lines around detectors (Fig. 9), as only the highest energy is taken away to collide with hadrons, leaving the other energies in the FFAGs that must bypass the detector.

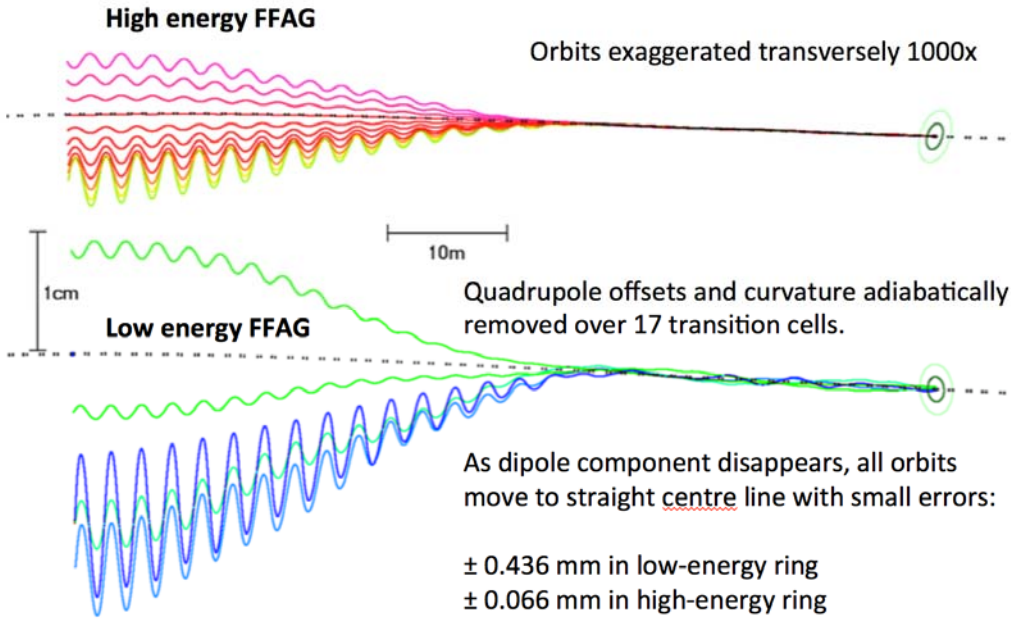

Figure 7: Matching the NS-FFAG arcs to the straight sections.

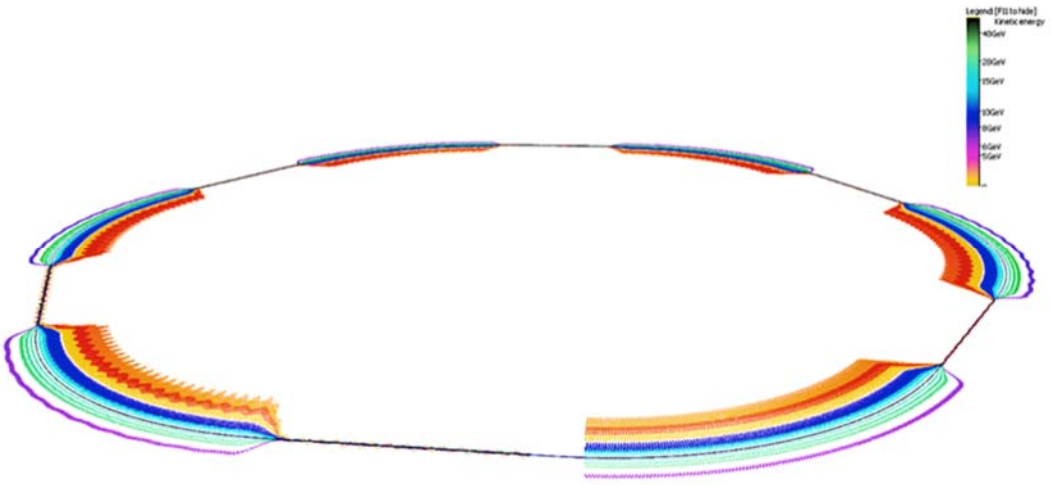

Figure 8: Straight sections and arcs' orbits magnified x1000.

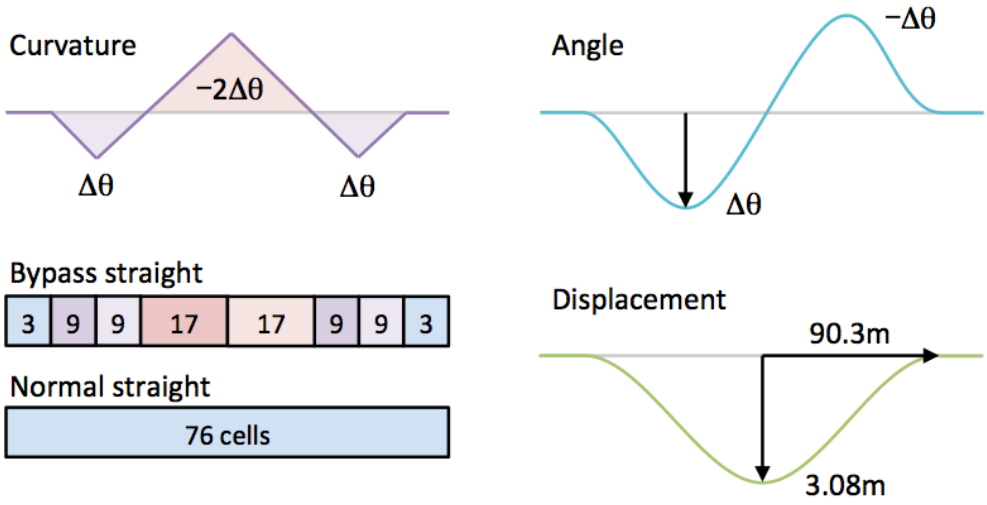

Figure 9: Principle of the bypass around the detectors.

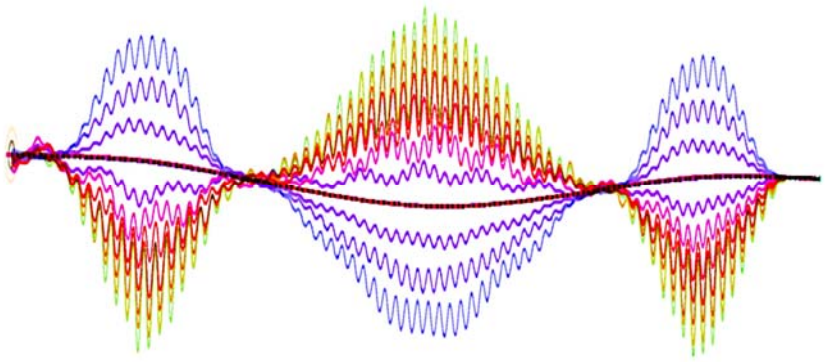

Figure 10: Details of the magnified x1000 orbits in the bypass around detectors in eRHIC.

2.7.1.8 *Effect of the Misalignment, Gradient, Magnetic Field Errors, Energy and Chromatic effects on the Orbit Stability and Correction Methods*

We have done extensive studies on the effect of misalignment and magnetic field errors on the orbit position (as shown in Fig. 11) and ways to correct them with an orbit and gradient correction system. There is a very clear magnification factor of 50-80x on the orbit errors depending linearly on the *rms* misalignment errors. The orbit correction was implemented in a couple of different ways: the RHIC orbit correction program was used with the initial assumption of having one horizontal, vertical, and one gradient corrector per cell. This was then replaced with one horizontal, vertical, and gradient corrector every two cells. After the correction was performed for the lowest energy it was continued with higher energies. The system is over determined as the magnetic

field is the same for all electron energies. The orbit correction mentioned is shown in Figure 12.

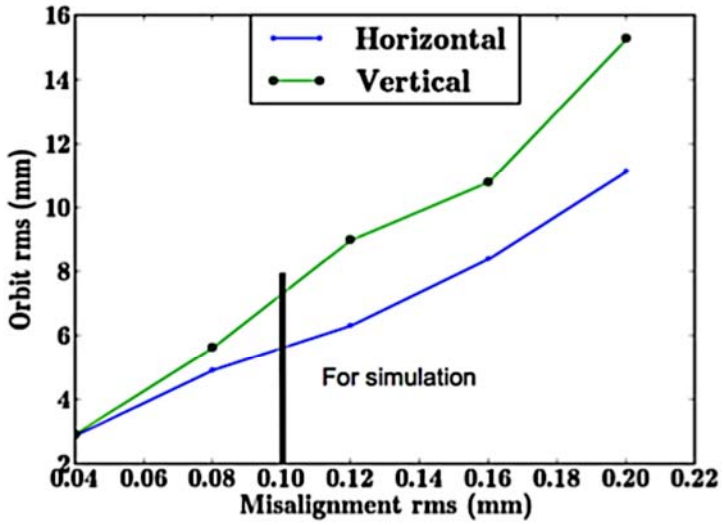

Figure 11: Magnification factor on the orbit due to misalignment errors (from Chuyu Liu).

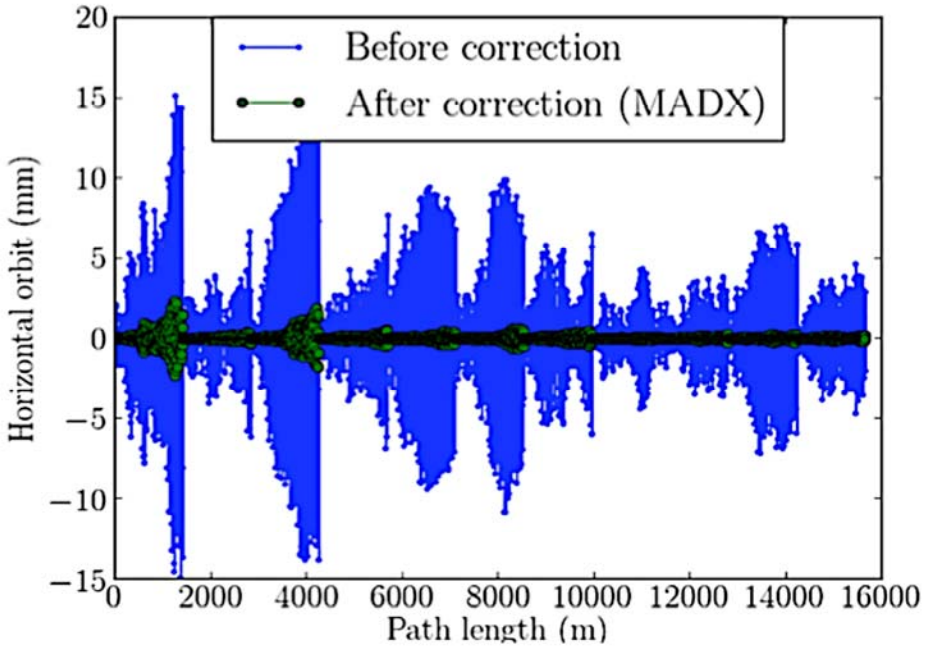

Figure 12: First iteration of the over-determined orbit correction system. It is over-determined as the magnetic field is the same for all energies in a BPM (from Chuyu Liu).

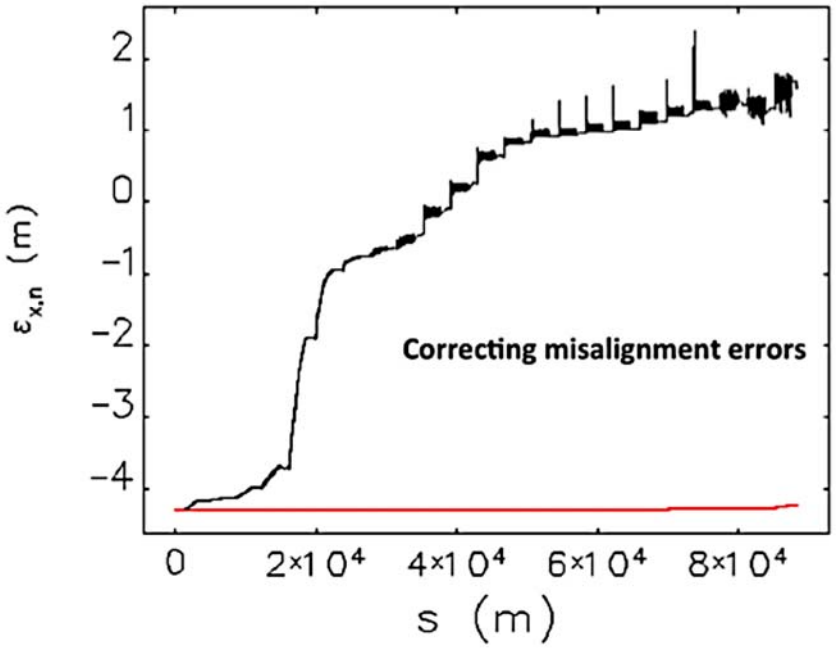

Figure 13: Emittance blow up due to misalignment and after correction (from Yue Hao).

2.7.2 **Magnet Design and Prototyping**

The eRHIC NS-FFAG magnets will use permanent magnet material. There was previous experience with permanent magnets used for the anti-proton storage ring placed in the Main Injector at Fermi National Laboratory. They had used passive temperature compensation of the permanent magnet with a material with opposite temperature dependence [11]. We have a couple of different approaches to the permanent magnet design: iron-dominated magnets with permanent magnet material SmCo or NdFeB designed by Wuzheng Meng (Fig. 14) and Holger Witte (Figs. 15 and 16), and Halbach type designs by Nick Tsoupas and Stephen Brooks (Fig. 17 and 18). Magnets are required to have an open aperture in the horizontal plane due to synchrotron radiation. In the case of Halbach magnet design this was accomplished by breaking the symmetry in both vertical and horizontal planes and displacing the Halbach elements in such a way that the 12 pole is reduced to a minimum. In the case of iron dominated magnets the permanent magnet material was placed in two different ways relative to the iron that allow an open horizontal plane as shown in Figs. 14 and 15.

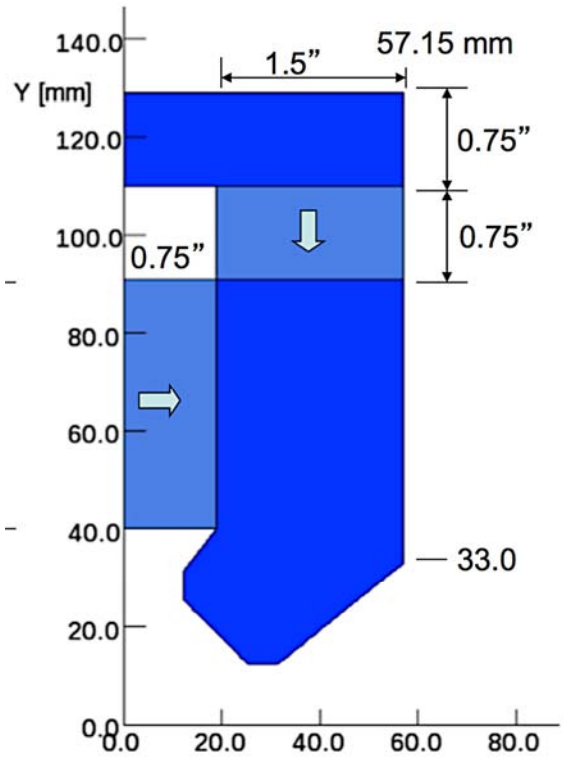

Figure 14: Iron dominated magnet with permanent magnet material (from Wuzheng Meng).

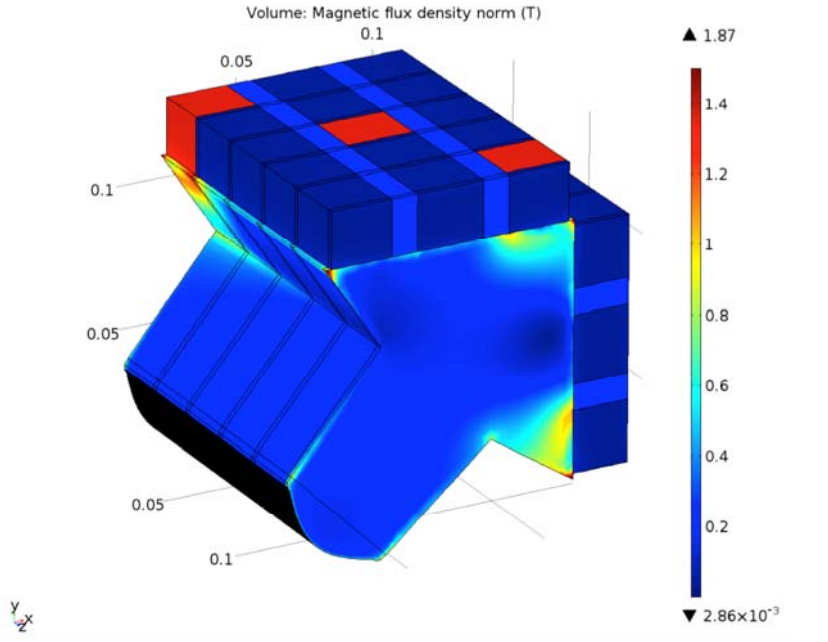

Figure 15: Second iron dominated magnet (from Holger Witte).

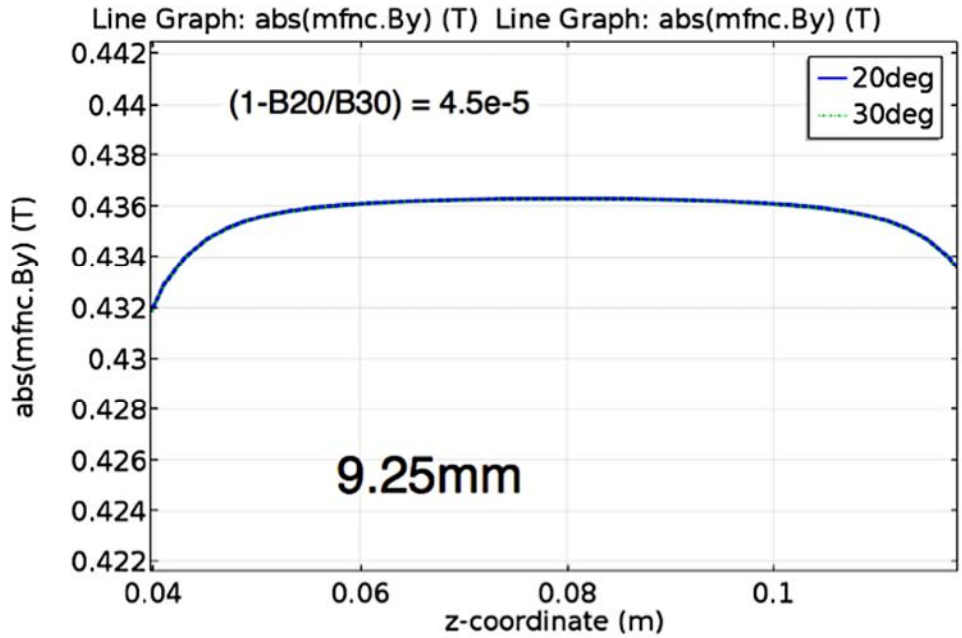

Figure 16: Temperature compensation of the iron dominated magnet (from Holger Witte).

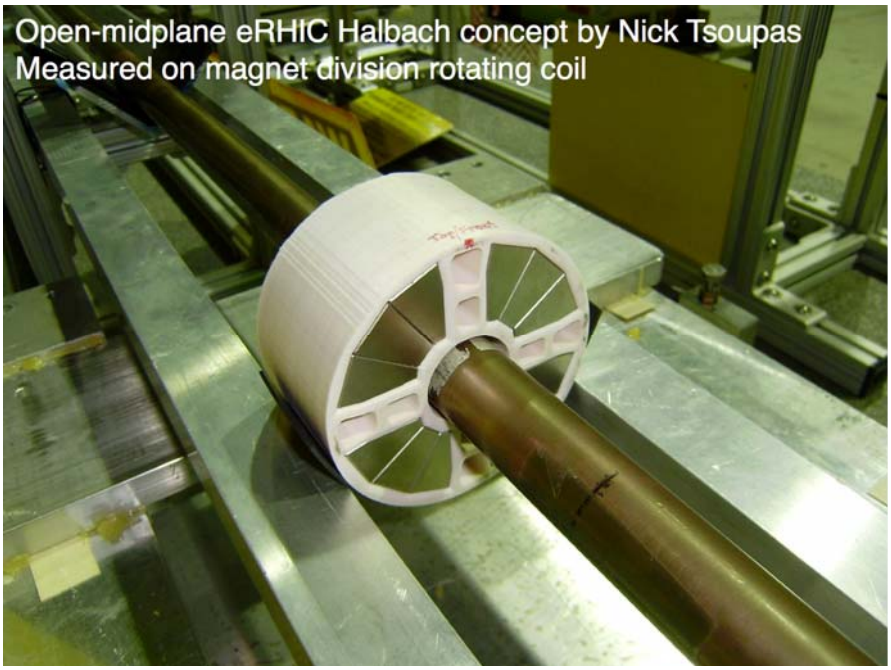

Figure 17: Magnetic measurements of the Halbach type magnet considered for eRHIC (from Nick Tsoupas and Stephen Brooks).

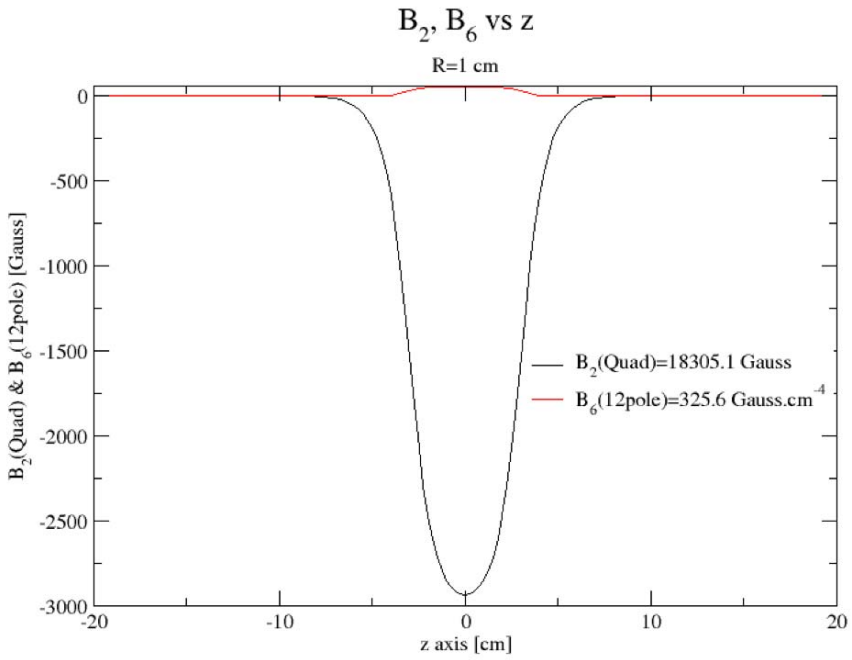

Figure 18: Three-dimensional magnetic field obtained by OPERA for the Halbach magnet (from Nick Tsoupas).

2.7.3 References

1. T. Ohkawa, University of Tokyo, Tokyo, Japan, FFAG structure suggested earlier at a Symposium on Nuclear Physics of the Physical Society of Japan in 1953 (private communication).
2. K. R. Symon, D.W. Kerst, L.W. Jones, L. J. Laslett, and K. M. Terwilliger, Phys. Rev. 103, 1837 (1956).
3. A. Kolomensky et al., Zh. Eksp. Teor. Fiz. 33, 298(1975).
4. D. Trbojevic, E. D. Courant, A.A. Garren. 1999-Presented at the High Energy Muon Colliders workshop in Montauk HEMC, published by AIP, Woodbury, New York, USA (2000). http://scitation.aip.org/content/aip/proceeding/aipcp/10.1063/1.1361693
5. C. Johnstone, et al., "Fixed Field Circular Accelerator Designs", PAC'99, New York, P. 3068. http://ieeexplore.ieee.org/stamp/stamp.jsp?tp=&arnumber=792155
6. S. Machida, "Fixed field alternating gradient" - arXiv preprint arXiv:1302.2026, 2013 - arxiv.org
7. D. Trbojevic and E. Courant, Proc. of the European Particle Accelerator Conference, 1994, p. 1000.
8. D. Trbojevic, J.S. Berg, M. Blaskiewicz, E.D. Courant, R. Palmer and A. Garren, Proc. of the Particle Accelerator Conference, 2003, p. 1816.
9. Acceleration in the linear non-scaling fixed-field alternating-gradient accelerator EMMA - Machida, S. *et al.* Nature Phys. 8 (2012) 243-247 FERMILAB-PUB-12-308-AD
10. Dejan Trbojevic, RLA with FFAG arcs, Muon Collider Design Workshop, Dec 1-3, 2009. Racetrack NS-FFAG with Halbach permanent magnets.
11. James Volk, "Permanent Magnet Work at Fermilab 1995 to Present", Fermilab Internal note.

2.8 Transverse Emittance Preserving Arc Compressor

Simone Di Mitri
Elettra – Sincrotrone Trieste S.C.p.A., S.S.14 km163,5 in Area Science Park,
Trieste, I-34149
Mail to: simone.dimitri@elettra.eu

2.8.1 Introduction

The advent of short electron bunches in high brightness linear accelerators has raised the awareness of the accelerator community to the degradation of the beam transverse emittance by coherent synchrotron radiation (CSR) emitted in magnetic insertions for bunch length compression. Beam optics control has been proposed to mitigate that CSR effect. In this article, we follow the findings presented in [1,2] in order to review the linear optics approach in a periodic, locally achromatic arc compressor. We study the dependence of the CSR-perturbed emittance on beam optical functions, mean energy, and bunch charge. The analytical expectations are compared with particle tracking runs. We thereby identify a range of parameters that allows feasibility of an arc compressor for driving, for example, a free electron laser or a linear collider. Application to a recirculating linac-based free electron laser is discussed with some detail.

2.8.2 CSR Kicks in a Linear Optics Model

2.8.2.1 *Theoretical Background*

Linear optics analysis in the presence of CSR kicks was introduced in [3]. It considers the effect of CSR on the particle transverse motion through the first order energy dispersion only. This may be justified if the kick (i.e., change in particle's transverse momentum) provided by the radial forces associate to the CSR field [4], is much smaller than the CSR-induced chromatic kick. This is actually the case for the compressed beam parameters considered in this article, as well as for many realistic cases of ultraviolet and x-ray free electron laser (FEL) linac drivers. The effect of radiation shielding by the vacuum chamber [5,6] can be neglected as long as the wavelength at which CSR starts being suppressed, $\lambda \geq 2g(g/\rho)^{1/2}$ (g is the vacuum chamber gap and ρ the bending radius), is longer than the compressed electron bunch length, σ_z. In the present article, we will consider practical situations in which $\lambda \geq 1$mm and $\sigma_z \leq 0.1$ mm. Particles' motion is linear in the particle betatron coordinates, which implies preservation of the particle Courant-Snyder (C-S) invariant and of the beam rms emittance in between consecutive kicks. This assumption may be invalidated in practice by geometric and chromatic optical aberrations, which may affect the rms emittance in the presence of strong quadrupole and sextupole gradients, and large energy spread. Finally, the CSR chromatic kick is concentrated in the middle of the dipole magnet, and in fact the dipole is treated as a thin lens. The latter point was shown in [7] to be a limitation for the evaluation of the optics solution that minimizes the CSR emittance, and the analysis was extended in that work to take into account the evolution of the CSR wakefield along the dipole magnet:

$$\begin{pmatrix} \Delta x_{CSR} \\ \Delta x'_{CSR} \end{pmatrix} = \begin{pmatrix} \rho^{4/3} k(\theta - \sin(\theta)) \\ \rho^{1/3} k(1 - \cos(\theta)) \end{pmatrix} = \delta_{CSR} \begin{pmatrix} \rho\left(1 - \dfrac{\sin(\theta)}{\theta}\right) \\ \dfrac{1-\cos(\theta)}{\theta} \end{pmatrix} \tag{1}$$

We adopted in Eq.1 the same notation than in [7], where ρ is the dipole bending radius, $\delta_{CSR}=\rho^{1/3}k\theta$ is the particle relative energy deviation induced by CSR after a bending angle θ, and $k=0.2459 r_e Q/(e\gamma\sigma_z^{4/3})$ is the CSR kick factor, which is function of the number of electrons per bunch Q/e, the electron classical radius r_e and the energy Lorentz factor γ. k relates the transverse CSR effect to the rms bunch length σ_z, and applies to a Gaussian longitudinal charge distribution emitting CSR in the steady-state regime. In general, a different dependence of k on σ_z could be considered for different current profiles [8].

Eq.1 can be used to evaluate the single particle C-S invariant along an arbitrary beamline: the effect of a CSR kick is added with the prescription $x \rightarrow x + \Delta x_{CSR}$, $x' \rightarrow x' + \Delta x'_{CSR}$ [3]. The particle coordinates are then propagated through the beamline, in the absence of kicks, with the standard transfer matrix given in terms of the beamline Twiss parameters β and α (in the plane of interest):

$$\begin{pmatrix} x \\ x' \end{pmatrix}_{s_1} = \begin{pmatrix} \sqrt{\dfrac{\beta_1}{\beta_0}}(\cos\Delta\mu + \alpha_0 \sin\Delta\mu) & \sqrt{\beta_0\beta_1}\sin\Delta\mu \\ \dfrac{\alpha_0 - \alpha_1}{\sqrt{\beta_0\beta_1}}\cos\Delta\mu - \dfrac{1+\alpha_0\alpha_1}{\sqrt{\beta_0\beta_1}}\sin\Delta\mu & \sqrt{\dfrac{\beta_0}{\beta_1}}(\cos\Delta\mu - \alpha_1\sin\Delta\mu) \end{pmatrix} \begin{pmatrix} x \\ x' \end{pmatrix}_{s_0} \tag{2}$$

In Eq.2, $\Delta\mu$ is the betatron phase advance between the longitudinal location s_0 and s_1 in the beamline. The single particle invariant is $J = \beta x'^2 + 2\alpha x x' + \left(\dfrac{1+\alpha^2}{\beta}\right)x^2$.

The more accurate expression for the CSR kick cumulated over a non-zero dipole length, see Eq.1, was borrowed in [1] to extend the revised optics balance to the case of varying bunch length in an arc compressor; we recall that treatment in the next Section. Clearly, the constraint of identical CSR kicks (in module) at different dipole magnets falls short there, because the bunch length is compressed along the line.

2.8.2.2 *Periodic and Locally Achromatic Arc Compressor*

The periodic, achromatic 180 deg arc compressor introduced in [1] is made of 6 identical DBA cells. The single DBA magnetic lattice and its periodic optics solution is shown in Fig.1. At first, we focus on the single DBA cell and write down the particle coordinates at the end of the second dipole:

$$\begin{cases} x_3 = -\rho^{4/3}k_1(\theta C_\theta - 2S_\theta) + \rho^{4/3}k_2(\theta C_\theta - 2S_\theta) \\ x'_3 = -\rho^{1/3}k_1\theta S_\theta - \rho^{1/3}k_2\theta S_\theta - \dfrac{2\alpha_2}{\beta_2}\rho^{4/3}k_1(\theta C_\theta - 2S_\theta), \\ \delta_3 = \rho^{1/3}k_1\theta + \rho^{1/3}k_2\theta \end{cases} \tag{3}$$

where $C_\theta=\cos(\theta/2)$ and $S_\theta=\sin(\theta/2)$, k_1 (k_2) is the CSR kick factor in the first (second) dipole, and the subscript "2" of the Twiss parameters refers to the middle point of the second dipole of the DBA. We thus calculate the expression of the single particle C-S

invariant at the end of the second dipole magnet for arbitrary Twiss parameters in the dipoles, by considering a dependence of the CSR kick factor on the rms bunch length $k \sim 1/\sigma_z^{4/3}$, so that $k_2 = k_1 \times C^{4/3}$. Doing so, we consider: i) optics symmetry w.r.t. the DBA central axis, which implies π betatron phase advance (in the bending plane) between the dipoles [9], and ii) expand the trigonometric terms up to the third order in the bending angle, $\theta << 1$ [1]:

$$\begin{aligned} J_3 &= \beta_2 x_3'^2 + 2\alpha_2 x_3 x_3' + \left(\frac{1+\alpha_2^2}{\beta_2}\right) x_3^2 = \\ &\cong \left(\frac{k_1 \rho^{1/3}\theta^2}{2}\right)^2 \left[\beta_2 \left(C^{4/3}+1\right)^2 + \frac{1}{\beta_2}\left(\frac{l_b}{6}\right)^2 \left[\left(C^{4/3}-1\right)^2 + \alpha_2^2\left(C^{4/3}-3\right)^2\right] + 2\alpha_2 \left(\frac{l_b}{6}\right)\left(C^{4/3}+1\right)\left(C^{4/3}-3\right)\right] \end{aligned} \tag{4}$$

In Eq.4, $l_b = \rho\theta$ is the dipole arclength, and C the *local* linear compression factor. An inspection of Eq.4 shows that the invariant can be made exactly zero *only* for C = 1. To show this, we point out that minimization of J_3 requires [2]:

$$\begin{aligned} \left(\frac{dJ_3}{d\alpha_2}\right)_{\beta_2} &= \left(\frac{k_1 \rho^{1/3}\theta^2}{2}\right)^2 \left[\frac{2\alpha_2}{\beta_2}\left(\frac{l_b}{6}\right)^2 \left(C^{4/3}-3\right)^2 + 2\left(\frac{l_b}{6}\right)\left(C^{4/3}+1\right)\left(C^{4/3}-3\right)\right] \equiv 0 \\ \left(\frac{dJ_3}{d\beta_2}\right)_{\alpha_2} &= \left(\frac{k_1 \rho^{1/3}\theta^2}{2}\right)^2 \left[\left(C^{4/3}+1\right)^2 - \frac{1}{\beta_2}\left(\frac{l_b}{6}\right)^2 \left[\left(C^{4/3}-1\right)^2 + \alpha_2^2\left(C^{4/3}-3\right)^2\right]\right] \equiv 0, \end{aligned} \tag{5}$$

from which we get:

$$\begin{aligned} \alpha_{2,opt} &= -\frac{\beta_2}{\left(\frac{l_b}{6}\right)} \frac{\left(C^{4/3}+1\right)}{\left|C^{4/3}-3\right|} \\ \beta_{2,opt} &= \left(\frac{l_b}{6}\right) \frac{\sqrt{\left(C^{4/3}-1\right)^2 + \alpha_2^2\left(C^{4/3}-3\right)^2}}{\left(C^{4/3}+1\right)} \end{aligned} \tag{6}$$

By substituting $\alpha_{2,opt}$ into the expression for $\beta_{2,opt}$ or vice versa, we find that the derived expression is satisfied for C=1 only, in which case we obtain $\alpha_{2,opt}(C=1) = -\frac{6\beta_{2,opt}}{l_b}$. This is the solution for the non-compressed beam in a symmetric DBA already found in [7]. We observe that $\alpha_{2,opt}$ is negative for any C, which in our case corresponds to a diverging (converging) beam size in the second (first) dipole magnet, and that it is always different from zero. In other words, a solution with $\alpha_2 = 0$ like that adopted in [1] does not minimize J_3 in *absolute* sense, although it may be practical from the optics design point of view. As expected, Eq.6 reduces to Eq.5 in [1] for $\alpha_2 = 0$.

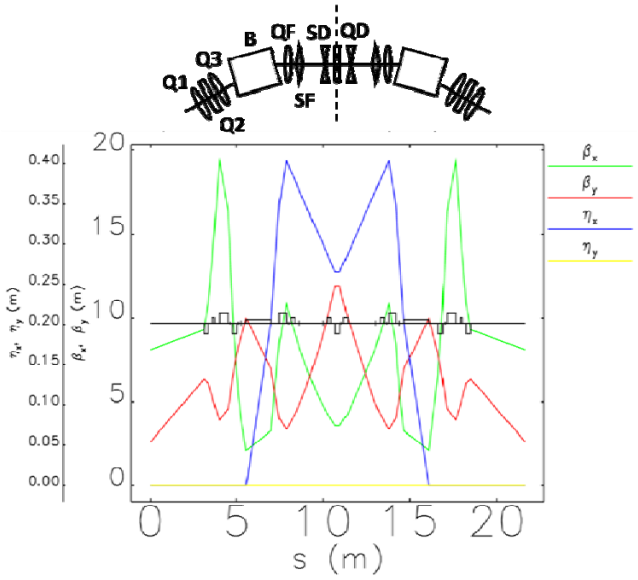

Figure 1: Sketch, not to scale, of the magnetic lattice of a DBA cell of the arc compressor (top), and periodic linear optics functions through the cell. Dipole magnets (B), focusing (QF, Q1 and Q3) and defocusing (QD, Q2) quadrupole magnets, focusing (SF) and defocusing sextupole magnets (SD) are labelled. The geometry and the magnets' arrangement is symmetric with respect to the middle axis (dashed line). Copyright of Elsevier [2].

It is quite common to have $\alpha_1 = \alpha_2 = 0$ in a rather compact and symmetric DBA design, such as that shown in Fig.1. In the following, we will keep it as a constraint on the optics design, and will study how β_2 should be tuned along the DBA according to the local value of the bunch length compression factor, C. That is defined by $C=1/|1+hR_{56}|$, where R_{56} is the transfer matrix element of the DBA cell, identical in all cells, and h is the incoming linear energy chirp, h=dE/(Edz). Bunch length compression is achieved as far as the energy spread correlated along the bunch, typically imparted to the beam by an upstream RF section running far from the accelerating crest, is much larger than the uncorrelated energy spread. In that case we can also write $h \approx \sigma_{\delta,0}/\sigma_{z,0}$, with $\sigma_{\delta,0}$ the initial rms value of the beam relative energy spread, and $\sigma_{z,0}$ the rms value of the initial bunch length. While σ_δ does not change substantially during the compression process, σ_z clearly shortens with C, that is h increases along the arc, and C so does. Eventually, the local compression factor, C^{loc}, and that cumulated through the lattice, C^{tot}, depends on the cell number:

$$C_i^{loc} = \frac{1}{|1 + C_{i-1} h_{i-1} R_{56}|}, \quad i = 1,...,6$$
$$C_j^{tot} = \prod_{i=1}^{j} \frac{1}{|1 + C_{i-1} h_{i-1} R_{56}|}, \quad j = 1,...,6 \qquad (7)$$

C^{tot} grows nonlinearly with the s-coordinate along the arc, and, according to Eq.6, β_2 should be tuned accordingly in each DBA, in order to optimally minimize the CSR-induced emittance growth (henceforth simply "CSR emittance"). In particular, β_2 should be made larger in the dipoles of the last DBA cells. Since the CSR effect is larger for shorter bunches, we might be allowed to relax the condition on β_2 in the first

few cells, where the bunch is longer, while ensuring optimum optics tuning in the last ones. The CSR emittance at the end of the arc is the result of the cumulative effect of CSR kicks in each cell. We assume that the CSR emittance in each cell sums in quadrature to the total emittance of the incoming beam, where the normalized emittance in the *i-th* cell is estimated by means of the "sigma matrix formalism" [10] and it reads:

$$\varepsilon_{n,i} \cong \sqrt{\varepsilon_{n,i-1}^2 + \varepsilon_{n,i-1}\gamma_i J_i} \tag{8}$$

γ_i is the usual relativistic Lorenz factor for the beam energy, J_i was defined in Eq.4 and we have to evaluate it with the prescription $C=C_i^{loc}$ according to Eq.7. Figure 2-left plot shows C_i^{loc}, $\beta_{x,opt}$ and γJ_i along the arc, for the beam parameters listed in Tab.1 (henceforth, β_x always refers to the betatron function in the dipole magnets). Figure 2-right plot compares J_i evaluated for $\beta_{x,opt}$ as in the left plot, to that for an identical value of β_x in all the dipoles. The CSR emittance is dominated by the CSR effect in the very last cell of the arc.

It is worthwhile noticing here that the uncorrelated sum of initial emittance and CSR emittance in each DBA cell, depicted by Eq.8, may over-estimate, after several CSR kicks along the whole beamline, the final emittance growth. In fact, CSR chromatic kicks are correlated along the bunch. As explained in the introduction of this article, that property allows partial or full cancellation of CSR emittance at the beamline's end, through proper balance of successive kicks. Such a balance (correlation) stays behind the prescription of linear superposition of the CSR chromatic kick and the particle's coordinate, at any kick location. Hence, following [3], one should compute the evolution of the particle's coordinates throughout the entire beamline, and eventually calculate the C-S invariant; this will be coding both the information on the Twiss functions and the CSR kicks. This is actually what we did for formulating Eq.4, and, in order to be more rigorous, we should have continued following the invariant expression till the end of the arc. In that case, we would have found an expression for the final emittance of the same form of Eq.8, but with an optics coefficient that would allow partial cancellation of CSR emittance, as provided by the algebraic sum of successive CSR kicks along the arc, each of them properly "weighted" by the local bunch length (i.e., compression factor) and Twiss parameters. Eq.8, instead, shows no possibility of cancellation (although partial) when moving from one DBA cell to the next one.

Still it shows, like in the more general formulation of optics balance [3], that the CSR contribution to emittance growth is proportional to the unperturbed emittance (see the second term under square root in Eq.8). This property can be understood, for example, by interpreting the result of a CSR chromatic kick like a residual betatron oscillation around a new dispersive trajectory. If, however, beam has ideally no emittance at the line's entrance, namely particles do not perform betatron oscillations, the CSR kick would only translate the beam on a new trajectory, with null betatron amplitude (see also the Appendix and Fig.5 in [11]). This way, the beam emittance would remain null after the kick. The same property implies that, for CSR emittance much smaller than the initial emittance, namely $\gamma_i J_i << \varepsilon_{n,i-1}$, the difference of final and initial emittance does not depend on the initial emittance value, i.e. $\Delta\varepsilon_{n,i} = \varepsilon_{n,i} - \varepsilon_{n,i-1} \approx \gamma_i J_i / 2$.

Table 1: Main beam and arc compressor parameters for the analysis reported in Fig.2.

Parameter	*Value*	*Units*
Energy	2.4	GeV
Charge	0.5	nC
Initial Bunch Length, RMS	900	μm
Initial Peak Current	45	A
Correlated Energy Spread, RMS	0.4	%
R_{56} per DBA Cell	35	mm
Number of DBA Cells	6	
Total Compression Factor	45	
Final Peak Current	2000	A

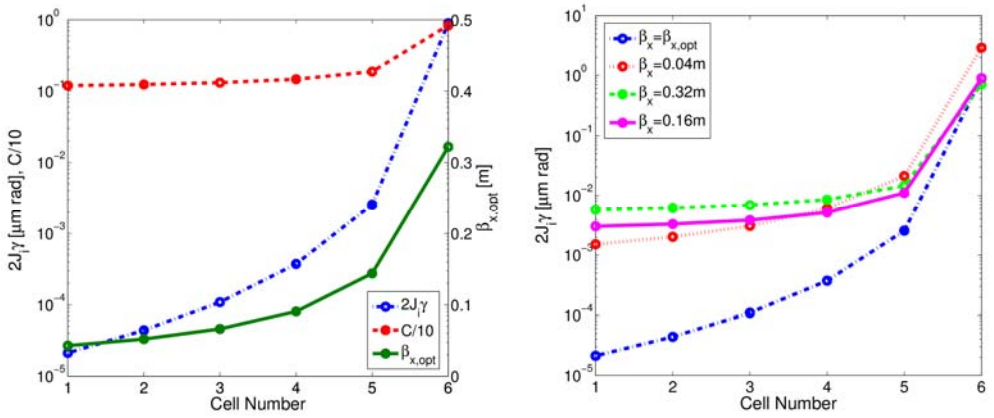

Figure 2: left, local value of the linear compression factor (normalized to 10; see Eq.7), and of the β_x-minimized CSR emittance (see Eq.4), along the arc; on the right axis, $\beta_{x,opt}$ in each cell predicted by Eq.6. Right, the local value of the β_x-minimized CSR emittance along the arc (dashed-dot line) is compared with its value evaluated for an identical β_x value in all the dipoles (3 cases are shown). Both left and right plots assume the electron beam parameters listed in Tab.1, and a CSR-induced relative energy spread of 2.5×10^{-6} in the first dipole of the arc. Copyright of Elsevier [2].

2.8.3 **Particle Tracking**

2.8.3.1 *Emittance Dependence on Optics Functions, Charge and Energy*

The dependence of the final horizontal emittance on the optics, charge and mean energy is investigated through Elegant [12] particle tracking runs, and compared with analytical predictions based on the linear optics analysis. Beam and arc parameters used for these studies are listed in Tab.2. Figure 3 shows the behaviour of the final projected emittance as a function of the betatron function in the dipole magnets (both intended in the bending plane), respectively with (*enx_csr*) and without CSR (*enx_chrom*), at different beam charges. The minimum value of β_x in the dipoles is scanned by varying the strength of a family of quadrupole magnets external to the DBAs (Q1 in Fig.1); the beam is matched to the periodic optics solution at every step. Since the initial bunch

length and the total compression factor are kept fixed at different charges, the final peak current is different: it is 0.4 kA for 0.1 nC and approximately 4 kA at 1 nC. The initial emittance is also kept the same, for direct comparison of its value at the arc's end.

Table 2: Electron beam and arc compressor parameters for sensitivity studies. The set of beam parameters used in particle tracking runs does not necessarily reflect an optimized beam from the injector.

Parameter	***Value***	***Units***
Charge	0.1 / 1.0	nC
Mean Energy	0.5 – 2.4	GeV
Initial Bunch Length, FWHM	3	mm
Linear Energy Chirp	-4.7	m^{-1}
Initial Normalized Emittance, RMS	0.8(x), 0.8(y)	μm
R_{56} per DBA cell	35	mm
Number of DBA Cells	6	
Total Compression Factor	45	

When the optics is varied, the sextupole strengths (see Fig.1) are kept fixed, and thereby aberrations are not cancelled at each step. At this stage, however, we care of the CSR emittance only, which is proportional to the difference between *enx_chrom* and *enx_csr*. At 0.1 nC, the CSR effect is negligible over the entire range of β_x considered; the emittance growth is dominated by chromatic aberrations. The CSR effect is notable at 1.0 nC. The effect is minimum at $\beta_x \cong 0.26$ m, which is in between the theoretical optimum for the last but one and the very last cell (see also Fig.2-left plot). One can notice that similar values of β_x correspond in some cases to slightly different CSR emittance contributions: this is because when a new optics solution is found, the value of α_x also changes in the dipoles, thereby providing a different CSR emittance as depicted by Eq.4. There is a clear correlation between β_x and the final emittance value. It is a remarkable result that smallest β_x value does not lead to optimum suppression of the CSR effect, in agreement with the analytical and somehow counterintuitive prediction of Eq.4.

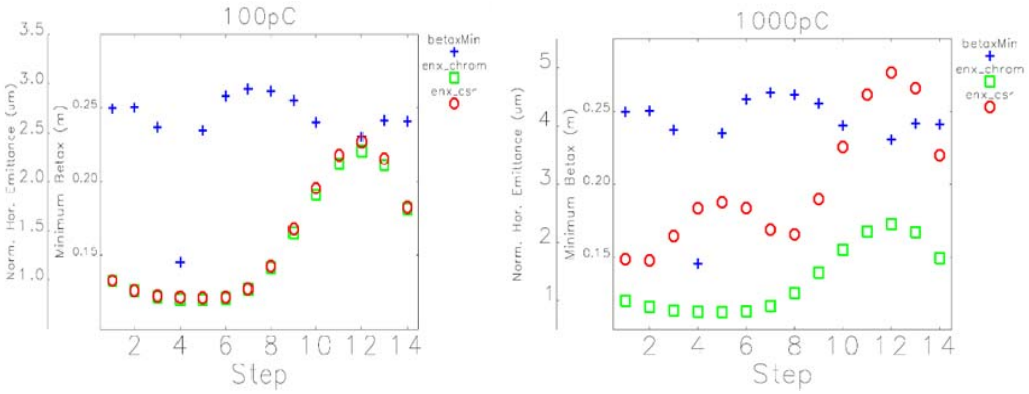

Figure 3: Horizontal normalized projected emittance (rms value) and minimum betatron function in the arc dipoles, at different simulation steps. Each step corresponds to a different periodic optics along the arc (Q1 strength is varied, see Fig.2). Bunch charge is 0.1 nC (left) and 1.0 nC; all other beam parameters are fixed (see Tab.2). Emittance is computed with (*enx_csr*) and without CSR (*enx_chrom*). Optical aberrations up to, and including 3rd order, and incoherent synchrotron radiation are always included. CSR transient field at the dipoles' edges and in drift sections following the dipole magnets is included when CSR is turned on. Copyright of Elsevier [2].

The arc compressor has also been investigated for different beam mean energies, as shown in Fig.4. The magnets' normalized strengths are kept fixed in order to provide the same optics for all energies. The quadratic difference of the final projected emittance and the initial unperturbed one is shown, for beam charges of 0.1, 0.3 and 0.5 nC. Particle tracking results are compared with the analytical prediction of Eq.8. CSR emittance control at 0.1 μm rad level is allowed at any energy $E \geq 0.5$ GeV for 0.1 nC, at $E \geq 1$ GeV for 0.3 nC, and at $E > 2$ GeV for 0.5 nC. It is worth noticing that the magnets' length and therefore the entire lattice was optimized for the maximum beam energy of 2.4 GeV, which is the maximum energy considered in our study. This implies that shorter magnets could be used at lower energies, and shorter drift sections accordingly. Thus, we envisage room for optimization of the lattice at lower energies that will provide a CSR emittance smaller than that shown in Fig.4. For the analytical case, the CSR-induced energy spread was evaluated according to the steady-state emission of a uniform charge distribution, as predicted by [8]. That value reasonably matches all simulation results, and is supported by a parabolic current profile which is used in the simulations (not shown).

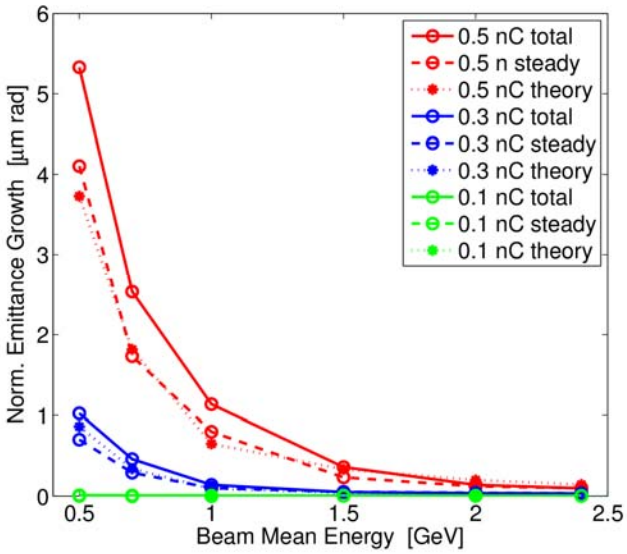

Figure 4: The normalized emittance growth is the quadratic difference (under square root) of the final projected normalized emittance and the initial one (rms values). Theoretical predictions (dotted lines) are from Eq.8, for steady-state CSR emission. Particle tracking results are for steady-state emission (dashed lines), and including transient CSR field at the dipoles' edges, and in drift sections (solid lines). The arc lattice is made of 6 consecutive cells, whose unit is shown in Fig.1. The optics is the same for all beam charges and energies. Copyright of Elsevier [1].

2.8.3.2 *Low and High Charge Beams*

A characterization of the electron distribution at the arc's end is provided here for two sets of initial beam parameters, one for high charge – long bunch, the other for low charge – short bunch; they are summarized in Tab.3. The high charge case is recalled from [1] for Reader's convenience, and for immediate comparison with the low charge. The bunch length compression process is linearized through the arc with the help of 4 families of sextupole magnets, 24 magnets in total (see Fig.1). In fact, linear compression is achieved as long as $|T_{566}|\sigma_{\delta,0} << |R_{56}|$ through the arc, whereas T_{566} is proportional to the second order momentum compaction. In addition, second and higher order energy chirp has to be small with respect to the linear one. While T_{566} can be controlled, *e.g.*, with an appropriate number and strength of sextupole magnets [13–15], a nonlinear energy chirp is realistically present in the beam's longitudinal phase space: at the entrance of the arc compressor due to upstream RF curvature, and developing along the arc because of the nonlinear energy correlation established by CSR along the bunch. Then, a non-zero T_{566} can be used to linearize the nonlinear chirp [13], the actual value of T_{566} (typically in the cm range) depending on the specific charge distribution. Magnetic linearization of the compression process has the advantage of avoiding the need for an RF harmonic linearizer [16]. However, it introduces a potential disruption of the beam rms emittance by geometric and chromatic aberrations induced by the sextupoles themselves. The single magnet aberration can be analytically estimated through the sigma matrix formalism, whose determinant, under square root, is the rms beam emittance. We assume that each magnet adds an error angular kick, $\Delta u'$, to the beam angular divergence. The beam geometric emittance after the kick reads:

$$\varepsilon = \sqrt{\det\begin{pmatrix} \beta & -\alpha \\ -\alpha & \gamma + \dfrac{\langle \Delta u'^2 \rangle}{\varepsilon_0} \end{pmatrix}} = \sqrt{\varepsilon_0^2 \left(1 + \frac{\beta \langle \Delta u'^2 \rangle}{\varepsilon_0} \right)} \approx \varepsilon_0 + \frac{1}{2} \beta \langle \Delta u'^2 \rangle, \tag{9}$$

where ε_0 is the unperturbed emittance, all symbols refer to the same plane of motion; β and γ are here Twiss parameters. The sextupole aberration is excited by a kick $\langle \Delta u'^2 \rangle = (k_2 l_s)^2 \langle u^2 \rangle^2$, with $k_2 l_s$ the integrated normalized sextupole strength in m^{-2}, $\langle u^2 \rangle = \beta \varepsilon_0$ for the geometric aberration, and $\langle u^2 \rangle = \eta_x^2 \sigma_\delta^2$ for the chromatic one. We consider the scenario in which the final relative emittance growth is given by the largest sextupole's contribution folded by the square root of the number of sextupoles in the lattice. With the beam parameters listed in Tab.3 for the 0.5 nC charge beam, and the optics depicted in Fig.1, we have at the sextupoles' location: $k_2 l_s \leq 8$ m^{-2}, $\beta\varepsilon_0 \leq 2\times 10^{-9}$ m^2, and $(\eta_x\sigma_\delta)^2 \leq 1.4\times 10^{-6}$ m^2. The total relative emittance growth from geometric aberrations is than smaller than 0.01%, while that due to chromatic aberrations is above 100%. That explains the modulation of the projected emittance along the arc shown in Fig.5.

The effect of chromatic aberrations was eventually minimzed by a numerical optimization of the sextupole strengths, and by profiting of the betatron phase advance between the magnets. As a result, the rms normalized projected emittance of the 0.5 nC beam grows from 0.8 μm rad to 1.1 μm rad at the arc's end, with residual contributions from incoherent synchrotron radiation (ISR), chromatic aberrations and CSR. Chromatic aberrations are also responsible for (small) horizontal slice emittance growth shown in Fig.6-left plot. Non-uniformity of the horizontal C-S invariant of the slices' centroid, shown in Fig.6-right plot, reflects the slices' misalignment in the transverse phase space due to CSR kicks. In order to damp the CSR-induced microbunching instability [17–19], the initial electron beam uncorrelated energy spread is set at 40 keV rms, in order to simulate the effect of a laser heater [20]. Quiet start of a 5 million particle input distribution, and filtering was adopted to ensure suppression of numerical sampling noise at uncompressed wavelengths shorter than 35 μm [21]. Residual CSR-induced microbunching shows up in the longitudinal phase space at compressed wavelengths longer than 10 μm. The final slice energy spread is approximately 2 MeV, and dominated by the initial uncorrelated energy spread times the total compression factor. Similar performances were obtained with the 0.1 nC beam, as shown in Fig.5-right plot and in Fig.7. The CSR-induced emittance growth is at same 0.1 μm rad level as in the 0.5 nC case, in agreement with Eq.8 and with the scaling of CSR effect with charge and bunch length [8]. Residual CSR-induced microbunching at final wavelengths longer than 5 μm is barely visible in Fig.7.

The 1-D steady-state theory of CSR emission from a Gaussian bunch allows an estimation of the CSR-induced mean energy loss per dipole magnet [22], $\langle\delta_{CSR}\rangle = -0.3505 r_e Q/(e\gamma\rho^{2/3}\sigma_z^{4/3})$. A more realistic evaluation from particle tracking included the energy loss associated to the electrons-field interaction in drift regions. We found that the 0.5 nC charge beam at 2.4 GeV (see Tab.3) emits along the whole arc, at a repetition rate of 1 MHz, an average coherent synchrotron radiation power of up to 6 kW, that is 12 kW per mA or 50 W per meter. The average power associated the classical synchrotron radiation emission amounts to 130 W, i.e. 260 W per mA or 1.1 W per

meter. That power can produce some relevant heating and therefore requires cooling and a careful evaluation of the machine run duration to prevent vacuum pressure rise.

Table 3: Electron beam parameters at the entrance and at the exit of the arc compressor (simulation results). Rms values are computed over 100% of the beam charge.

Input beam			
Energy	2.4	2.4	GeV
Charge	0.1	0.5	nC
Bunch Length, RMS	300	900	μm
Peak Current	30	45	A
Projected Normalized Emittance, RMS (x,y)	0.2, 0.2	0.8, 0.8	μm rad
Uncorrelated Energy Spread, RMS	30	40	keV
Correlated Energy Spread, RMS	0.1	0.4	%
Output beam			
Compression Factor	~45	~45	
Peak Current	~1400	~2000	A
Projected Normalized Emittance, RMS (x,y)	0.3, 0.2	1.1, 0.8	μm rad
Slice Energy Spread, RMS	≤1.6	≤2.0	MeV

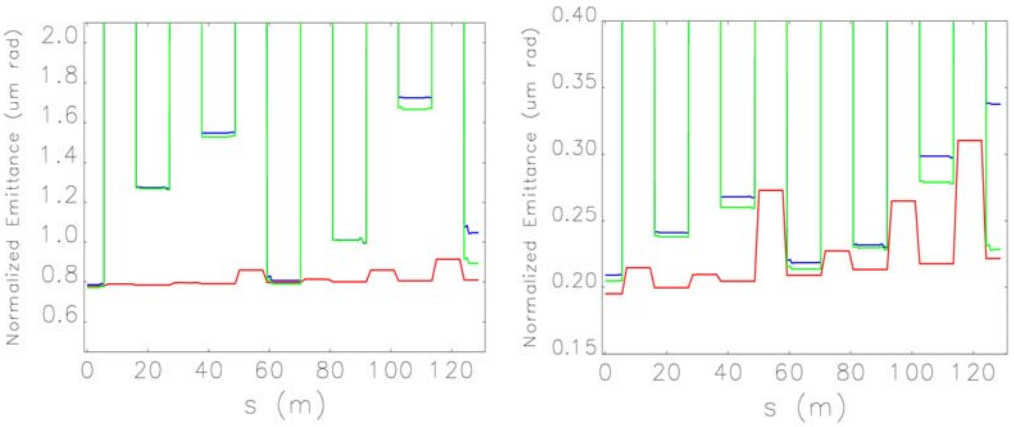

Figure 5: Projected normalized emittance (rms value) in the bending plane along the arc, for the 0.5 nC (left) and 0.1 nC beam (see Tab.3; notice that the vertical scale is different in the two plots). The emittance evolution is shown, respectively, in the presence of ISR-only for the fully compressed beam (red), with the addition of compression and optical aberrations (green) and with the further addition of CSR (blue). Upper value of the emittance along the arc is ~10 μm, not shown to appreciate the small emittance growth at the end of the line. Left plot is Copyright of Europhysics Letters [1]. Right plot is Copyright of Elsevier [2].

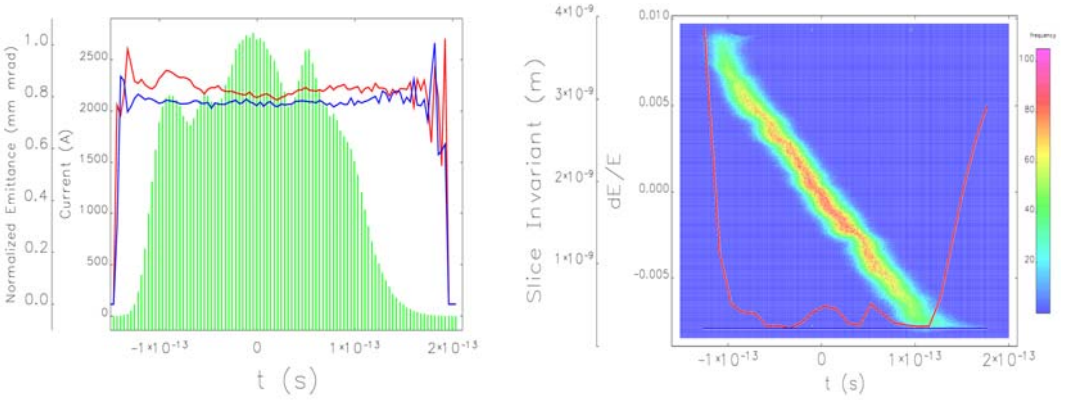

Figure 6: output from Elegant particle tracking for the 0.5 nC beam (see Tab.3). Bunch head is at negative time coordinates. Left: current profile (histogram), superimposed to the slice rms normalized emittance (horizontal, in red). Right: longitudinal phase space, superimposed to the slice C-S invariant (solid line): the horizontal one varies along the bunch because of CSR kicks. In both plots, spiky variations of the slice parameters at the bunch edges are due to poor particle sampling. Both plots are Copyright of Europhysics Letters [1].

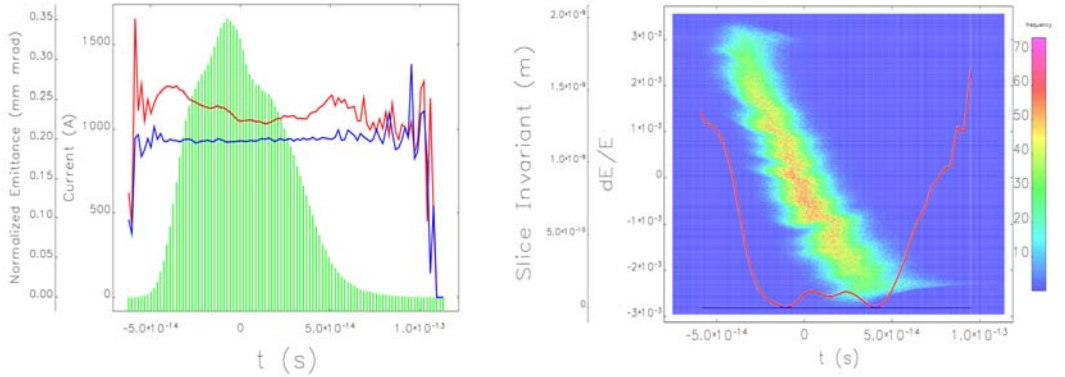

Figure 7: Output from Elegant particle tracking for the 0.1 nC beam (see Tab.3). Contents as in Fig.6. Both plots are Copyright of Elsevier [2].

2.8.4 **Applications**

The capability of controlling CSR effects in an arc compressor (not necessarily constrained to a 180 deg total bending angle) – and thus to increase the beam peak current while preserving its 6-D brightness using an approach that goes beyond those offered by the existing literature [23] – quite generally opens the door to new geometries in accelerator design and new schemes of beam longitudinal gymnastic. For example, after single- or multi-pass acceleration in an FEL linac-driver, the beam can be arc-compressed at high energy and counter-propagated into an undulator, which could then lie parallel to the accelerator. At least two advantages are seen: one is that cost savings are achieved in civil construction, the other is that the operation of the system is simplified, as much as the beam does not undergo any manipulation other than acceleration until it reaches the arc compressor. A similar layout may also apply to linear particle colliders. As an example, the CLIC design [24] includes optics matching insertions and a magnetic chicane both devoted to bunch length compression before an

isochronous turnaround arc, and a similar configuration (two chicanes aside an arc) is before beam deceleration. On the basis of our findings, the arc could be investigated as either compressor (together with a proper setting of the upstream RF phases to match the arc's positive R_{56}) or a CSR-immune transfer line, if the beam has no energy chirp at its entrance. A similar option might apply to the International Linear Collider, which is currently planning an isochronous turnaround followed by two compressor chicanes [25].

Our arc compressor design is also recommended for an ERL-, or recirculated linac-driven FEL such as that described in [26]. In this case, the electron beam may be accelerated and recirculated in isochronous beam lines until it reaches the target energy and energy chirp, and eventually compressed. From the entrance to the exit of the arc compressor, the energy spread, normally dominated by the energy chirp, remains substantially unchanged. In order for the FEL amplification process to be efficient, $\sigma_{\delta,0}$ must be matched to the normalized FEL energy bandwidth, ρ [27]. For lasing in x-rays, $\rho \geq 10^{-4}$ and this may require a removal of the energy chirp downstream of the arc, i.e. with a dedicated RF section. With the 500 pC beam parameters of Tab.1, we estimate [28] lasing at 1.3 nm with 2.1 m long 3-D gain length, $\rho = 1.1\times 10^{-3}$ and FEL power saturating at 2.6 GW in a 36 m long undulator.

If the incoming energy chirp is imposed to the beam at full energy with a linac running close to the zero-crossing RF phase, some concerns could be raised about the shot-to-shot jitter of the final beam energy, energy chirp and peak current, i.e. compression factor. It is shown below that such concerns are not justified when, e.g., stabilities typical of superconducting linacs are met. In the approximation of linear compression and for C>>1, the relative variation of C is linearly proportional to the relative variations of R_{56} and h, times C. In a periodic arc made of N DBAs we have:

$$R_{56} = N\int_0^{l_b} \frac{\eta_x(s)}{\rho} ds = N\int_0^{\theta} \rho(1-\cos\theta')d\theta' = 2Nl_b\left(1-\frac{\sin\theta}{\theta}\right) \propto \theta^2 \qquad (11)$$

Hence, we may estimate, $\Delta R_{56}/R_{56} = 2\Delta\theta/\theta \leq 2\times 10^{-4}$ where the bending angle relative stability is the same as the dipole magnetic field relative stability, and all dipoles are powered by the same current source. At the same time, the energy chirp $h \approx k_{RF}eV\cos(\phi)/E$ for $\phi \to 0$, with k_{RF} the RF wave number, V the RF peak voltage of the linac section imposing the energy chirp, ϕ the RF phase and E_i the beam mean energy at the linac entrance (maximum acceleration is for ϕ=90 deg). From this we get: $(\Delta h/h)_V \approx \Delta\phi tg(\phi) \leq 3\times 10^{-4}$ for RF set point $|\phi| < 20$ deg and RF phase jitter $\Delta\phi \approx$ 0.05 deg, and $(\Delta h/h)_\phi \approx \Delta V/V \leq 1\times 10^{-4}$. The uncorrelated sum of the jitters due to magnetic field, RF phase and RF peak voltage results in a peak current jitter smaller than 2% for C = 45. The beam mean energy jitter in the linac-chirper is also small, 0.02% rms at 2.4 GeV. This is equivalent to an arrival time jitter of 150 fs rms at the L-band linac entrance.

2.8.5 **Conclusions**

We have shown that linear optics transfer matrices associated to 1-D steady-state theory of CSR emission allow an estimation of projected emittance dilution due to CSR kicks in a periodic, achromatic, 180 deg arc compressor. The agreement with Elegant simulation results is at the level of 0.1 μm rad total normalized emittance growth (rms

value) for bunch charges lower than 0.5 nC. Above such a value, that accuracy is ensured at energies higher than 1.5 GeV. Our study shows a clear correlation between the optics design and the emittance value. As predicted by theory, a too small value of the betatron function in the arc's dipoles does not lead to optimum CSR suppression; an optimum betatron function is prescribed instead, and the overall CSR effect is minimized by optimum optics tuning in the very last cells of the arc. The theoretical background was eventually used to design a compressor arc largely immune to CSR-induced emittance growth.

Because of intrinsic higher order optics terms in the magnetic lattice and in the beam longitudinal phase space, sextupole magnets turned out to be essential to restore the linearity both of the optics and of the bunch length compression process. After an initial manual set up of the sextupoles' strengths in order to approach a compression as linear as possible, they were later on numerically optimized in order to minimize the final projected emittance. The last step ensured not only minimization of the optical aberrations, but also a linear longitudinal phase space because, as opposite, nonlinearities in the phase space would have led to current spikes, thus to larger CSR emittance.

Although CSR-induced microbunching shows up with a deeper modulation of the longitudinal phase space and a final current modulation around 20%, those tracking results should be considered as pessimistic estimates of the real beam quality: first, the smearing effect of transverse emittance on the microbunching, which may be particularly important as the bunch shortens in the last DBA cells, is ignored; second, the effect of numerical noise gradually diminishes as the number of particles is increased from 10^5 to $5\cdot 10^6$ (not shown); in addition, we have suppressed numerical noise at final wavelengths shorter than 1 μm, a value much shorter than those at which the instability develops (>5 μm). Finally, further optimization of the arc lattice with shorter drift sections and shorter dipole magnets is expected to reduce the CSR-induced microbunching.

The agreement of theory and simulations on the CSR-perturbed transverse emittance promises further reduction of the transverse CSR effect for smaller compression factors and/or improved tuning of the beam size in the dipole magnets. The optics that minimizes the transverse CSR effect in the arc is typically in conflict with the one cancelling chromatic effects, in analogy with the conflict of low emittance optics and chromaticity correction in storage rings. This fact leaves room for numerical optimization of both the arc lattice and its optics functions. Asymmetric arc designs with different optics arrangement can alternatively be considered [29], but we find that the periodic solution has several advantages: for example, energy dispersion leakage is easier to suppress if the dipole magnets are all identical and the optics is periodic. Optics symmetry allows tuning of the momentum compaction, thus of the compression factor, with equally spaced sub-families of quadrupoles (two families are available in the present design) and tune splitting to suppress coupling error effects ($\nu_x = 7.82$, $\nu_y = 3.41$ for the proposed arc). It also allows fast check of beam optics matching with screen systems along the line, as the beam sizes is the same at equivalent locations in the DBAs. Finally, periodicity of the lattice geometry allows cost-saving production of identical lattice elements (magnets, power supplies, diagnostics, etc.).

In conclusion, in spite of non-negligible non-steady state CSR effects, the present analysis can be used as a guidance for the design of a periodic and symmetric arc compressor in the presence of CSR, naturally further improved by numerical

optimization algorithms, and possibly modelling 3-D CSR effects. It is worth noticing that the CSR 1-D model in Elegant assumes that the bunch transverse size is much smaller than the bunch length. This requirement is often named "Derbenev criterion" and written in the form $\kappa = \sigma_x / \left(\rho \sigma_z^2\right)^{1/3} << 1$ [30]. In our case, the horizontal beam size in the dipoles is enlarged and dominated by the dispersive motion, and the criterion starts falling short already at the middle of the arc, where we have $\kappa \approx 0.1$; in the final cell we find $\kappa = 0.4$.

The proposed lattice, although not fully optimized for any specific application, promises an out coming electron beam quality at a level suitable for FELs in the ultra-violet to x-ray wavelength range. Similar electron beam parameters are of concern in nowadays linear collider projects.

2.8.6 **Acknowledgments**

This work took advantage of several stimulating discussions with, and suggestions by, colleagues in the accelerator community: M. Cornacchia, D. Douglas, Y. Jiao, X. Huang, M. Venturini, V. Litvinenko, D. Pellegrini, and A. Latina. This work was funded by the FERMI project and by the ODAC project of Elettra Sincrotrone Trieste.

2.8.7 **References**

1. S. Di Mitri and M. Cornacchia, Europhys. Letters **109**, 62002 (2015).
2. S. Di Mitri, "Feasibility Study of an Arc Compressor in the Presence of Coherent Synchrotron Radiation", accepted in Nucl. Instrum. Meth. Phys. Res., Vol. A (2015).
3. S. Di Mitri, M. Cornacchia, and S. Spampinati, Phys. Rev. Letters **110**, 014801 (2013).
4. R. Li, Ya.S. Derbenev, JLAB-TN-02-054 (2002).
5. J.S. Nodvick and D. Saxon, Phys. Rev. **96** (1954) 1.
6. V. Yakimenko, M. Fedurin, V. Litvinenko, A. Fedotov, D. Kayran, and P. Muggli, Phys. Rev. Lett. **109**, 164802 (2012).
7. Y. Jiao, X. Cui, X. Huang, G. Xu, Phys. Rev. Special Topics – Accel. Beams **17**, 060701 (2014).
8. E.L. Saldin, E.A. Schneidmiller, M.V. Yurkov, Nucl. Instrum. Meth. Phys. Research, Sect. A **398** (1997) 373.
9. A. Jackson, Part. Accel. 1987, 22, 111.
10. A.W. Chao and M. Tigner, *Handbook of Accelerator Physics and Engineering*, World Scientific, Singapore, 3rd ed. (2006) 66.
11. M. Venturini, "Design of a triple-bend isochronous achromat with minimum CSR-induced emittance growth", to be published (2015).
12. M. Borland, Advanced Photon Source LS-287 (2000).
13. D. Dowell, in Proc. of the 1997 Part. Accel. Conf., Vancouver, B.C., Canada (1997) 1888.
14. D. Douglas, in Proc. of the 2010 Beam Instrumentation Workshop, Santa Fe, NM, USA, WEIMNB02 (2010).
15. S. Thorin, M. Eriksson, S. Werin, D. Angal-Kalinin, J.W. McKenzie, B.L. Militsyn and P.H. Williams, in Proc. of the 32nd Intern. Free Electron Laser Conf., WEPB34, Malmö, Sweden (2010).
16. T. Smith, in Proc. of the 1984 Linear Accel. Conf., Stanford, CA, USA (1984), and in SLAC report 303 (1986).
17. E.L. Saldin, E.A. Schneidmiller, and M.V. Yurkov, Nucl. Instrum. Methods Phys. Res., Sect. A **490**, (2002) 1.

18. S. Heifets, S. Krinsky, G. Stupakov, Phys. Rev. Special Topics – Accel. Beams **5**, 064401 (2002).
19. Z. Huang and K.-J. Kim, Phys. Rev. Special Topics – Accel. Beams **5**, 074401 (2002).
20. E.L. Saldin, E.A. Schneidmiller, and M. Yurkov, Nucl. Instr. Meth. Phys. Research A **528** (2004) 355.
21. M. Borland, Phys. Rev. Special Topics – Accel. Beams **11**, 030701 (2008).
22. M. Borland, Phys. Rev. Special Topics – Accel. Beams **14**, 070701 (2001).
23. S. Di Mitri and M. Cornacchia, Physics Reports **539** (2014) 1–48.
24. CLIC Conceptual Design Report (2012), http://project-clic-cdr.web.cern.ch/project-CLIC-CDR/CDR_Volume1.pdf
25. C. Adoplphsen et al., Report No. CERN-ATS-2013-037 (2012), http://arxiv.org/ftp/arxiv/papers/1306/1306.6328.pdf
26. R.C. York, Phys. Rev. Special Topics – Accel. Beams **17**, 010705 (2014).
27. R. Bonifacio, C. Pellegrini and L. Narducci, Opt. Commun. 50, 373-378 (1984).
28. M. Xie, in Proc. of 1995 Part. Accel. Conf., Dallas, TX, USA, IEEE, 183–185 (1995).
29. D. Douglas et al., in Proc. of the 6th Intern. Part. Accel. Conf., TUPMA034, Richmond, VA, USA (2015), and references therein.
30. Ya.S. Derbenev, J. Rossbach, E.L. Saldin, and V.D. Shiltsev, TESLA-FEL 95-05 (1995), DESY, Hamburg, Germany.

2.9 Considerations of SRF Linac for High Current ERL

Wencan Xu, BNL, Upton, NY 11790
Mail to: wxu@bnl.gov

2.9.1 Introduction

The Collider-Accelerator Department at BNL proposed a FFAG lattice based electron-ion collider, eRHIC [1], which will use 80 5-cell 647 MHz SRF cavities for a 1.67 GeV main linac. The FFAG lattice based eRHIC design requires a SRF cavity design with capability of heavy damping HOMs, and keep high fundamental mode performance at the same time. The 5-cell 647 MHz BNL4 cavity is an evolution design of the 5-cell 704 MHz BNL3 cavity [3,4,5]. BNL4 was designed to reduce both loss factor of monopole HOMs (HOM power) and impedance of the dipole HOMs, while maintaining similar performance of the fundamental mode. The operation requirement of BNL4 cavity is 18.7 MV/m with Q_0 @ 3×10^{10}. A 5-cell prototype cavity is undergoing fabrication to demonstrate and study this performance. This paper addresses the design of BNL4 cavity.

To reach full luminosity of eRHIC at intermediate energies, about 7 kW HOM power per BNL4 cavity should be damped. It is a big challenge to develop such a high power, full spectrum HOM damping scheme. This paper will address the different HOM damping schemes that are studying at BNL. The goal is to develop a reliable, full HOM damping scheme for eRHIC and other high current ERL machines.

2.9.2 **647 MHz 5-cell BNL4 Cavity Design**

2.9.2.1 ***Fundamental Mode***

The same as 704 MHz BNL3 cavity, the 5-cell 647 MHz BNL4 cavity, employs a concept of using a large beam tube to propagate all HOMs but its end cells have irises that improve the confinement of the fundamental mode inside the structure. To reduce the cross-talk between neighboring cavities, tapered sections to a reduced diameter beam pipe are added on both sides of the cavity. Figure 1 (top) shows Superfish model of the BNL4 cavity. The field profile of the fundamental mode by Superfish is shown in Figure 1 (bottom). The fundamental mode's performance of the BNL3 and BNL4 cavities is listed in Table 1.

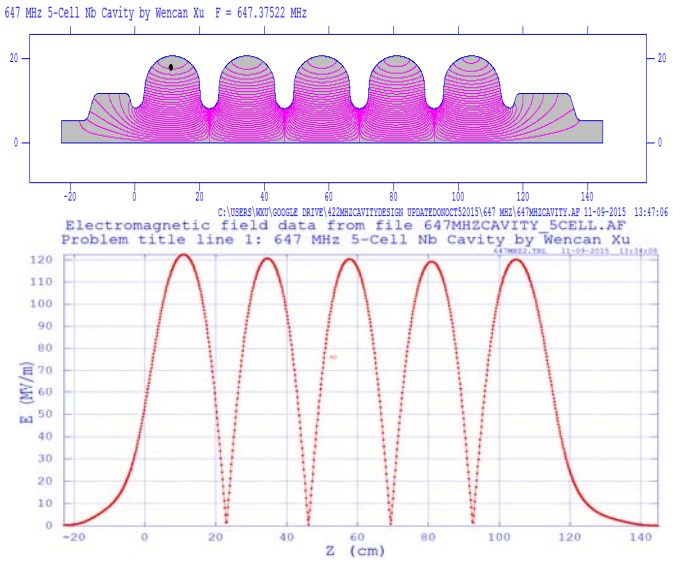

Figure 1: BNL4 cavity configuration (top) and fundamental mode field profile (bottom).

Table 1: RF parameters of the BNL3 and BNLI cavities.

Parameters	**BNL3**	**BNL4**
Frequency [MHz]	703.79	647
Number of cells	5	5
Geometry factor [Ω]	283	273
(R/Q)/Cavity [Ω]	506.3	502
Epeak/Eacc	2.46	2.27
Bpeak/Eacc [mT/MV/m]	4.27	4.42
Coupling factor [%]	3.0	2.8
Loss factor @ 4mm rms bunch length [V/pC]	2.63	2.18

2.9.2.2 *Monopole Modes and HOM Power*

An average monopole mode HOM power in a cavity is proportional to the bunch charge Q_b, beam current I_b, and the longitudinal loss factor k_p:

$$P_{\text{ave}} = k_{\square} I_{\text{b}} Q_{\text{b}} \tag{1}$$

As the average HOM power is linear with the loss factor. The loss factor should be an important optimization factor for high current ERL machine. The loss factor of the BNL4 cavity was calculated with ABCI to be 2.18 V/pC for a Gaussian bunch of 4 mm RMS bunch length, which reduced from 2.63 V/pC for 704 MHz BNL3 cavity. Figure 2 shows the loss factor for BNL4 cavity various with bunch length.

With eRHIC beam parameters (12 passes, 50 mA ERL, 5.3 nC per bunch) for an intermediate energy, where HOM damping is the limitation of the luminosity, an average value of monopole mode HOM power in one BNL4 cavity is 7 kW per cavity. However, this power can be much higher if one considers the beam spectrum, as shown in Figure 3. This presents a big challenge for removing it out of the cryostat and it has to be damped outside the cryomodule.

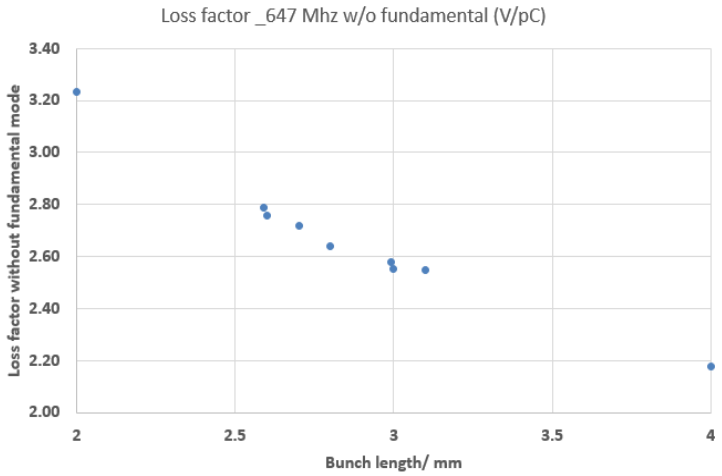

Figure 2: Integrated loss factors of the BNL4 cavity for different rms bunch length.

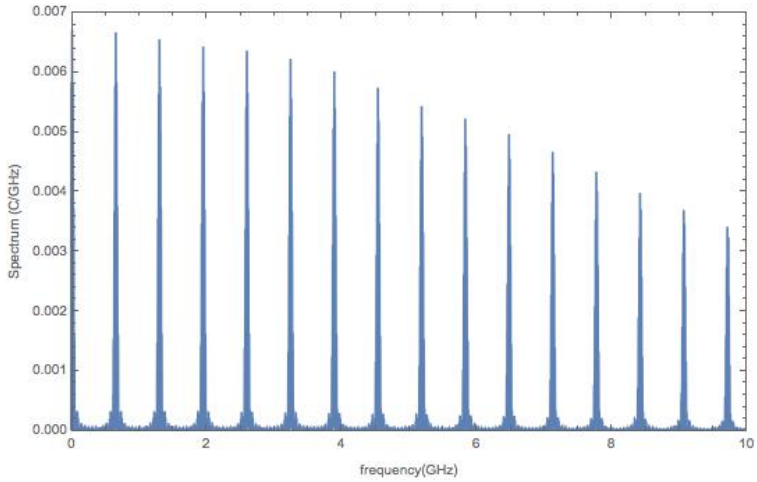

Figure 3: eRHIC beam sprectrum (only show up to 10 GHz)

2.9.2.3 *Transversal Beam-Break-Up (BBU)*

The FFAG lattice based eRHIC design is a multi-pass (up to 12), high current ERL design is a multi-pass (up to 12), high current ER design. One important concern for the linac cavity design is to increase the beam break up (BBU) threshold current. The transverse BBU threshold beam current depends mainly on the strength of dipole HOMs. Assuming that HOMs behave independently and do not interfere with each other, the threshold current in the presence of a single HOM can be approximated as [7]

$$I_{\mathrm{th}} = \frac{2pc}{Q_{\mathrm{b}} k (R_{\mathrm{d}} / Q) Q_{\mathrm{ext}} M_{12} \sin(\omega T_{\mathrm{r}})} \tag{2}$$

Where p is the beam momentum, c is the speed of light, k is the higher-order-mode's wave number, R_d/Q is the shunt impedance and Q_{ext} is the quality factor, M12 is the transport matrix parameter, and T_r is the bunch return time. From the threshold current formula (2), it is clear that a small R_d/Q and/or Q_{ext} can increase the threshold current. A smaller Q_{ext} means shorter damping time and larger current needed to deposit enough energy to disturb the beam.

One should notice that this formula fits for one cavity, one pass case. The threshold current reduces approximately square of number of passes. Also, it also reduces approximately number of cavities in the linac. So, there is a trade of between linac energy and number of passes. Eventually, BBU has to be simulated with computer codes, such as TDBBU, GBBU. GBBU code simulation shows that the threshold current of BNL4 cavity for eRHIC has at least a factor of 4 above the operation beam current, which is 0 frequency spread in the HOM spectrum.

2.9.2.4 *Mechanical Design and Prototype Cavity*

In eRHIC design, the electron beams will collide with different proton energy from 40 GeV to 250 GeV, which corresponds to a frequency shift up to 174 kHz for 647 MHz cavity. ANSYS simulation shows that the cavity's tuning sensitivity is 84 kHz/mm, so the tuning range requirement for BNL4 cavity is 2 mm. With a 3.2 mm thickness of Nb sheet, the cavity can be tuned up to 2.8mm without exceeding the yield strength of Nb: 7000 psi. In the prototype cavity, we use 4 mm thickness for the Nb sheets. Figure 5 shows the 5-cell prototype cavity, which is fabricated to study cavity's performance ($Q0=3\times10^{10}$ at 18.5 MV/m), with different surface treatment. It will also be used for HOM damping study as well.

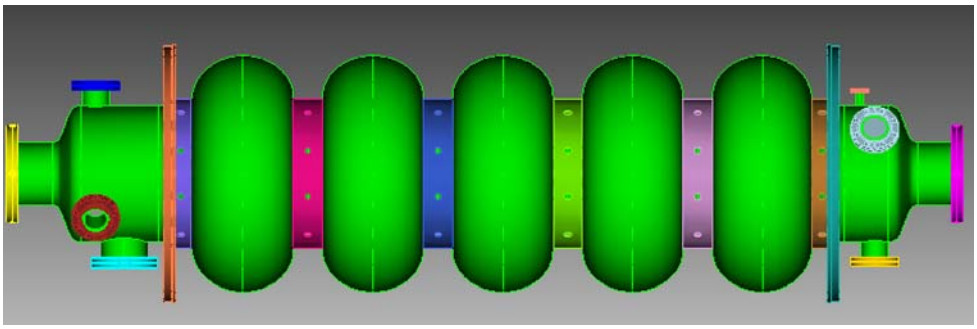

Figure 5: 5-cell prototype of the BNL4 cavity.

2.9.3 **Hom Damping Scheme**

HOM damping can be separated operationally into three steps: 1) HOMs propagate out of the cavity's cells and travel to the location of HOM couplers; 2) The HOM couplers pick up the HOM fields but reject the fundamental mode; 3) The HOM power is transmitted out of the SRF cavity or cryomodule. *The first step* was accomplished in the cavity design: all of the dipole modes have external quality factors (Q's) lower than 2.5×10^4 and all of the monopole modes have external Q's below 1.7×10^4. *The second step*, to damp the full HOM spectrum (which depends on bunch length, for example, a rms 4 mm bunch length can excite HOMs up to 30 GHz), can employ different types of HOM damping scheme. There are four HOM damping scheme undergoing R&D at BNL:

1) six coaxial-line HOM couplers (for frequency < 5 GHz HOM) and three waveguides (for HOMs with frequency > 5 GHz), which waveguide is very small;
2) six coaxial-line HOM couplers (for frequency < 5 GHz HOM) and one beampipe absorber (for HOMs with frequency > 5 GHz), which beampipe absorber can be inside the cryomode with reasonable heat load;
3) only waveguide HOM damper, which has to resolve the cooling issue;
4) room temperature HOM absorber, which will reduce the real estate gradient dramatically.

The third step for HOM damping is to divert and absorb the HOM power generated inside the cavity outside the cryomodule. A crucial component in achieving *the third step* is an RF window, which isolates the cavity vacuum from outside components, but at the same time transmits all HOM power through it. It is very important to design a high power, broadband, low loss, and reliable RF window. Also, thermal design has to be carried out carefully to reduce heat load on the cryomodule, when delivering the HOM power outside.

2.9.4 **Conclusion**

A 5-cell 647 MHz BNL4 cavity is developed for the FFAG lattice based eRHIC design, with consideration to the reduction of the loss factor (HOM power) and dipole HOM impedance for higher BBU threshold current. This cavity's performance will be demonstrated with a 5-cell Nb prototype Nb cavity. Study of different treatment will be carried out with this cavity. The eRHIC electron beams can excite up to 7 kW HOM power per cavity, which has to be damped outside the cryomodule. Different HOM damping schemes are undergoing study. The goal is to develop a high power, full spectrum HOM damping and reliable HOM damping scheme for high current ERL applications.

2.9.5 **References**

1. eRHIC, "eRHIC Design Study: An Electron-Ion Collider at BNL", arXiv:1409.1633, December 2014.
2. S. Belomestnykh, et al., "On the frequency choice for the eRHIC SRF linac," IPAC2014, p. 1547.
3. Wencan Xu, I. Ben-Zvi, R. Calaga, H. Hahn, E.C. Johnson, J. Kewish, "High current cavity design at BNL", Nucl. Instr. and Meth. A 622 (2010) 17-20.

4. Wencan Xu, et al, “Progress on the high-current 704 MHz superconducting RF cavity at BNL”, Proc. IPAC2012, pp. 2486-2488.
5. Wencan Xu, et al, “Vertical test results of 704 MHz BNL3 SRF cavities”, Proc. LIAC2012.
6. ABCI, Azimuthal Beam Cavity Interaction, http://abci.kek.jp/
7. G. H. Hoffstaetter and I. V. Bazarov, Phys. Rev. ST Acecel Beams 7, 054401 (2004).
8. C. Song and G. Hoffstaetter , “Beam breakup simulation for the Cornell X-Ray ERL”, PAC 2007, Japan. http://www.lepp.cornell.edu/~hoff/papers/07bbu_pac.pdf

3 Workshop and Conference Reports

3.1 The 56th ICFA Advanced Beam Dynamics Workshop on Energy Recovery Linacs, ERL2015

Sergey Belomestnykh, Fermilab
Mail to: sbelomes@fnal.gov

Energy recovery linacs generate a lot of interest in the accelerator and user communities as the recent 56th ICFA Advanced Beam Dynamics Workshop on Energy Recovery Linacs (ERL2015, https://www.bnl.gov/erl2015/) has demonstrated. The workshop was held at Stony Brook University, Stony Brook, NY, USA from June 7 to 12, 2015 and was attended by 114 participants representing institutions from Asia, Europe and USA. ERL2015 was the sixth workshop in the series of international workshops covering accelerator physics and technology of Energy Recovery Linacs.

The scientific program of the workshop was set up by the International Organizing Committee, chaired by S. Belomestnykh (BNL and Stony Brook University), and International Program Committee, chaired by D. Kayran (BNL). The workshop was hosted by Brookhaven National Laboratory, its Local Organizing Committee was chaired by V. Ptitsyn and included P. Manning, A. Petway, C. Hoffman, S. Belomestnykh and D. Kayran.

72 talks were presented during plenary and parallel working group (WG) sessions. Along with “traditional” applications of ERLs such as X-ray light sources, FELs, electron-ion colliders, and electron coolers, several new proposals and ideas were presented at the workshop. Among those are: a compact ultra-high flux X-ray and THz source at John Adams Institute, ERLs for nuclear physics research MESA at Mainz University and particle physics experiments at the jointly proposed BNL/Cornell demonstration multi-pass FFAG machine, γ-ray sources, an ERL facility at CERN for applications and even a concept of lepton ERL scalable to TeV energies presented by V.N. Litvinenko (Stony Brook University and BNL). However, only a few big proposals are actually funded. The field is very active, but is still in the development/demonstration stage. M. Tigner (Cornell University) in his talk outlined challenges to realization of ERLs.

The five working groups covered a wide spectrum of topics essential for ERLs. WG1, convened by T. Kamps (HZB) and A. Bartnik (Cornell University), was dedicated to exploring the results and new technologies available in injectors (lasers,

cathodes, guns) since the previous ERL Workshop. WG2, where conveners were M. Abo-Bakr (HZB) and V. Ptitsyn (BNL), addressed the optics and beam dynamics challenges in ERLs: lessons learnt from past and present ERL operation as well as issues arising during the design work on future ERL facilities. WG3, directed by T. Obina (KEK) and C. Gulliford (Cornell University), discussed beam instrumentation, controls, beam losses and halo management. WG4 was organized by H. Sakai (KEK) and E. Jensen (CERN) focused on Superconducting RF technology, RF and RF control to identify the critical issues of each component in cryomodule construction, assembly works and beam operation for ERL. Finally, V.N. Litvinenko (Stony Brook University and BNL) and O. Bruning (CERN), conveners of WG5, arranged talks on potential applications of the ERL technology, covering a broad range of applications.

There was one poster session, where 12 posters have been presented, including a 3D HDTV demonstration of the BNL's eRHIC FFAG accelerator layout and BNL/Cornell Cbeta project. The two plenary sessions at the end of the workshop were devoted to the summary presentations from each working group.

The detail program and talks are available via the workshop website. The workshop proceedings will be published at JACoW.

Figure 1: ERL2015 Workshop poster.

Figure 2: Participants of the ERL2015 Workshop.

3.2 ICFA Mini-Workshop on Beam Commissioning for High Intensity Accelerators

Sheng Wang and Shinian Fu
Dongguan Branch, Institute of High Energy Physics, No.1, Zhongziyuan road,
Dalang, Dongguan, Guangdong province, 523803, China
Mail to: wangs@ihep.ac.cn

ICFA Mini-workshop on High Intensity Accelerator Commissioning, hosted by the Dongguan Branch of Institute of High Energy Physics, has been held in June 8th-10th 2015 at CSNS site, Dongguan, Guangdong Province of China. The workshop was the first workshop devoted to the high intensity accelerator commissioning. In addition to ICFA, the workshop was also sponsored by IHEP and CCAST (China Center of Advanced Science and Technology).

About 60 experts attended the workshop. The participants come from SNS, FRIB, J-PARC, ISIS, ESS, CERN, C-ADS, Peking University, SSRF, BEPCII and CSNS. The scientific program of the workshop has been set up by Organizing Committee. The organizing committee, as well as the program and collection of talks are available on the indico web site:

http://indico.ihep.ac.cn/conferenceDisplay.py?confId=4749

Totally 4 sessions and a CSNS site tour were arranged for this 3-day workshop. Prof. Li Ma, deputy director of the CSNS, gave a welcome address to welcome the attendees especially those from outside of CSNS.

In the Opening Session, Prof. Shinian Fu presented an overview talk on linac to introduce the challenges and design principles in some high intensity linacs. Prof. Tadashi Koseki presented an overview talk on the high intensity synchrotron, overviewed the High power proton synchrotrons, high luminosity colliders and challenges for high power accelerator operation.

In Linac Session, the commissioning procedure, results and experiences for the linacs of several projects were presented. (1)Dr. Yong Liu presented “Front end, linac upgrade, and commissioning of J-PARC”. Typical procedures for J-PARC linac commissioning are introduced. Front end new hardware (J-PARC RF IS and its test-bench, RFQIII fabricated and installed) commissioning for energy and intensity upgrade were done in 2014. Emittance growth and halo studies, initial twiss parameter setting were lessons learnt in linac upgrade commissioning. (2) Dr. Huafu Ouyang presented “Beam Commissioning of CSNS Front End”. Ion source commissioning, LEBT overview, RFQ cold measurement and RF conditioning, MEBT bunchers RF conditioning were introduced. Up to now, front end beam commissioning and chopping experiments with beam emittance measurement and MEBT BPM test were finished. (3) Dr Zhijun Wang presented “10-mA proton beam commissioning of demo facility of C-ADS Injector II”. A transmission of 96.9% @ 10.5mA and a momentum spread of 0.95% (FWHM) were achieved during the commissioning of RFQ. Bunchers amplitude and phase, transverse emittance were measured, BBA experiment and calibration of HWR cavity amplitude, 10 mA CW beam tuning of MEBT & TCM were done successively. Beam loss detection for the SC linac, MPS for the high beam power machine, and calibration of BPM offset for Solenoid are existing problems and further plans. (4) Fang Yan presented “Front end commissioning for China-ADS Injector-I test

facility". Emittance was measured as 0.14 πmm.mrad during LEBT commissioning. RFQ commissioning was lasted for 4 and a half months and achieved a pulse width of 19.8 ms/20 ms and an RF duty factor of 99%@256 kW, and now is still on the way towards CW. Beam energy, beam profile and emittance were measured during RFQ commissioning. (5) Dr. Andrei Shishlo presented "Commissioning Experience of SNS Linac". Most of used softwares were developed before commissioning and the linac algorithm are now still being improved. The sets of insertable apertures in MEBT to reduce peak current. Present day warm linac tuning procedures are done automatically using OpenXAL app for MEBT-DTL-CCL tuning. Experiences and lessons in linac commissioning were concluded in the talk. The panel discussions were focused on the topics of basic and optional monitors/applications /procedures, Offline vs. online measurements, beam loss problems, identification of halo, keys for improvement.

In Synchrotron Session, the commissioning procedure, experiences, lessons and preparation for commissioning were presented. (1) Dr. Hiroyuki Harada presented "Commissioning experience of J-PARC RCS". Simulation model for beam commissioning was done before the ring optics tuning and the lattice imperfection measurement. Injection tuning, painting injection, foil scattering and extraction kicker field ringing compensation was commissioned for high intensity beam study. (2) Dr. Christopher Warsop presented "Commissioning Experience on the ISIS Ring". ISIS ring commissioning history was introduced. Cavity tuning and Q-damping, feedforward beam compensation and dual harmonic RF upgrade including the TH558 based HPD upgrade, digitized LPRF, anode power supplies, bias power supplies, and bias regulators upgrade were key points in dual harmonics RF system commissioning. (3) Dr. Sheng Wang presented "Preparation for CSNS Accelerator Commissioning". Planed commissioning schedule was listed and simulation results of DTL commissioning, DTL phase scan, the emittance at the exit of RFQ and the field compensation of harmonic injection were given. Finally, discussions focused on uncertain problems. (4) Dr. Michael Plum presented "Commissioning experience of SNS Ring". During low beam power commissioning, some problems especially the tilted beam on the target happened inevitably. Stripper foil failures in two occasions, momentum dump and target failures were high power commissioning issues. Most important/ minimum set of beam instruments and applications were discussed. Lessons was summarized finally. (5) Dr. Rossano Giachino presented "LHC preparation for beam commissioning". It's showed that LHC dry run and machine checkout are very important for beam commissioning after a long shutdown over 2 years. Hardware commissioning including checking magnet circuits, confirming cryogenics performance and beam instruments preparation. Lessons learnt during LHC beam commissioning were discussed finally. The panel discussion was focused on the beam Commissioning experience of ISIS Ring, presented by Christopher Warsop. Machine protection, beam loss control, high intensity tuning and importance of RCS injection set-up were key issues in the beam commissioning of ring.

In Operation Session, many topics related to the operation were presented. (1) Dr. Dapeng Jin presented "CSNS Accelerator Control and Beam Instrumentation". Overall design and progress of CSNS control system including IS, timing system, MPS, FPS, LLRF and BLM station was introduced. Beam instruments along the beam and data acquisition electronics of beam instruments were showed and some of these devices have already been used during front end beam commissioning. (2) Dr. Michael Plum presented "SNS beam loss and control". Beam loss reduction by scraping in MEBT, increasing beam size in SCL, and adjusting quadrupole magnet and RF phase setpoints

were introduced. Occasional beam loss due to RF trips off (due to an interlock), fluctuations in the ion source, drifts in the RF system (e.g. due to temperature in klystron gallery), pulsed magnets miss a pulse or provide only a partial pulse was discussed. Finally gives the plan for further improvements. (3) Dr. Rossano Giachino presented “Beam loss and LHC beam operation”. LHC beam dumping system, beam collimation (cleaning), machine protection system and a concept of beam masking were introduced. During beam commissioning, beam losses and UFO were monitored. Machine protection diagnostics and software interlock were important for machine availability. (4) Dr.Masanori Ikegami presented “Machine and Personnel Protection System”. Challenges and design approaches in PPS were focused on faults analysis, beam inhibit device designs, confinements of radiated air, and the design verification with beam. And in MPS, problems came to be beam loss detection methods, MPS architecture and commissioning strategy. (5) Dr. Fumihiko Tamura presented “LLRF and beam loading cancellation”. Magnet alloy FT-3M loaded RF cavities used in RCS&MR of J-PARC were introduced, which will be upgraded by another high μQf material FT-3L loaded cavities (higher shunt impedance). VME and FPGA based LLRF system functions dual harmonic AVC control and feed forward compensation for heavy beam loading. (6) Dr. Yasuhiro Watanabe presented “Tracking between bending magnet and quadrupole families”. The eddy current effect from 25 Hz excitation was reduced and corrected. The harmonic field correction using field measurement data was imperfection because of the saturation problem of the bending magnet. The harmonic field correction using measured tune data has been successfully demonstrated the reduction of the tune variation during acceleration. (7) Dr. Shouyan Xu presented “Harmonic Injection for Magnets of RCS”. A new method to perform harmonic injection for RCS magnets was tried at CSNS/RCS B/Q, which is based on the transfer function between the current and magnetic field. (8) Dr. Paul Chu presented “XAL and Open XAL Software: the Development and Applications”. Due to its right software architecture and flexible data handling application, XAL are widely used in accelerator controls. Programming Interface/Automation, control system connectivity, online model, tools, GUI framework, general purpose applications and beam tuning applications were discussed. (9) Dr. Weibin Liu presented “Development of Commissioning Software for CSNS”. Some general applications were ported to CSNS, e.g. optics calculation, orbit correction, PASTA, etc. Special applications such as orbit correction of RCS, BBA, kicker settings, collimator Adjustment were developed based on XAL. Some applications with database was under development in magnet manager and model manager, etc. All of these applications need to be test in CSNS commissioning and operation. (10) Dr. Thomas Pelaia presented “ SNS High Level Control Room and Physics Applications”. XAL/Open XAL, EPICS Display Manager and Control System Studio were SNS control room softwares. Sampling of applications such as Energy Manager, Energy Meter, Knobs, Lancher, Linac Tuning, Loss Viewer, Orbit Correciton etc were introduced in detail. Finally a concept and realization of virtual accelerator was shown. In panel discussion, Commissioning Painting Injection at the J-PARC RCS, presented by Yoshiro Irie, Operational Requirement of High-Intensity, Low-Energy Proton Linac for Canther Therapy (BNCT), presented by Shin-ichi Kurokawa, Operation Issues—Software, presented by Paul Chu, led the participants into a hot discussion of accelerator operation.

In the closing session, Dr. Kazuo Hasagawa and Dr. Michael Plum summarized the lianc session and synchrotron session respectively.

The workshop group photo taken beside the sand box of CSNS is shown in the following.

Figure 1: ICFA Mini-workshop group photo.

3.3 Ninth International Accelerator School for Linear Colliders

Weiren Chou, Fermilab
Mail to: chou@fnal.gov

The Ninth International Accelerator School for Linear Colliders was held at Delta Whistler Village Suites, Whistler, British Columbia, Canada from October 26 to November 6, 2015 (http://www.linearcollider.org/school/2015/). This school took place at the same time and same town with the LCWS2015 workshop, a major annual event of the ILC and CLIC. This gave the students an opportunity to meet with the world's best linear collider experts and learn from them. A special joint session was organized by the school and the workshop. The leaders of the linear collider community were very pleased to see many young eager-to-learn students sitting in the audience and listening to their presentations – these students are the future of this field.

This year we received more than 100 applications and 49 students were selected. The selection was based on two criteria: first, if an applicant has financial support from his/her own institute, he or she will be admitted; second, if an applicant needs support, the selection will be based on merit. During the visa application process, however, a number of students unfortunately did not receive visa and could not come, including 5 from China, 3 from Russia, 1 from Thailand, 1 from India and 1 from Ukraine. 36 students who attended the school were divided into three classes: A – linear collider physics, B – linear collider technology, and C – XFEL physics and technology. The curriculum and lecture slides can be found on the school website. On the last day of the

school, each student took a 4-1/2 hour-long final exam. Twelve students with top scores were honoured at the Award Ceremony, each receiving a certificate and a book (*Reviews of Accelerator Science and Technology*, Volume 7, Colliders, published by the World Scientific in 2014).

The 2016 school will be hosted by KEK in Japan. A Local Organizing Committee chaired by Nobuhiro Terunuma has been formed. The venue and dates will be announced in the next newsletter.

4 Recent Doctoral Theses Abstracts

4.1 Heavy-ion Performance of the LHC and Future Colliders

Michaela Schaumann
Mail to: Michaela.Schaumann@cern.ch

Graduation date: 9 October 2015
Institutions: CERN, Geneva, Switzerland,
RWTH Aachen University, Aachen, Germany
Supervisors: Prof. Dr. rer. nat. Achim Stahl (RWTH Aachen University),
Dr. John M. Jowett (CERN)

Abstract

In 2008 the Large Hadron Collider (LHC) and its experiments started operation at the European Centre of Nuclear Research (CERN) in Geneva with the main aim of finding or excluding the Higgs boson. Only four years later, on the 4th of July 2012, the

discovery of a Higgs-like particle was proven and first published by the two main experiments ATLAS and CMS. Even though proton–proton collisions are the main operation mode of the LHC, it also acts as a heavy-ion collider. Here, the term "heavy-ion collisions" refers to the collision between fully stripped nuclei. While the major hardware system of the LHC is compatible with heavy-ion operation, the beam dynamics and performance limits of ion beams are quite different from those of protons. Because of the higher mass and charge of the ions, beam dynamic effects like intra-beam scattering and radiation damping are stronger. Also the electromagnetic cross-sections in the collisions are larger, leading to significantly faster intensity decay and thus shorter luminosity lifetimes. As the production cross-sections for various physics processes under study of the experiments are still small at energies reachable with the LHC and because the heavy-ion run time is limited to a few days per year, it is essential to obtain the highest possible collision rate, i.e. maximize the instantaneous luminosity, in order to obtain enough events and therefore low statistical errors. Within this thesis, the past performance of the LHC in lead-lead (Pb-Pb) collisions, at a center-of-mass energy of 2.76 TeV per colliding nucleon pair, is analyzed and potential luminosity limitations are identified. Tools are developed to predict future performance and techniques are presented to further increase the luminosity. Finally, a perspective on the future of high energy heavy-ion colliders is given.

4.2 Study on Polarization Issues in High Energy Circular Accelerators

Zhe Duan
Mail to: zhe.duan@ihep.ac.cn

Graduation date: 29 May 2015
Institution: Institute of High Energy Physics, CAS, China
Supervisors: Prof. Qing Qin and Prof. Mei Bai

Abstract

Spin is a unique probe in accelerator-based nuclear and particle physics experimental studies. Implementation and optimization of polarized beams in in circular accelerators is a challenging endeavor and includes a lot of interesting questions to be addressed. In this thesis, several topics of stored polarized beams are studied, regarding the polarized proton beams in the Relativistic Heavy Ion Collider (RHIC), as well as polarized electron and positron beams in several electron positron storage rings.

First, a simulation framework of the spin dynamics for polarized proton beam as well as polarized electron and positron beams, is established on the basis of the Polymorphic Tracking Code (PTC). Utilizing the capability of orbital and spin normal form in PTC, the strengths of first order spin resonances can be evaluated, as well as the spin-orbit coupling function with linearized orbital and spin motion. Moreover, stroboscopic averaging is used to compute the invariant spin field in a non-perturbative manner. Finally, a Monte-Carlo simulation of the non-spin-flip synchrotron radiation induced beam depolarization is implemented, to evaluate the equilibrium beam polarization in electron positron storage rings.

RHIC is the world's only polarized proton-proton collider, which can accelerate and smash polarized proton beams with beam energy up to 255GeV, and over 50\% beam

polarization. The polarimeter data indicate moderate polarization deterioration during a typical 8 hours physics store, in the past several polarized proton runs. To understand the physical mechanism behind the polarization loss of stored beam, a careful study of the RHIC history data is presented, by exploring the correlation between measured beam polarization and various beam parameters. In addition, the static beam polarization limit of a practical RHIC lattice is also studied and its dependence on various beam parameters is explored.

Longitudinally polarized electron and positron beams are favored for electron-positron circular colliders in the τ-charm energy range, which are expected to largely enrich the physics program and physics outcome. In this thesis, the feasibility of implementing longitudinally polarized electron and positron beams are preliminarily explored for Beijing Electron Positron Collider (BEPCII).

With the global interests in building a next generation of circular electron-positron colliders, to study the properties of the Higgs boson, and other important topics in particle physics at ultra-high beam energies, it is also important to pursue the possibility of implementing polarized beams at this energy scale. The beam polarization aspects in Circular Electron Positron Collider (CEPC) are discussed, as a section of the CEPC-SPPC Preliminary Conceptual Design Report. Moreover, Monte-Carlo simulations are launched to study a model storage ring with parameters similar to the proposed circular colliders in this energy range, and they are compared with the suggestion that there are different regimes for the spin dynamics underlying the polarization of a beam in the presence of synchrotron radiation at ultra-high beam energies. In particular, it has been suggested that the so-called "correlated" crossing of spin resonances during synchrotron oscillations at current energies, evolves into "uncorrelated" crossing of spin resonances at ultra-high energies. The simulation results support the theory of "uncorrelated" regime at ultra-high energies.

4.3 Preliminary Design of CEPC and Study of Beam-beam Compensation in SPPC

Yuanyuan Guo
Mail to: guoyy@ihep.ac.cn

Graduation date: 18 May 2015
Institution: Institute of High Energy Physics, CAS, China
Supervisor: Prof. Gang Xu

Abstract

The discovery of a Higgs Boson on the Large Hadron Collider (LHC) indicates a new era beyond "Standard Model". To study the property of Higgs and new physics beyond "Standard Model", the high-energy physics community over the world is investigating the feasibility of a Higgs factory. Institute of High Energy Physics(IHEP), Chinese Academy of Sciences(CAS) has proposed to build a circular electron-positron collider which is called CEPC, and later a super proton-proton collider(SPPC) in the same tunnel.

Beam-beam effects are a main factor to limit the performance of colliders. The limitation may be alleviated by compensation techniques.

The one work of this thesis is preliminary design of CEPC and another work is study of beam-beam effects compensation in SPPC. CEPC is a 54.4km long electron positron circular collider which will operate at a centre-of-mass energy of 240GeV. With the given circumference, beam energy and synchrotron radiation power, we started from the required luminosity goal and study some effects which limit the luminosity, then calculated and optimized the beam parameters, finally we got the main parameters and preliminary lattice design of CEPC.

We proposed three types of beam-beam compensation scheme with four beams and analyzed the principle of these schemes in theory. With the limit of strong coherent beam-beam effect, these beam-beam compensation schemes are not beneficial very much, so we improve the scheme and consider the compensation of head-on beam-beam effect with the Energy Recovery Linac (ERL).

We study the head-on beam-beam compensation with ERL in SPPC. With weak-strong and strong-strong beam-beam interaction models, we investigated the effects of head-on beam-beam compensation with ERL on the proton beam dynamics in SPPC. The beam distribution, tune footprint and beam loss rate are analyzed. From the simulation result, we found that ERL can reduce the tune footprint of each bunch and improve the beam lifetime effectively. Therefore bunch current and so the luminosity will increase very much with the beam-beam compensation.

4.4 Study of the Intra-beam Scattering and Touschek Effects for the Beijing Advanced Photon Source

Saike Tian
Mail to: Tiansk@ihep.ac.cn

Graduation date: 15 May 2015
Institution: Institute of High Energy Physics, CAS, China
Supervisor: Prof. Jiuqing Wang

Abstract

Along with the progress in accelerator technology and the growing requirements of brighter photon flux, the scientific case is growing for X-ray applications requiring at least an order of magnitude higher brightness, i.e. exceeding ~ 10^{22} photons s^{-1} mm^{-2} $mrad^{-2}$ (0.1% bandwidth)$^{-1}$, and significantly higher coherent photon flux than presently available.

In order to increase the brilliance, one needs to correspondingly increase the bunch intensity, so a newer generation of storage-ring light sources, named diffracted-limited storage rings (DLSRs), have begun to emerge in the last years, which having horizontal emittance in the few nanometers range. Intra-beam scattering (IBS) describes multiple Coulomb scattering that in electron machines leads to an increase in all bunch dimensions and in energy spread, whereas the Touschek effect concerns large single Coulomb scattering events where energy transfer from transverse to longitudinal leads to immediate particle loss. In low-emittance machines, such as DLSRs, both effects tend to be important: IBS will limit the smallest emittances that can be achieved and the Touschek effect sets the beam lifetime.

We take a design lattice composed of thirty six 7BAs with ε_0 = 51 pm.rad for the Beijing Advanced Photon Source (BAPS), we write a program to study the

incensements of the emittance caused by IBS, and the influence of beam parameters on the growth rate of IBS, which assists in qualitative and quantitative analysis for the intra-beam scattering effect. Further emittance reduction to the level of DLSRs requires a damping wiggler in a region with zero dispersion. The wiggler parameters must be optimized in order to achieve maximum damping efficiency. Touschek lifetime relies strongly on the 6D emittance: it grows with increasing longitudinal emittance which makes higher harmonic cavities for bunch lengthening attractive. Furthermore, the emittance blow up from IBS is also reduced, because they increase the bunch length of the bunch. We evaluate the performance of harmonic RF systems and their interaction with all longitudinal beam dynamics under various operations, we also do some simulations by means of the particle-tracking method. Meanwhile, we do particle tracking for simultaneous long and short electron bunches in the BAPS storage ring by using two harmonic RF systems with different frequencies. A number of possible instabilities and an estimate of their impact on the ring performance are briefly surveyed. The effects considered include fast beam-ion instability, coherent synchrotron radiation, and so on.

5 Forthcoming Beam Dynamics Events

5.1 International Conference on Cyclotrons and their Applications (Cyclotron2016)

The 21st conference in this series will take place from September 11 to 16, 2016 at the Federal Institute of Technology in Zurich, Switzerland.

The International Conference on Cyclotrons and their Applications has a long and healthy history, dating back to the 1950s. The conference takes place every 3 years with the most recent events being held in Vancouver/Canada (2013) and Lanzhou/China (2010). The 2016 edition will be hosted by the Paul Scherrer Institute, PSI, and the Swiss Federal Institute of Technology, ETH. The program covers cyclotron technology, theoretical and numerical aspects of beam dynamics, new concepts, operational aspects of cyclotrons, together with their applications.

The conference will be held in the historic settings of ETH Zurich. There are numerous sights in the former Roman city of Zurich at which you can marvel. You find architecture highlights, historical squares, streets and districts, churches, artworks and lots more. Thanks to its central location in the very heart of Europe, it is easy to reach by plane or train, and it also boasts a first-class infrastructure and public transportation system. The Paul Scherrer Institute is located about 30km from the venue and participants of the conference will have the opportunity to visit the accelerator facilities at PSI, including a number of cyclotrons. The workshop website

http://www.cyc2016.ch

will be regularly updated to include the latest information as it becomes available.

Mike Seidel, IOC Chair Cyclotrons 2016

5.2 High Intensity and High Brightness Hadron Beams (HB2016)

The 57th Advanced Beam Dynamics Workshop on High Intensity and High Brightness Hadron Beams (HB2016) will be held in Malmö, Sweden, from 3rd to 8th of July 2016.

As the previous workshops in this series, HB2016 will be a platform to present and discuss the progress, status and planned developments of physics and technology related to high intensity hadron machines. The main part of the workshop will be oral and discussion sessions for five working groups: Beam Dynamics in Rings, Beam Dynamics in Linacs, Accelerator Systems, Commissioning and Operations, and Beam Instruments and Interactions.

The workshop also includes plenary and poster sessions and provides industrial exhibitors an opportunity to present their cutting edge products to the community.

The workshop website is:
http://hb2016.esss.se

For any questions please contact:
hb2016@esss.se

We are looking forward to your contribution and active participation in making HB2016 another stimulating and memorable workshop.

Mamad Eshraqi, HB 2016 Chair

5.3 International Beam Instrumentation Conference (IBIC 2016)

On behalf of the organizing committee, I am pleased to announce the next International Beam Instrumentation Conference, IBIC 2016, to be held in Barcelona (Spain) from September 11 to 15, 2016.

IBIC 2016, hosted by the ALBA synchrotron, is an international conference focused broadly on beam instrumentation and diagnostics for particle accelerators.

The conference venue is the World Trade Center, set right on the Barcelona harbour (Port Vell), in the heart of the city and surrounded by a wide offer of hotels and restaurants.

For more information, visit our website:
http://www.ibic2016.org/news/IBIC2016_NEWS_191115.html

We look forward to welcoming you to Barcelona, so please save the dates!

Francis Perez, Conference Chair
Ubaldo Iriso, Scientific Chair

6 Announcements of the Beam Dynamics Panel

6.1 ICFA Beam Dynamics Newsletter

6.1.1 Aim of the Newsletter

The ICFA Beam Dynamics Newsletter is intended as a channel for describing unsolved problems and highlighting important ongoing works, and not as a substitute for journal articles and conference proceedings that usually describe completed work. It is published by the ICFA Beam Dynamics Panel, one of whose missions is to encourage international collaboration in beam dynamics.

Normally it is published every April, August and December. The deadlines are 15 March, 15 July and 15 November, respectively.

6.1.2 Categories of Articles

The categories of articles in the newsletter are the following:

1. Announcements from the panel.
2. Reports of beam dynamics activity of a group.
3. Reports on workshops, meetings and other events related to beam dynamics.
4. Announcements of future beam dynamics-related international workshops and meetings.
5. Those who want to use newsletter to announce their workshops are welcome to do so. Articles should typically fit within half a page and include descriptions of the subject, date, place, Web site and other contact information.
6. Review of beam dynamics problems: This is a place to bring attention to unsolved problems and should not be used to report completed work. Clear and short highlights on the problem are encouraged.
7. Letters to the editor: a forum open to everyone. Anybody can express his/her opinion on the beam dynamics and related activities, by sending it to one of the editors. The editors reserve the right to reject contributions they judge to be inappropriate, although they have rarely had cause to do so.

The editors may request an article following a recommendation by panel members. However anyone who wishes to submit an article is strongly encouraged to contact any Beam Dynamics Panel member before starting to write.

6.1.3 How to Prepare a Manuscript

Before starting to write, authors should download the template in Microsoft Word format from the Beam Dynamics Panel web site:

http://www-bd.fnal.gov/icfabd/news.html

It will be much easier to guarantee acceptance of the article if the template is used and the instructions included in it are respected. The template and instructions are expected to evolve with time so please make sure always to use the latest versions.

The final Microsoft Word file should be sent to one of the editors, preferably the issue editor, by email.

The editors regret that LaTeX files can no longer be accepted: a majority of contributors now prefer Word and we simply do not have the resources to make the conversions that would be needed. Contributions received in LaTeX will now be returned to the authors for re-formatting.

In cases where an article is composed entirely of straightforward prose (no equations, figures, tables, special symbols, etc.) contributions received in the form of plain text files may be accepted at the discretion of the issue editor.

Each article should include the title, authors' names, affiliations and e-mail addresses.

6.1.4 **Distribution**

A complete archive of issues of this newsletter from 1995 to the latest issue is available at

http://icfa-usa.jlab.org/archive/newsletter.shtml.

This is now intended as the primary method of distribution of the newsletter.

Readers are encouraged to sign-up for electronic mailing list to ensure that they will hear immediately when a new issue is published.

The Panel's Web site provides access to the Newsletters, information about future and past workshops, and other information useful to accelerator physicists. There are links to pages of information of local interest for each of the three ICFA areas.

Printed copies of the ICFA Beam Dynamics Newsletters are also distributed (generally some time after the Web edition appears) through the following distributors:

Weiren Chou	chou@fnal.gov	North and South Americas
Rainer Wanzenberg	rainer.wanzenberg@desy.de	Europe[++] and Africa
Toshiyuki Okugi	toshiyuki.okugi@kek.jp	Asia[**]and Pacific

++ Including former Soviet Union.

** For Mainland China, Jiu-Qing Wang (wangjq@mail.ihep.ac.cn) takes care of the distribution with Ms. Su Ping, Secretariat of PASC, P.O. Box 918, Beijing 100039, China.

To keep costs down (remember that the Panel has no budget of its own) readers are encouraged to use the Web as much as possible. In particular, if you receive a paper copy that you no longer require, please inform the appropriate distributor.

6.1.5 **Regular Correspondents**

The Beam Dynamics Newsletter particularly encourages contributions from smaller institutions and countries where the accelerator physics community is small. Since it is impossible for the editors and panel members to survey all beam dynamics activity worldwide, we have some Regular Correspondents. They are expected to find interesting activities and appropriate persons to report them and/or report them by themselves. We hope that we will have a "compact and complete" list covering all over the world eventually. The present Regular Correspondents are as follows:

Liu Lin	Liu@ns.lnls.br	LNLS Brazil
Sameen Ahmed Khan	Rohelakan@yahoo.com	SCOT, Oman

Jacob Rodnizki Jacob.Rodnizki@gmail.com Soreq NRC, Israel
Rohan Dowd Rohan.Dowd@synchrotron.org.au Australian Synchrotron

We are calling for more volunteers as Regular Correspondents.

6.2 ICFA Beam Dynamics Panel Members

Name	eMail	Institution
Rick Baartman	baartman@lin12.triumf.ca	TRIUMF, 4004 Wesbrook Mall, Vancouver, BC, V6T 2A3, Canada
Marica Biagini	marica.biagini@lnf.infn.it	INFN-LNF, Via E. Fermi 40, C.P. 13, Frascati, Italy
John Byrd	jmbyrd@lbl.gov	Center for Beam Physics, LBL, 1 Cyclotron Road, Berkeley, CA 94720-8211, U.S.A.
Yunhai Cai	yunhai@slac.stanford.edu	SLAC, 2575 Sand Hill Road, MS 26 Menlo Park, CA 94025, U.S.A.
Swapan Chattopadhyay	swapan@fnal.gov	Northern Illinois University, Dept. of Physics, DeKalb, Illinois, 60115, U.S.A.
Weiren Chou (Chair)	chou@fnal.gov	Fermilab, MS 220, P.O. Box 500, Batavia, IL 60510, U.S.A.
Wolfram Fischer	wfischer@bnl.gov	Brookhaven National Laboratory, Bldg. 911B, Upton, NY 11973, U.S.A.
Yoshihiro Funakoshi	yoshihiro.funakoshi@kek.jp	KEK, 1-1 Oho, Tsukuba-shi, Ibaraki-ken, 305-0801, Japan
Jie Gao	gaoj@ihep.ac.cn	Institute for High Energy Physics, P.O. Box 918, Beijing 100039, China
Ajay Ghodke	ghodke@cat.ernet.in	RRCAT, ADL Bldg. Indore, Madhya Pradesh, 452 013, India
Ingo Hofmann	i.hofmann@gsi.de	High Current Beam Physics, GSI Darmstadt, Planckstr. 1, 64291 Darmstadt, Germany
Sergei Ivanov	sergey.ivanov@ihep.ru	Institute for High Energy Physics, Protvino, Moscow Region, 142281 Russia
In Soo Ko	isko@postech.ac.kr	Pohang Accelerator Lab, San 31, Hyoja-Dong, Pohang 790-784, South Korea
Elias Metral	elias.metral@cern.ch	CERN, CH-1211, Geneva 23, Switzerland
Yoshiharu Mori	mori@rri.kyoto-u.ac.jp	Research Reactor Inst., Kyoto Univ. Kumatori, Osaka, 590-0494, Japan
George Neil	neil@jlab.org	TJNAF, 12000 Jefferson Ave., Suite 21, Newport News, VA 23606, U.S.A.
Toshiyuki Okugi	toshiyuki.okugi@kek.jp	KEK, 1-1 Oho, Tsukuba-shi, Ibaraki-ken, 305-0801, Japan
Mark Palmer	mapalmer@fnal.gov	Fermilab, MS 221, P.O. Box 500, Batavia, IL 60510, U.S.A.
Chris Prior	chris.prior@stfc.ac.uk	ASTeC Intense Beams Group, STFC RAL, Chilton, Didcot, Oxon OX11 0QX, U.K.
Yuri Shatunov	Yu.M.Shatunov@inp.nsk.su	Acad. Lavrentiev, Prospect 11, 630090 Novosibirsk, Russia
Jiu-Qing Wang	wangjq@ihep.ac.cn	Institute for High Energy Physics, P.O. Box 918, 9-1, Beijing 100039, China
Rainer Wanzenberg	rainer.wanzenberg@desy.de	DESY, Notkestrasse 85, 22603 Hamburg, Germany